

MECHANISTIC STUDIES ON HORSERADISH PEROXIDASE AND ITS ROLE
IN THE CATALYSIS OF OXIDATION REACTIONS

A Dissertation

Presented to the Faculty of the Graduate School

of Cornell University

In Partial Fulfillment of the Requirements for the Degree of

Doctor of Philosophy

by

Raheleh Ravanfar

December 2019

© 2019 Raheleh Ravanfar

MECHANISTIC STUDIES ON HORSERADISH PEROXIDASE AND ITS ROLE
IN THE CATALYSIS OF OXIDATION REACTIONS

Raheleh Ravanfar, Ph. D.

Cornell University 2019

The catalyzed oxidation reactions by horseradish peroxidase (HRP) comprise a conversion of the ferric state of the heme to the ferryl heme by hydrogen peroxide (H_2O_2). However, studies barely investigate the effect of other components in the reaction mixtures on HRP function. Thus, we desire to investigate the HRP-catalyzed oxidation reactions in exposure to histidine (His). Herein, we report the first use of His and HRP to initiate the photocatalytic oxidation reactions without the exogenous addition of hydrogen peroxide. We demonstrate that the oxidation reactions of organic molecules proceed 2-times faster using HRP/His system in comparison with HRP/ H_2O_2 system. During this work, we noticed that non-aromatic amino acids are fluorescent in solid state. We also demonstrate that the polymorph A crystal of L-His contains hydrophobic domains within the structure's interior, which can serve as vehicles for the highly efficient entrapment and transport of hydrophobic small molecules.

Despite the importance of H_2O_2 in the HRP-catalyzed reactions, the detection and quantification of low concentrations of H_2O_2 is still limited using current methods. In this regard, we demonstrate that high-valent iron-oxo intermediates of HRP are well suited to detect ultratrace amount of H_2O_2 impurities in alcohols in the range of 0.001–

1000 μM using just a UV/Vis spectrophotometer. We monitor the optical spectra of low concentrations of HRP (0.1-1 μM) for the red shift in the Soret and Q-band regions upon the addition of alcohols, as well as the reversibility of this shift to the original wavelength over time due to the spontaneous decay of ferryl intermediates to the ferric state.

The motivation for this thesis lie in an industrially-funded project on Cheddar cheese. The aim of this project was to obtain white whey from the yellow whey proteins recovered from the Cheddar cheese making process without using oxidative agents. To address this issue, we conducted several experiments which resulted in all fascinating chapters of this thesis based on our observations, while none of them solved the problem. Thus, we designed microcapsules, which release the cargo only when exposed to lipase during the ripening step, selectively coloring the cheese matrix and obtaining the white whey.

BIOGRAPHICAL SKETCH

The author was born April 10th, 1987 in Shiraz, Iran, and raised by her parents, Baha Ravanfar and Zahra Karimi, alongside her siblings, Najme, Mahdi, Fahime, and Nastaran. She originally became interested in science as a child when she was fascinated by discovery and analysis of the insects and flowers. She finished her high school being recognized as a “gifted student” in 2005. She was ranked among the first 0.3% of total applicants in Iran’s national exam and admitted to Shiraz University (Pahlavi), where she began studying in the highly regarded Food Science and Technology program. Continuing on her graduate studies, her research became her passion and she endeavored every day to be creative and productive. After earning both her B.S. and M.S. degrees in 2012, she decided to expand her knowledge in the United States. She believed that immigration brings her the greatest educational and professional satisfaction, although she realized this would be difficult to live so far away from her family. She began her second master’s degree in the Department of Chemistry at Ball State University in Indiana, establishing a solid background in chemistry. Her background led her to pursue her Ph.D. studies in food science at Cornell University with minors in pharmacology and chemical biology.

Raheleh joined Alireza Abbaspourrad’s laboratory in June of 2016, where she focused on methods bridging chemistry, drug development, and protein chemistry to investigate the mechanism of heme-containing enzymes and their role in catalysis. She wrote 9 first-author articles (published/submitted) during her PhD, and has more than 5 articles in collaboration with her lab mates. She looks forward to continuing her passion for hard work and scientific inquiry in bioinorganic chemistry during post doc.

for my family

ACKNOWLEDGMENTS

I would like to acknowledge everyone who has helped with my personal development, giving me the courage for this achievement. First and foremost, I would like to thank Professor Alireza Abbaspourrad, who has been an excellent mentor, always showing enthusiasm and support for my projects and career development. He truly is an exemplary graduate advisor and scientist; following his guidance is a real privilege to success. I owe a great debt of gratitude to Dr. Serena DeBeer and Dr. Chris Pollock, and Dr. Warren Zipfel, whom we collaborated with throughout my graduate work, and they helped me tremendously with their invaluable comments and supports. I would also like to acknowledge Dr. Justin Wilson, Dr. Brian Crane and Dr. Boris Dzikovski. They have offered me advice on numerous occasions. Additionally, I made great friends in all these laboratories: Sergio Jannuzzi, Nelli Kremer, Maurice Van Gastel, Casey Van Stappen and Joshua Woods. I have been very fortunate to have Dr. Barbara Baird and Dr. Richard Cerione as my committee members. They are excellent Professors and mentors; it has been a real pleasure to learn from them. I have also been fortunate to grow within the dynamic laboratory that could only be Ali's. To the Ali's laboratory members, who have always offered me sound advice and guidance, both scientifically and personally, and I am very grateful to have had the pleasure of working alongside all of you. There are faculty in the Department of Food Science that need acknowledgement: Dr. David Barbano, Dr. Terry Acree, Dr. Robin Dando, Dr. Chang Lee, Dr. Carmen Moraru, Dr. Olga Padilla-Zakour, Dr. Gavin Sacks, Dr. Martin Wiedmann, Dr. Sam Alcaine, Dr. John Brady, Dr. Patrick Gibney, Dr. Julie Goddard, Dr. Rui Hai Liu, Dr. Dennis Miller, Dr. Motoko Mukai, Dr. Sam Nugen, Dr.

Syed Rizvi, Dr. Randy Worobo, and Dr. Kathryn Boor (the Dean of the CALS), who have been a noteworthy source of encouragement and I can't quite express how much I appreciate. I also appreciate all the staff in the Department of Food Science. One that requires significant highlight is Erin Atkins, who I admire for her considerable brilliance, kindness and helpfulness. And last, but surely not least, I dedicate this achievement to my family: Mom, Dad, Nastaran, Mahdi, Najme, and Fahime. There really are no words adequate to describe my gratitude for your love, patience, and unconditional support. It hasn't gone overlooked or unappreciated, and this achievement is truly yours to share. Although distance has separated us, we have remained as close as we were living together. Thank you all.

TABLE OF CONTENTS

Table of Contents

CHAPTER 1	1
INTRODUCTION	1
1.1. The conceptual origin and motivation	1
1.2. The mechanism of HRP in oxidation of organic substrates.....	4
CHAPTER 2.....	10
CATALYZED OXIDATION OF CAROTENOIDS BY LACTOPEROXIDASE IN THE PRESENCE OF ETHANOL ¹	10
ABSTRACT	10
2.1. INTRODUCTION.....	11
2.2. MATERIALS AND METHODS	13
2.2.1. Materials.....	14
2.2.2. Decoloration of carotenoids by the addition of either ethanol or hydrogen peroxide.....	14
2.2.3. Extraction and quantification of norbixin from whey proteins	14
2.2.4. Assessment of the whey proteins by UV-VIS spectrophotometry.....	15
2.2.5. Color analysis	16
2.2.6. Direct Analysis in Real Time Mass Spectrometry (DART-Mass).....	16
2.2.7. Lactoperoxidase activity	16
2.2.8. Fourier Transform Infrared Spectroscopy (FTIR)	17
2.2.9. Cyclic voltammetry	17
2.2.10. Assessment of the pure lactoperoxidase upon the addition of ethanol	17
2.3. RESULTS AND DISCUSSION.....	18
2.4. CONCLUSION	27
2.5. SOPPORTING INFORMATION	27
Contributions	34
CHAPTER 3.....	35
HIGH-VALENT IRON-OXO COMPOUND OF HORSERADISH PEROXIDASE AS A CRITICAL INTERMEDIATE FOR THE DETECTION OF ULTRATRACE AMOUNT OF HYDROGEN PEROXIDE IN ALCOHOLS.....	35
ABSTRACT	35
3.1. INTRODUCTION.....	36
3.2. MATERIALS AND METHODS	39
3.2.1. Materials.....	39
3.2.2. Detection of H ₂ O ₂ through the Analysis of the Ferric State of HRP and its Ferryl Intermediate Using UV/Vis Spectrophotometry	39

3.2.3. Analysis of the Ferric State of HRP and its Ferryl Intermediate Using Cyclic Voltammetry	40
3.2.5. Quantification of H ₂ O ₂ through the Oxidation of ABTS	41
3.2.6. Statistical Analysis	41
3.3. RESULTS AND DISCUSSION.....	41
3.4. CONCLUSION	56
3.5. SUPPORTING INFORMATION	57
Contributions	64
CHAPTER 4.....	65
THE MOLECULAR MECHANISM OF PHOTOCATALYTIC REACTIONS BY HORSE RADISH PEROXIDASE IN THE PRESENCE OF HISTIDINE	65
.....	65
ABSTRACT	65
4.1. INTRODUCTION.....	66
4.2. MATERIALS AND METHODS	68
4.2.1. Materials.....	68
4.2.2. Purification of HRP.....	69
4.2.3. Preparation of reaction mixtures	69
4.2.4. Kinetic studies on the oxidation of NBX using HRP/His and HRP/H ₂ O ₂ systems	70
4.2.5. Conformation Analysis Using UV/Vis Spectrophotometry.....	70
4.2.6. Analysis of HRP/His system using EPR Spectroscopy	71
4.2.7. Analysis of the oxidized products of NBX using LC-MS	71
4.3. RESULTS AND DISCUSSION.....	72
4.4. CONCLUSION	85
4.5. SUPPLEMENTARY INFORMATION	86
CHAPTER 5.....	92
STRUCTURAL CHEMISTRY ENABLES FLUORESCENCE OF AMINO ACIDS IN THE CRYSTALLINE SOLID STATE.....	92
ABSTRACT	92
5.1. INTRODUCTION.....	93
5.2. MATERIALS AND METHODS	95
5.2.1. Preparation of the amino acid crystals	95
5.2.2. Characterization	96
5.3. RESULTS AND DISCUSSION.....	97
5.4. CONCLUSION	106
5.5. SUPPORTING INFORMATION	106
Contributions	117
CHAPTER 6.....	118

L-HISTIDINE CRYSTALS AS EFFICIENT VEHICLES TO DELIVER HYDROPHOBIC MOLECULES	118
ABSTRACT	118
6.1. INTRODUCTION.....	119
6.2. MATERIALS AND METHODS	121
6.2.1. Preparation and characterization of the L-His crystals with entrapped small molecules.....	121
6.2.2. Synthesis of thiolated HA (SH-HA)	123
6.2.3. Synthesis of thiolated histidine methyl ester (SH-HME).....	124
6.2.4. Synthesis of HAase-responsive, HA-modified histidine crystals with entrapped DOX (HA-His crystals).....	124
6.2.5. In Vitro Enzyme-Triggered Drug Release of DOX-Loaded HA-His crystals	125
6.2.6. Statistical analysis	126
6.3. RESULTS AND DISCUSSION.....	126
6.4. CONCLUSION	139
6.5. SUPPORTING INFORMATION	140
Contributions	142
CHAPTER 7.....	143
CONTROLLING THE RELEASE FROM ENZYME-RESPONSIVE MICROCAPSULES WITH A SMART NATURAL SHELL ¹⁶	143
ABSTRACT	143
7.1. INTRODUCTION.....	144
7.2. MATERIALS AND METHODS	146
7.2.1. Materials.....	146
7.2.2. Preparation of color-loaded microcapsules	146
7.2.3. Characterization of microcapsules	147
7.2.4. Employing the microcapsules in the Cheddar cheese making process	150
7.2.5. Statistical analysis	151
7.3. RESULTS AND DISCUSSION.....	151
7.4. CONCLUSIONS	165
7.5. SUPPORTING INFORMATION	166
Contributions	170
CHAPTER 8.....	171
CONCLUSION AND FUTURE DIRECTIONS	171

CHAPTER 1

INTRODUCTION

1.1.The conceptual origin and motivation

The story of my thesis on horseradish peroxidase (HRP) begins with a result from an industrial project on Cheddar cheese funded by National Dairy Council (NDC).¹ The project was on presenting an alternative method to obtain the white whey proteins from the yellow-colored whey proteins recovered from the Cheddar cheese making process. This yellow color of whey proteins from the Cheddar cheese making process is due to the presence of annatto.¹⁻² Annatto is a common yellowish-red colorant used in the production of Cheddar cheese. This colorant is extracted from *Bixa orellana* L. seeds and is composed of two main carotenoids, the oil-soluble bixin and water-soluble norbixin.³ A fraction of Annatto used in the production of Cheddar cheese is transferred to whey. The carryover colorant in whey negatively impact the visual quality of the resultant powder, and could induce allergic responses, which is a concern when the powder is to be used as an ingredient in other products, such as infant formula and food supplements.² Current strategy used by dairy industries is based on chemical methods (bleaching with hydrogen peroxide or benzoyl peroxide), with additional operational costs and quality concerns. These chemical methods harness the native lactoperoxidase system of milk to decolor yellow whey proteins recovered from colored Cheddar cheese.⁴ Lactoperoxidase catalyzes the formation of thiocyanate radicals in milk upon the addition of hydrogen peroxide, which reacts with the heme center of lactoperoxidase to form ferryl intermediates.⁵⁻⁶ These thiocyanate radicals are subsequently quenched by carotenoids, disturbing their conjugated double bonds⁷⁻⁸ and decoloring the

carotenoids in ~30 minutes due to the loss of visible light absorption by their conjugated π -system.⁹⁻¹⁰ The carotenoids may eventually decompose to carbonyl products including aldehydes and ketones, resulting in oxidized flavors development in bleached whey.¹¹ Some unsaturated decomposition products of annatto can also react with whey components, for instance, 3-acetylacrylic acid reacts with cysteine.¹² These reactions decrease the nutritive value of final whey protein product.² Moreover, the resulted whey protein concentrate and powder after bleaching using these oxidizing agents has a higher concentration of compounds from lipid oxidation than untreated samples, which negatively affect sensory attributes.² Considering the nutritional and functional value of whey proteins, and increased demand for these compounds by food and pharmaceutical industries, different methods have been investigated to reduce the amount of carryover colorant in the resultant whey protein powder.^{8, 13-14} Current strategies used by the dairy industry or that have been proposed to address this issue are based on physical (e.g., microfiltration),¹³ enzymatic (e.g., using lactoperoxidase),⁸ and chemical methods (e.g., discoloration/bleaching with hydrogen or benzoyl peroxide).¹⁴

Our primary mission to solve this issue and find an alternative method to obtain the white whey was to extract annatto from the colored whey using a food-grade solvent, ethanol. However, upon the addition of ethanol we observed the whey to turn white in less than 5 s without the addition of any exogenous oxidizing agent. This observation sparks our attention to question if the addition of ethanol causes the oxidation of carotenoids in the presence of whey proteins. Thus, we thoroughly studied the catalyzed oxidation of carotenoids by lactoperoxidase in the presence of ethanol (**Chapter 2**).¹⁵ The results of this study showed that the heme in lactoperoxidase is affected by ethanol.

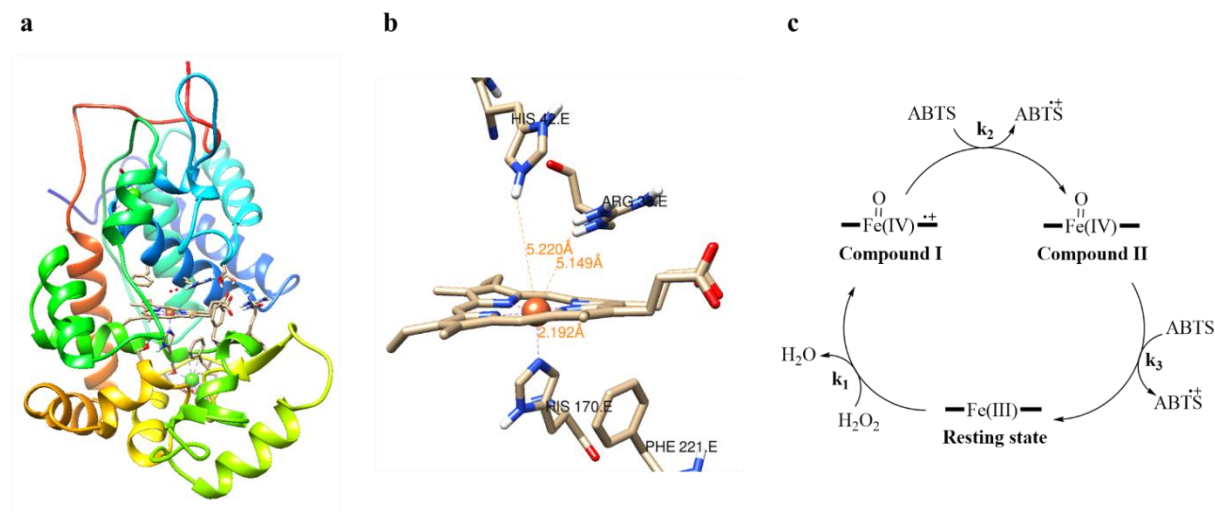
Thus, we proposed two hypothesis: first, ethanol can bind to the iron at the heme center of lactoperoxidase; second, ethanol can cause a conformational change in the enzyme in the way that the distal histidine at the top of heme center can bind to the iron at the heme center. We decided to use HRP to investigate these hypothesis because of its availability and the similarity of its heme structure to the heme structure of lactoperoxidase. We tested our first hypothesis, investigating the effect of ethanol on HRP. The results showed that ethanol contains adventitious amount of H₂O₂, which is not detectable by the current available methods such as hydrogen peroxide test strips. We showed that this adventitious amount of H₂O₂ was the reason for catalysis of oxidation reactions of carotenoids in the presence of heme-containing enzymes, such as lactoperoxidase and HRP. Our study resulted in presenting a new method to identify ultratrace amount of H₂O₂ in alcohols (**Chapter 3**). In parallel to test of the first hypothesis, we also examined the second hypothesis. We added exogenous histidine solution to the HRP to investigate the binding of histidine to the iron at the heme center. Despite our hypothesis, histidine could not react with the iron at the heme center. However, we demonstrate that histidine initiate a new photocatalytic pathway of HRP without the addition of exogenous H₂O₂ (**Chapter 4**). The study on HRP/histidine system also resulted in two new discoveries: first, the crystallization-induced fluorescence of amino acids in the crystalline solid state (**Chapter 5**); second, the L-histidine crystals contain hydrophobic domains within the structure's interior, and can serve as vehicles for the highly efficient entrapment and transport of hydrophobic small molecules (**Chapter 6**).¹⁶ None of these studies can address the issues associated with obtaining the white whey protein from the yellow whey recovered from the Cheddar

cheese making process. However, the last study on the entrapment of hydrophobic small molecules in L-histidine crystals motivated us to propose a microencapsulation technique as an alternative to obtain the white whey. Thus, we present a natural and simple enzyme-responsive core-shell-structured microcapsule to encapsulate carotenoids in the core and control their release only when exposed to lipase. Since lipases are mainly found in cheese curds during cheese ripening, we apply the platform to selectively deliver the color to the cheese curd by lipase-triggered release, leaving the whey proteins colorless (**Chapter 7**).¹⁷ Although we started from Cheddar cheese, we could propose the special capabilities of HRP in this work, which can expand its application in immunochemistry,¹⁸ diagnostic assays,¹⁹ chemical reactions,²⁰ bioremediation,²¹ and fuel cells.²²

1.2. The mechanism of HRP in oxidation of organic substrates

Peroxidases are oxidoreductase enzymes that exhibit a crucial protective effect in preventing oxidative damage of cellular components caused by hydrogen peroxide (H_2O_2).²³ Horseradish peroxidase (HRP) is one of the most extensively used peroxidases in immunochemistry, diagnostic assays, chemical reactions, and bioremediation.²⁴⁻²⁷ The broad application range of HRP is due to its ability to translate catalysis into an electrochemical signal, as well as its stability and commercial availability.²⁸ HRP is able to catalyze the heterolytic cleavage of the peroxidic bond in H_2O_2 and form a high-valent iron-oxo (ferryl heme) intermediate of the enzyme (compound I).²⁹⁻³² In compound I, the iron at the heme center is oxidized from Fe^{III} to $\text{Fe}^{\text{IV}}=\text{O}$, and the porphyrin or an amino acid in the side chain of HRP is oxidized to a radical.³³ Thus,

compound I oxidizes two molecules of substrate through two consecutive single electron reactions to form compound II, and finally reduced back to the Fe^{III} state (Scheme 1.1).³³⁻³⁹ These compound I and II are the crucial intermediates in a diverse group of catalytic heme enzymes and are involved in many processes, including drug metabolism and other important oxidation reactions.⁴⁰



Scheme 1.1. a) The crystal structure of horseradish peroxidase, isozyme C (PDB entry 1ATJ).⁴¹ b) Active site of horseradish peroxidase based on the crystal structures of HRP isozyme C (PDB entry 1ATJ).⁴¹ c) Reactions catalyzed by horseradish peroxidases using hydrogen peroxide (H₂O₂). The catalytic cycle begins with compound I formation. Compound I recovers the resting state via the peroxidatic reaction, in which compound I sequentially reacts with two molecules of a one-electron donating substrate (e.g., ABTS), passing through another intermediate named compound II.

The active sites of peroxidases are generally accessible to solvent molecules, thus it is believed that water molecules play a key role in catalysis.^{38, 42} Studies have suggested that the mechanism of compound I formation includes the catalytic distal His, which

shuttles a proton from the iron-linked peroxide oxygen atom to the distal peroxide oxygen atom. This proton-transfer is mediated by a water molecule and promotes the heterolytic fission of the O-O bond.⁴³⁻⁴⁴ Thus, one can imagine the importance of the solvent used in the reactions catalyzed by HRP. Moreover, two key catalytic residues in the distal heme pocket are involved in peroxide activation and the two-step mechanism of compound I formation, including (1) charge stabilization of the enzyme-substrate precursor complex by Arg 38 and (2) acid-base catalysis by His 42. These two residues catalyze the proton transfer between the oxygen atoms of heme-bound H₂O₂ and polarize the O-O bond.³⁹ The polar character of Arg 38 may facilitate the access of the H₂O₂ molecule to the heme and/or provide an electrostatic interaction with the incoming peroxide, which may also induce the deprotonation of H₂O₂ at neutral pH.⁴⁵ Studies also show that Arg 38 not only modulates the formation of compound I by facilitating the binding of H₂O₂ to the heme, but also changes the reactivity of both compound I and compound II.⁴⁵ However, the exact role of His 42 and Arg 38 has not been resolved, and the exact nature of the reducing substrate binding site of HRP is still not known. Blumberg, et al. ⁴⁶ have shown the optical spectra of the ferryl heme intermediate of HRP, which has a Soret of 418 nm and two Q-bands of 528 nm and 553 nm (Figure 1.1, A). Ascorbate peroxidase also shows almost the same features for the ferryl intermediate (Figure 1.1, B).

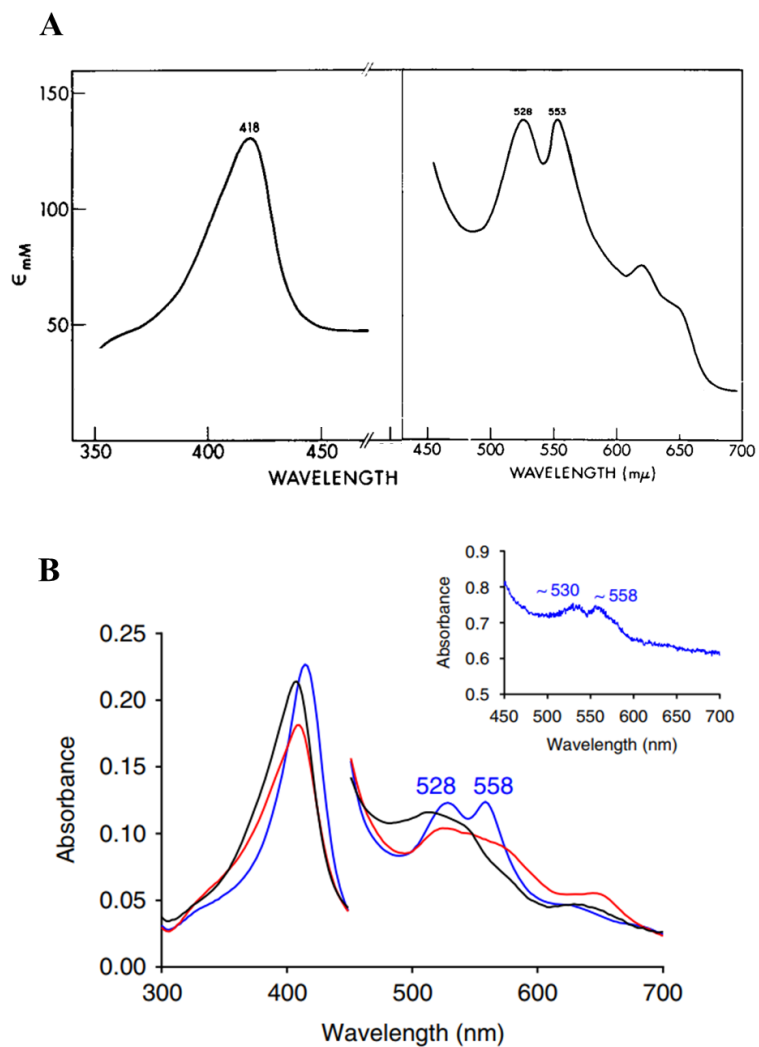


Figure 1.1. **A**) Optical spectra of the ferryl intermediate of HRP, generated through the addition of H_2O_2 ,⁴⁶ **B**) Optical spectra of the ferryl intermediate of ascorbate peroxidase generated through the addition of H_2O_2 .⁴⁷

Previous studies of HRP and H_2O_2 have also characterized the formation of compound I using electron paramagnetic resonance (EPR), and show that HRP with H_2O_2 generates a broad EPR signal characteristic of compound I, oxyferryl porphyrin π -cation radical ($g = 2.0$, Figure 1.2, A-D).³⁹ This signal must have arisen from a radical cation located

more than $\sim 10 \text{ \AA}$ from the iron because it was relatively easily saturated and remained observable above 40 K (Figure 1.2, Ab).³⁹

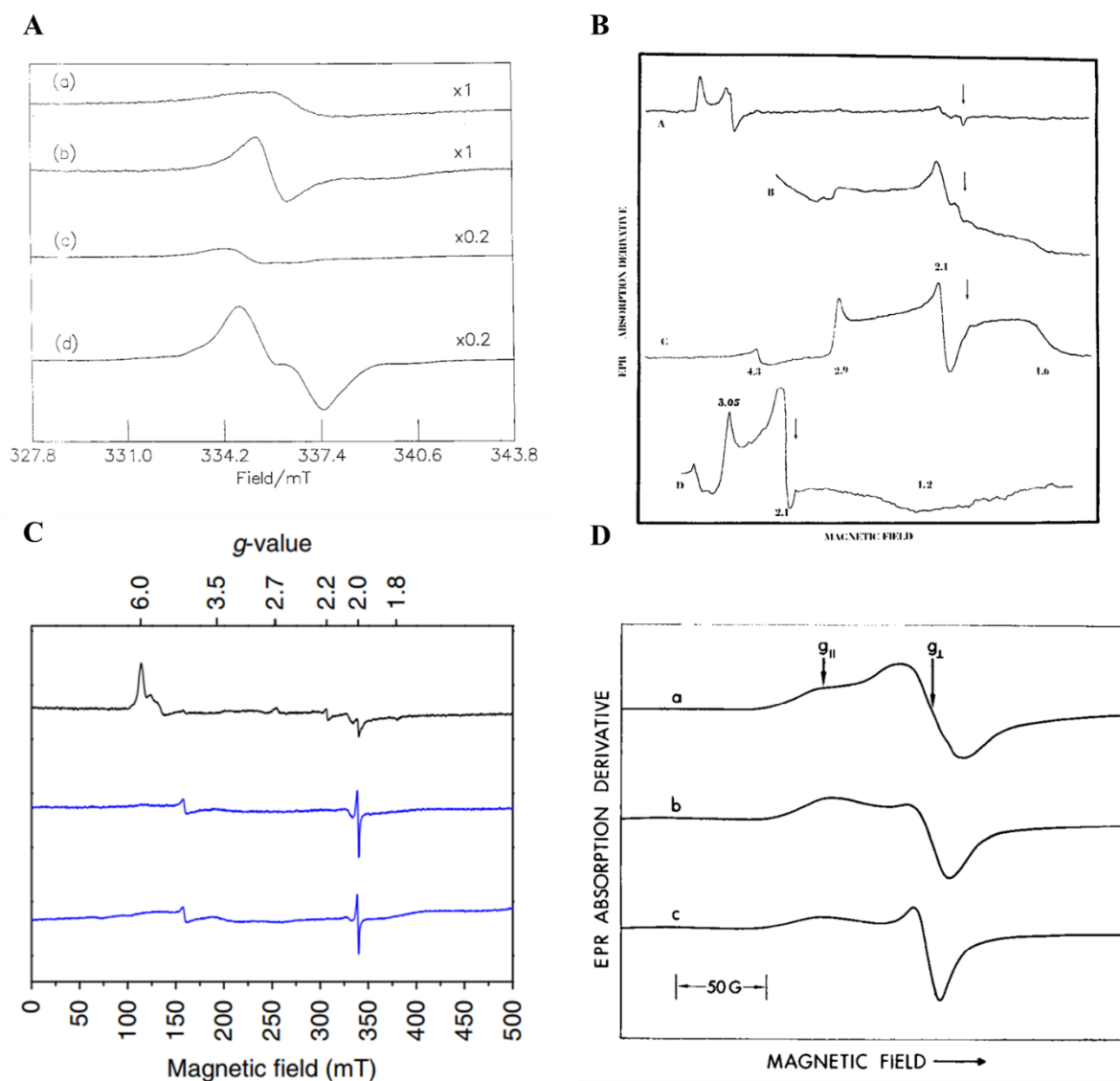


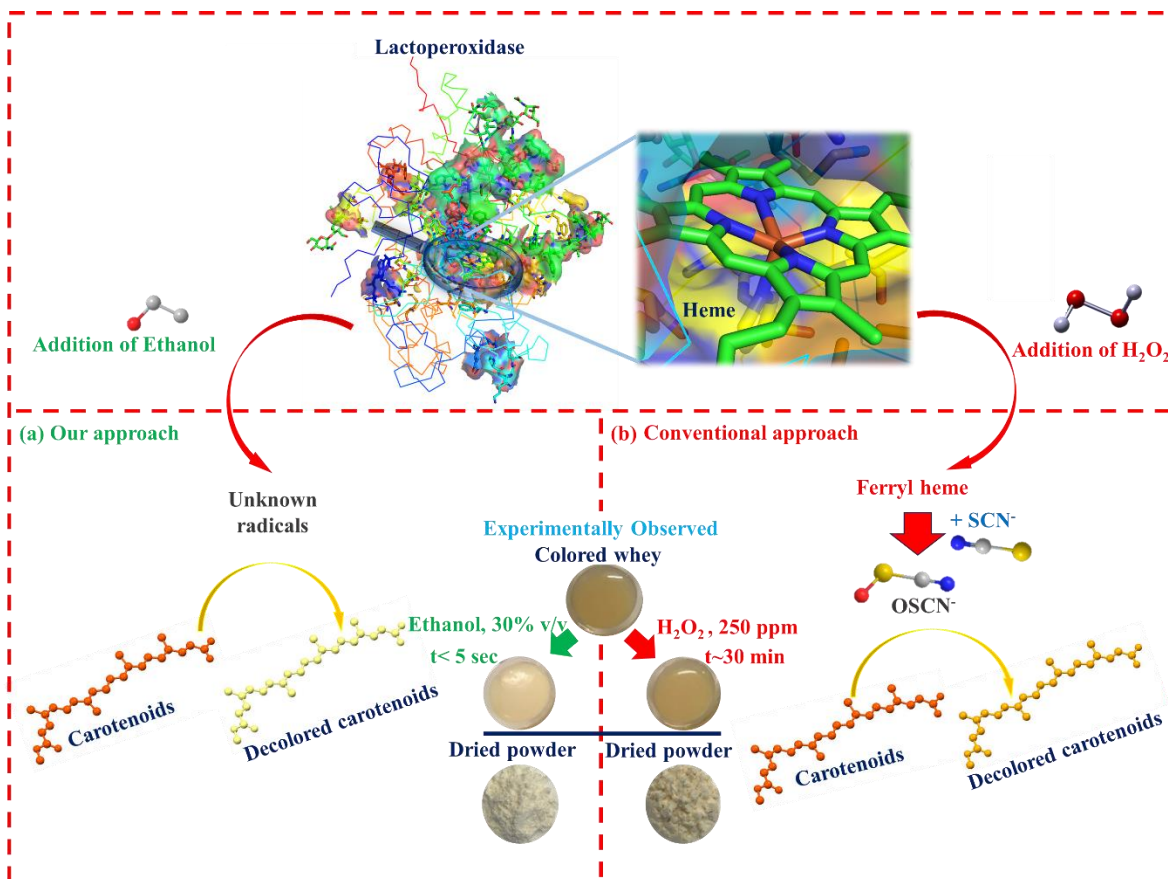
Figure 1.2. **A)** EPR spectra of (a) compound I formed after 2 s reaction of HRP with stoichiometric H_2O_2 ; (b) the intermediate formed after 15 s reaction of HRP with an excess amount of H_2O_2 in 10 mM phosphate buffer, pH 7.0.³⁹ **B)** EPR spectra of HRP compound I at different pHs (8.1, 11.0, and 11.4). The spectrum (c) is entirely due to

low spin heme iron with principal g value = 2.0.⁴⁶ **C)** EPR spectra of a solution of ascorbate peroxidase (black line), and compound II with the expected high-spin and low-spin (blue lines, $g= 2.69$, $g= 2.22$, $g= 1.79$),⁴⁷ **D)** EPR spectrum of cytochrome *c* peroxidase (Ccp) products. a, Ccp-H₂O₂ product.⁴⁸

The rate of oxidation reaction by HRP has been shown to decrease with increasing concentrations of alcohols, such as ethanol.⁴⁹⁻⁵¹ Alcohols have also been shown to have a significant influence on heme protein electrostatic interactions and stability depending on the alcohol's concentration and chain length.⁵² For example, low concentrations of ethanol (<1 M) enhance the heme protein stability,⁵³⁻⁵⁴ while the same concentration of alcohols with higher hydrocarbon content increases partial protein denaturation through disorganization of the enzyme's hydrophobic interior domains.^{53, 55} The arguments are emerging in the mechanistic discussions of this system as to whether the reason for decreasing the rate of oxidation reactions should rather be described as a competitive inhibitory effect of alcohol through weak binding to the iron at the heme center or its binding to the protein moiety.^{49, 51, 56-57} Many results concerning the decrease in rate of oxidation reactions by peroxidases in the presence of alcohols have been interpreted in terms of the viscosity and dielectric constant of the medium,^{49, 51, 58} which affect the hydrogen-bonding network and transport of H₂O₂ to the enzyme's catalytic active site.^{41, 59-63} Thus, another long-standing controversy among scientists is whether the formation of compound I through the reaction of H₂O₂ with Fe(III) at the heme center of HRP is a diffusion-controlled reaction.^{49, 64}

CHAPTER 2

CATALYZED OXIDATION OF CAROTENOIDS BY LACTOPEROXIDASE IN THE PRESENCE OF ETHANOL¹



ABSTRACT

The discovery of the lactoperoxidase system as a biocatalyst in milk was a landmark finding. The activation of this system using hydrogen peroxide (H₂O₂) raised hopes for oxidation of various organic substrates. The involvement of lactoperoxidase system in the catalyzed-oxidation of carotenoids in the whey proteins, and the effect of various solvents on carotenoids' oxidation reaction rate has been studied. However, there is no evidence for this reaction without the addition of oxidizing agents, such as peroxides.

Here, we reveal that carotenoids are oxidized through the addition of just ethanol in the presence of lactoperoxidase. The oxidation of carotenoids through this exquisite strategy is ~360-times faster than harnessing the lactoperoxidase system in whey proteins via the addition of hydrogen peroxide. Bearing in mind that ethanol is not an oxidizing agent, this observation suggests a potential paradigm shift in our understanding of lactoperoxidase and catalyzed oxidation in biochemical systems.

2.1. INTRODUCTION

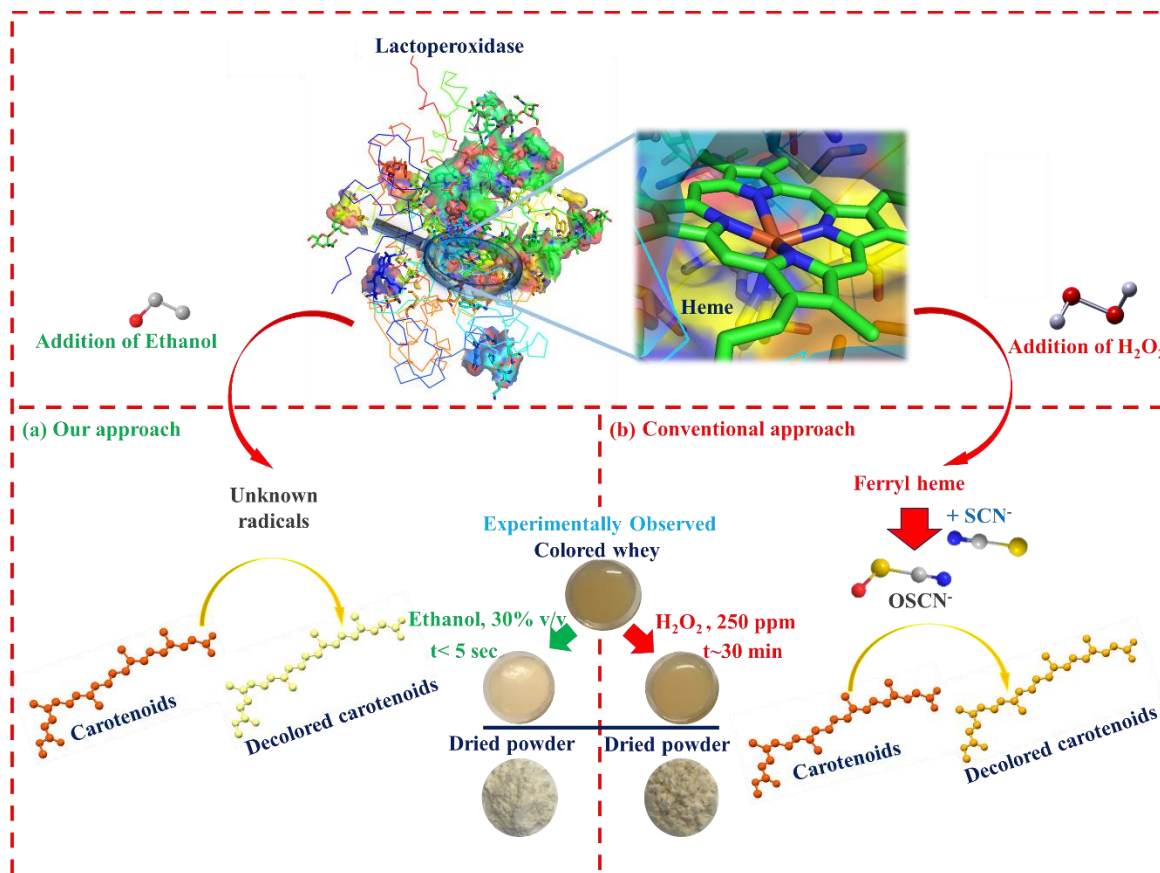
Several reports have proposed that carotenoids can boost antioxidant functions, the immune system,⁶⁵⁻⁶⁷ and protect living organisms against photodynamic damage⁶⁸⁻⁶⁹ through the quenching of free radicals.^{66, 68} Upon this quenching reaction, the carotenoids become oxidized and decolorized due to the disturbance of their conjugated polyene chains.^{68, 70-71} The rate of these oxidation reactions is dependent on the polarity of the solvents in the reaction mixture⁷²⁻⁷⁴ and the type of free radicals encountered, which can be formed via different methods, such as chemical and enzymatic reactions. For instance, lactoperoxidase catalyzes the formation of thiocyanate radicals in milk upon the addition of hydrogen peroxide, which reacts with the heme center of lactoperoxidase to form ferryl intermediates.⁵⁻⁶ These thiocyanate radicals are subsequently quenched by carotenoids, disturbing their conjugated double bonds⁷⁻⁸ and decoloring the carotenoids due to the loss of visible light absorption by their conjugated π -system.⁹

The food industry harnesses this behavior of the native lactoperoxidase system of milk to decolor yellow whey proteins recovered from colored Cheddar cheese.⁴ The yellow color of whey proteins is due to the partitioning of the annatto carotenoids to the whey

proteins, which are used to color Cheddar cheese (Figure S2.1).⁷⁵ The presence of these carotenoids in the whey proteins, however, is not industrially desired due to the unpleasant appearance of whey proteins, which limits their application in other food products.^{2, 17} To utilize the lactoperoxidase system in the decoloration of carotenoids in yellow whey, hydrogen peroxide is added to the colored whey proteins, which contain native lactoperoxidase enzyme and thiocyanate.⁷⁶ The reaction of hydrogen peroxide with lactoperoxidase leads to the formation of thiocyanate radicals, which are quenched by the annatto carotenoids, norbixin and bixin, decoloring them in ~30 minutes.¹⁰

In this work, we report the discovery that the addition of just ethanol to yellow whey proteins catalyzes the oxidation of the annatto carotenoids (Scheme 2.1a) and results in a white whey ~360-times faster compared to the lactoperoxidase system activated via the addition of hydrogen peroxide (Scheme 2.1b). To understand this effect, we compare the carotenoid oxidation products extracted from ethanol-treated (ETW) and hydrogen peroxide-treated colored whey proteins (HTW) using direct analysis in real time mass spectrometry (DART-MS). Based on these results and additional observations with UV/Vis spectroscopy, high performance liquid chromatography (HPLC), colorimetry, and the relative oxidation times, we hypothesize that the addition of ethanol to the whey proteins leads to a radical reaction that can be quenched via the carotenoids. After comparing the lactoperoxidase activity, the oxidation rate of 2,2'-azino-bis(3-ethylbenzthiazoline-6-sulfonic acid) (ABTS), the redox potential, and Fourier-transform infrared (FTIR) spectra of the ETW and HTW samples, we postulate that lactoperoxidase is implicated in this intriguing oxidation of carotenoids upon the addition of ethanol. To confirm our postulation, we also examine the decoloration of

pure norbixin in the presence of pure lactoperoxidase upon the addition of ethanol. Since ethanol is a convenient solvent used in biological systems and can be evaporated from the reaction mixture without any harmful residual, we believe that exploring this observation can greatly expand our understanding of oxidation reactions in biochemical systems.



Scheme 2.1. a) Schematic of carotenoid decoloration through the addition of ethanol to whey proteins and the hypothetical involvement of whey proteins containing lactoperoxidase. b) Schematic of carotenoid decoloration through the addition of hydrogen peroxide to whey proteins via the involvement of the lactoperoxidase system.

2.2. MATERIALS AND METHODS

2.2.1. Materials

Pure 200 proof ethanol was purchased from KOPTEC (PA, US), while lyophilized powder of lactoperoxidase from bovine milk (essentially salt-free), sodium citrate, 2,2'-azino-*bis* (3-ethyl-benzthiazaoline-6-sulfonic acid) (ABTS), n-hexane, acetone, acetonitrile, diethyl ether, and formic acid were purchased from Sigma-Aldrich (St. Louis, MO, US). Chloroform and methanol were purchased from Fisher Scientific (Waltham, MA, USA). Glacial acetic acid was purchased from Merck Millipore corporation (MA, US). Hydrogen peroxide (30% solution) was purchased from Anachemia (Que, Canada). Norbixin and bixin were kindly provided by the Chr. Hansen Laboratory A/S, Denmark. Diafiltered colored whey protein samples were kindly provided by Cabot cheese, Agri-Mark, Inc., Middlebury, Vermont.

2.2.2. Decoloration of carotenoids by the addition of either ethanol or hydrogen peroxide

Decoloration was conducted on liquid colored whey using different concentrations of ethanol (10–30%, v/v) at pH= 6.3. The purpose of this experiment was to identify the optimum concentration of ethanol to obtain white whey. The colored whey was also diluted with the same concentrations of deionized water to correct the dilution factor in control samples. The obtained white whey was compared to the decolored whey using 250 ppm hydrogen peroxide and colored whey (control).

2.2.3. Extraction and quantification of norbixin from whey proteins

Norbixin was extracted⁸ and quantified by HPLC. Briefly, 0.6 g of colored whey sample was diluted with 6 mL of water. Then, 3 mL absolute ethanol, 3 mL chloroform, and 1 mL glacial acetic acid (1% w/v) were added to the previous solution. The sample was centrifuged at 16,500 g for 10 min at 4 °C and the bottom chloroform layer containing the annatto was collected. Solid-phase extraction (SPE) was performed to filter and purify the extracted annatto using a strata NH2 SPE cartridge (Sep-Pak Vac, Waters). The extraction was done inside the SPE cartridge placed in a 12 port SPE vacuum manifold (Avantor, J.T.Baker, PA, US). To condition the column, 4 mL of n-hexane was used and 1 mL of the collected aliquot from the previous step was transferred onto the conditioned SPE column. The column was rinsed with 2.5 mL of a 1:1 n-hexane and diethyl ether solution and 1 mL of acetone. The annatto was eluted with 2 mL of a 7:3 solution of methanol and glacial acetic acid. The samples were quantified by HPLC. An Agilent 1200 LC System with a Binary SL Pump & Diode Array Detector, Shodex RI-501 Refractive Index Detector (single channel), and an Agilent 1100 Column Compartment (G1316) was utilized to carry out the analysis. An isocratic mobile phase (7:3, acetonitrile: water with 0.1% (w/v) formic acid) was used at a flow rate of 1 mL/min with a binary pump. The sample (15 µL) was injected into the column (CORTECS C18 Column, 2.7 µm, 4.6 mm×100 mm, Waters, MA, US), which was heated to 40 °C. The sample was sent through a photodiode array detector. A standard curve was created by preparing a serial dilution of norbixin aqueous solutions and monitored at the maximum wavelength of 460 nm.

2.2.4. Assessment of the whey proteins by UV-VIS spectrophotometry

The absorbance of the whey protein samples was measured using UV-Vis spectrophotometry (UV-Vis Spectrophotometer UV-2600, Shimadzu Scientific Instruments/ Marlborough, Massachusetts–USA) at a wavelength range between 200 nm and 800 nm.

2.2.5. Color analysis

The color of the liquid and solid whey protein samples was measured using a Chroma Meter CR-400 (Konica Minolta Sensing Inc., Japan) and reported in terms of lightness (L^*) and blue-yellow (b^*) values.⁷⁷

2.2.6. Direct Analysis in Real Time Mass Spectrometry (DART-Mass)

A DART Standardized Voltage and Pressure (SVP) ion source (Ionsense Inc. Saugus, MA) was coupled to a triple quadrupole ThermoFinnigan TSQ Discovery MAX mass spectrometer (Waltham, MA) by a Vapur® interface (Ionsense Inc. Saugus, MA). The source was controlled by the DART-SVP web-based software, which was operated at 300 °C with helium as the carrier gas. The MS was operated in full scan, positive ion mode with high purity nitrogen gas with a scan width of 0.10, scan time of 0.10 s and scan modes over a mass range of 30–500 m/z. Samples were introduced to the DART source drop-wise, by a glass pipette.

2.2.7. Lactoperoxidase activity

The assay for lactoperoxidase activity was performed based on the oxidation of the synthetic substrate ABTS.⁷⁸ Briefly, 4 ml of 1.73 mM ABTS in 0.1 M sodium citrate

buffer (pH = 5.5) was mixed with 140 μL of 5.35 mM H_2O_2 and 10 μL of sample. The linear increase in the absorbance at 405 nm was measured at 25 $^\circ\text{C}$ in 1 s intervals for 300 s. The slope $\Delta A/\Delta t$ (a.u./min) times 11.15 was equal to the lactoperoxidase activity (U/ml).⁷⁸

2.2.8. *Fourier Transform Infrared Spectroscopy (FTIR)*

FTIR spectra of the freeze-dried whey protein samples were investigated in the region from 4000 to 400 cm^{-1} (120 scans, resolution of 2 cm^{-1}) using a IRAffinity-1S Fourier Transform Infrared Spectrophotometer (Shimadzu Scientific Instruments/Marlborough, MA).

2.2.9. *Cyclic voltammetry*

Cyclic voltammetry (CV) studies on the colored whey proteins and ethanol-treated colored whey protein (ETW) were carried out at scan rates of 0.1 V/s using an Autolab PGSTAT302N (Metrohm Autolab B.V., Netherlands). Carbon paste screen-printed electrodes (DRP-110) were purchased from Dropsens (Spain).

2.2.10. *Assessment of the pure lactoperoxidase upon the addition of ethanol*

The UV/Vis spectrum of lactoperoxidase (5 μM) after treatment with ethanol was compared to the untreated lactoperoxidase (control). To simulate the colored whey protein system, 950 μL of pure lactoperoxidase from bovine milk (0.5 μM) in 0.1 mM potassium phosphate buffer (pH= 6.0) was added to 50 μL of pure norbixin solution (0.002 g/mL). Then, 300 μL ethanol (equivalent to 30% v/v) was added to the

lactoperoxidase/norbixin solution and the UV/Vis spectra were compared with the ethanol-treated norbixin and untreated norbixin (control).

2.3. RESULTS AND DISCUSSION

The story begins with a landmark result demonstrating that the addition of ethanol decolors the annatto carotenoids in colored whey proteins (pH= 6.3) recovered from the Cheddar cheese making process.¹ Our primary mission by the addition of ethanol was to extract annatto from the colored whey using a food-grade solvent to obtain a white whey. However, upon the addition of ethanol we observed the whey to turn white in less than 5 s without the addition of any exogenous oxidizing agent (Scheme 2.1a). This observation sparks our attention to question if the addition of ethanol causes the oxidation of carotenoids in the presence of whey proteins. After optimizing the process, we demonstrate that the addition of 30% (v/v) ethanol to colored whey proteins decolors the carotenoids in less than 5 s. In contrast, the addition of 250 ppm hydrogen peroxide to the same proteins decolors the carotenoids in ~30 minutes (Scheme 2.1b), which is in agreement with the results of other studies.⁷⁹ The lactoperoxidase activity decreases through the addition of higher ethanol concentrations (>30% v/v). Moreover, the composition analysis of ethanol-treated whey protein for calcium, iron, copper, and total nitrogen content does not show any significant difference in comparison with the colored whey protein (control) (Table S2.1). Interestingly, the excess addition of hydrogen peroxide to the colored whey does not accelerate the rate of oxidation of the carotenoids to the order of seconds. It has also been reported that the decoloration of

carotenoids becomes less effective at high concentrations of hydrogen peroxide due to the inactivation of the peroxidase.⁸⁰

We then studied the ETW and HTW to determine any difference between the samples. HPLC analysis indicates that the concentration of norbixin in the ETW sample decreases approximately 7% more than the corresponding concentration in the HTW (Figure 2.1a). Hydrogen peroxide treatment shows a 38% decrease of norbixin in the colored whey after ~30 min, while the addition of ethanol to the colored whey decreases the norbixin by ~45% in less than 5 s. The colorimetry results also show a significant increase in lightness (L^*) and a significant decrease in yellowness (b^*) of the colored whey proteins treated with ethanol in comparison with hydrogen peroxide and the untreated colored whey protein (control) (Figures 1b, & S2).

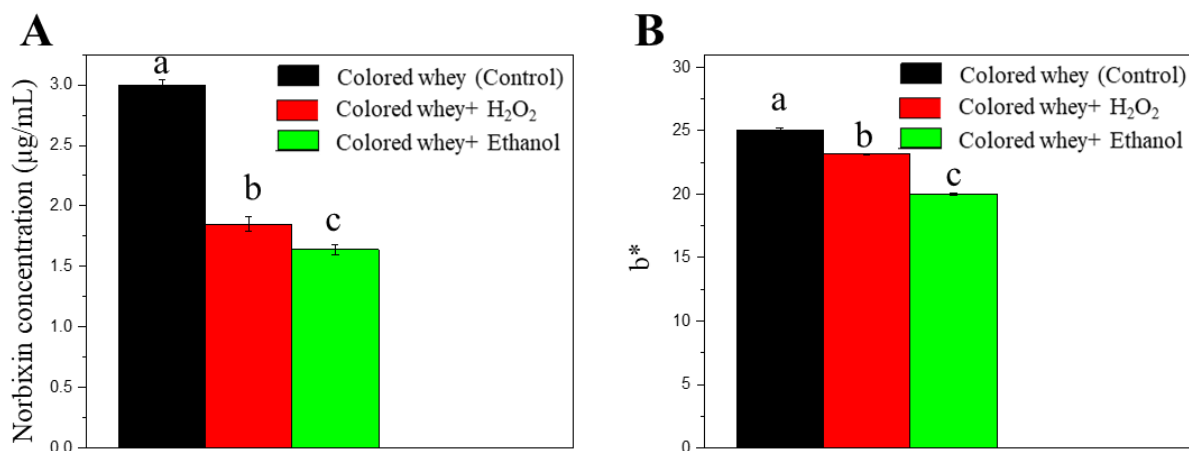


Figure 2.1. A) HPLC results of the norbixin concentration ($\mu\text{g/mL}$) in the colored whey treated with either 250 ppm hydrogen peroxide or 30% (v/v) ethanol in comparison with the untreated colored whey (control). B) The b^* -value (yellowness) of the colored whey treated with either 250 ppm hydrogen peroxide or 30% (v/v) ethanol in comparison with the untreated colored whey (control).

To explore the unexpected effect of ethanol addition on carotenoid oxidation, we investigate the effect of ethanol on aqueous solutions of annatto carotenoids over a wide pH range. The results show that the addition of ethanol to the solution of annatto carotenoids in the pH range of 2–12 does not decolor them, and the slight color change is due to the dilution with 30% ethanol (Figure S2.3). We also show that ethanol addition does not decolor the carotenoids in the presence of casein proteins (Figure S2.4), which raises our curiosity as to the role of the whey protein components in the oxidation reaction of carotenoids upon ethanol addition. The UV/Vis spectra of the colored whey proteins illustrate the elimination of the annatto carotenoid peaks in the range of 400–500 nm upon the addition of ethanol to the colored whey proteins (Figure 2.2a). We also compare the carotenoids' oxidation products found in the ETW and HTW samples using DART-MS and compare the results to the untreated colored whey control (Figure 2.2 (b-g)). Norbixin (Figure 2.2b) and bixin (Figure 2.2c) contain nine conjugated double bonds in their molecular structure, which are disturbed by the oxidation reactions with ethanol or hydrogen peroxide. A decrease in the intensity of the annatto carotenoids' main fragment (150 m/z) (Figure S2.5) and another dominant fragment (243 m/z) (Figure S2.6) in the ETW in comparison with the HTW sample illustrates that the annatto carotenoids are converted to other species in the ETW more effectively than the HTW (Figure S2.6). Based on the appearance of two fragments (359 m/z and 341 m/z) originating from either norbixin or bixin in the ETW and HTW (Figure S2.7), we propose their possible molecular structures (Figure 2.2, d-g), which illustrate a disturbance of the carotenoids' conjugated π -systems through the reduction of a mere

single double bond in the middle of the carotenoid molecule (Figure 2.2d & 2.2e), which is sufficient to cause its decoloration. The proposed structures also demonstrate the addition of hydroxyls to the carotenoid molecules in both the ETW and HTW samples (Figure 2.2, d-g). Figure 2.2 (f-g) shows the proposed structure of carotenoid molecules with the hydroxyl groups added to their structures in both the ETW and HTW, which can be formed one step before the formation of single bond in the middle of carotenoid molecule.

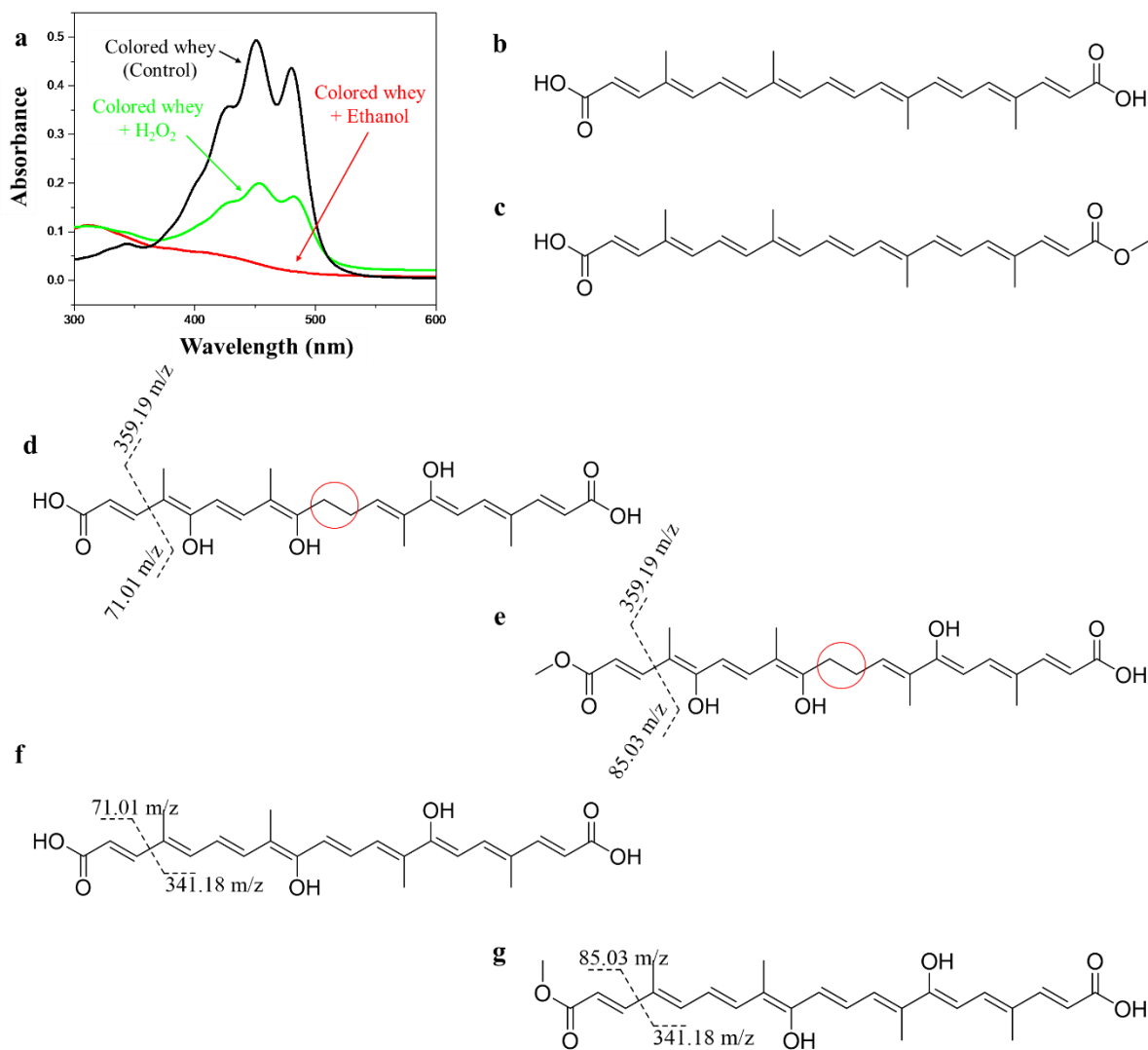


Figure 2.2. a) UV/Vis spectra of the colored whey proteins treated with ethanol and H₂O₂ in comparison to the untreated colored whey protein control. b) The molecular structure of norbixin and c) bixin. d) The proposed structure of the main fragment (359 m/z) originating from norbixin through the decoloration of whey proteins using ethanol or hydrogen peroxide. e) The proposed structure of the main fragment (359 m/z) originating from bixin through decoloration of whey proteins using ethanol or hydrogen peroxide. f) The proposed structure of fragment (341 m/z) originating from norbixin through the decoloration of whey proteins using ethanol or hydrogen peroxide. g) The proposed structure of fragment (341 m/z) originating from bixin through decoloration of whey proteins using ethanol or hydrogen peroxide.

To investigate the effect of ethanol on whey proteins, we measure the lactoperoxidase activity. Lactoperoxidase contains a heme group in the catalytic domain,⁸¹⁻⁸² which is covalently bound to the polypeptide chains.²¹⁻²³ In the presence of hydrogen peroxide, the heme center of lactoperoxidase reacts with hydrogen peroxide and produces an active ferryl intermediate of the enzyme.⁸³ These intermediates oxidize organic molecules, such as carotenoids, and ABTS, which is a substrate to assay the lactoperoxidase activity (Figure S2.8).⁸⁴ The oxidation rate of ABTS is directly proportional to the lactoperoxidase activity. Using this assay, we demonstrate that the addition of ethanol decreases the rate of ABTS oxidation significantly (Figure 2.3a), and subsequently causes a sharp decrease in lactoperoxidase activity (Figure 2.3b). The voltammogram obtained from the ETW sample indicates the formation of new species with higher oxidative potentials upon the addition of ethanol in comparison with the

voltammogram of the control colored whey (Figure 2.3c). A shift to the higher oxidative potentials (from 0.55 V to 0.65 V) in the cyclic voltammograms (Figure 2.3c) may be due to the attachment of a ligand to the heme center and subsequent change of the iron oxidation state from Fe(III) to Fe(IV).⁸⁵ Moreover, the FTIR spectrum in the range of 1680–1630 cm^{-1} for the ETW sample is blue-shifted to a higher energy level in comparison with the HTW and the colored whey protein control (Figure 2.3d). The vibrational infrared absorption shifts are associated with the change of heme's redox potentials.⁸⁶ The region of 1680–1630 cm^{-1} belongs to the carbon-carbon double bonds in the alkenes, which can be found in the heme structure of the lactoperoxidase. Studies report that the bands in the range of 1626–1613 cm^{-1} are assigned to porphyrin skeletal and vinyl modes in cytochrome b559.⁸⁶ Thus, the upshifted peaks to the higher energy upon the addition of ethanol, specifically the peak shifted from 1646 cm^{-1} to 1649 cm^{-1} , as well as the increase in cyclic voltammetry oxidation potential, may be associated with the formation of an oxidized form of lactoperoxidase (Figure 2.3d). This oxidized form of lactoperoxidase can be created through the attachment of a ligand to the vacant 6th coordination site of the heme. The ligand, which competes with hydrogen peroxide to attach to the iron, inhibits the formation of the ferryl intermediate and disrupts ABTS oxidation. This hypothesis can explain our previous observation of a decrease in the rate of ABTS oxidation and lactoperoxidase activity upon the addition of ethanol (Figures 3a, & 3b).

Moreover, previous studies have assigned the peaks at 1656 and 1641 cm^{-1} to peptide C=O mode(s) in cytochrome b559, and speculate that these signals reflect the change in strength of a hydrogen bond formed between the histidine ligand(s) and the polypeptide

backbone upon oxidation-reduction of the cytochrome b559.⁸⁶ Thus, we believe that the slight blue shift in the range of 1676–1663 cm^{-1} in the FTIR spectra caused by the addition of ethanol may be due to the change in the pattern of hydrogen bonds formed between the heme and polypeptide chain ligands of lactoperoxidase (Figure 2.3d). The FTIR results also show a peak at 2349 cm^{-1} , which is only formed in HTW (Figure S2.9). This peak is associated with the production of carbon dioxide in HTW, which may be due to different mechanisms of carotenoid oxidation upon the addition of hydrogen peroxide compared to ethanol. Moreover, the presence of carbon dioxide in HTW can produce off-flavors in the whey protein.

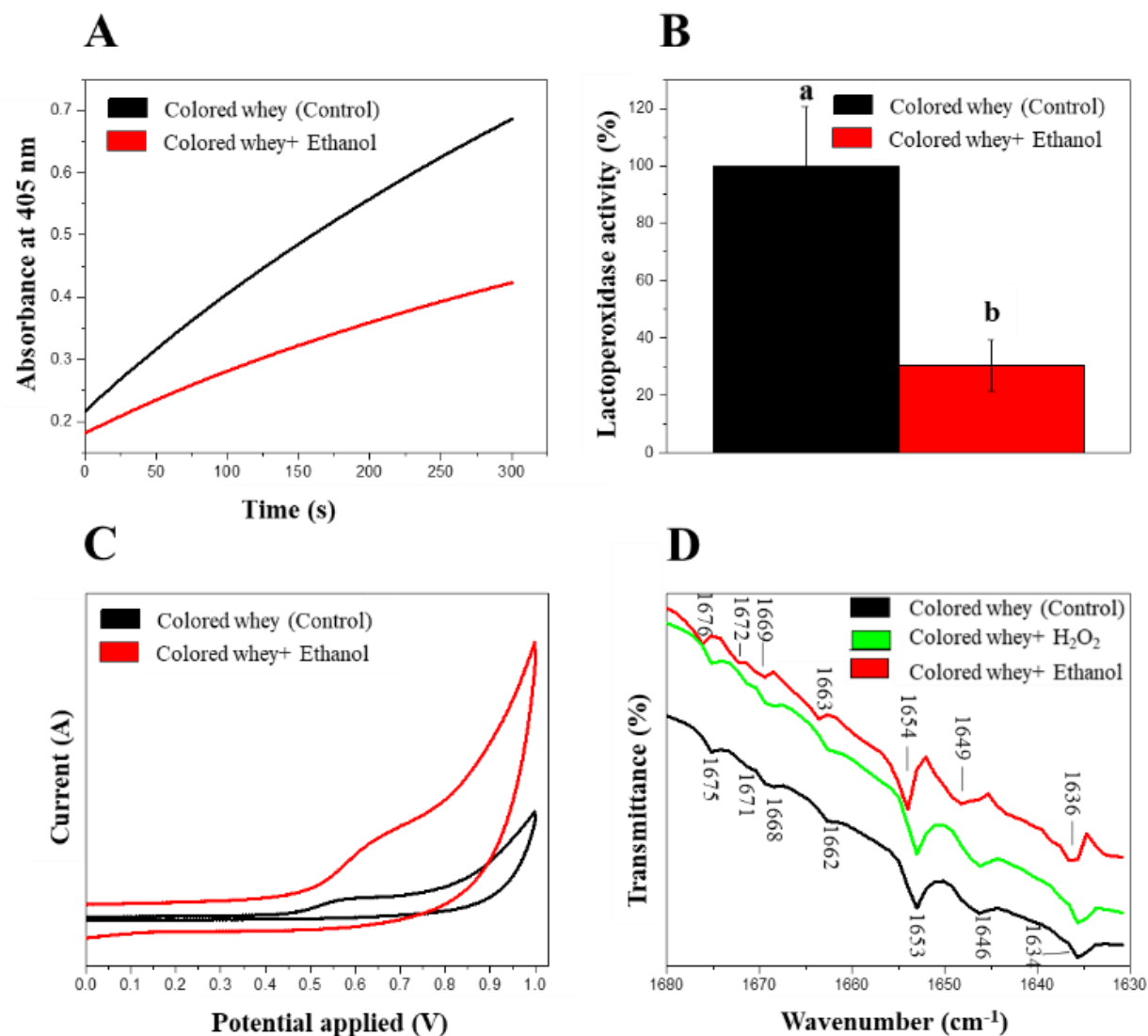


Figure 2.3. A) Rate of ABTS oxidation in the lactoperoxidase assay with hydrogen peroxide. B) Lactoperoxidase activity (%) of the untreated and ethanol-treated colored whey. C) Cyclic voltammetry of colored whey proteins in comparison to the whey proteins treated with ethanol. D) FTIR spectra of the colored whey proteins treated with ethanol and hydrogen peroxide in comparison with the control.

To confirm our hypothesis on the formation of an oxidized form of lactoperoxidase, we compare the UV/Vis spectra of pure lactoperoxidase from bovine milk with the ethanol-

treated lactoperoxidase (Figure 2.4a). In native lactoperoxidase, the Soret band appears at 412 nm with the Q-band maxima at 497 nm⁸⁷. The addition of ethanol to the lactoperoxidase solution (5 μ M) in 0.1 M potassium phosphate buffer (pH 6.0) causes a red shift in the Soret band to 430 nm with a shoulder at 350 nm, and the appearance of Q-bands at 536 nm, and 566 nm (Figure 2.4a). It has been previously reported for lactoperoxidase and other heme-containing peroxidases that the 350 nm shoulder in the Soret peak and the red shift in Soret and Q-bands are indicative features of ferryl intermediates^{46, 87-89}. We also simulate the decoloration of carotenoids in the whey proteins containing lactoperoxidase (\sim 0.5 μ M) upon the addition of ethanol using the pure solution of lactoperoxidase (0.5 μ M) and norbixin. The results show that just ethanol does not decolor the norbixin (Figure 2.4b). However, the addition of ethanol (30%, v/v) to the norbixin in the presence of lactoperoxidase results in the decoloration of norbixin (Figure 2.4b), which can be due to the oxidation of norbixin by ferryl intermediates of lactoperoxidase.

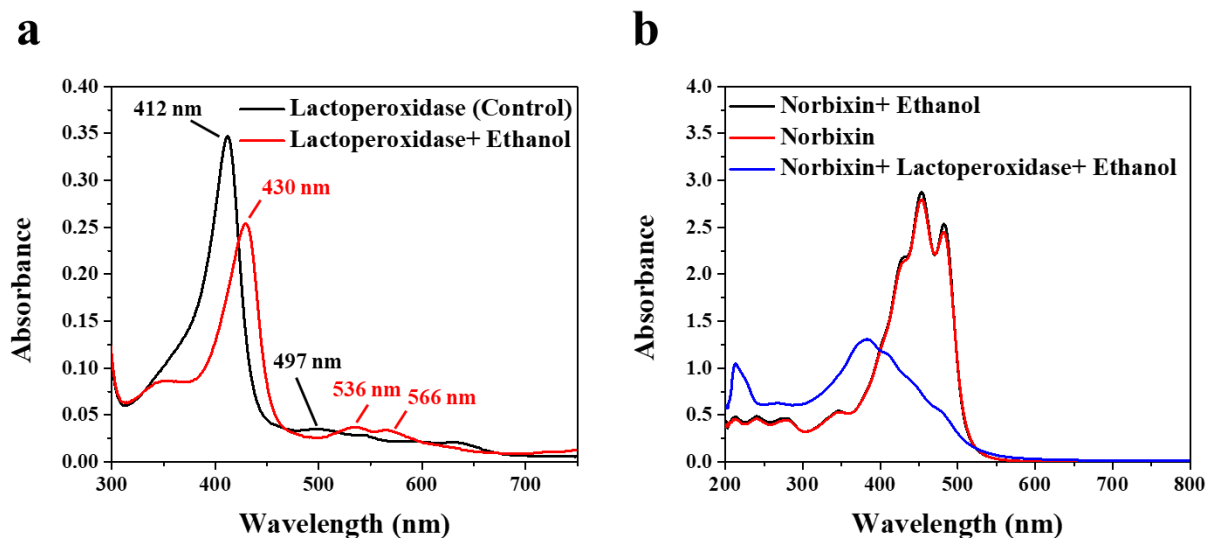


Figure 2.4. a) UV-Vis absorbance spectra of native lactoperoxidase (5 μ M) in 0.1 M potassium phosphate buffer (pH 6.0), and upon the addition of ethanol. b) The UV-Vis absorbance spectra of ethanol-treated solution of norbixin containing lactoperoxidase in comparison with untreated norbixin, and ethanol-treated solution of norbixin without lactoperoxidase.

2.4. CONCLUSION

In conclusion, adding 30% (v/v) ethanol oxidizes annatto carotenoids in the presence of lactoperoxidase. This intriguing strategy catalyzes the oxidation of the carotenoids 360-times faster than hydrogen peroxide/lactoperoxidase oxidation and results in the conversion of more carotenoids to other colorless species and white whey proteins. Since ethanol is not an oxidizing agent, exploring the mechanism of the carotenoid catalyzed-oxidation reaction upon the addition of ethanol to the lactoperoxidase may have a prominent influence on the biochemistry of peroxidases. Ongoing work is focused on proposing a novel mechanism for the oxidation reactions of other organic molecules in a pure peroxidase system upon the addition of ethanol.

2.5. SOPPORTING INFORMATION

Cheddar cheese production

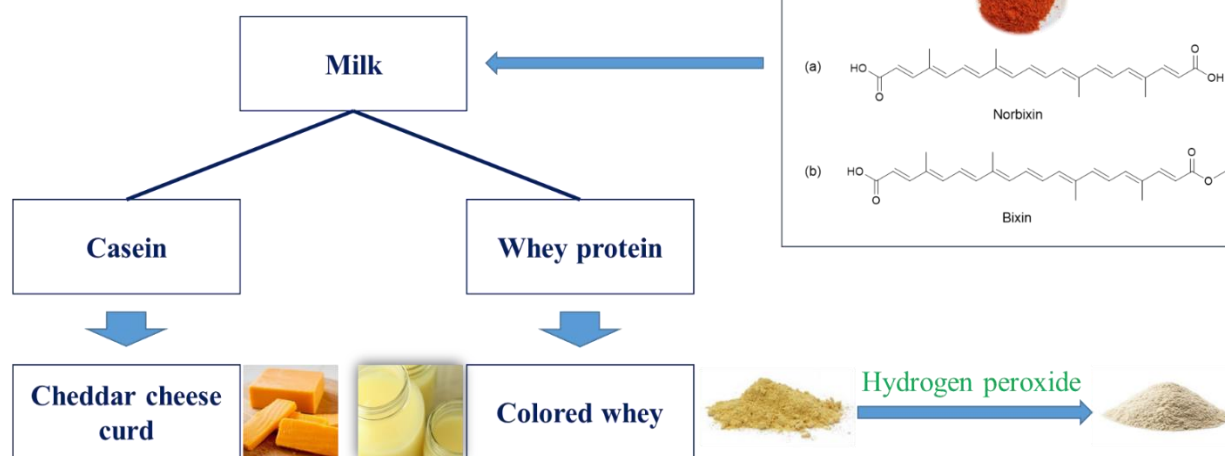


Figure S2.1. Schematic of Cheddar cheese production, colored using annatto carotenoids.

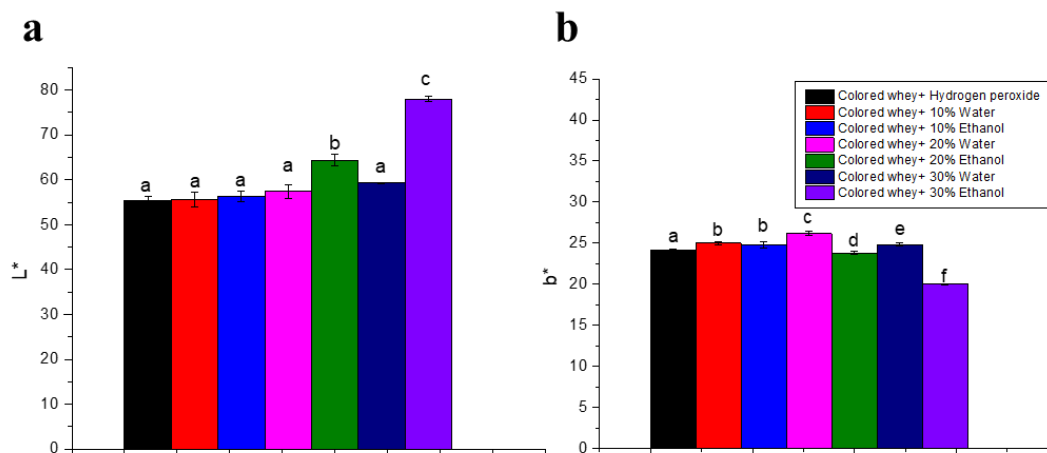
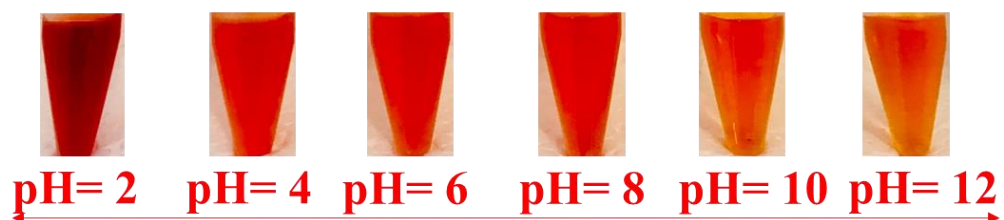


Figure S2.2. a) L* (lightness) and b) b* (yellowness) values of the colored whey treated with 250 ppm hydrogen peroxide, different ethanol concentrations, and water to correct the dilution factor.

Annatto Carotenoid



↓ Ethanol

No decoloration



Figure S2.3. Ethanol addition to the annatto carotenoid solution at a pH range of 2–12.

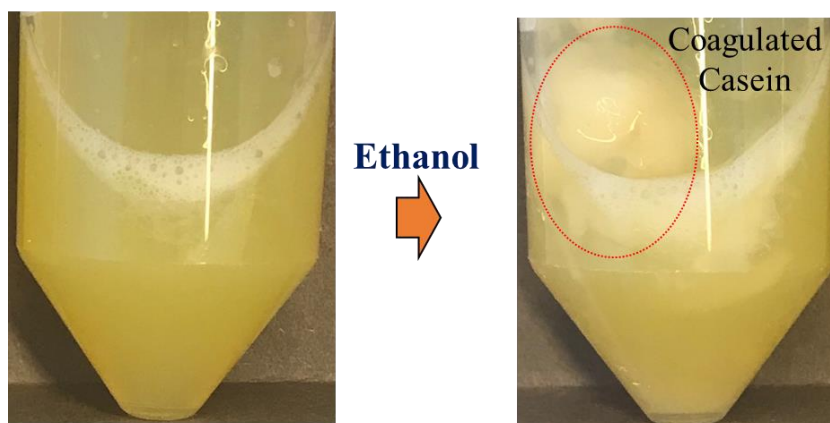


Figure S2.4. The addition of ethanol to annatto carotenoids and casein, indicating a lack of color change and coagulation of casein upon addition of ethanol.

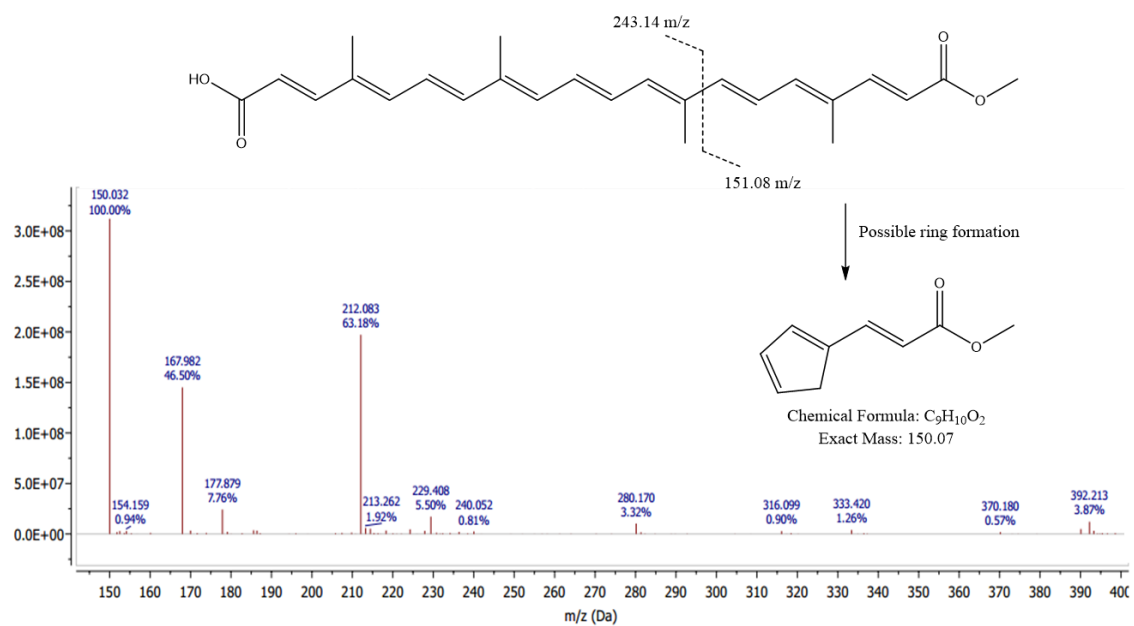


Figure S2.5. The DART-MS spectrum of the annatto, and a proposed structure for its main peak at 150 m/z.

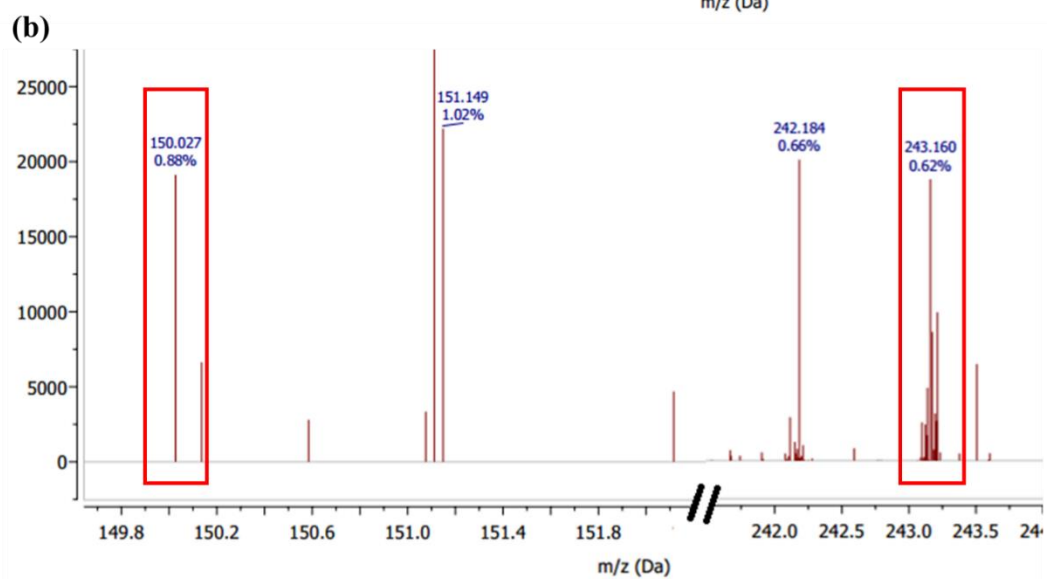
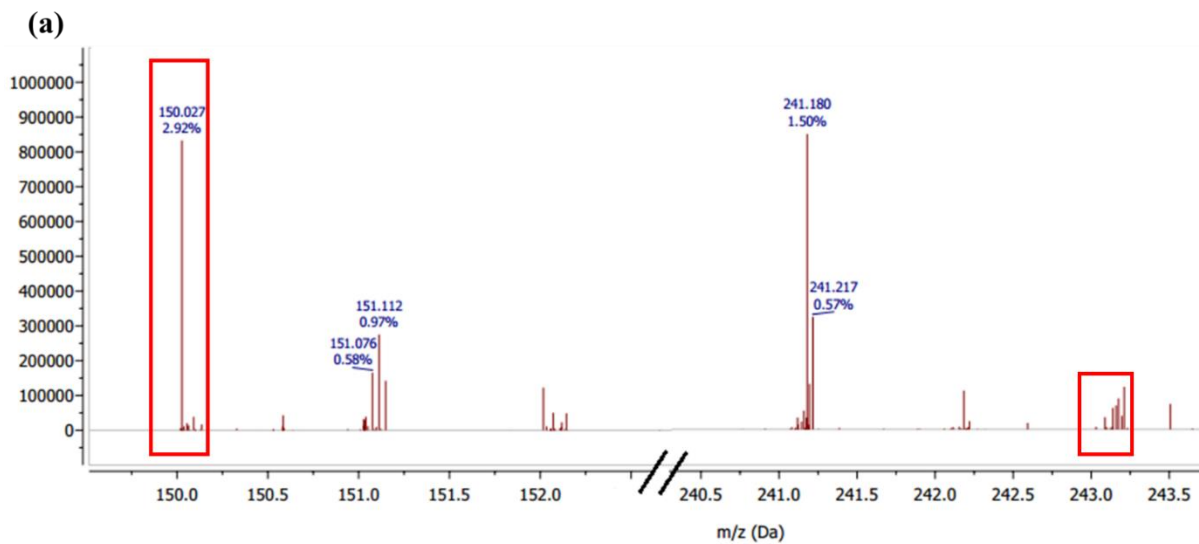


Figure S2.6. DART-MS spectra of the colored whey proteins treated with a) ethanol (30%, V/V) and b) hydrogen peroxide (250 ppm).

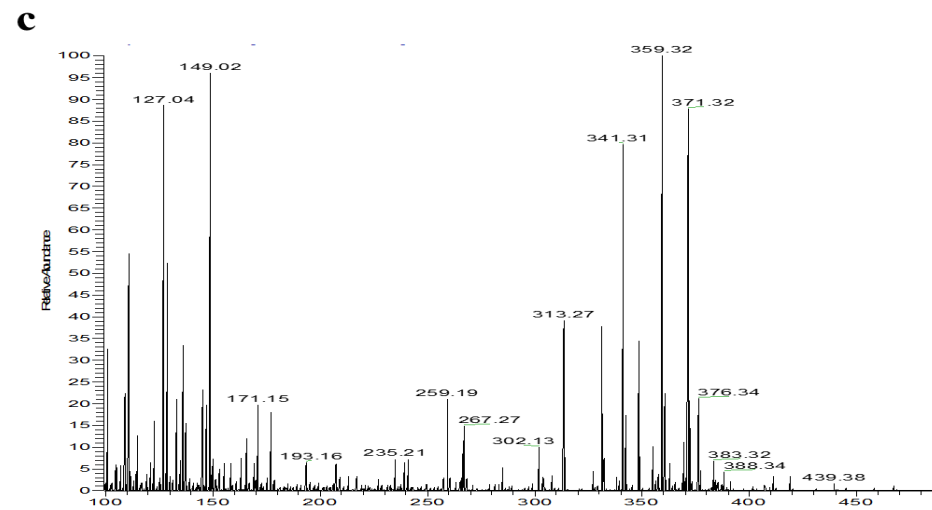
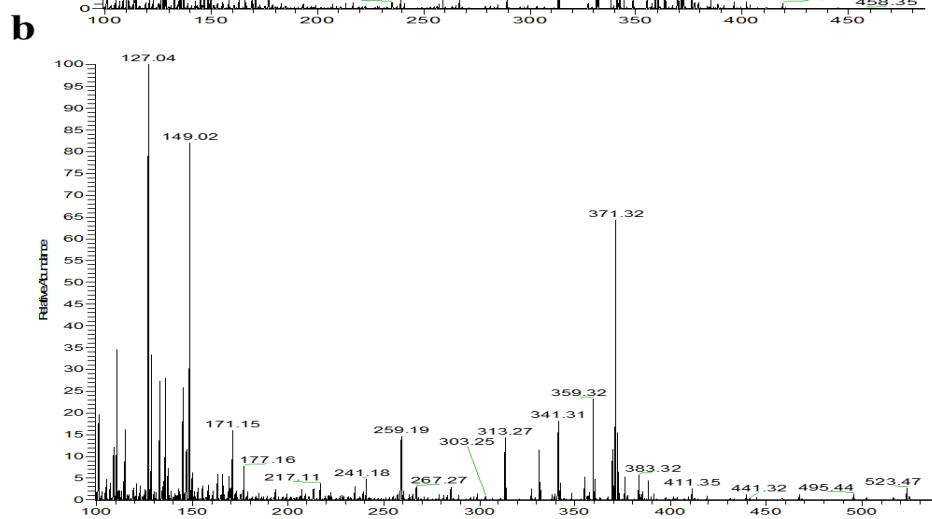
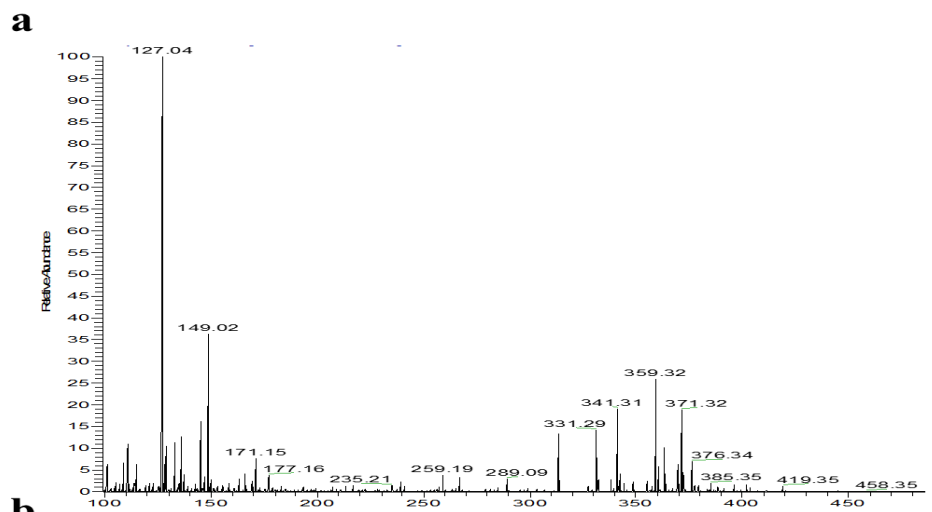


Figure S2.7. DART-MS spectra of the colored whey proteins treated with a) 30% (V/V) ethanol and b) 250 ppm hydrogen peroxide. c) Control, untreated colored whey proteins.

- E (Enzyme) + $H_2O_2 \rightarrow EO$ (active form of the enzyme) + H_2O
- $EO + ABTS$ (colorless) \rightarrow Oxidized ABTS + E

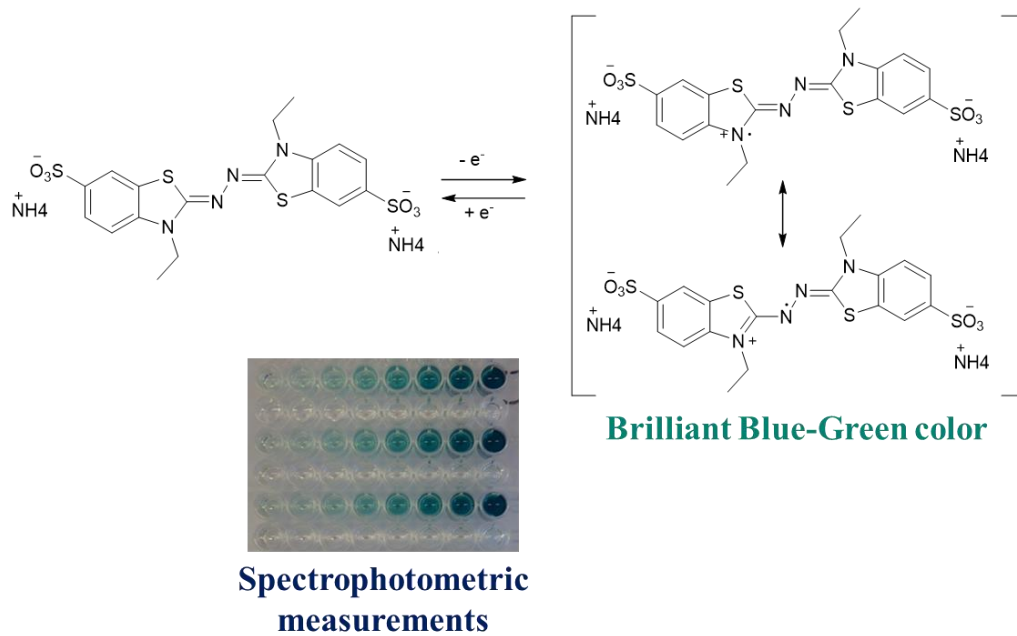


Figure S2.8. Schematic of the lactoperoxidase activity assay.

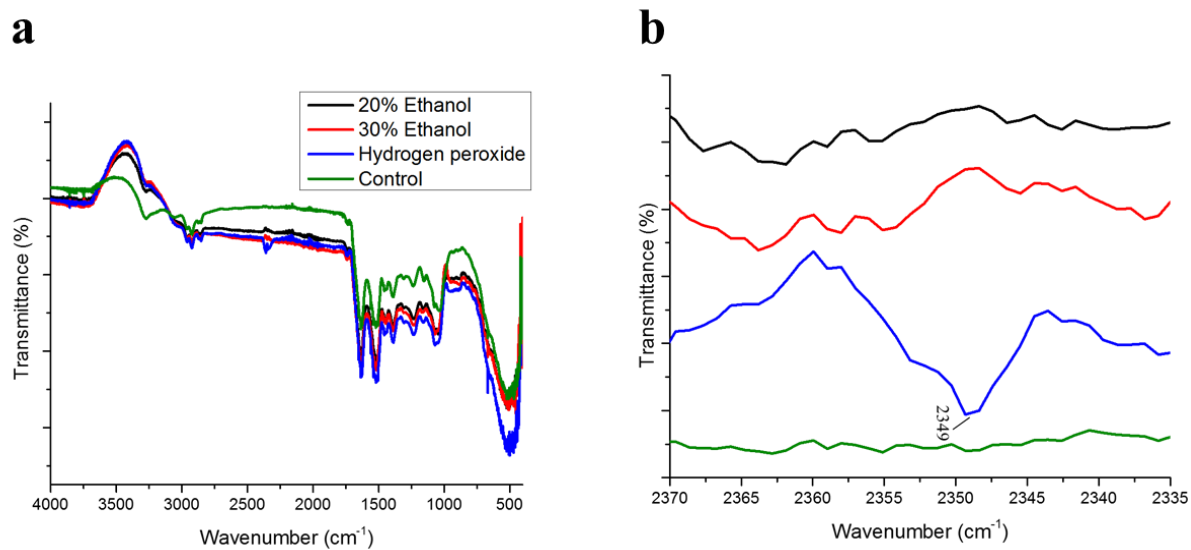


Figure S2.9. a) FTIR spectra of the ETW and HTW in comparison with the colored whey control. b) The peak at 2349 cm^{-1} associated with CO_2 in the FTIR spectrum of HTW in comparison with ETW and the colored whey control.

Table S2.1. Composition analysis of the colored whey proteins.

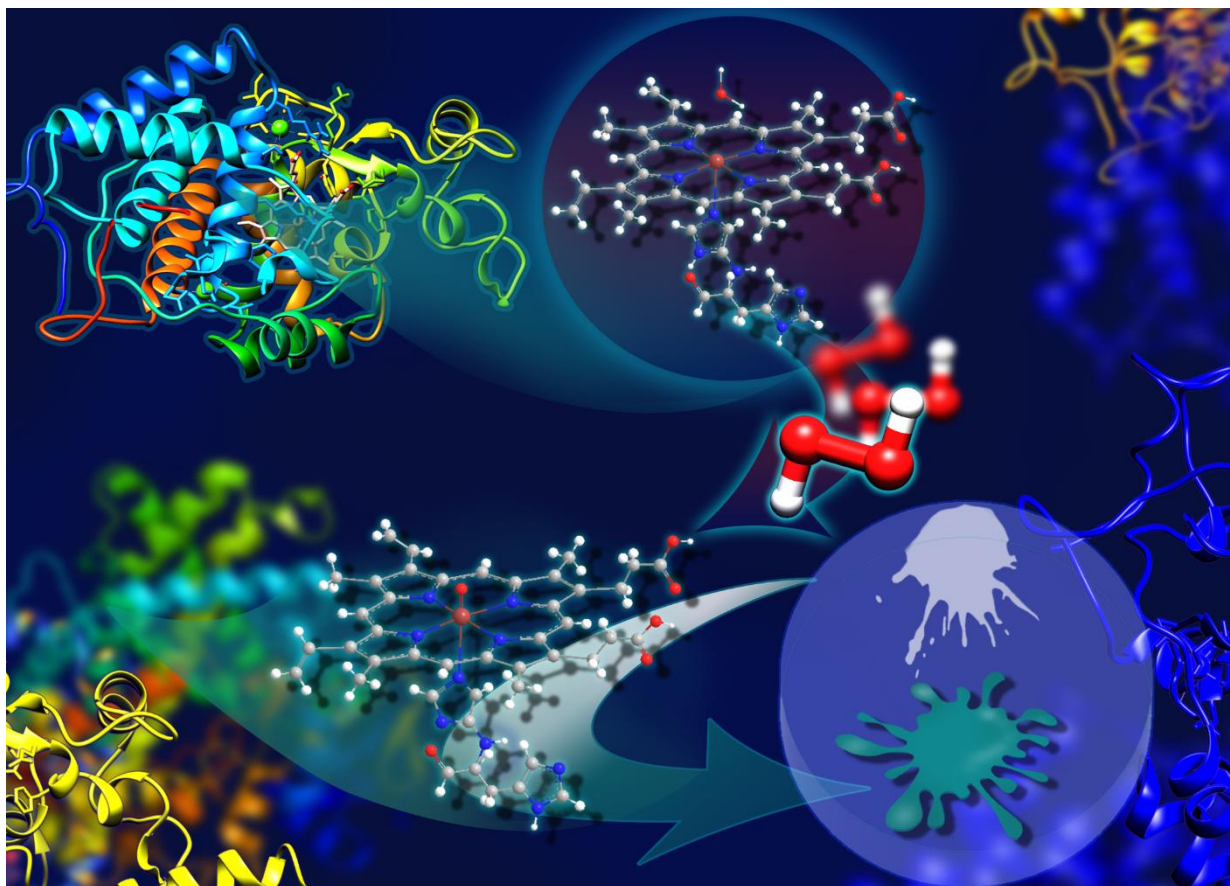
Components	ETW	HTW	Colored Whey Control
Calcium (%)	0.59	0.57	0.58
Iron (ppm)	15	11	13
Copper (ppm)	8	3	6
Total Nitrogen (%)	13.27	13.30	13.36

Contributions

Raheleh Ravanfar wrote the manuscript and performed the experiments with support and advice from Alireza Abbaspourrad. Alireza Abbaspourrad supervised the project. Peter Lawrence helped with mass spectrometry. Kyle Kriner helped with HPLC and provided invaluable comments.

CHAPTER 3

HIGH-VALENT IRON-OXO COMPOUND OF HORSERADISH PEROXIDASE AS A CRITICAL INTERMEDIATE FOR THE DETECTION OF ULTRATRACE AMOUNT OF HYDROGEN PEROXIDE IN ALCOHOLS



ABSTRACT

Despite the importance of hydrogen peroxide (H_2O_2) in initiating oxidative damage and its connection to various diseases, the detection and quantification of low concentrations of H_2O_2 ($<10 \mu\text{M}$) is still limited using current methods, particularly in non-aqueous systems. Most of these techniques require the synthesis and fabrication of sensors to probe H_2O_2 using complex, expensive instrumentation. We are interested in developing a simple, fast, and inexpensive method to detect and quantify H_2O_2 in both aqueous and

non-aqueous systems, including alcohols. In this regard, we demonstrate that high-valent iron-oxo intermediates of horseradish peroxidase (HRP) are well suited to detect ultratrace amount of H₂O₂ impurities in alcohols in the range of 0.001–1000 μM using just a UV/Vis spectrophotometer. We monitor the optical spectra of low concentrations of HRP (0.1-1 μM) for the red shift in the Soret and Q-band regions upon the addition of alcohols, as well as the reversibility of this shift to the original wavelength over time due to the spontaneous decay of ferryl intermediates to the ferric state. We confirm the formation of ferryl intermediates using electron paramagnetic resonance (EPR) and cyclic voltammetry (CV). Integrating heme chemistry and the oxidation of ABTS (2,2'-Azinobis [3-ethylbenzothiazoline-6-sulfonic acid]-diammonium salt), we also quantify H₂O₂ impurity of alcohols in the range of 0.1–1000 μM. Thus, ferryl intermediates of HRP are potential candidates for the detection and quantification of H₂O₂ in alcohols at ppb levels through a simple UV/Vis spectrophotometric method.

3.1. INTRODUCTION

Hydrogen peroxide (H₂O₂) is an essential oxygen metabolite in living systems and serving as a messenger in cellular signal transduction.⁹⁰ The overproduction of H₂O₂ from the mitochondrial electron transport chain results in oxidative stress, causing functional decline in organ systems.⁹¹ Such oxidative stress over time is also connected to various diseases, including cancer,⁹² cardiovascular disorders,⁹³ and Alzheimer's and related neurodegenerative diseases.⁹⁴ Moreover, H₂O₂ and its derivatives are strong oxidative agents employed in many industrial and medical processes, such as the synthesis of organic compounds and disinfection.⁹⁵⁻⁹⁶ The significant impact of H₂O₂

on a variety of oxidative damage mechanisms,⁹⁷⁻⁹⁸ environmental hazards,^{96, 99} and human health¹⁰⁰⁻¹⁰¹, as well as its application in biosensing,¹⁰² provide motivation to develop a sensitive and selective diagnostic method for detecting and quantifying H₂O₂, particularly at low concentrations.

Over the past several decades, many H₂O₂ sensing techniques have been devised based on spectrophotometry,¹⁰³⁻¹⁰⁴ fluorescence,^{101, 105} chemiluminescence,¹⁰⁶ enzymatic, and electrochemical methods.¹⁰⁷⁻¹¹¹ One of the most extensively used enzymatic systems for H₂O₂ sensing is horseradish peroxidase (HRP)-H₂O₂.^{24-27, 110-111} The broad application of HRP in H₂O₂ sensing is due to its ability to translate catalysis into an electrochemical signal, as well as its stability and commercial availability.²⁸ HRP is able to catalyze the heterolytic cleavage of the peroxidic bond in H₂O₂ and form a high-valent iron-oxo (ferryl heme) intermediate of the enzyme (compound I).²⁹⁻³² In compound I, the iron at the heme center is oxidized from Fe^{III} to Fe^{IV}=O, and the porphyrin or an amino acid in the side chain of HRP is oxidized to a radical.³³ Thus, compound I can oxidize two molecules of a substrate, such as ABTS, through two consecutive single electron reactions to form compound II, before finally reducing back to the Fe^{III} state.³³⁻⁴⁰

Most HRP-based methods, however, are limited by some serious disadvantages, such as environmental instability, complex fabrication design, tedious immobilization procedures, and high cost.^{104, 107} Moreover, most of these methods are only efficient for H₂O₂ detection in aqueous media and encounter low efficiency and sensitivity in other organic solvents, such as alcohols. For example, the partial oxidation of primary or secondary alcohols due to autoxidation results in the production of H₂O₂, which

produces an aldehyde or ketone as a coproduct.¹¹² Since alcohols are commonly applied in various chemical and enzymatic reactions, the presence of an adventitious amount of H₂O₂ can interfere with reaction cascades.¹ Therefore, providing a selective, rapid, convenient, and low cost analytical method for detection and quantifying H₂O₂ in alcohols is of great interest.

Here, we report a simple spectrophotometric method to detect and quantify H₂O₂ in alcohols at ppb levels through the direct detection of the ferryl intermediate of HRP. In this manner, we are able to detect adventitious amount of H₂O₂ in alcohols, such as ethanol, glycerol, 2-chloroethanol, and isopropanol. In this method, we monitor the red shift in the Soret and Q-band regions of the HRP's optical spectrum upon the addition of alcohols to the HRP aqueous solution at pH 6.0. The red shift of the Soret band from 402 nm to 418 nm with a shoulder at 350 nm, and the appearance of two Q-bands at 527 nm and 557 nm are indicative of the formation of the ferryl intermediates of HRP, which can be formed only in the presence of H₂O₂ impurity.^{46, 88-89} Furthermore, we monitor the reversibility of the red shifts over time to their original wavelengths as an indication of the spontaneous decay of the ferryl intermediates to the ferric state, distinguishing these red shifts from possible solvatochromic shifts. Using this method, we can efficiently detect ppb levels of H₂O₂ (0.001-1000 μ M) in the alcohols, where it is barely possible to detect this amount of H₂O₂ using other common methods, such as hydrogen peroxide test strips. We characterize the ferryl intermediates and their decay to ferric heme upon the addition of alcohols to HRP using UV/Vis spectrophotometry and confirm their presence using electron paramagnetic resonance (EPR) and cyclic voltammetry (CV). Furthermore, we quantify H₂O₂ in alcohols based on the oxidation

of the ABTS substrate using low concentrations of HRP (0.1-1 μM) in the range of 0.1-1000 μM . This demonstration suggests the importance of monitoring the ferryl intermediates for the detection and quantification of H_2O_2 impurity in alcohols at ppb levels using a simple, cost-effective, and accurate method.

3.2. MATERIALS AND METHODS

3.2.1. Materials

The salt-free, lyophilized powder of HRP isozyme C type VI-A (950-2000 units/mg solid), monobasic and dibasic potassium phosphate ($\geq 98\%$), potassium ferricyanide ($\geq 99.0\%$), and ABTS ($\geq 98\%$) were purchased from Sigma Aldrich (St. Louis, MO). Hydrogen peroxide (30% w/w solution) was purchased from Anachemia (Que, Canada). Pure 200 proof ethanol was purchased from KOPTEC (PA, US) and glycerol was purchased from Mallinckrodt Chemicals (Wilkes-Barre, PA). Other alcohols including isopropanol, methanol, 2-mercaptoethanol, 2-chloroethanol, 2,2-dichloroethanol, 2,2,2-trichloroethanol, trifluoroethanol, and ethylene glycol were purchased from Sigma Aldrich (St. Louis, MO).

3.2.2. Detection of H_2O_2 through the Analysis of the Ferric State of HRP and its Ferryl Intermediate Using UV/Vis Spectrophotometry

The aqueous solution of HRP at three different concentrations (0.1 M, 1 M, and 10 M) was prepared in potassium phosphate buffer pH 6.0. Ethanol containing H_2O_2 at different concentrations (0.001 μM , 0.01 μM , 0.1 μM , 1 μM , 10 μM , 100 μM , 1000 μM , and 10^4 μM) were prepared through serial dilution of the 10^5 μM stock solution of

H₂O₂ in ethanol. The HRP solution (500 μL) was treated with 500 μL of different solutions of H₂O₂ in ethanol to form ferryl intermediates. The UV/Vis absorption spectra of the ferryl intermediates were recorded using UV/Vis spectrophotometry (UV-vis Spectrophotometer UV-2600, Shimadzu Scientific Instruments/Marlborough, MA) in the range of 200–800 nm. The spectra were investigated at the Soret and Q-band regions.

3.2.3. Analysis of the Ferric State of HRP and its Ferryl Intermediate Using Cyclic Voltammetry

The CV data was collected using a BASi EC Epsilon potentiostat. The reference electrode was a silver wire immersed in a saturated solution of KCl, the counter electrode consisted of a platinum wire coil with 10 cm length, and the working electrode was a glassy carbon electrode of 0.3 mm diameter. The working electrode was polished to a mirror-like finish on a pad with 0.3 μm alumina and deionized water, and then sonicated for 30 s in deionized water. The platinum counter electrode was burned with a butane flame for 30 s. The reference electrode solution was made fresh for every measurement and at the end of each experiment, a small amount of potassium ferricyanide was added as an internal reference. Anhydrous nitrogen gas was purged through the HRP solution for at least 10 minutes prior to analysis.

3.2.4. Analysis of the Ferric State of HRP and its Ferryl Intermediate Using EPR

EPR spectra were recorded on a Bruker EMX (BRUKER, Billerica, MA) spectrometer at a frequency of 9.24 GHz under standard conditions in 4

mm ID quartz tubes. A liquid helium cryostat ESR-10 (Oxford Instruments Ltd, England) was used to stabilize the temperature at 12 K. The spectra were recorded with a modulation amplitude of 8G and microwave power of 625 μ W.

3.2.5. Quantification of H₂O₂ through the Oxidation of ABTS

The H₂O₂ was measured spectrophotometrically based on the oxidation of the substrate, 2,2'-Azino-bis(3-ethylbenzothiazoline-6-sulfonic acid) diammonium salt (ABTS), in the presence of HRP using UV/Vis spectrophotometry (UV-vis Spectrophotometer UV-2600, Shimadzu Scientific Instruments/ Marlborough, MA). Briefly, 50 μ L of ABTS (2 mM, 20 mM) in 0.1 M potassium phosphate buffer (pH 6.0) was mixed with 50 μ L of HRP (0.1 μ M, 1 μ M, and 10 μ M) and 50 μ L of alcohols containing different concentrations of H₂O₂ (0.001 μ M, 0.01 μ M, 0.1 μ M, 0.5 μ M, 1 μ M, 10 μ M, 50 μ M, 100 μ M, 500 μ M, and 1000 μ M). The linear increase in the absorbance at 420 nm (λ_{max} of the oxidized product of ABTS) was recorded at 25 °C. Three main formulas were derived from the linear fits and were used to measure the H₂O₂ impurity in alcohols.

3.2.6. Statistical Analysis

Data were subjected to analysis of variance (ANOVA) using SPSS software package version 15.0 for Windows. All measurements were performed in triplicate. Mean comparisons were performed using the post hoc multiple comparison Duncan test to examine if differences were significant at $P < 0.05$.

3.3. RESULTS AND DISCUSSION

We used common hydrogen peroxide test strips to detect any impurity of H₂O₂ in ethanol, the minimum detectability of which is 30 μM H₂O₂ (Figure 3.1a, i). The results showed no hydrogen peroxide in ethanol (Figure 3.1a, ii). We prepared different concentrations of H₂O₂ in both water and pure ethanol, and compared the color of hydrogen peroxide test strips in exposure to these solutions (Figure 3.1a, iii). The results showed the test strips can barely detect H₂O₂ in ethanol at low concentrations (< 100 μM), and cannot accurately quantify the concentrations of H₂O₂ (<1 mM) (Figure 3.1a, iii). Thus, we aim to develop an accurate method to detect and quantify the H₂O₂ impurity of alcohols.

Studies have shown that the optical spectra of the resting state of HRP (Fe^{III}) has a Soret band of 402 nm and a Q-band of 497 nm, while the ferryl heme intermediate of HRP (Fe^{IV}=O) has a Soret of 418 nm and two Q-bands of 527 nm and 557 nm (Figure 3.1b).^{46, 88-89} We hypothesized that these indicative peaks could be used to detect the H₂O₂ impurity of alcohols and developed a simple spectrophotometric method utilizing HRP to detect and quantify H₂O₂ based on the formation of ferryl intermediates (Figure 3.1c).⁴⁶

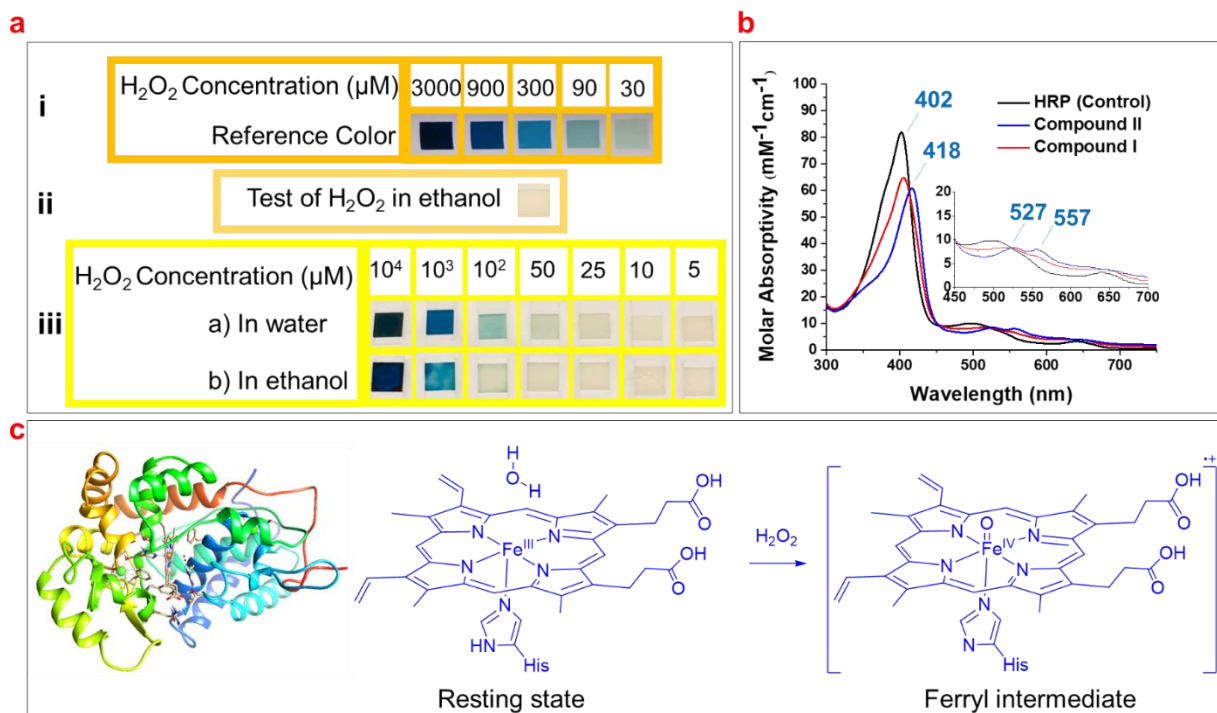


Figure 3.1. a) The detection and quantification of H₂O₂ according to the reference colors using H₂O₂ test strips: i) reference colors with a detection limit of 30 μM; ii) examination of ethanol for H₂O₂ impurity using the test strip; iii) comparing the detection limit of H₂O₂ in ethanol and water using the test strips. b) The UV/Vis spectra of the resting state of HRP (control), in comparison with its ferryl intermediates, compound I and compound II). c) The schematic of HRP (PDB code: 1ATJ), and its heme structure in the resting state and ferryl intermediate upon reacting with H₂O₂.

We added different concentrations of H₂O₂ in ethanol to the aqueous solution of two different HRP concentrations, 1 and 10 μM, and investigated the red shifts relevant to the formation of ferryl intermediates. Surprisingly, the results showed that 1 μM HRP can detect lower concentrations of H₂O₂ impurity in ethanol (0.001 μM) by making a red shift in the Soret band from 402 nm to 404 nm (Figure S3.1a-b), while 10 μM HRP

can detect higher concentration of H₂O₂ impurity of ethanol (10 μM) by making a red shift in the Soret band from 402 nm to 404 nm (Figure 3.2, a-f). The 1 μM and 10 μM HRP solutions cause a red shift from 402 nm to 418 nm upon the addition of 100 and 1000 μM H₂O₂ in ethanol, respectively (Figure S3.1a-g and Figure 3.2a-h). Both HRP concentrations show Soret bands shift to 418 nm at higher concentrations of H₂O₂ in ethanol (Figure S3.1h,i and Figure 3.2i), and only 1 μM HRP is able to detect low concentrations of H₂O₂ impurity of ethanol (e.g. 0.001 μM). Thus, we suggest to use 1 μM HRP for detection of high and low H₂O₂ impurity of ethanol in the range of 0.001-1000 μM.

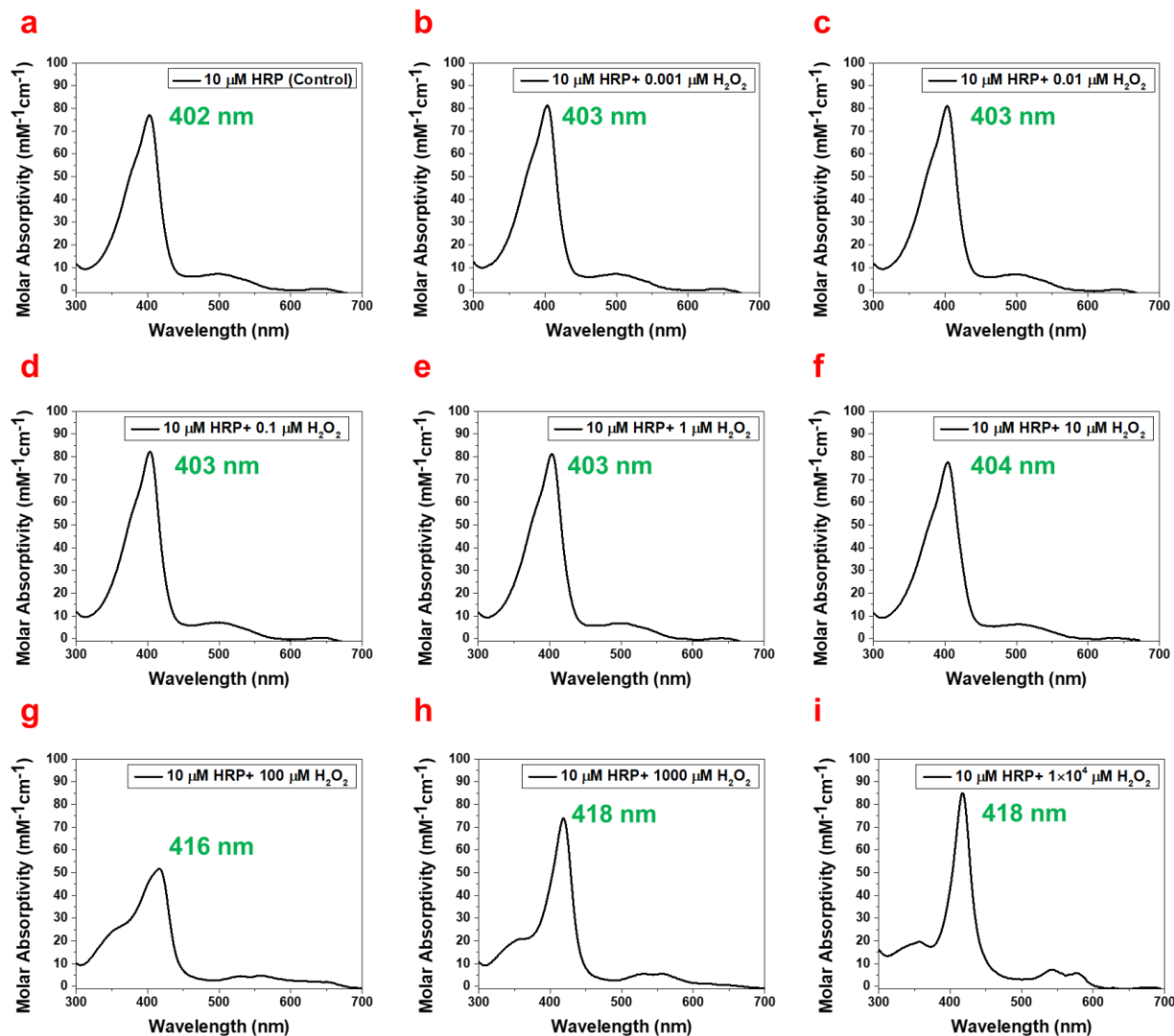


Figure 3.2. UV/Vis spectra of the 10 μM HRP upon the addition of H_2O_2 in ethanol at different concentrations, including a) 0 μM , b) 0.001 μM , c) 0.01 μM , d) 0.1 μM , e) 1 μM , f) 10 μM , g) 100 μM , h) 1000 μM , and i) 10^4 μM . The wavelengths associated to Soret bands are shown in green.

The red shifts correlated to the ferryl intermediates can be distinguished easily from solvatochromic shifts. First, it is noteworthy that the addition of higher concentrations of ethanol containing H_2O_2 impurity do not increase the red shift to more

than 418 nm (Figure 3.3a). Second, the ferryl intermediates of HRP are not thermodynamically stable and decay spontaneously (Figure 3.3b).^{33, 113} Thus, the red shifts of the ferryl intermediates would be reversible. These two characteristics of the red shifts correlated to the ferryl intermediates can distinguish them from solvatochromic shifts. Even at lower concentrations of H₂O₂ impurity of ethanol, the red shift can reach 418 nm upon the titration of the HRP solution (either 1 μM or 10 μM) with more ethanol, which adds more H₂O₂ to the system (Figure 3.3c, d). However, over time (~2 h) the Soret band moved back to 402 nm, showing that the ferryl intermediates decay to ferric state. Treating HRP with different ethanol concentrations, we show that the time for the ferryl intermediates of HRP to decay to 402 nm increases from 2 h for 10% ethanol to 2.5 h for 20% ethanol (containing 80 μM H₂O₂) in the reaction mixture (Figure 3.3e, f). This increase in the decay time is because of the addition of more H₂O₂ in the reaction mixture along with the ethanol, which makes it possible for each molecule of HRP to produce ferryl intermediates for longer time. Thus, the ferryl intermediates are accumulating in the reaction mixture for longer time, and subsequently, the shifts come back to the original wavelength in longer time.

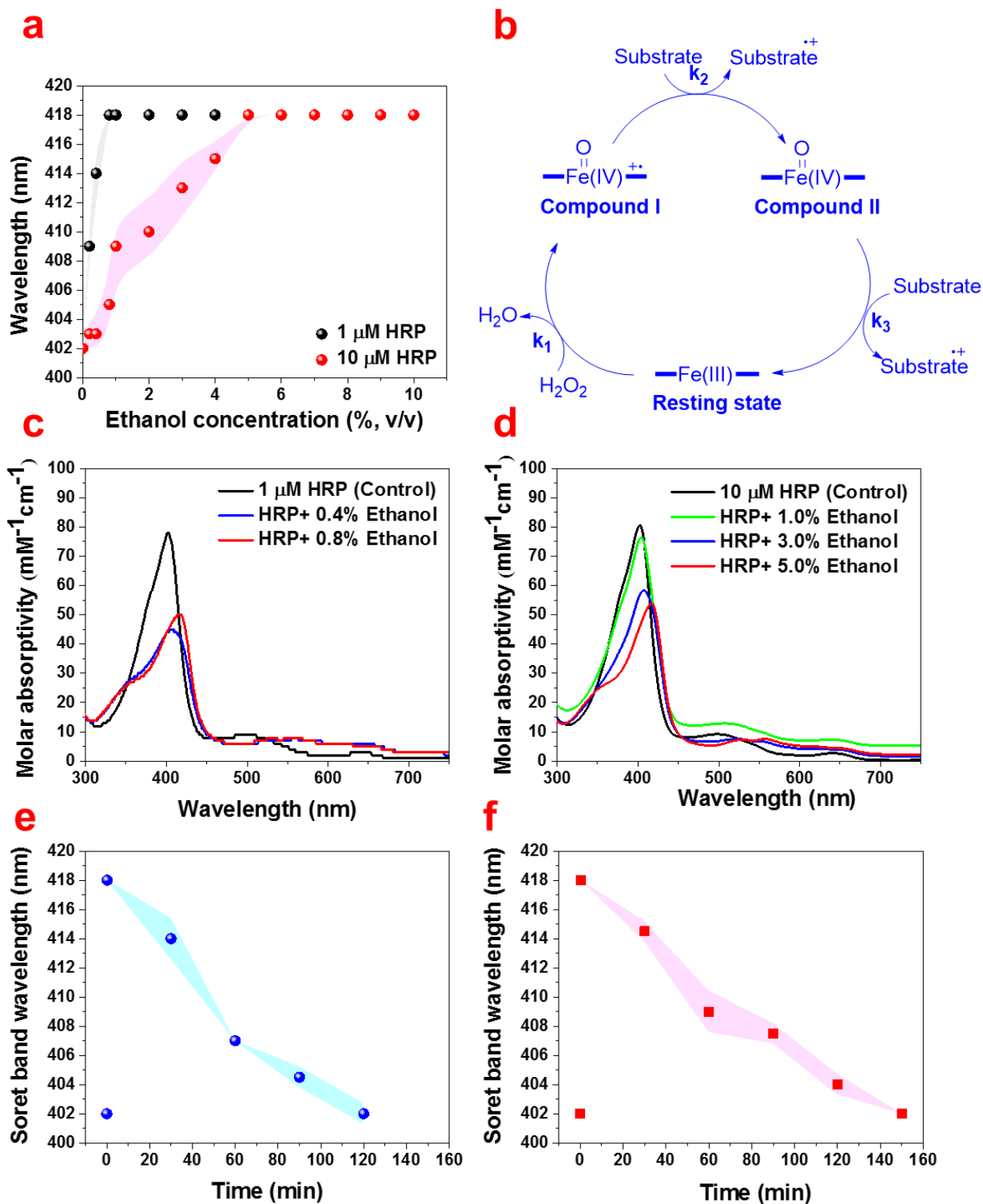


Figure 3.3. a) The change in the wavelength of the Soret band through the titration of HRP (1 μM and 10 μM) with ethanol containing 80 μM H₂O₂. b) The schematic for the

decay of ferryl intermediates to the ferric state. c) Titration of HRP (1 μM) with ethanol containing 80 μM H_2O_2 to achieve a redshift of 418 nm. d) Titration of HRP (10 μM) with ethanol containing 80 μM H_2O_2 to achieve 418 nm. e) The reversibility of the red shift from 418 nm to 402 nm over 2 h for HRP treated with 10% (V/V) ethanol containing 80 μM H_2O_2 . f) The reversibility of the red shift from 418 nm to 402 nm over 2.5 h for HRP treated with 20% (V/V) ethanol containing 80 μM H_2O_2 .

We investigated the detection of H_2O_2 impurity in a few different alcohols using our system. The UV/Vis spectra show that the Soret band of HRP red shifts to 418 nm upon the titration of HRP solution with ethanol, glycerol, isopropanol, and 2-chloroethanol, with a shoulder at 350 nm, as well as Q-bands at 527 nm and 557 nm (Figure S3.2a-d). However, methanol, 2,2-dichloroethanol, 2,2,2-trichloroethanol, trifluoroethanol, 2-mercaptoethanol, and ethylene glycol do not show any red shift in the Soret band or Q-band of HRP (Figure S3.3), suggesting they do not contain any detectable H_2O_2 impurity. Interestingly, when ferryl intermediates decay to the ferric state over time, HRP can show the same red shift from 402 nm to 418 nm upon the second addition of these alcohols (Figure S3.4). Thus, the HRP can be used as a recyclable method to detect H_2O_2 impurities.

Previous studies on HRP and H_2O_2 have shown that the ferryl intermediates of HRP formed through the reaction of ferric state of HRP and H_2O_2 are EPR-silent and generate only a broad EPR signal characteristic of the oxyferryl porphyrin π -cation radical ($g = 2.0$).^{39, 46-48} EPR spectra for HRP treated with ethanol (Figure 3.4) and glycerol (Figure S3.5) containing H_2O_2 impurity confirm the formation of ferryl

intermediates, which are also shown in the UV/Vis spectra shown earlier (Figure S3.2a-b). The initial formation of an EPR-silent intermediate upon the reaction of ferric HRP with alcohol molecules over short timescales (30 s) shows that the ferric signals in native HRP (control) (Figure 3.4a and S3.5a) disappear in the high-spin region of heme while a new resonance is observed in the region of the low spin heme ($g = 2.0$) arisen from a radical cation located on the heme (Figures 3.4b and S3.5b). These EPR spectra of the intermediates formed upon the addition of impure ethanol and glycerol to HRP are also in agreement with previous reports of EPR analysis of ferryl intermediates upon the addition of H_2O_2 to HRP, ascorbate peroxidase, and cytochrome C peroxidase.⁴⁶⁻⁴⁸ Examining the EPR spectra for one hour, we found that the features of the high spin ferric heme (Fe^{III}) begin to reappear over time, while the organic radical signal decays in the low-spin region (Figure 3.4c-e, and Figure S3.5c-e). Thus, we also confirmed the decay of the ferryl intermediates through the reversibility of the EPR signals at both high-spin and low-spin regions.

High-spin Region

Low-spin Region

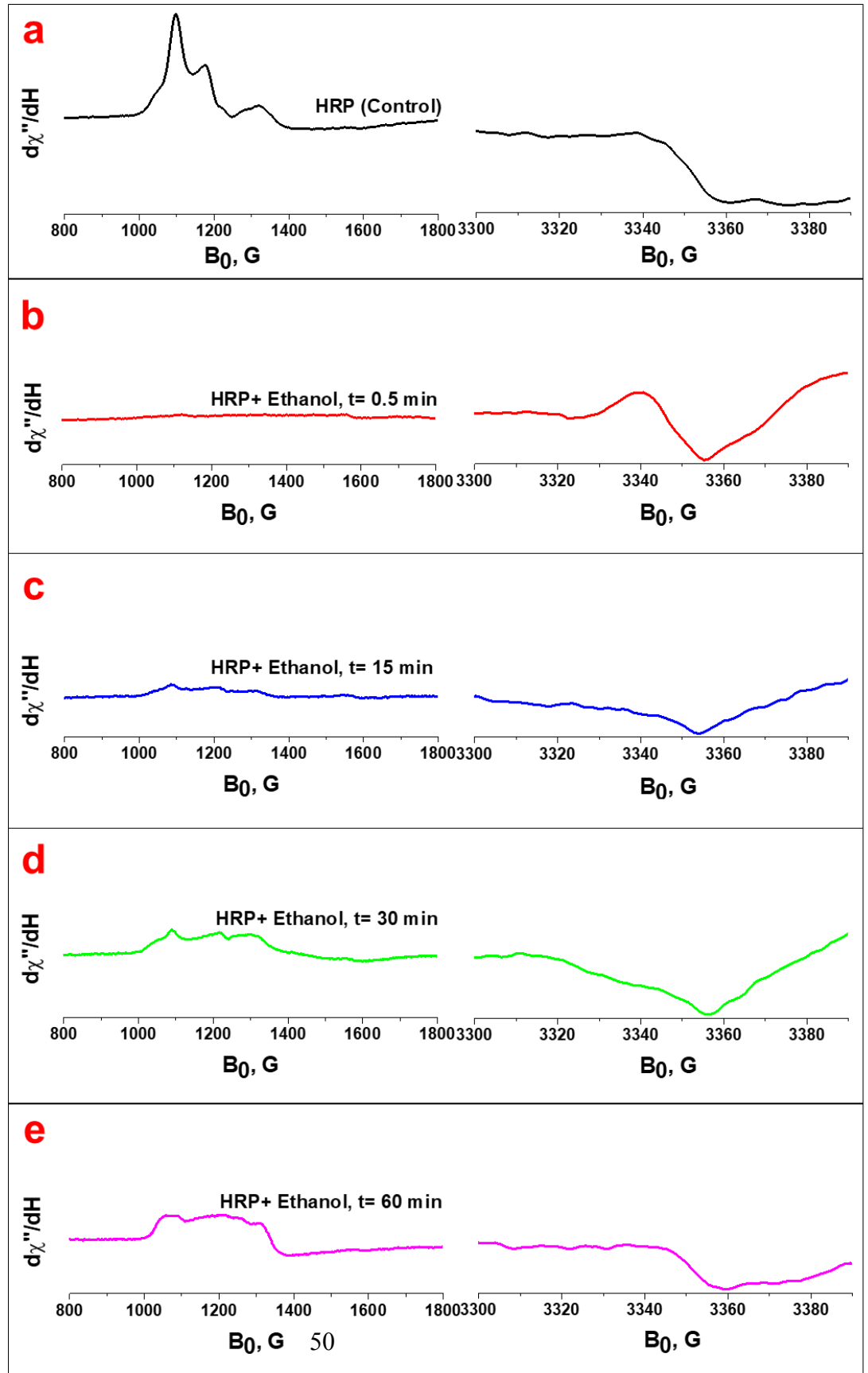


Figure 3.4. a) EPR spectra of the native HRP (control) at both high-spin and low-spin regions. b, c, d, e) EPR spectra of the HRP upon the addition of ethanol containing H₂O₂ impurity at 0.5 min, 15 min, 30 min, and 60 min, respectively. The spectra were collected at 12 K and 625 μW.

We also confirmed the formation of the ferryl intermediate (Fe^{IV}=O) and its decay to Fe^{III} using CV. The voltammogram of the HRP solution shows the appearance of a reduction peak associated with the ferryl intermediate upon the addition of ethanol containing 80 μM H₂O₂ (Figure 3.5a), which is the same as the reduction peak appeared upon the addition of H₂O₂ aqueous solution to HRP (Figure 3.5b). The intensity of this reduction peak increases upon the addition of more ethanol percentage (v/v) containing 80 μM H₂O₂ impurity (Figure 3.5c). The decay of the ferryl intermediate over time is also shown by the decreasing peak intensity over 10 minutes (Figure 3.5d). This result is in agreement with the decay of the Fe^{IV}=O intermediate demonstrated in the UV/Vis spectra (Figure 3.3e-f) and EPR spectra (Figure 3.4a-e), and the formation of ferryl intermediates upon the reaction of heme and H₂O₂.¹¹³

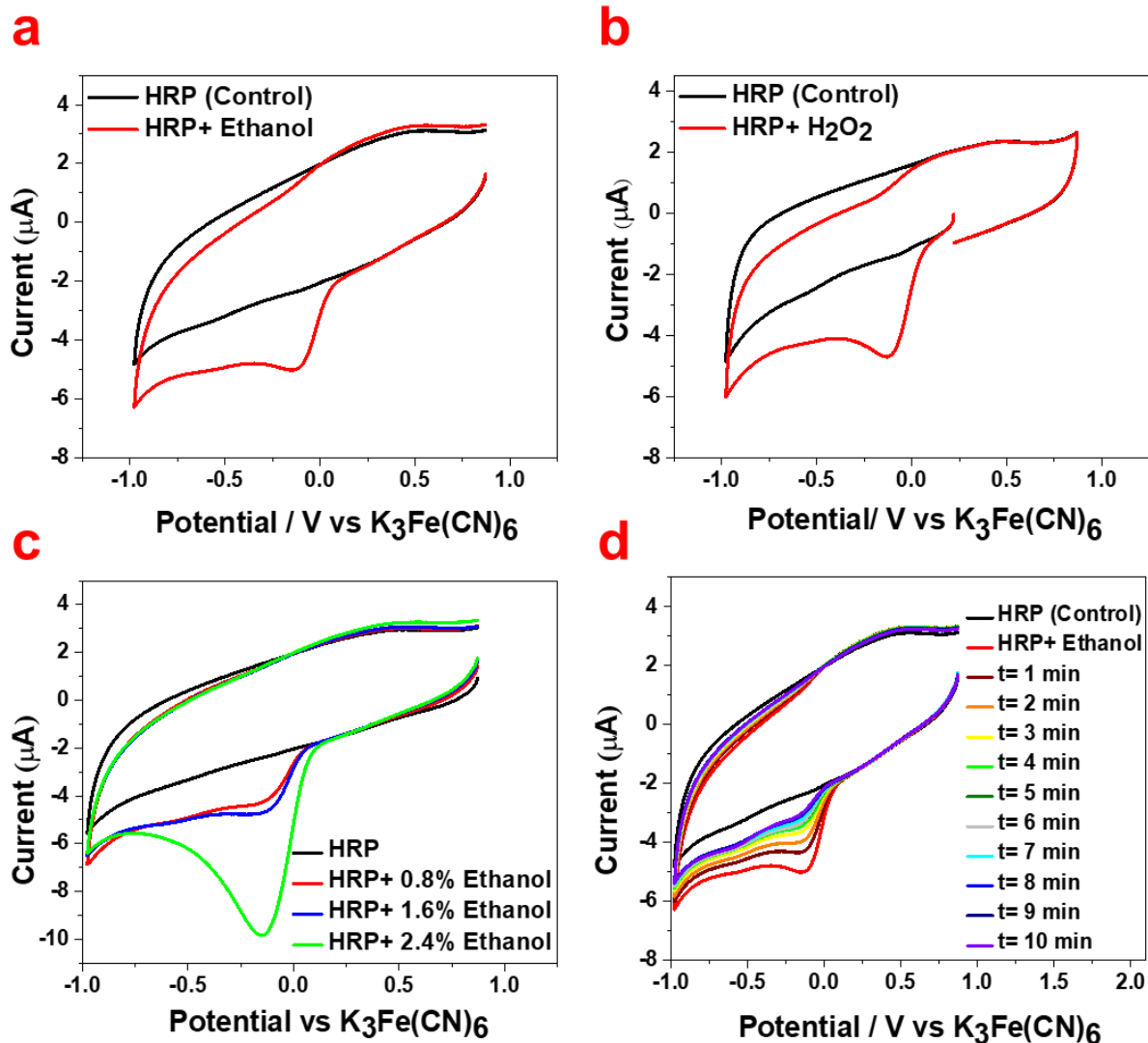


Figure 3.5. Electroreduction catalysis by HRP (control, black) upon treatment (red) with a) ethanol containing $80 \mu\text{M}$ H_2O_2 and b) aqueous solution of H_2O_2 ($80 \mu\text{M}$). c) The increase of intensity of the reduction peak upon the addition of more ethanol percentage (v/v) containing $80 \mu\text{M}$ H_2O_2 impurity. d) The decrease of the intensity of the reduction peak over a 10 min period for HRP treated with ethanol containing $80 \mu\text{M}$ H_2O_2 impurity. Cyclic voltammograms were

measured in N₂-saturated potassium phosphate buffer (0.1 M, pH 6.0) at a scan rate of 100 mV sec⁻¹.

In order to quantify the detected H₂O₂ impurity in alcohols, we use ABTS as an organic substrate in the aqueous solution of HRP (pH 6.0). ABTS can donate electrons to ferryl intermediates of HRP (Figure 3.6a, i). ABTS, which has been widely used in the literature to measure HRP activity, changes from white to blue-green in color upon oxidation, and the intensity of this color can be easily measured by UV/Vis spectrophotometry (Figure 3.6a, ii). Measuring the color intensity of ABTS (2 mM and 20 mM) after 30 minutes after the reaction with HRP (0.1 μM, 1 μM, and 10 μM) and ethanol containing different concentrations of H₂O₂ impurity, we optimized the best concentrations for measuring each range of H₂O₂ impurity. Our results show different trends at different ranges of H₂O₂ impurity based on the HRP and ABTS concentrations. Using both 2 mM and 20 mM ABTS solutions, all HRP concentrations result in a linear and significantly increasing trend for the absorption of ABTS in the range of 1–1000 μM H₂O₂ impurity in ethanol (Figure 3.6b-d and Figure S3.6a-c). However, the 1 μM and 10 μM HRP do not show a significant increasing trend in the range of 0–1 μM H₂O₂ impurity in ethanol (Figure 3.6c,i and d,i, and Figure S3.6b,i and c, i). Figure 3.6b, i illustrates that at 20 mM ABTS solution, 0.1 μM HRP shows significant increasing absorption along with the concentration of the H₂O₂ impurity of ethanol in the range of 0–1 μM. The 2 mM ABTS, however, is not appropriate for measuring the H₂O₂ impurity of

ethanol in the range of 0–1 μM due to the non-significant change of absorption along with the concentration of the H_2O_2 impurity of ethanol (Figure S3.6a,i). Thus, we suggest using 0.1 μM HRP in a solution of 20 mM ABTS to quantify the H_2O_2 impurity in alcohols in the ranges of 0–1000 μM .

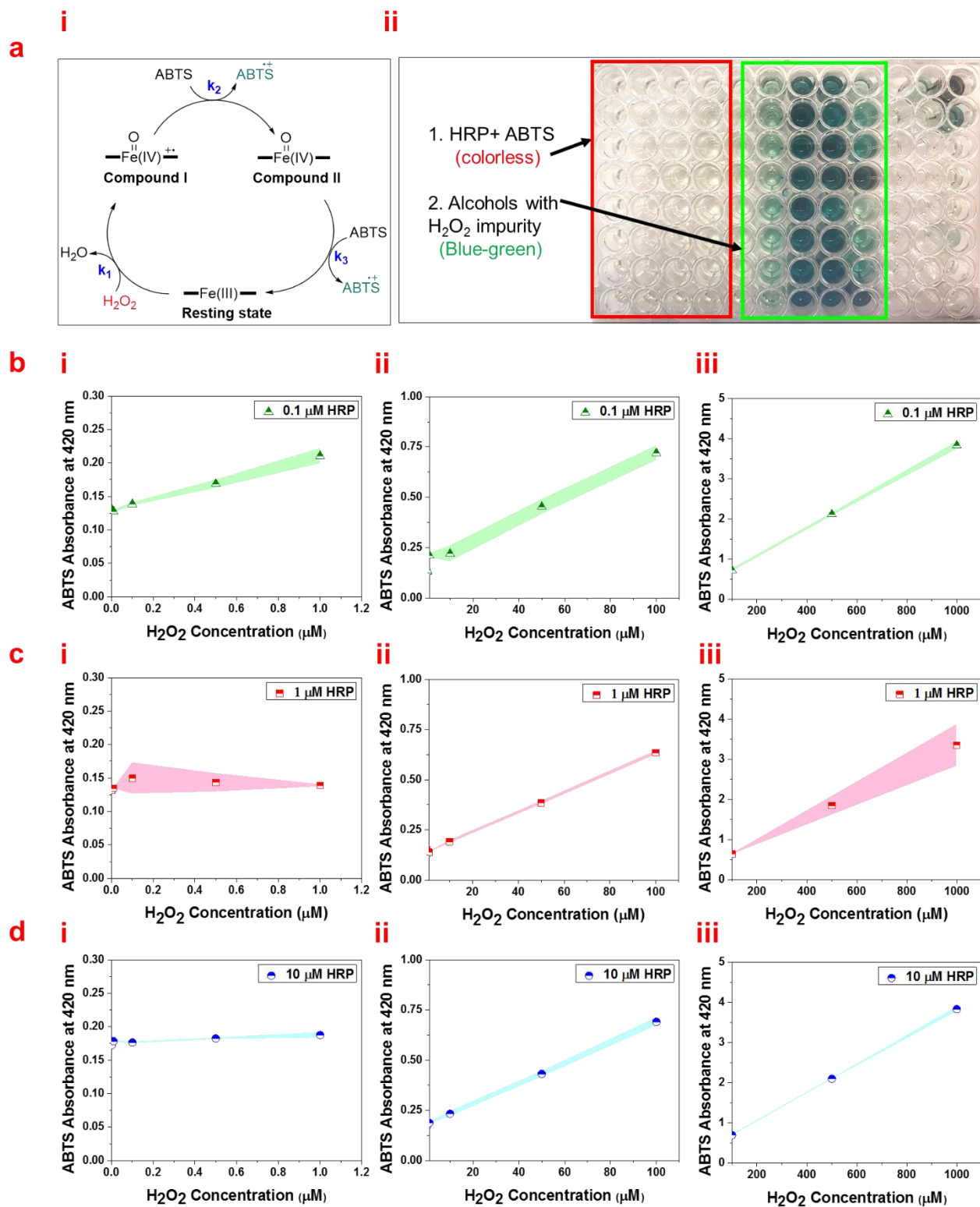


Figure 3.6. a, i) The schematic of the oxidation of ferric heme to ferryl intermediates and subsequent reduction to ferric heme using electron transfer to oxidize ABTS. ii) A

96-well plate containing HRP and ABTS upon the addition of alcohols with different concentrations of H₂O₂. b) UV/Vis absorbance at 420 nm of 0.1 μM HRP, c) 1 μM HRP, and d) 10 μM HRP reacted with 20 mM ABTS at different ranges of H₂O₂ impurity of ethanol (i: 0–1 μM, ii: 1–100 μM, and iii: 100–1000 μM).

Since the slope of the graphs for ABTS absorption versus H₂O₂ concentration in the range of 0-1000 μM follows a step gradient, we propose three formulas to measure the accurate level of H₂O₂ impurity in alcohols in the range of 0-1 μM, 1-100 μM, and 100-1000 μM, individually (Table S3.1). These formulas are derived from the linear fits based on the UV/Vis absorbance of ABTS at 420 nm for three ranges of 0–0.3 a.u., 0.3–1 a.u., and 1–4 a.u. Using these formulas based on the absorbance of ABTS, we successfully measured the H₂O₂ impurity in a few common primary and secondary alcohols (Table S3.2).

3.4. CONCLUSION

We demonstrate that ferryl intermediates of HRP are potential candidates for the detection and quantification of H₂O₂ in alcohols at ppb levels through a simple UV/Vis spectrophotometric method. We measured the red shift in the Soret band in the optical spectra of the HRP from 402 nm up to 418 nm upon the addition of alcohols, and characterized the reversibility of this shift to 402 nm over time. Using this method, we can efficiently detect and quantify ppb levels of H₂O₂ in alcohols, where it is barely possible using other common methods such as hydrogen peroxide test strips. The EPR spectra and CV results confirm the formation and spontaneous decay of ferryl

intermediates upon the reaction of ferric state of HRP and H_2O_2 . We also successfully detected an adventitious amount of H_2O_2 in alcohols, such as ethanol, glycerol, 2-chloroethanol, and isopropanol. This demonstration suggests a simple, cost-effective, and accurate method for the detection and quantification of ultratrace amount of H_2O_2 impurity in alcohols using UV/Vis spectrophotometry, which enables the use of this method in biological and chemical applications.

3.5. SUPPORTING INFORMATION

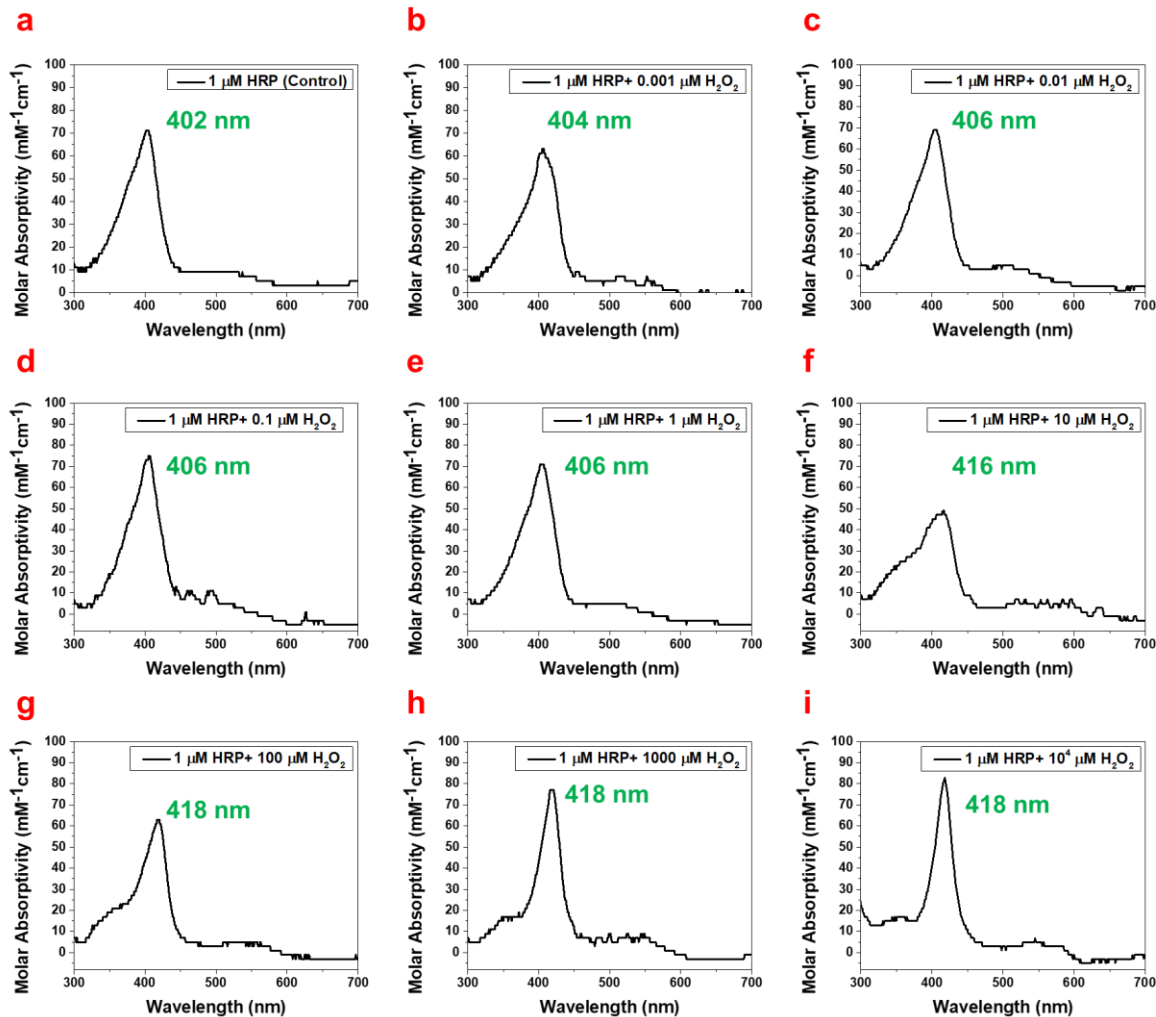


Figure S3.1. UV/Vis spectra of 1 μM HRP upon the addition of H_2O_2 in ethanol at different concentrations, including a) 0 μM , b) 0.001 μM , c) 0.01 μM , d) 0.1 μM , e) 1 μM , f) 10 μM , g) 100 μM , h) 1000 μM , and i) 10^4 μM . The wavelengths associated to Soret bands are shown in green.

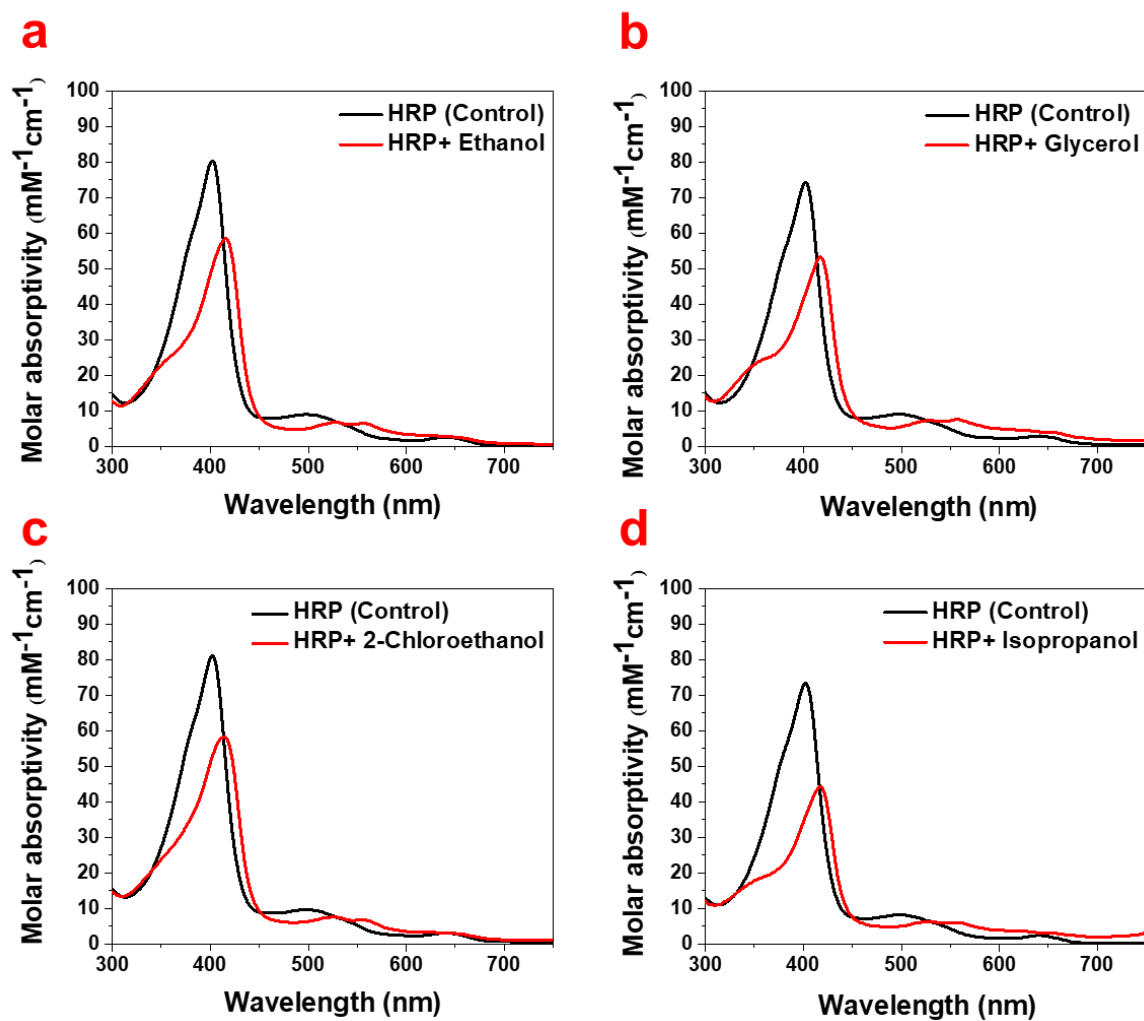


Figure S3.2. UV/visible absorption spectra of HRP after treatment with a) ethanol, b) glycerol, c) 2-chloroethanol, and d) isopropanol, containing adventitious amounts of H_2O_2 .

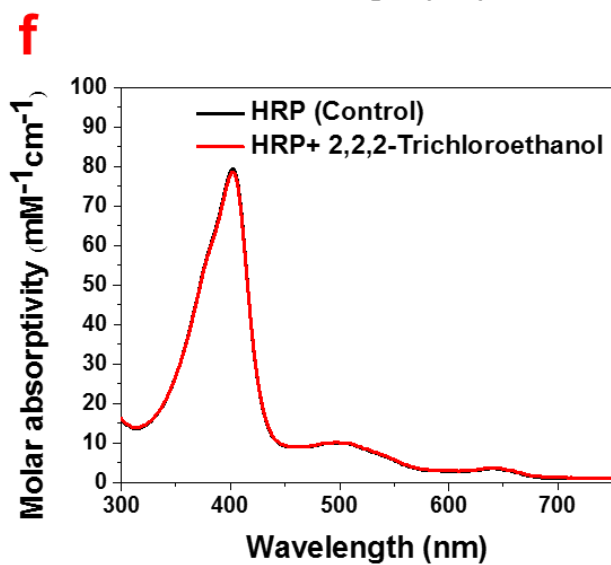
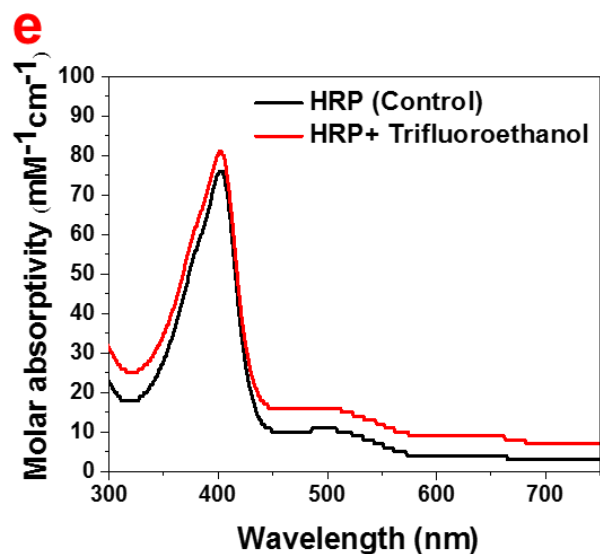
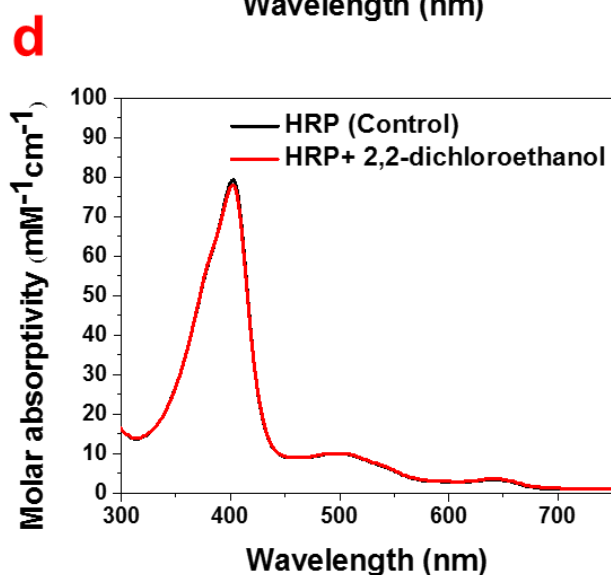
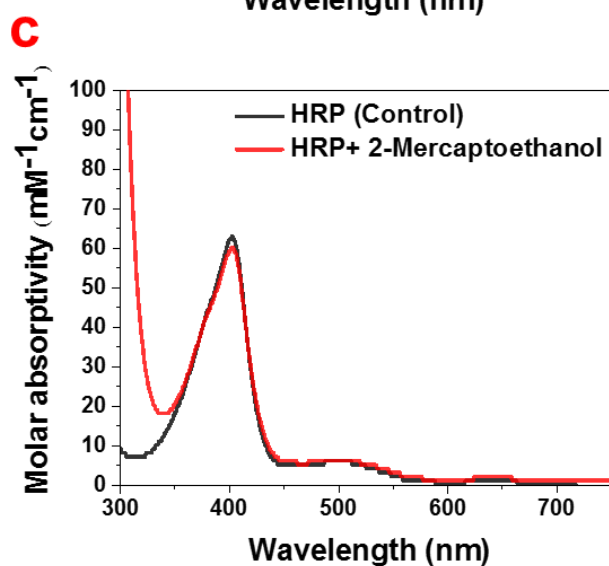
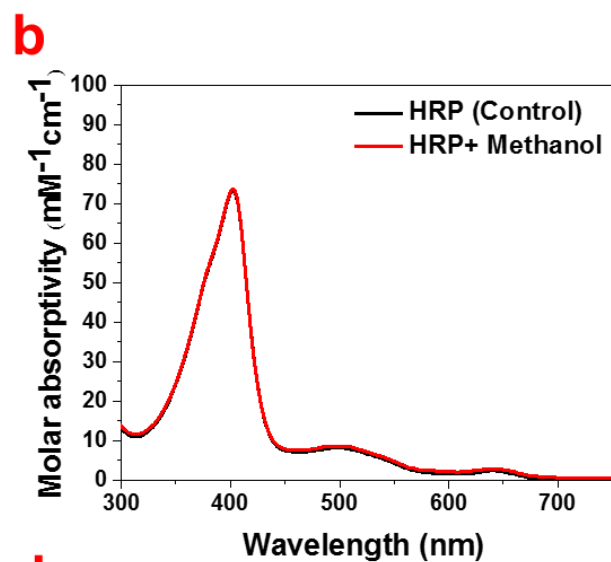
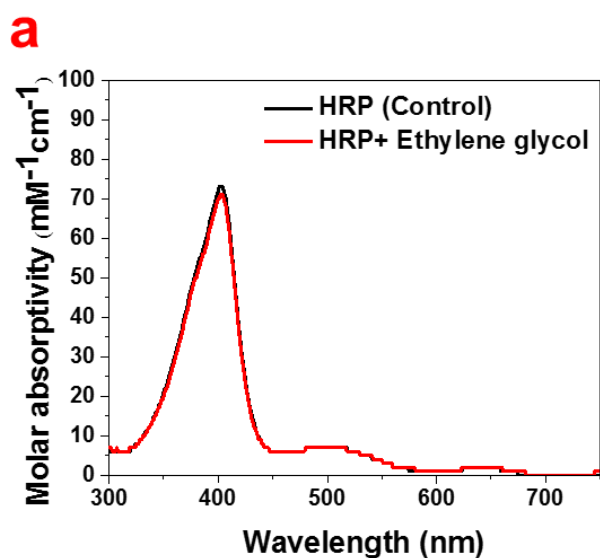


Figure S3.3. UV/visible absorption spectra of HRP after treatment with a) ethylene glycol, b) methanol, c) 2-mercaptoethanol, d) 2,2-dichloroethanol, e) trifluoroethanol, and f) 2,2,2,-trichloroethanol.

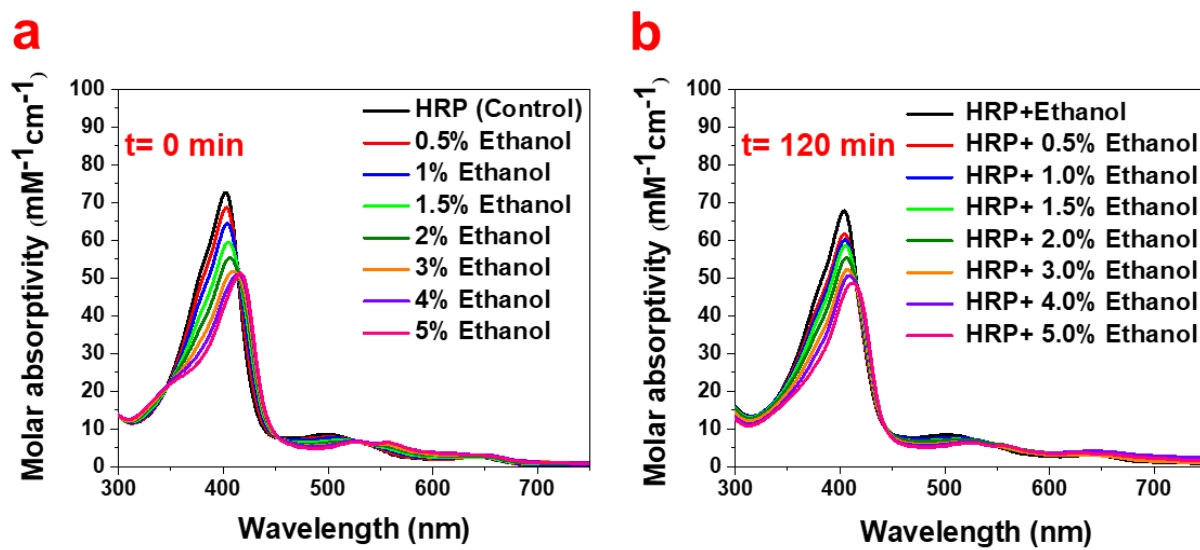


Figure S3.4. The red shifts upon a) the first addition of ethanol and b) the second addition of ethanol after the decay of the ferryl intermediate formed from the first addition of ethanol.

High-spin Region

Low-spin Region

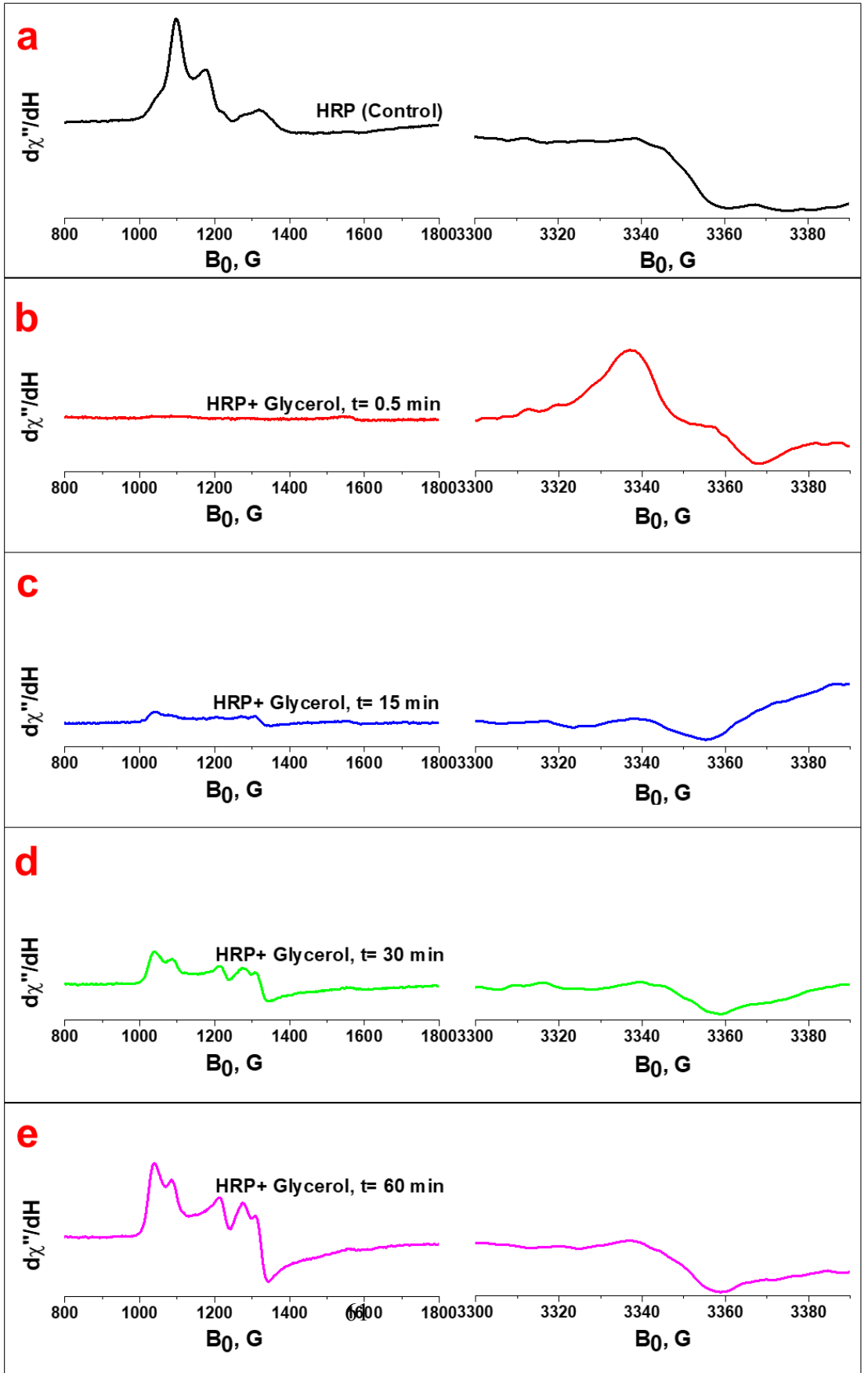


Figure S3.5. a) EPR spectra of the native HRP (control) at both high-spin and low-spin regions. b, c, d, e) EPR spectra of the HRP upon the addition of glycerol containing H_2O_2 impurity at 0.5 min, 15 min, 30 min, and 60 min, respectively. Spectra were collected at 12 K and $625 \mu\text{W}$.

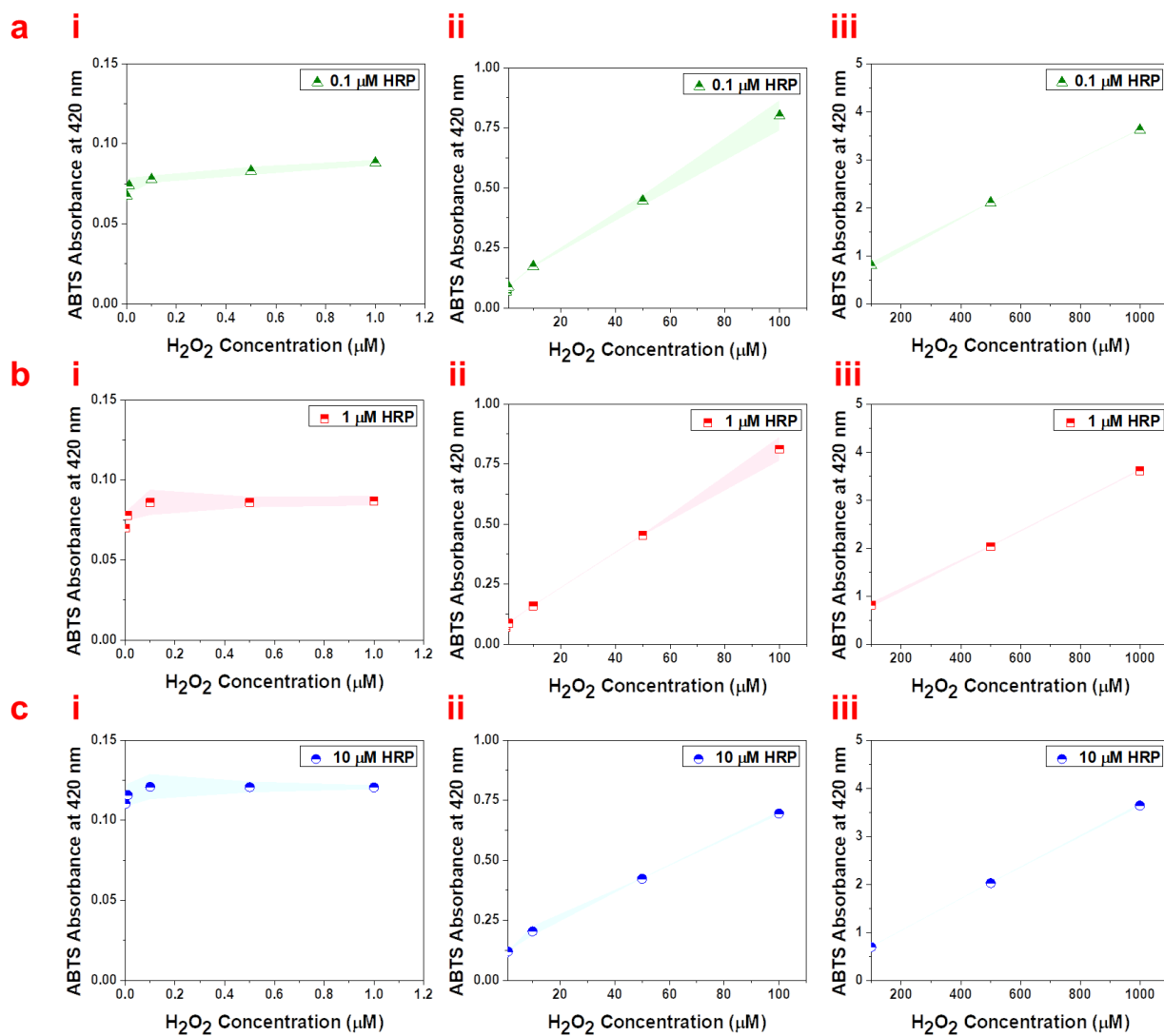


Figure S3.6. UV/Vis absorbance of 2 mM ABTS at 420 nm at different ranges of H_2O_2 impurity of ethanol (i: 0–1 μM , ii: 1–100 μM , and iii: 100–1000 μM) using HRP concentrations of a) 0.1 μM , b) 1 μM , and c) 10 μM .

Table S3.1. The formulas to measure the impurity of H₂O₂ in alcohols based on the absorbance range of ABTS.

Formula No.	Formula	R ²	Range of ABTS absorbance (a.u)	Range of H ₂ O ₂ impurity (μM)
1	y= 0.081x + 0.13	0.97	0-0.3	0-1
2	y= 0.005x + 0.20	0.99	0.3-1.0	1-100
3	y= 0.003x + 0.37	0.99	1.0-4.0	100-1000

Table S3.2. Quantification of H₂O₂ impurity in common primary and secondary alcohols.

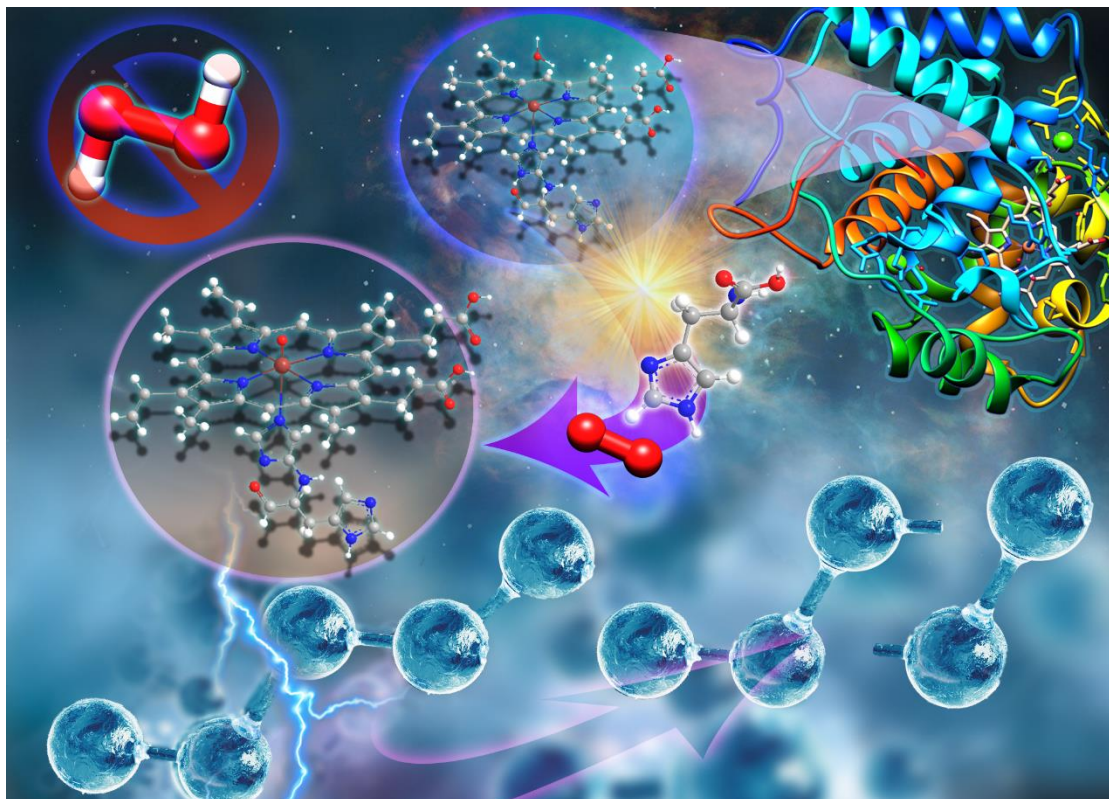
Alcohol	ABTS absorbance (a.u.)	Applied Formula No.	H ₂ O ₂ impurity (μM)
Ethanol	0.600± 0.013	2	79.9
Glycerol	0.279± 0.003	1	1.8
Benzyl alcohol	3.479± 0.003	3	1036.4
2-Chloroethanol	1.844± 0.026	3	491.4
1-Butanol	0.187± 0.005	1	0.7
1-Hexanol	0.304± 0.004	1	2.1
1-propanol	0.191± 0.002	1	0.8
Isopropanol	0.136± 0.008	1	0.1

Contributions

Raheleh Ravanfar wrote the manuscript and performed the experiments with support and advice from Alireza Abbaspourrad. Alireza Abbaspourrad supervised the project. Boris Dzikovski helped with EPR. Dr. Serena DeBeer provided invaluable comments.

CHAPTER 4

THE MOLECULAR MECHANISM OF PHOTOCATALYTIC REACTIONS BY HORSERADISH PEROXIDASE IN THE PRESENCE OF HISTIDINE



ABSTRACT

Oxidation reactions catalyzed by horseradish peroxidase (HRP) involve the conversion of ferric heme to the ferryl state by hydrogen peroxide (H_2O_2). As a result, HRP is typically considered unreactive without the presence of H_2O_2 . Herein, we report the first use of histidine (His) and HRP to initiate photocatalytic oxidation reactions without the exogenous addition of H_2O_2 . We demonstrate that the oxidation reactions of norbixin (NBX) molecules proceed 1.7-times faster using this HRP/His system in comparison with HRP/ H_2O_2 . Most importantly, we also demonstrate that new species of NBX breakdown products are formed using HRP/His. In this work, we investigate the key

steps of the HRP mechanism in the presence of His using electron paramagnetic resonance, liquid chromatography-mass spectrometry, and ultraviolet-visible spectrophotometry. Bearing in mind that H_2O_2 is normally thought indispensable for initiating the oxidation reactions of HRP, this work suggests a potential paradigm shift in our understanding of potential HRP mechanisms in the catalysis of biochemical reactions. The use of His, a natural essential amino acid, to mediate the formation of ferryl heme intermediates suggests that the HRP/His system could serve as a natural catalyst for applications in photochemistry and bioelectrocatalysis.

4.1. INTRODUCTION

Horseshoe peroxidase (HRP) plays a protective role in preventing oxidative damage of cellular components caused by H_2O_2 , which is naturally produced as a byproduct of aerobic metabolism²⁹. HRP catalyzes the heterolytic cleavage of the peroxidic bond in H_2O_2 to form a high-valent iron-oxo (ferryl heme) intermediate of the enzyme (compound I) (Figure 4.1a)²⁹⁻³². In compound I, the iron at the heme center is oxidized from Fe^{III} to $\text{Fe}^{\text{IV}}=\text{O}$, and the porphyrin or an amino acid in the side chain of HRP is oxidized to a radical³³ (Figure 4.1b). Thus, compound I oxidizes two molecules of the organic substrate through two consecutive single electron reactions to form the second catalytic intermediate, compound II, and finally reduces back to the Fe^{III} state³³⁻⁴⁰ (Figure 4.1b). The heterolytic cleavage of the peroxidic bond prevents the accumulation of reactive oxygen species in cells and also regulates their concentration in cellular signaling pathways¹¹⁴. Inspired by this naturally occurring mechanism, a broad range of applications has been developed using HRP to catalyze the oxidation reactions of

various organic molecules with H_2O_2 as HRP's specific oxidant^{28, 115}. This heme-containing peroxidase is currently one of the most extensively used enzymes in immunochemistry, diagnostic assays, chemical reactions, and bioremediation²⁴⁻²⁷. Low levels of H_2O_2 , however, can induce oxidative damage to the enzyme or other components of a biochemical system¹¹⁶⁻¹¹⁷.

Rather than using H_2O_2 to generate ferryl intermediates of the heme, we sought to introduce a more biocompatible and rapid strategy for the oxidation of organic molecules by HRP. For our design, we drew inspiration from the well-studied function of the distal histidine (His42) in HRP. Previous studies have suggested that the protonated form of His42 plays a critical role in the activation of compound II and heme-linked ionization¹¹⁸⁻¹¹⁹. The hydrogen bond between the $\text{N}\epsilon$ -proton of the imidazolium side chain of His42 and the oxygen atom of the ferryl heme determines the reactivity of compound II¹¹⁸⁻¹¹⁹.

In this study, we explored the ability of HRP to catalyze oxidation reactions of organic molecules only in the presence of His molecules (Figure 4.1c). We chose norbixin (NBX) as a model organic substrate, and investigated the oxidation mechanism of this HRP/His system using electron paramagnetic resonance (EPR), liquid chromatography-mass spectrometry (LC-MS) and ultraviolet-visible (UV/Vis) spectrophotometry. Our study demonstrates that HRP can catalyze the oxidation of organic molecules in the presence of just His without the addition of H_2O_2 . Furthermore, the speed of the oxidation reaction is increased by a factor of 2 using HRP/His system compared to HRP/ H_2O_2 system. We also demonstrate that natural daylight and oxygen are crucial to induce the catalytic reactivity of this HRP/His system; thus, we propose a photocatalytic

pathway for HRP to form ferryl intermediates in the presence of His, opening myriad potential applications in catalysis of chemical reactions.

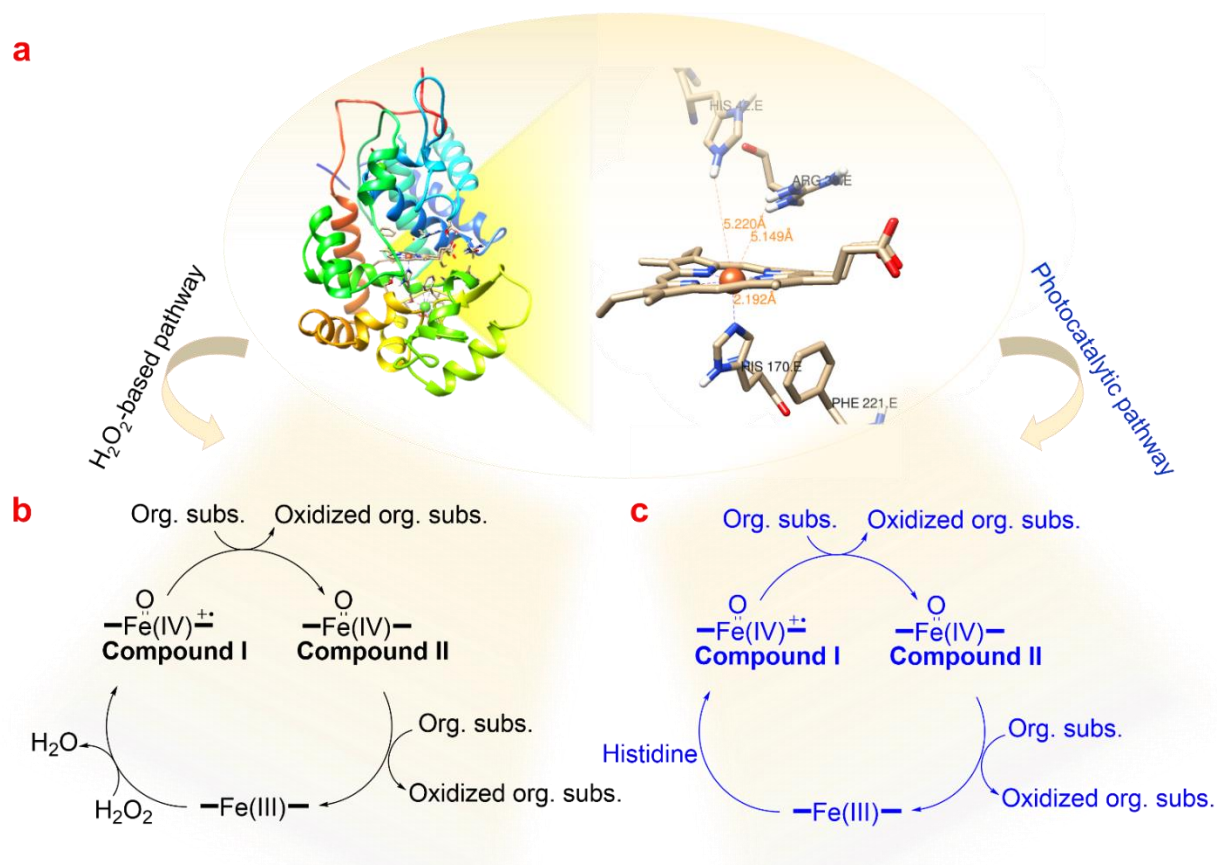


Figure 4.1. a) The schematic of HRP structure (left) and a close-up view of the heme in the active site of HRP (right). b) The mechanism of HRP for the formation of ferryl intermediates in the presence of H₂O₂. c) The photocatalytic pathway of HRP to form ferryl intermediates in the presence of His.

4.2. MATERIALS AND METHODS

4.2.1. Materials

Lyophilized powder of HRP isozyme C type VI-A, monobasic and dibasic potassium phosphate, potassium ferricyanide, 2,2'-azino-bis(3-ethylbenzothiazoline-6-sulfonic acid) diammonium salt ($\geq 98\%$), histidine ($\geq 99\%$), and DMPO ($\geq 97\%$) were purchased from Sigma Aldrich (St. Louis, MO). Hydrogen peroxide (30% w/w solution) was purchased from Anachemia (Que, Canada). NBX was kindly provided by the Chr. Hansen Laboratory A/S, Denmark. D₂O (D, 99.9%) was purchased from Cambridge Isotope Laboratories (Andover, MA).

4.2.2. Purification of HRP

An aqueous solution of HRP (12 mg/mL) in 0.1 M potassium phosphate buffer (pH 6.0) was prepared. The protein solution was applied to a Superdex 200 prep grade gel filtration column (XK26/70, GE Healthcare Life Sciences) at a 2.5 mL/min flow rate.

4.2.3. Preparation of reaction mixtures

A solution of 60 μ M HRP was prepared in 0.1 M potassium phosphate buffer (pH 6.0). 10 μ L of this HRP solution was then added to 50 μ L of NBX aqueous solution (5.26 mM). To this mixture, 100 μ L of aqueous solution of 0.2 M His in milli-Q water was added. This HRP/His system was compared with the system containing HRP solution, to which 10 μ L solution of 60 μ M H₂O₂ was added, and 90 μ L milli-Q water was added to correct the dilution factor. We used a 1:1 mole ratio for the amount of H₂O₂ and HRP used. Both HRP/His and HRP/H₂O₂ systems were also compared with the mixture of NBX/HRP without His, and NBX/His without HRP solutions, as well as NBX (control), keeping the same dilution factors. Both systems were stored at different conditions,

including light/aerobic, dark/aerobic, and light/anaerobic at room temperature. To provide anaerobic conditions, all solutions were bubbled with N₂ gas and mixing was performed in an anaerobic glove box containing N₂ gas. All experiments with dark conditions were covered by aluminum foil, while the ones under light were exposed under natural daylight.

4.2.4. Kinetic studies on the oxidation of NBX using HRP/His and HRP/H₂O₂ systems

A solution of 60 μM HRP was prepared in 0.1 M potassium phosphate buffer (pH 6.0). HRP solution (10 μL) was added to 50 μL NBX aqueous solution (5.26 mM). The UV/Vis absorption of NBX at 450 nm was recorded upon the addition of 100 μL aqueous solution of 0.2 M His to the mixture of HRP and NBX and at different time intervals up to 25 h. This system was compared with the UV/Vis absorption of NBX upon the addition of 10 μL of 60 μM H₂O₂ and 90 μL milli-Q water at different time intervals up to 25 h. The curves were fitted to obtain the order and the rate constants of the reactions (k).

4.2.5. Conformation Analysis Using UV/Vis Spectrophotometry

UV/Vis absorption spectra of the native HRP (10 μM) and HRP treated with aqueous solution of His (0.2 M) were obtained using UV/Vis spectrophotometry (UV-vis Spectrophotometer UV-2600, Shimadzu Scientific Instruments/Marlborough, MA) in the scan range of 200–800 nm. The spectra were recorded immediately upon the addition of 500 μL His solution to 500 μL HRP solution in potassium phosphate buffer (pH 6.0).

4.2.6. Analysis of HRP/His system using EPR Spectroscopy

The EPR spectra were recorded on a Bruker EMX (BRUKER, Billerica, MA) spectrometer at a frequency of 9.24 GHz under standard conditions in 4 mm ID quartz tubes. A liquid helium cryostat ESR-10 (Oxford Instruments Ltd, England) was used to stabilize the temperature at 12 K. Spectra were recorded with a modulation amplitude of 8G and microwave power of 625 μ W. To investigate the effect of light on only the His solution in the presence of oxygen, the aqueous solution of His (0.2 M) was irradiated using an intense source of light (1000-Lumen Portable Work Light, Model WL160203, 120V, 13W) in a box.

4.2.7. Analysis of the oxidized products of NBX using LC-MS

The samples were analyzed using a Thermo LTQ Linear Ion Trap with an electrospray ionization (ESI) source and an Agilent 1100 high-performance liquid chromatography (HPLC) on the front end (Thermo Fisher Scientific, Waltham, MA). ESI source parameters were negative ionization, capillary temperature of 325 °C, sheath gas flow 20, and capillary voltage 4.5kV. Samples were separated using a Waters Cortecs C18 2.7 μ m 4.6 x100 mm column at room temperature. The isocratic run used a mobile phase consisting of 80 % A) 0.1% formic acid in water and 20 % B) acetonitrile with a flow rate of 0.4 ml/ min and a total run time of 20 minutes. MS2 mode was used to quantify masses 154 m/z, 323 m/z, 342 m/z, and 379 m/z with a mass isolation window of 4 mass units and a collision energy of 35 Act Q of 0.250 and activation time (ms) of 30 for all. The concentration of residual NBX in the HRP/His and HRP/H₂O₂ systems was

compared with the NBX control, monitoring the area under the curves for the selected reaction monitoring (SRM) scans related to each analyte to the total area of the MS1 scans. The peak areas were calculated using Thermo Excalibur software.

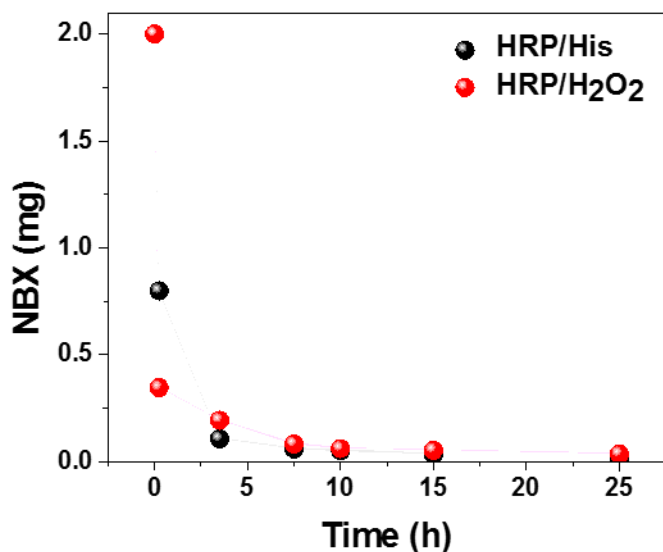
4.3. RESULTS AND DISCUSSION

We began our investigation by studying the ability of HRP to catalyze the oxidation of an organic substrate without the addition of H₂O₂. We first tested whether NBX (Figure 4.2ai), as a model organic substrate, could be oxidized in the presence of only His (Figure 4.2aai), only HRP (Figure 4.2aaii), and both HRP and His (Figure 4.2aaiii) in potassium phosphate buffer at pH 6.0 and room temperature. Interestingly, our results show that under these conditions the NBX is oxidized in the presence of the HRP/His system, decoloring the normally yellow color of the NBX (Figure 4.2aaiii). The UV/Vis spectrum of the NBX features three indicative peaks (Figure 4.2b, black line) in the wavelength range of 400–500 nm, which disappear in the presence of the HRP/His system under natural daylight/aerobic conditions (Figure 4.2b, red line). However, NBX is not oxidized in the presence of just HRP (Figure 4.2b, green line) or His (Figure 4.2b, blue line) under the same conditions. We examined the oxidation of NBX using the HRP/His system under other conditions, including dark/aerobic, and light/anaerobic and found that NBX is not oxidized by HRP/His when either light or oxygen is absent (Figure 4.2c).

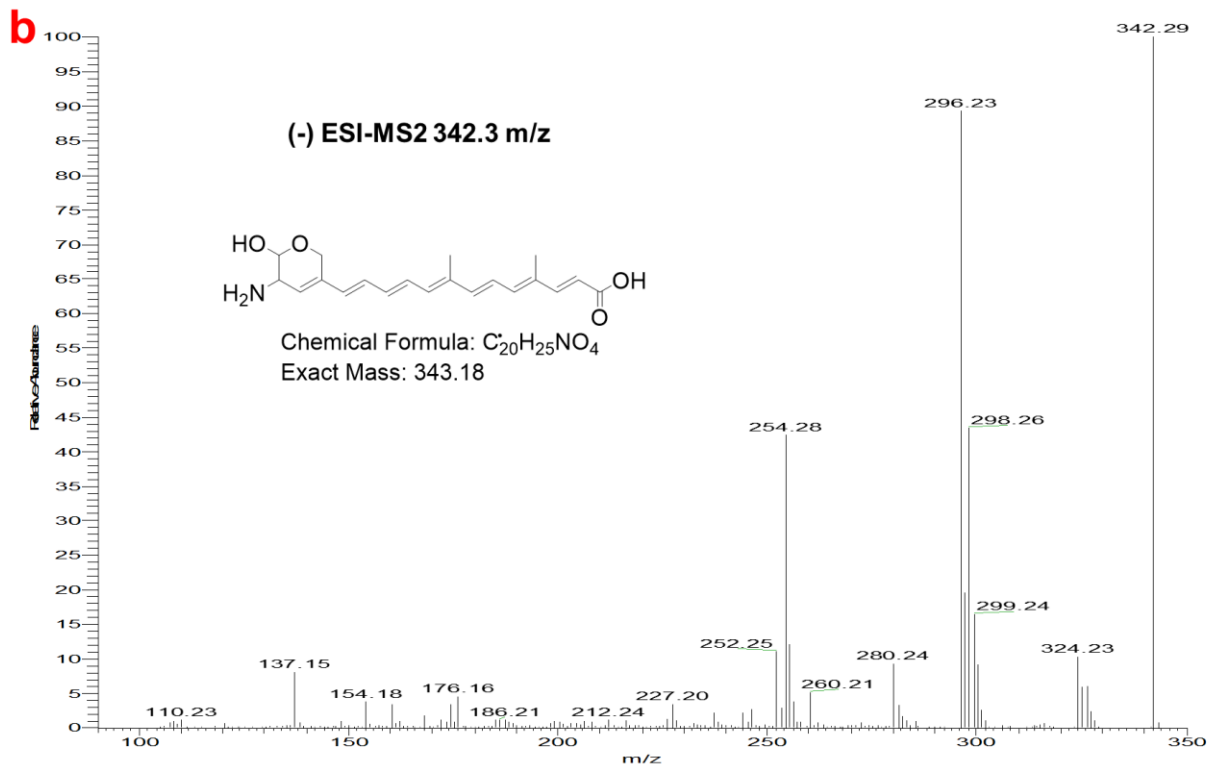
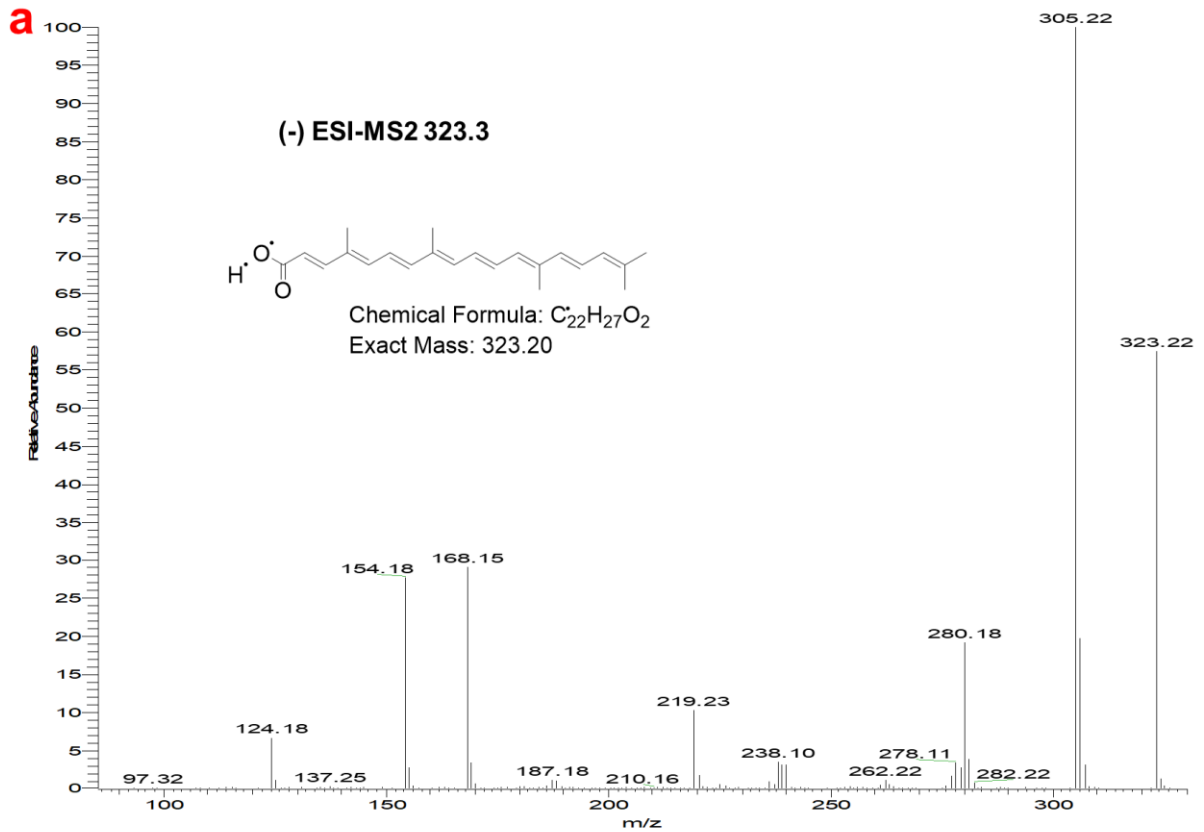
We also observed that the oxidation of NBX by the HRP/His system follows a second-order reaction (Figure 4.2d). The rate constant (*k*) of the oxidation reactions of NBX using HRP/His and HRP/H₂O₂ were determined by fitting the progress curves for

the NBX concentration versus time based from the UV/Vis absorption of NBX at 450 nm at different time intervals (Supplementary Figure 4.1). These curves fitted to the second order equations yield rate constants of $0.2 \text{ M}^{-1}\text{s}^{-1}$ and $0.1 \text{ M}^{-1}\text{s}^{-1}$ with good quality ($R^2 = 0.9918$ and $R^2 = 0.9685$) for the HRP/His and HRP/H₂O₂ systems, respectively (Figure 4.2d). Remarkably, the rate constant for the oxidation of NBX using the HRP/His system (without the addition of any H₂O₂) is 2-times faster than the HRP/H₂O₂ system. Moreover, the LC-MS mass spectra show that the mass peak corresponding to NBX at 379 m/z decreases down to 33% and 58% of the original amount upon treatment with the HRP/His and HRP/H₂O₂ systems, respectively (Figure 4.2e). Additionally, upon the oxidation of NBX using both systems, a new peak emerges at 323 m/z associated with an oxidized product of NBX (Supplementary Figure 4.2a), the concentration of which using the HRP/His system is 32 times more than the HRP/H₂O₂ system (Figure 4.2e). The proposed structure of this oxidized product of NBX is shown in Supplementary Figure 4.2a. The oxidation reaction of NBX using only the HRP/His system also results in the appearance of another peak at 342 m/z (Figure 4.2e), and its proposed structure is shown in Supplementary Figure 4.2b. Supplementary Figure 4.3a-b shows the MS3 spectra of further oxidized products of NBX that originate from the peak at 342 m/z upon the treatment with HRP/His system. These intriguing results support our hypothesis that HRP could take a detour of photocatalysis in the presence of His to induce oxidation reactions of organic molecules without the exogenous addition of H₂O₂.

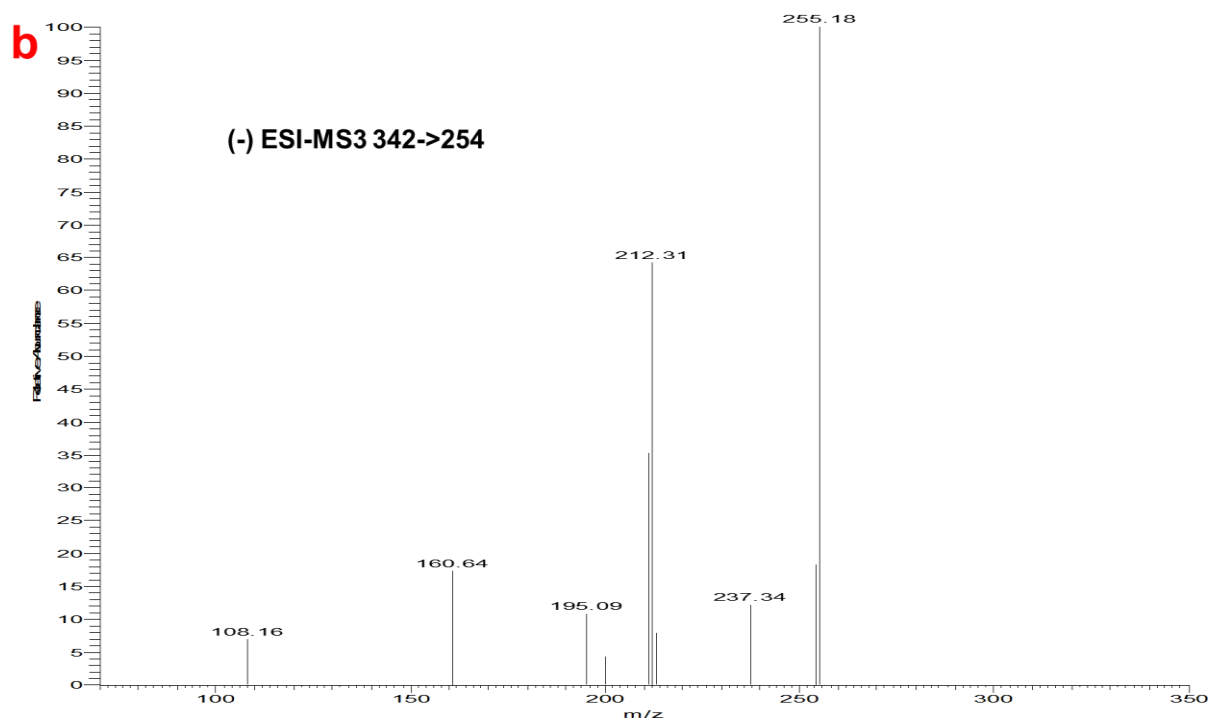
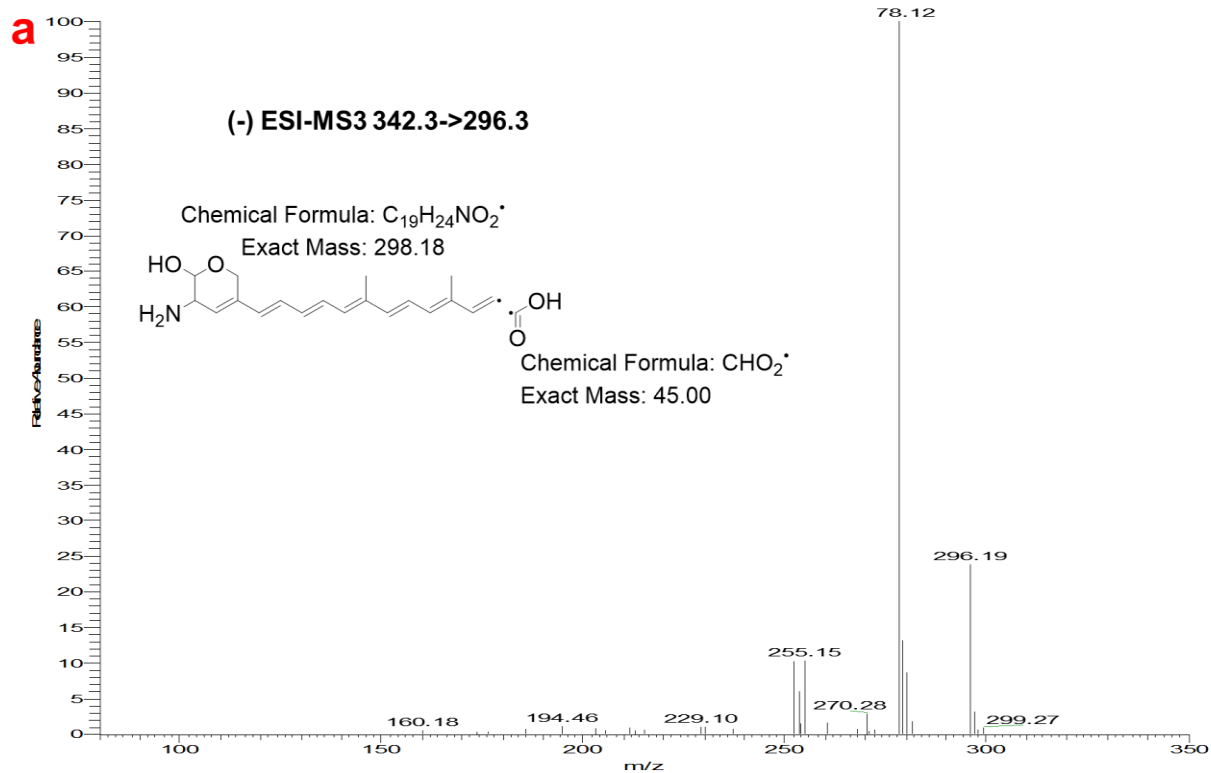
light/aerobic conditions. c) Aerobic/dark and anaerobic/light conditions for NBX treated using the HRP/His system in comparison with the untreated NBX control. d) Rate constants of the catalyzed oxidation of NBX using the HRP/His system in comparison with HRP/H₂O₂ system. e) Mass spectra peak area (%) of the NBX (gray) at 379 m/z after treatment with the HRP/His (red) and HRP/H₂O₂ systems (green), and the resulting oxidized products of NBX at 323 m/z and 342 m/z.



Supplementary Figure 4.1. The concentration of NBX (mg) at each time interval in the HRP/His and HRP/H₂O₂ systems.



Supplementary Figure 4.2. a) The mass spectra from the LC-ESI-MS2 analysis of the oxidized product of NBX with a peak at 323 m/z and its proposed structure formed upon the treatment by the HRP/His and HRP/H₂O₂ systems. b) The mass spectra from the LC-ESI-MS2 analysis of the oxidized product of NBX with 342 m/z and its proposed structure formed only upon the treatment by the HRP/His system.



Supplementary Figure 4.3. a) The mass spectra from the LC-ESI-MS3 analysis of the oxidized product of NBX at 296 m/z and its proposed structure, originating from the

peak at 342 m/z upon the treatment by the HRP/His system. b) The mass spectra from the LC-ESI-MS3 analysis of the oxidized product of NBX at 254 m/z, originating from the peak at 342 m/z upon the treatment with the HRP/His system.

Because these results identify the oxidization reaction of NBX using the HRP/His system as a photocatalytic reaction in aerobic conditions, we were curious as to how the molecular mechanism of HRP was initiated without the addition of H₂O₂. Previous studies have shown that His molecules are oxidized upon exposure to UV or visible light in the presence of oxygen and a suitable photosensitizer¹²⁰⁻¹²¹. They suggested that the imidazolium ring of His is potentially converted into a cycloperoxide (Figure 4.3a) in the presence of light and oxygen.

To test the formation of cycloperoxide intermediates (Figure 4.3a) upon the oxidation of His in the presence of oxygen under light, we irradiated an aqueous solution of His by light and investigate its EPR spectra in the presence of the spin trap 5,5-dimethyl-1-pyrroline N-oxide (DMPO). The result shows a spectrum (Figure 4.3b, red) similar to a 12-line EPR spectrum previously reported for the peroxide radical adducts¹²⁰⁻¹²⁵. However, the irradiated His molecules do not show any EPR lines without the DMPO spin trap (Figure 4.3b, blue line). Thus, based on EPR results (Figure 4.3a-b) and previous reports on the photooxidation of His¹²⁰⁻¹²¹, we suggest that the imidazolium ring of His can be converted into a cycloperoxide in the presence of light and oxygen (Figure 4.3a), and this oxidation reaction can be accelerated in the presence of a photosensitizer, such as the heme molecule in HRP¹²⁶.

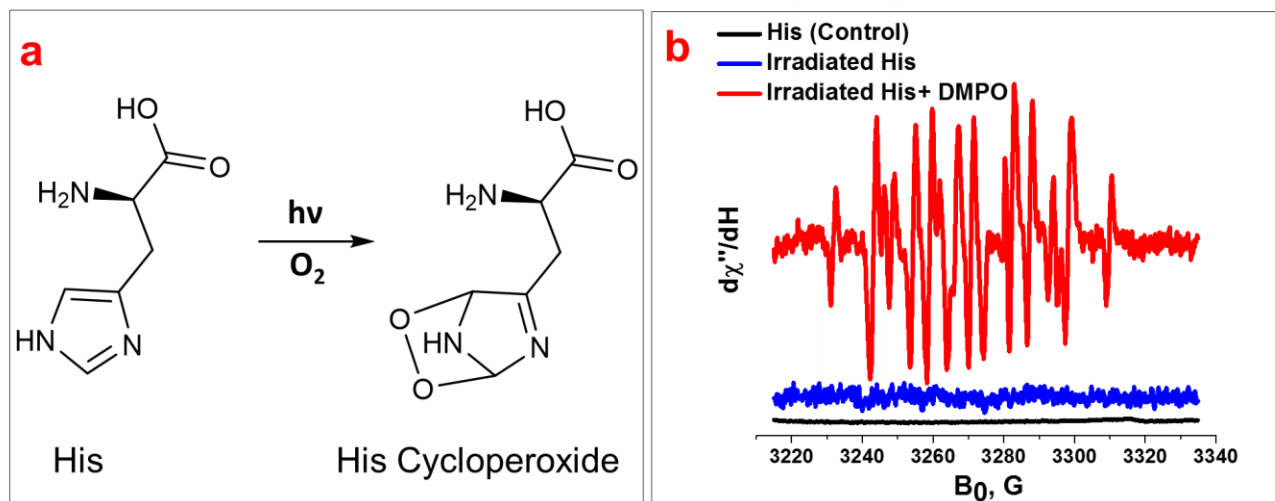


Figure 4.3. a) The proposed mechanism of His conversion to a cycloperoxide in the presence of light and oxygen. b) The EPR spectra of irradiated His in the presence (red line) and absence of DMPO (blue line), in comparison with the non-irradiated His control (black line).

Since HRP is naturally structured to capture peroxides, we hypothesize that the cycloperoxide intermediate of His molecules formed in the presence of oxygen under light can react with the Fe^{III} at the heme center of HRP and form ferryl intermediates containing Fe^{IV} (Figure 4.4a). We examined this hypothesized mechanism using UV/Vis and EPR spectroscopy. Studies have shown that the optical spectra of the resting state of HRP (Fe^{III}) has a Soret band at 402 nm and a Q-bands at 497 nm^{46, 88-89}. The formation of the ferryl intermediate of HRP is indicated by the red shift of the Soret band from 402 nm to 418 nm with a shoulder at 350 nm and the appearance of two Q-bands at 527 nm and 557 nm, which are typically formed upon the reaction of HRP with H_2O_2 ^{46, 88-89}. Similarly, we demonstrate that the addition of an aqueous solution of His to HRP in potassium phosphate buffer at pH 6.0 under light/aerobic conditions causes

a red shift in the Soret band to 418 nm with a shoulder at 350 nm, and the appearance of Q-bands at 527 nm, 557 nm, and 655 nm (Figure 4.4b). Therefore, we believe the HRP reacts with the cycloperoxide of His and forms the ferryl intermediate, as proposed in Figure 4.4a.

Previous studies on the HRP/H₂O₂ system have shown that the ferryl intermediates of HRP are EPR-silent and generate only a broad EPR signal characteristic of the oxyferryl porphyrin π -cation radical ($g = 2.0$)^{39, 46-48}. Figure 4.4c and Figure 4.4d-e illustrate the EPR survey scan and the short scans, respectively, for the HRP/His systems under light/aerobic and light/anaerobic conditions in comparison with the native HRP control. We freeze-quenched the HRP solutions upon the addition of His molecules in a short time (30 s) to detect any probable ferryl intermediates formed in the system (Figure 4.4c-e). The results show that in the presence of HRP/His system under aerobic/light conditions, the ferric signals in the native HRP control (Figure 4.4c-d, black lines) decrease in the high-spin region of heme while a new resonance is observed in the region of the low spin heme ($g = 2.0$) that arises from a potential radical cation located on the heme (Figure 4.4c and 4.4e, red lines). However, the EPR spectrum for HRP treated with His molecules under anaerobic/light conditions does not show the appearance of any new resonance at $g = 2.0$ (Figure 4.4c and 4.4e, blue lines). We did not observe any EPR-silent spectra upon the addition of His molecules to HRP. We hypothesize that this result is due to the affinity of the imidazole ring of His to the heme center, which causes a decrease in the high spin features of heme in the HRP/His system, even under light/anaerobic conditions (Figure 4.4c-d, blue lines). The EPR spectra of the intermediates formed upon the addition of His molecules to the HRP solution under

aerobic/light conditions are also in agreement with previous reports of the EPR analysis of ferryl intermediates upon the addition of H₂O₂ to HRP, ascorbate peroxidase, and cytochrome C peroxidase ⁴⁶⁻⁴⁸.

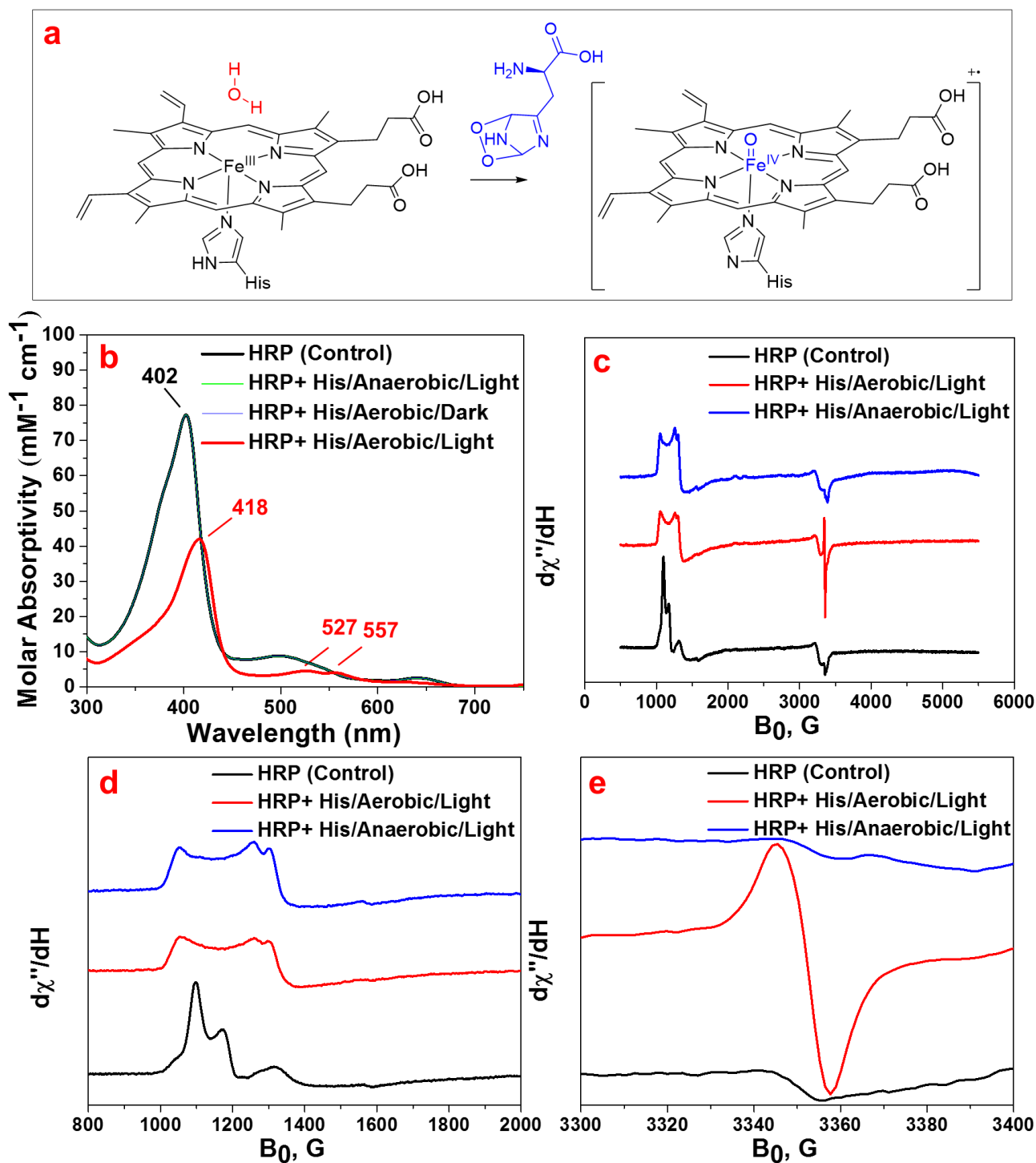


Figure 4.4. a) The proposed schematic for the reaction of Fe^{III} at the heme center of HRP with the cycloperoxide of His and formation of ferryl intermediates. b) The UV/Vis spectra of the HRP/His system under aerobic/light conditions (red line), HRP/His

system under anaerobic/light conditions (green line), and HRP/His system under aerobic/dark conditions (blue line) in comparison with the native HRP control under aerobic/light conditions (black line). c) The survey scan of EPR and d) the short scan of the high-spin region between 800 G and 2000 G, and e) the short scan of the low-spin region between 3300 G and 3400 G for the HRP treated with His molecules under light/aerobic (red line) and light/anaerobic (blue line) conditions in comparison with the native HRP (black line).

Based on the results obtained from the EPR, LC-MS, and UV/Vis spectra, we propose a mechanism for the photocatalytic pathway of HRP in the presence of His, catalyzing the highly efficient oxidation reactions of organic molecules (Figure 4.5). This mechanism demonstrates the formation of cycloperoxide intermediate of His molecules in the presence of oxygen and light, which are immediately captured by HRP to form the ferryl intermediates of the heme. These ferryl intermediates are able to oxidize organic substrates, such as NBX, in the reaction mixture. Previous studies have suggested that His42 in the HRP/H₂O₂ system plays a critical role in activation of the peroxide and the formation of ferryl intermediates of the heme¹¹⁸⁻¹¹⁹, in which this His residue catalyzes the proton transfer between the oxygen atoms of the heme-bound H₂O₂ and polarizes the O-O bond³⁹. Moreover, the hydrogen bond between the Nε- proton of the imidazolium side chain in His42 and the oxygen atom of the ferryl heme determines the reactivity of compound II¹¹⁸⁻¹¹⁹. We believe that the cycloperoxide of the His molecule can easily transfer the electron from the Nε- proton to the oxygen atom of the heme-bound cycloperoxide of His to facilitate the heterolytic cleavage of the O-O bond.

Thus, we hypothesize that the reason behind the faster oxidation of NBX by the HRP/His system in comparison with the HRP/H₂O₂ system is due to the faster formation of the ferryl intermediates of heme in the HRP/His system, which can subsequently oxidize the organic substrates faster and reduce back to the ferric state of HRP.

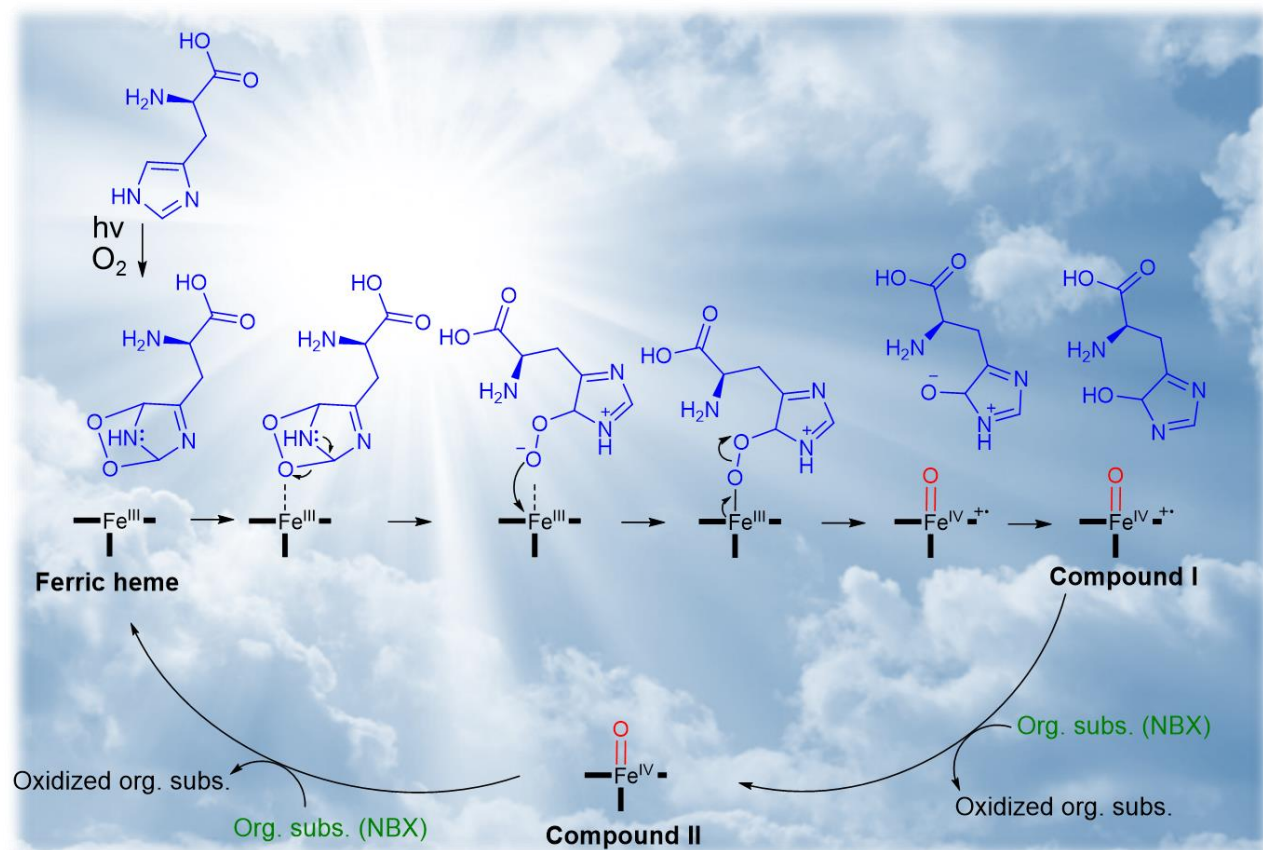


Figure 4.5. The proposed mechanism for the photocatalytic pathway of HRP to form ferryl intermediates in the presence of His under aerobic/light conditions, initiating the highly efficient oxidation of organic molecules.

4.4. CONCLUSION

We demonstrate that HRP can catalyze the oxidation of organic molecules in the presence of His molecules 2-times faster than the traditional HRP/H₂O₂ system. This HRP/His system is highly efficient under natural light and oxygen, however, these two key factors are critical to initiate the oxidation reactions. We probed the mechanism of how the HRP/His system oxidizes NBX, as a model organic substrate, and propose a new photocatalytic pathway for HRP to form ferryl intermediates. Our findings suggest that the His molecules are oxidized to cycloperoxide intermediates in the presence of light and oxygen, and this reaction can be facilitated by the heme group of HRP as a photosensitizer. The HRP captures the cycloperoxide to form ferryl intermediates of the heme, enabling the oxidation of organic substrates in the reaction mixture. We hypothesize that HRP/His system is faster because the cycloperoxide of His is more apt to polarize the O-O bond in comparison with H₂O₂, expediting the formation of ferryl intermediates and the subsequent oxidation of organic substrates. This photocatalytic pathway of HRP can open potential applications, particularly in bioelectrocatalysis and catalysis of chemical reactions.

4.5. SUPPLEMENTARY INFORMATION

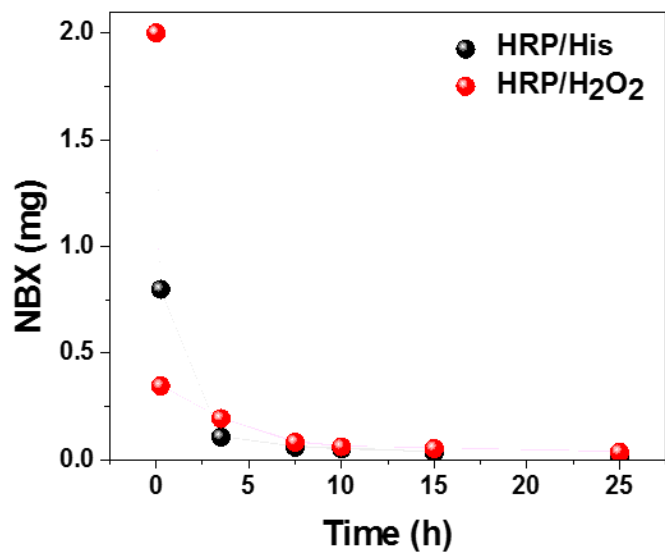


Figure S4.1. The concentration of NBX (mg) at each time interval in the HRP/His and HRP/H₂O₂ systems.

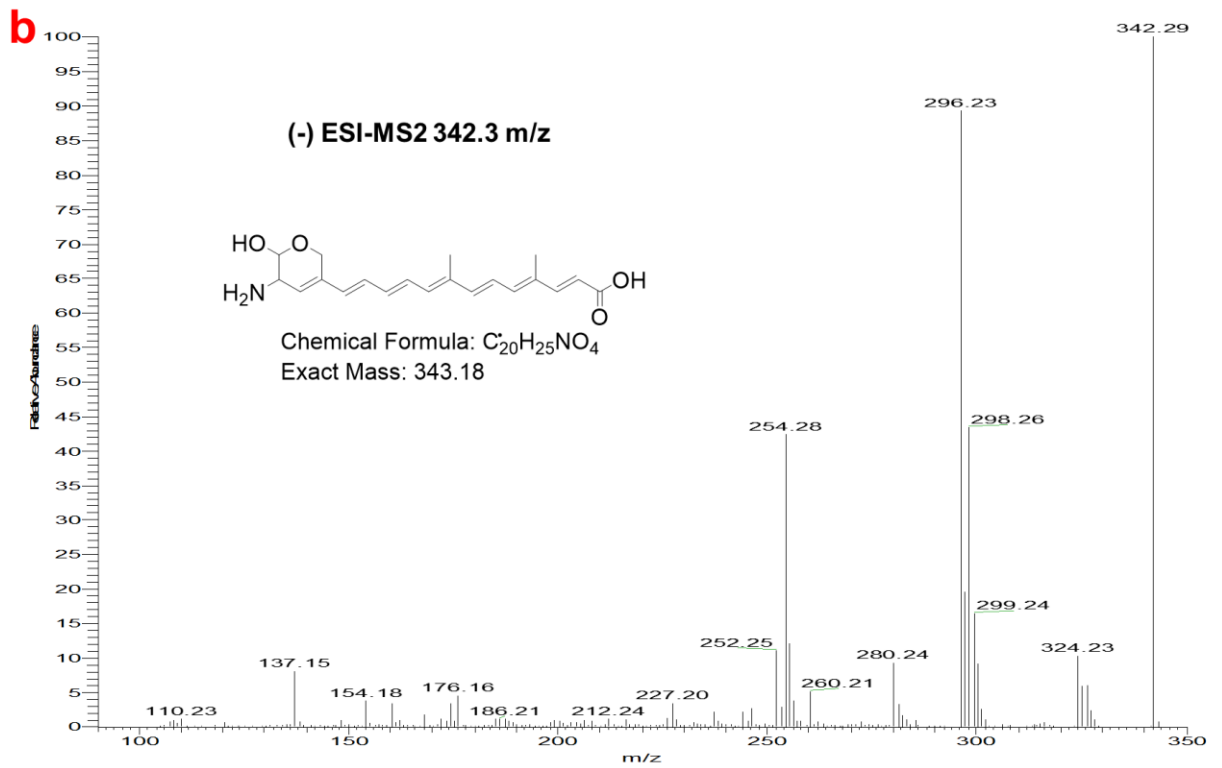
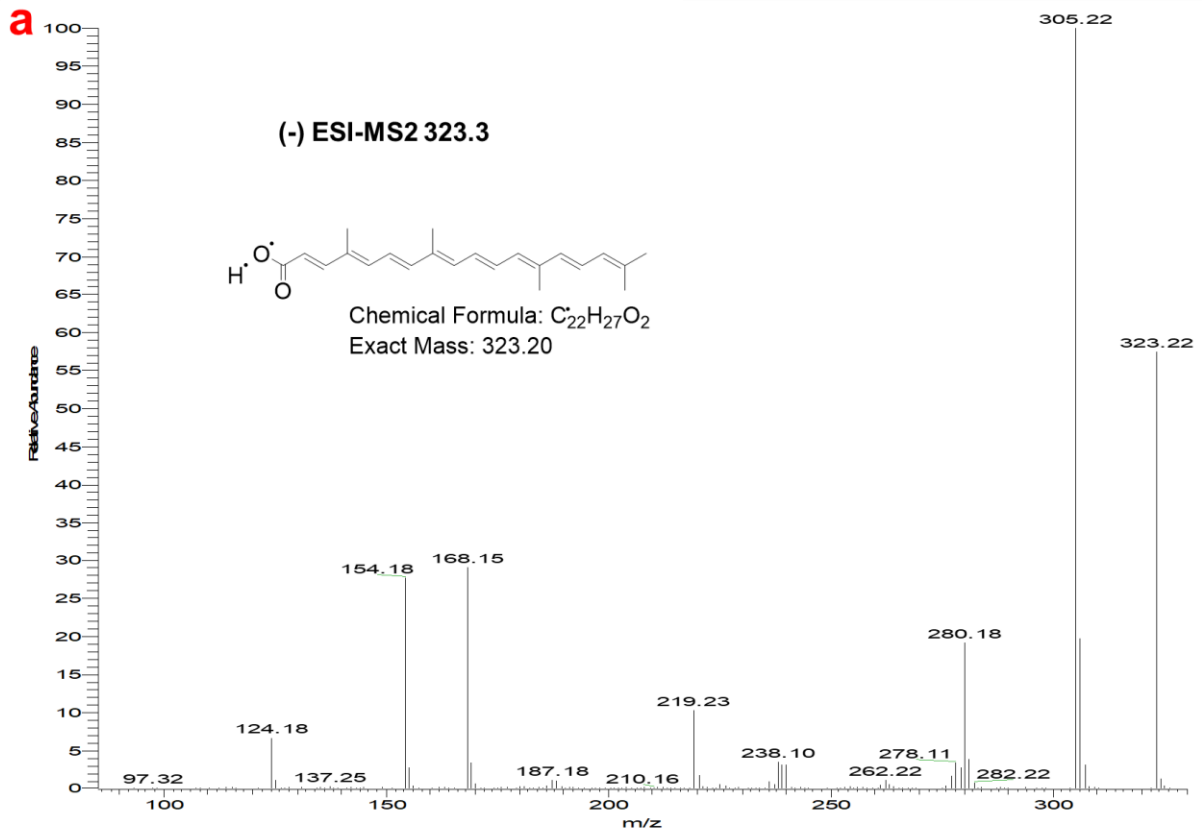


Figure S4.2. a) The mass spectra from LC-ESI-MS2 analysis of the oxidized product of NBX with 323 m/z and its proposed structure formed upon the treatment with HRP/His and HRP/H₂O₂ systems. b) The mass spectra from LC-ESI-MS2 analysis of the oxidized product of NBX with 342 m/z and its proposed structure formed only upon the treatment with HRP/His system.

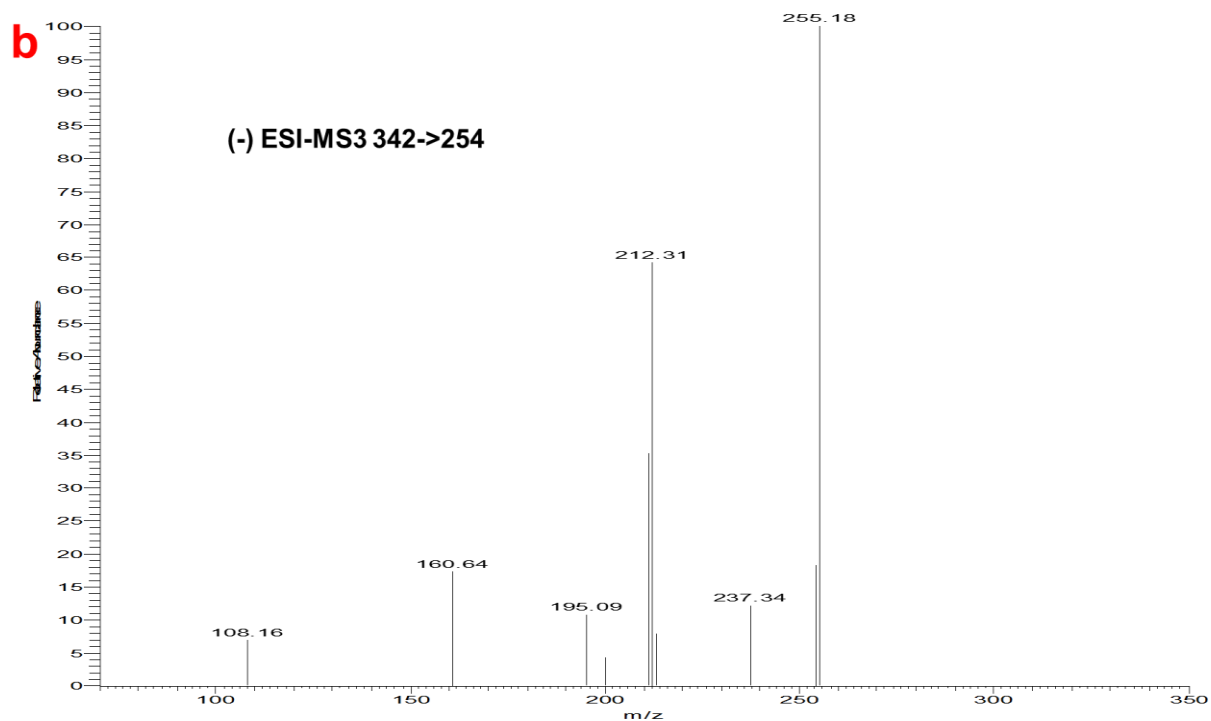
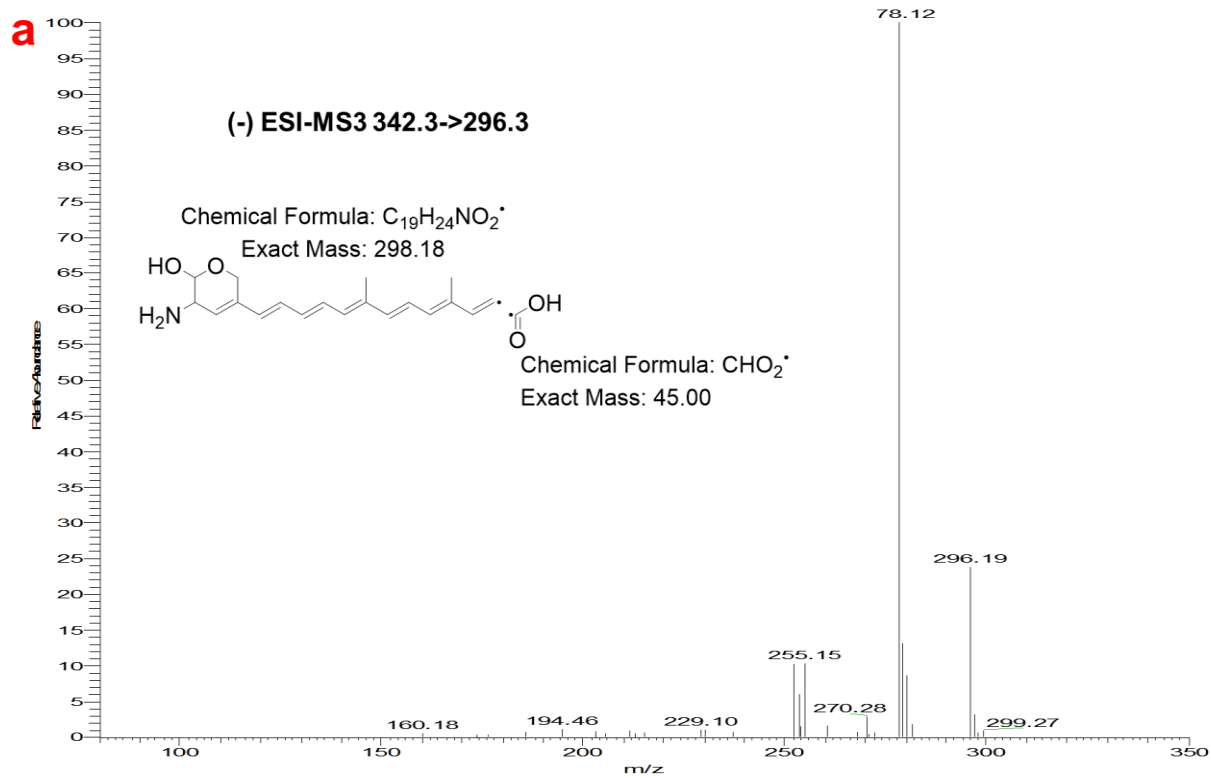


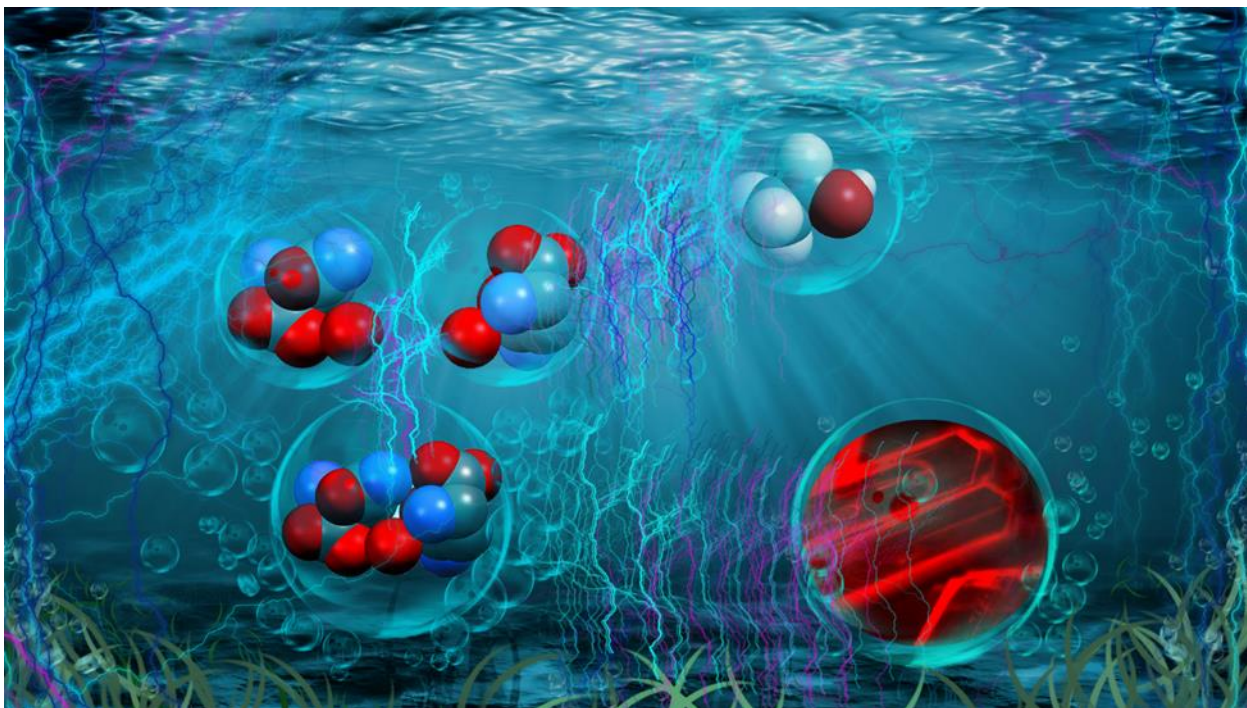
Figure S4.3. a) The mass spectra from LC-ESI-MS3 analysis of the oxidized product of NBX with 296 m/z and its proposed structure originated from the peak at 342 m/z upon

the treatment with HRP/His system. b) The mass spectra from LC-ESI-MS3 analysis of the oxidized product of NBX with 254 m/z originated from the peak at 342 m/z upon the treatment with HRP/His system.

Raheleh Ravanfar wrote the manuscript and performed the experiments with support and advice from Alireza Abbaspourrad. Alireza Abbaspourrad supervised the project. Boris Dzikovski helped with EPR.

CHAPTER 5

STRUCTURAL CHEMISTRY ENABLES FLUORESCENCE OF AMINO ACIDS IN THE CRYSTALLINE SOLID STATE



ABSTRACT

Nonaromatic luminogens have recently emerged as highly attractive materials for biological imaging and sensing applications, due to their good hydrophilicity and biocompatibility. Here, we report that natural, nonaromatic and aromatic amino acids, including L-histidine, L-glutamine, L-isoleucine, L-asparagine, L-valine, L-threonine, and L-methionine, exhibit crystallization-induced emission. The crystalline state of these amino acids shows a wide range of fluorescence emission, in striking contrast to barely any emission in solution phase. We determined the atomic structure of these amino acids in crystalline state using X-ray crystallography. The structural analysis implies that the compact interactions through the hydrogen bonding network of the

crystallized amino acids potentially restrict intramolecular rotations and vibrations and thus enhance the radiative transitions in the crystalline state. Because these noncovalent interactions can be easily modulated by varying the chemical environment, this phenomenon of crystallization-induced emission may represent a general strategy to induce the fluorescence from weakly or non-emissive nonaromatic molecules.

5.1. INTRODUCTION

The chemistry of the last century has largely focused on covalent bonding, while that of the present century is more likely to focus on noncovalent bonding and its fascinating effects on the physicochemical properties of the resulting material.¹²⁷ Noncovalent interactions, such as hydrogen bonding, π - π stacking, and cation- π interactions, occur ubiquitously in solid-state materials, biological structures, and organic molecules.¹²⁸⁻¹²⁹ These noncovalent interactions are well known to induce luminescence for both macromolecules and small molecules.¹³⁰⁻¹³³ For example, aromatic organic molecules, which are able to absorb photons and suppress nonradiative relaxation via their noncovalent interactions in rigid structure, have been widely studied as luminogens.¹³⁴⁻¹³⁶ In contrast, nonaromatic organic systems have not been extensively studied due to the belief that their flexible structures can induce frequent vibrations and rotations that enable nonradiative relaxation to dominate. However, recently several groups have reported nonaromatic polymers and biomacromolecules that displayed fluorescent emission in their aggregated form or solid state,¹³⁷⁻¹⁴⁰ confirming that photoluminescence does not require aromatic groups. For example, the fluorescence of

proteins lacking aromatic rings is attributed to electron delocalization through a dense network of intramolecular and intermolecular hydrogen bonds.¹⁴¹⁻¹⁴³ Moreover, it is thought that the fluorescence of nonaromatic polymers does not originate from a specific unit, but rather from interactions among polymer chains.^{136, 144-147} In these systems, multiple intrachain interactions, such as $n-\pi$ and $\pi-\pi$ coupling, in rigid conformations can inhibit molecular motion and prevent nonradiative relaxation, resulting in the enhanced intensity of fluorescence emission.¹³⁶

For a time, the existence of amino groups in the structure of these nonaromatic systems was also considered to play an essential role in their fluorescence emission.¹³⁶ However, polymers without an amino group have recently been reported as fluorescent in the solid state.¹⁴⁸ This observation suggests that the intra/interchain interactions originate from carbonyl groups (C=O) as the source of π electrons, together with oxygen (O) as the source of n electrons can also result in fluorescence.¹⁴⁸ Thus, three kinds of inter or intrachain interactions, including hydrogen bonding, $\pi-\pi$, and $n-\pi$ coupling, in nonaromatic materials have been suggested to contribute to fluorescence emission of nonaromatic organic systems in the rigid conformation. These nonaromatic luminogens are highly suitable for biological applications due to their biocompatibility, good hydrophilicity, and ease of preparation.¹⁴⁹ The present nonaromatic organic luminogens are synthetic polymers and/or are in the category of biomacromolecules. Therefore, introducing natural nonaromatic organic small molecules with fluorescent emission in crystalline form is remarkable, and can make extraordinary progress in the biological applications.

Here, we demonstrate that both aromatic amino acids, such as L-histidine, and nonaromatic amino acids, such as L-glutamine, L-isoleucine, L-asparagine, L-valine, L-threonine, and L-methionine, show fluorescence emission upon crystallization in the solid state, a remarkable phenomenon that has not been previously reported. We form the crystals of natural amino acids via antisolvent crystallization and investigate their unit cell and macrostructure using single crystal X-ray crystallography, X-ray powder diffraction (XRD), and scanning electron microscopy (SEM). We also demonstrate that the fluorescent lifetimes of these amino acids are different, being potentially dependent on the density of the hydrogen bonding network, π - π , and n- π coupling as well as the macrostructure of the amino acid crystals. Bearing in mind that the above mentioned amino acids are not fluorescent in solution,¹⁵⁰⁻¹⁵¹ this observation suggests a potential paradigm shift in our understanding of the crystallization-induced fluorescence emission of organic molecules.

5.2. MATERIALS AND METHODS

5.2.1. Preparation of the amino acid crystals

Amino acid solutions (30 mg/mL), including L-histidine ($\geq 99\%$), L-glutamine, L-isoleucin, L-asparagine, L-valine, L-threonine, and L-methionine ($>98\%$, Sigma-Aldrich) were prepared individually by dissolving the amino acid powder in milli-Q water using a vortex mixer at ambient temperature in a Corning® 15 mL centrifuge tube with a closed cap. Then, 3 mL of 200 proof ethanol (KOPTEC, PA, US) was added to 3 mL of the aqueous solution of amino acid as an antisolvent. The amino acid crystals were collected after 6 hours.

5.2.2. Characterization

Unit cell data for the amino acid crystals were collected on a Rigaku Synergy XtaLAB diffractometer. Morphologies of the crystals were observed using a Zeiss 710 Laser Scanning Confocal Microscope with a 25x/0.8 NA oil immersion objective (Carl Zeiss Microscopy, Thornwood, NY), an inverted optical microscope (DMIL LED, Leica) connected to a fast camera (MicroLab 3a10, Vision Research), and SEM (JCM-6000 Benchtop scanning electron microscope, software version 2.4 (JEOL Technics Ltd., Tokyo, Japan)). Moreover, the Zeiss 710 confocal microscope was equipped with lasers at 405 nm, 488 nm, 561 nm, and 633 nm, and the spectral detector allows the collection of a series of emission wavelengths with lambda scan mode. XRD measurements were performed using a Bruker D8 Advance ECO powder diffractometer (MA) operated at 40 kV and 30 mA (Cu K α radiation). The crystals were scanned at room temperature from $2\theta = 10\text{--}60^\circ$ under continuous scanning in 0.02 steps of $2\theta \text{ min}^{-1}$.

The lifetime of the amino acid crystals was investigated through time-correlated single photon counting fluorescence measurements (TCSPC), which were carried out using ~ 120 fs pulses at 800 nm delivered at an 80 MHz repetition rate from a Spectra-Physics Mai-Tai Ti:S laser equipped with DeepSee dispersion compensation. The Ti:S laser was coupled to a Zeiss 880 laser scanning microscope which was used to locate and focus on the crystals. Two-photon generated epi-fluorescence was separated from the excitation using a 670 nm long pass dichroic filter, which directed the emission to a GaAsP photomultiplier tube after passing through a broad blue band-pass filter (BGG22, Chroma Technology Corp, VT). The laser power was attenuated using a near

infrared (NIR) Acousto Optic Modulator (AOM) to keep the photon detection rate to less than 0.2% of the repetition rate to avoid photon pile-up. An instrument response function (IRF) was acquired using a Z-cut quartz crystal and used for fitting the TCSPC data. Time-correlated photon counts were acquired using a high-resolution TCSPC module (SPC-830, Becker & Hickl GmbH) and fit to a bi-exponential decay curve, convolved with the IRF, using the SPCImage software package (Becker & Hickl GmbH). The NaCl salt crystals were used as a negative control for the lifetime measurements. The weighed mean lifetime was calculated using the following formula:

$$\frac{(a_1 \times \tau_1) + (a_2 \times \tau_2)}{(a_1 + a_2)}$$

5.3. RESULTS AND DISCUSSION

In many cases, luminogens are highly emissive only in dilute solutions but are nonemissive in the solid state¹⁵²⁻¹⁵³ where molecules may experience strong π - π stacking interactions that lead to quenching.¹⁵⁴ In contrast, there are other small molecules that show induced emission in their solid state.^{136, 155} In solution, these molecules experience dynamic intramolecular motion that annihilate their excited state nonradiatively. However, in the solid state the molecules cannot pack through a π - π stacking process due to the restricted intramolecular motions.¹⁵²⁻¹⁵³ Here, we demonstrate crystallization-induced emission in amino acid crystals (Figure 5.1, a-b). The crystals of seven amino acids, including L-histidine, L-glutamine, L-isoleucine, L-asparagine, L-valine, L-threonine, and L-methionine were prepared through antisolvent crystallization (see the Methods for more details). Briefly, an aqueous solution of each amino acid was prepared and then ethanol was added as an antisolvent, resulting in the

formation of the amino acid crystals (Figure 5.1a). Since most of these amino acids are nonaromatic, very little attention has been paid to their photophysical properties in crystalline form. However, we found that these amino acids have a natural fluorescence emission in their crystalline state that ranges widely from blue to green and red when excited at 405 nm, 488 nm, and 561 nm under confocal laser scanning microscopy (CLSM; Figure 5.1c, Figure 5.2, a-b (i), and Figures S5.1–S5.5). We note that none of these amino acids are fluorescent in solution (data not shown). The amino acid crystals display different fluorescence emission intensities with maximum emission at 498 nm upon excitation at 405 nm, except L-methionine, which features a maximum emission at 459 nm when excited at 405 nm (Figure S5.6).

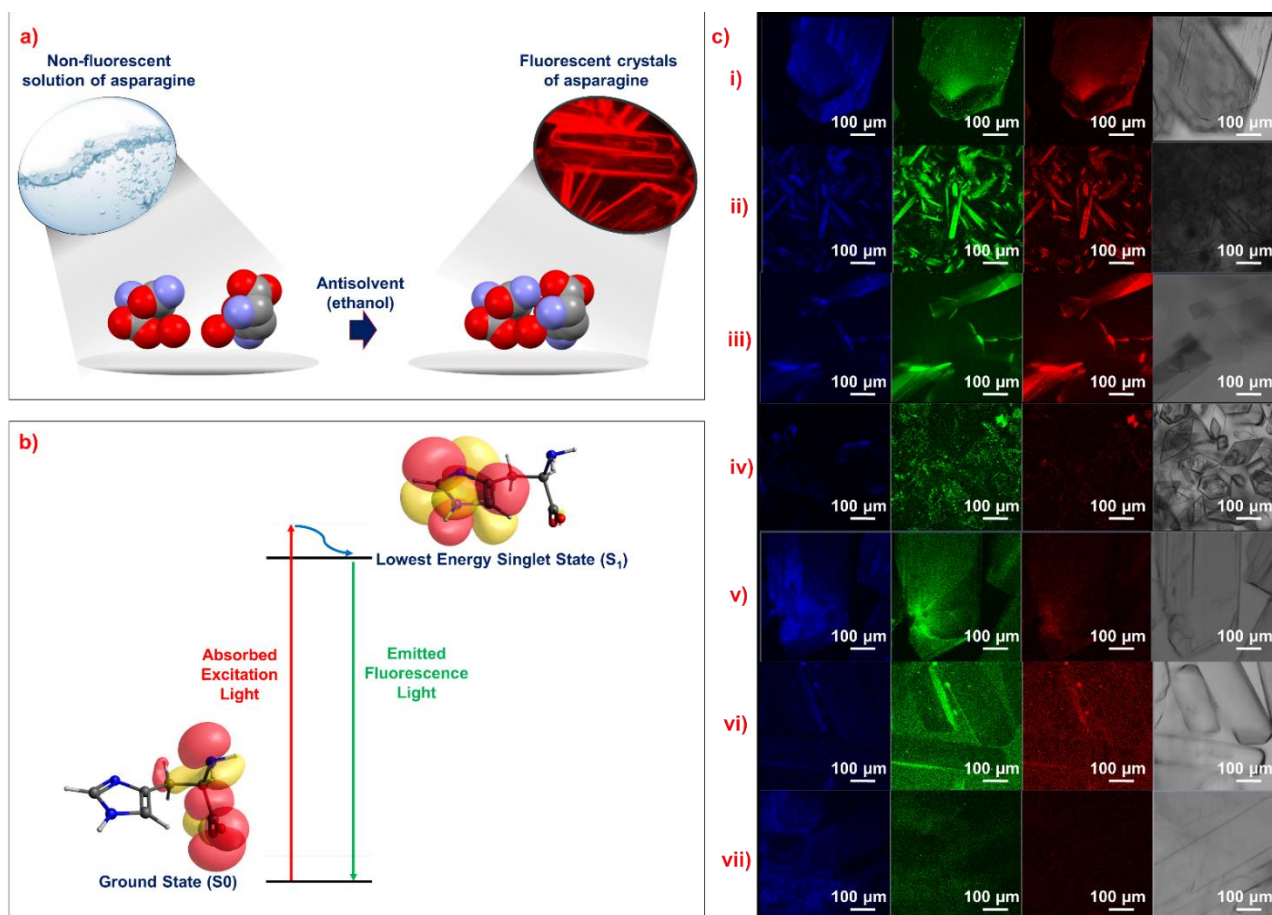


Figure 5.1. a) Schematic representation for the fluorescence of amino acids in the crystalline solid state in comparison with the non-fluorescence aqueous solution of amino acids. b) Schematic representation of Jablonski diagram for fluorescence. c) CLSM images of the amino acid crystals: i) L-histidine, ii) L-glutamine, iii) L-isoleucine, iv) L-asparagine, v) L-valine, vi) L-threonine, and vii) L-methionine, showing their bright fluorescence emission in a wide range, including blue (414–459 nm, first column), green (500–559, second column), and red wavelengths (587–673, third column). The fourth column shows the bright field images of the amino acid crystals.

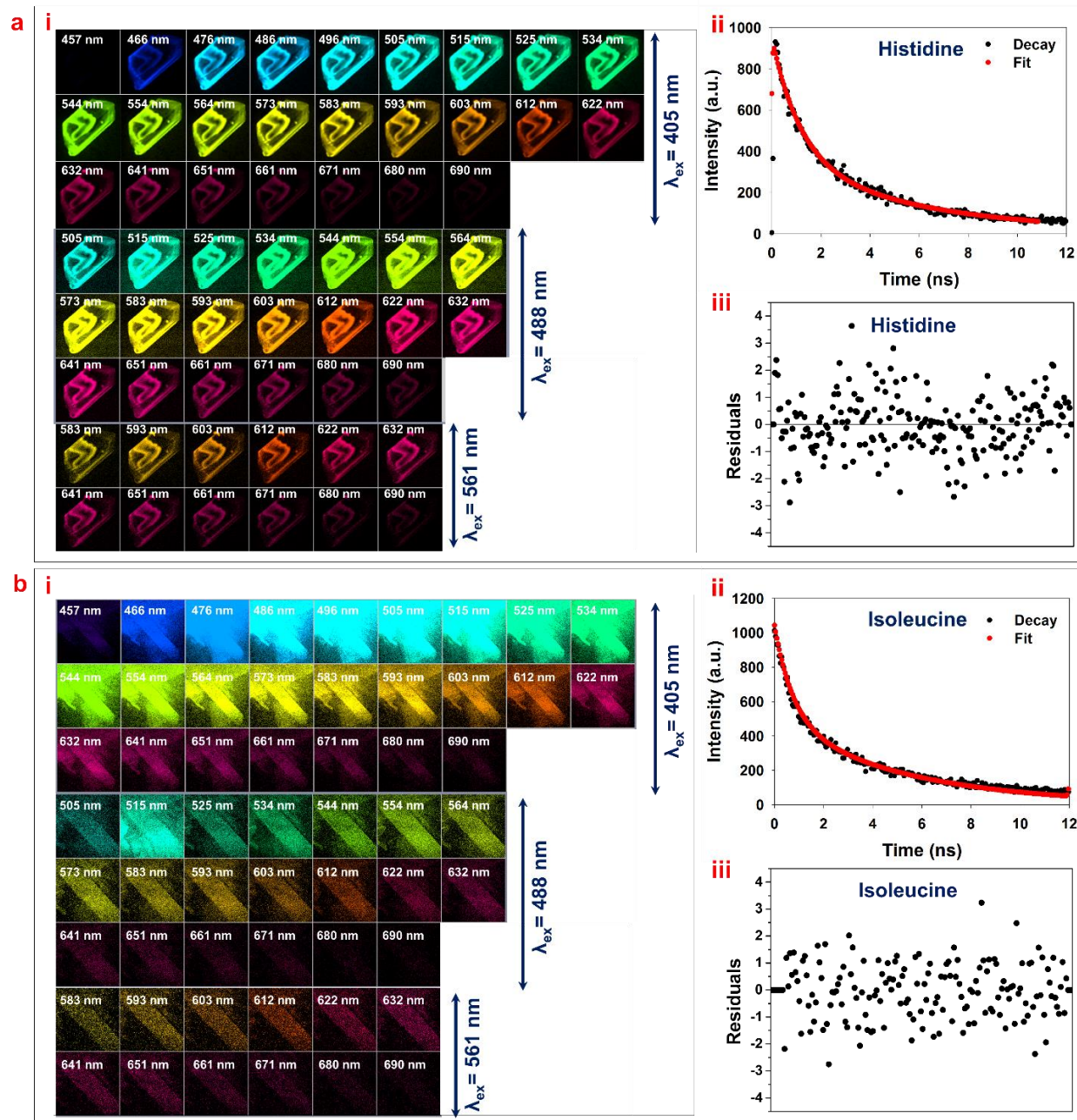


Figure 5.2. The fluorescence of a) L-His crystals, and b) L-isoleucine crystals. i) The confocal lambda scan of crystals excited at 405 nm, 488 nm, and 561 nm. The numbers on each image correspond to the emission wavelengths. ii) The fluorescent life-time of crystals at room temperature. The red lines represent the biexponential fits to the

experimental data points (black lines). iii) The residuals of fluorescent life-time of crystals fitted to a bi-exponential decay curve.

Figure 5.2, a-b (ii) and Figure S5.7 illustrate the decay of the excited state using single photon counting fluorescence measurements of the amino acid crystals. This decay is fitted perfectly with a double exponential model yielding two fluorescence lifetimes for each individual amino acid (Table 5.1, Figure 5.2, a-b (iii), and Figure S5.8). The weighed mean lifetimes for the L-histidine, L-glutamine, L-isoleucine, L-asparagine, L-valine, L-threonine, and L-methionine crystals are 2.20 ns, 2.53 ns, 2.76 ns, 5.38 ns, 6.52 ns, 4.90 ns, and 3.91 ns, respectively (Table 5.1). We observed no fluorescence lifetime for NaCl crystals (negative control) (Table 5.1). Figure S5.9 also shows the fluorescence lifetime imaging (FLIM) results of a L-histidine crystal that has been color-coded according to the weighed mean lifetime.

Table 5.1. The fluorescence lifetimes and weighed mean lifetimes of the seven amino acid crystals.

I	a₁ (%)	τ₁ (ns)	a₂ (%)	τ₂ (ns)	χ²	Mean lifetime (ns)
L-Histidine	56.51	0.67	43.48	4.19	1.32	2.20
Deuterated L-Histidine	65.08	0.73	34.91	4.24	1.46	1.95
L-Glutamine	77.93	0.85	22.06	8.49	1.18	2.53
L-Isoleucine	59.75	0.79	40.25	5.69	1.07	2.76
L-Asparagine	87.39	0.9	12.61	36.40	0.97	5.38
L-Valine	9.57	5.02	90.42	6.68	2.29	6.52
L-Threonine	61.02	1.31	21.07	19.46	1.29	4.90
L-Methionine	66.54	1.25	33.46	9.19	1.01	3.91
NaCl (Control)	0.12	0.02	99.87	0.02	1.08	0.02

The interplay between chemistry and crystallography is in fact the inter-relationship between the molecular properties and supramolecular assembly of

molecules. Therefore, we were interested to investigate the supramolecular assembly of these amino acids in the crystalline structure. We determined the structure of amino acid crystals by single crystal X-ray crystallography. The unit cell data of our crystals were consistent with previous studies of these materials (Figure 5.3, a-d (i) and Figure S5.10).¹⁵⁶⁻¹⁶² Our X-ray crystallography indicate the L-histidine, L-glutamine, L-asparagine, and L-threonine crystals are in the orthorhombic $P2_12_12_1$ space group and with $Z= 4$ molecules in the unit cell (CIF codes 1206541, 155068, 1103695, and 1060965, respectively) (Figure 5.3, a-b, d (i), and Figure S5.10 b). The crystals of L-isoleucine, L-valine, and L-methionine are in the $P2_1$ space group and also with $Z= 4$ molecules in the unit cell (CIF codes 126824, 1208817, and 1207980, respectively) (Figure 5.3c (i) and Figure S5.10 a, c).

The crystalline structure of the amino acid molecules are formed through the interactions between molecules directed by intermolecular forces.¹⁶³ The energetic and geometric properties of these intermolecular forces and their influence on the intramolecular forces, however, are much less understood than those of classical chemical bonds.¹⁶³ One of the strongest interactions is the hydrogen bond, which is holding the organic molecules together in a crystalline structure.¹⁶⁴ The X-ray crystallography results reveal the hydrogen bonds in the amino acid crystals (Figure 5.3, a-d (i) and Figure S5.10). We measured the length and number of hydrogen bonds in the crystal unit cells to compare the density of the hydrogen bonding network for these seven amino acids. Table S5.1 shows that L-asparagine features the maximum number of hydrogen bonds (8) in its unit cell, while the minimum number of hydrogen bonds (3) was observed for L-threonine and L-glutamine. The length of the hydrogen bonds

range from 2.6–3.0 Å (Table S5.1). So short is this distance that it is very reasonable to assume that such molecular contact is rare in a non-condensed solution state of amino acids.

Short-distance interactions in the crystal structure of organic compounds hinder intramolecular motions and vibrations and clearly indicate a definite electronic interaction between the atoms.¹⁵² Thus, the non-radiative energy loss in the excited state is reduced and enhances the photoluminescence character of the organic compound.¹⁵² To confirm the effect of the hydrogen bonding network on the fluorescence emission of the amino acid crystals, we prepared deuterated L-histidine crystals as a model of amino acid incapable of forming hydrogen bonds (Figure S5.11), and compared the lifetime with the original L-histidine crystals (Table 5.1). The deuterated L-histidine crystals show a lifetime of 1.95 ns and the original L-histidine crystals show a lifetime of 2.20 ns (Table 5.1). This change in the fluorescent lifetime indicates that the hydrogen bonding network due to close packing can contribute to the fluorescence emission of these nonaromatic and aromatic amino acids in crystalline form.

Figure 5.3, a-d (ii) and Figure S5.12 show the X-ray powder diffraction spectra of these seven amino acids in addition to their spacefil models in the crystalline state. The spacefil models also show the molecular packing of the amino acids, highlighting the extremely close contact between the carbonyl and amino moiety of the neighboring molecules (Figure 5.3, a-d (ii) and Figure S5.12). The n and π electrons of these functional groups can enable electron delocalization between these units due to the effective orbital overlap made possible at the close intermolecular distance.^{136, 147} Such electron delocalization by n- π and π - π coupling in the rigid conformation of

nonaromatic systems can allow the suppression of nonradiative processes and stabilization of the excited states in nonaromatic amino acid crystals. Moreover, according to recent studies on luminescent small molecules, such rigid structures in the crystalline state are capable of restricting vibrational/rotational movements during the electronic transitions and thus alter their optical properties.^{136, 152-153} Therefore, we anticipate that the restriction of the rotation/vibration due to the close packing of amino acids,^{154, 165} the stronger intramolecular n- π and π - π coupling interactions,¹³⁶ and the hydrogen bonding network in the crystalline state (compared to the solution state) may all account for the fluorescence emission of the amino acids.^{152-153, 163, 166-167} The same phenomenon, interactions conducted by carbonyl and amino moieties, has been suggested to explain the fluorescence properties of poly(amido amine) (PAMAM) in its aggregated state.¹⁴⁷

It has recently been shown that the optical properties of organic crystals are intimately linked to their crystal macrostructure and the relative spatial arrangement of those molecules across many length scales within the crystal.¹⁶⁸ This phenomenon may explain the different fluorescence emission intensities that we observed for the amino acid crystals depending on their molecular structure (Figure 5.2, a-b, Figures S5.1–S5.5). Thus, we investigate the macrostructural differences in the amino acid crystals using scanning electron microscopy (SEM) to better understand how it may affect their optical behavior (Figure 5.3 and Figure S5.13). The SEM images demonstrate differences between the macrostructures of the amino acid crystals. However, we could not find any specific relationship between these macrostructures and the amino acids' fluorescence emission intensity. This study sheds light on a general strategy to induce

the fluorescence of nonaromatic compounds by taking advantage of the readily available non-covalent interactions in the assembled crystalline form.

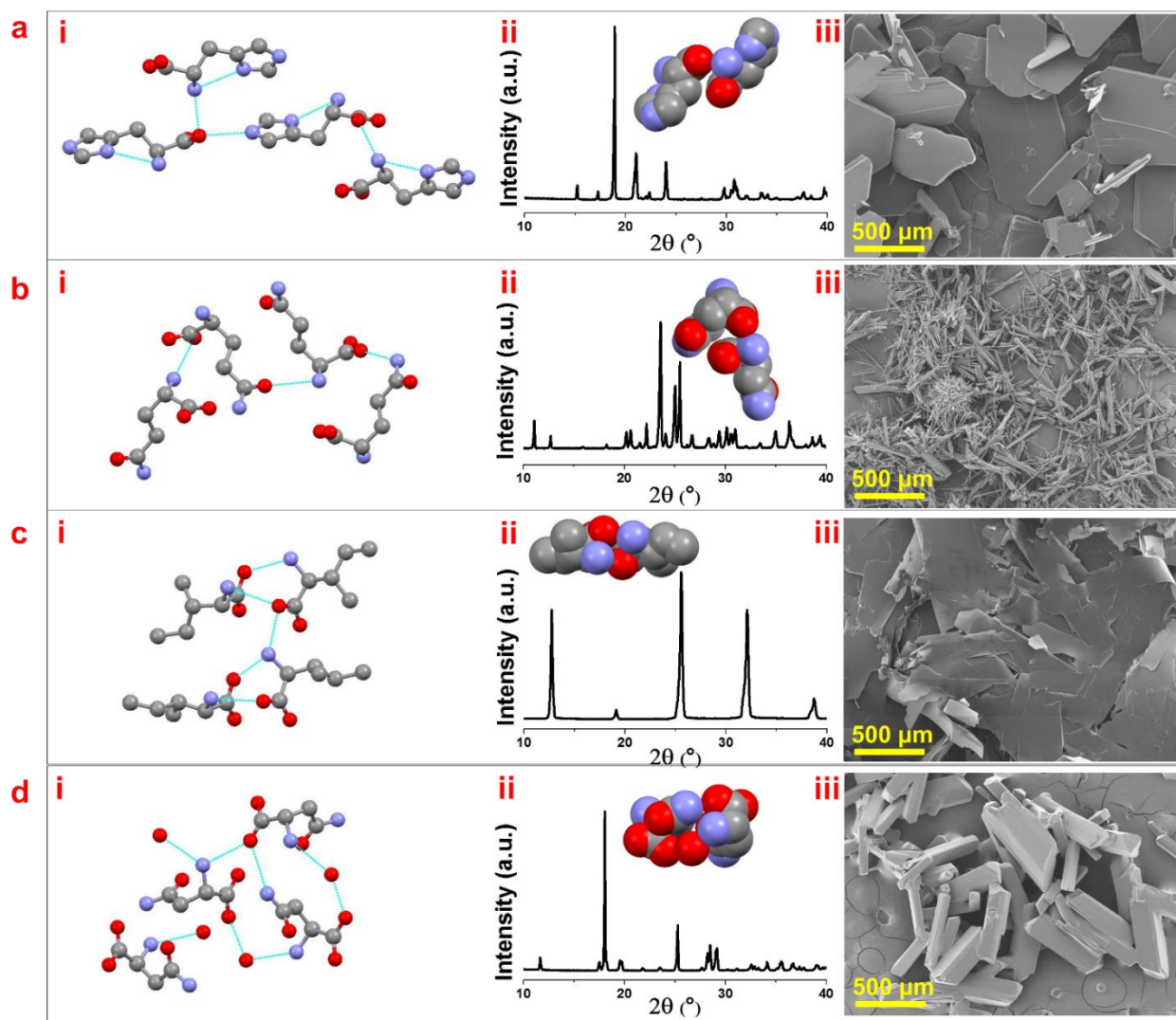


Figure 5.3. The structure of a) L-histidine, b) L-glutamine, c) L-isoleucine, and d) L-asparagine. i) The crystalline structure of amino acids with their intermolecular hydrogen bonds as determined by single crystal X-ray crystallography. ii) XRD spectra of the crystals. iii) SEM images of the crystals.

5.4. CONCLUSION

Due to the application of long lived luminescent solid organic materials in electroluminescent devices, sensors, and cell imaging there has been a resurgent interest in the past few years towards the development of new organic molecules with room temperature fluorescence in the solid state.^{153, 169} In this work, we demonstrate that pure crystals of L-histidine, L-glutamine, L-isoleucine, L-asparagine, L-valine, L-threonine, and L-methionine amino acids are fluorescent at room temperature, while none of these molecules are fluorescent in solution. Crystal structure, an emergent property, is not simply related to molecular structure.¹⁷⁰ In this work, we confirm this statement and anticipate that the restriction of intramolecular motion and electronic interactions among electron-rich groups in amino acids favored by their close proximity in the crystalline state are the most important factors for observing fluorescent amino acid crystals. However, we note that a conformation may also be responsible for the differences observed in the fluorescence emission intensity of these aromatic and nonaromatic amino acids. With the understanding that active intramolecular motion can effectively dissipate exciton energy, while restricted intramolecular motions can activate radiative transitions, numerous opportunities can be explored. Indeed, the principle of crystallization-induced emission may trigger new developments in an array of fields, ranging from bioimaging, chemosensing, optoelectronics, and stimuli-responsive systems.^{17, 152, 171-172}

5.5. SUPPORTING INFORMATION

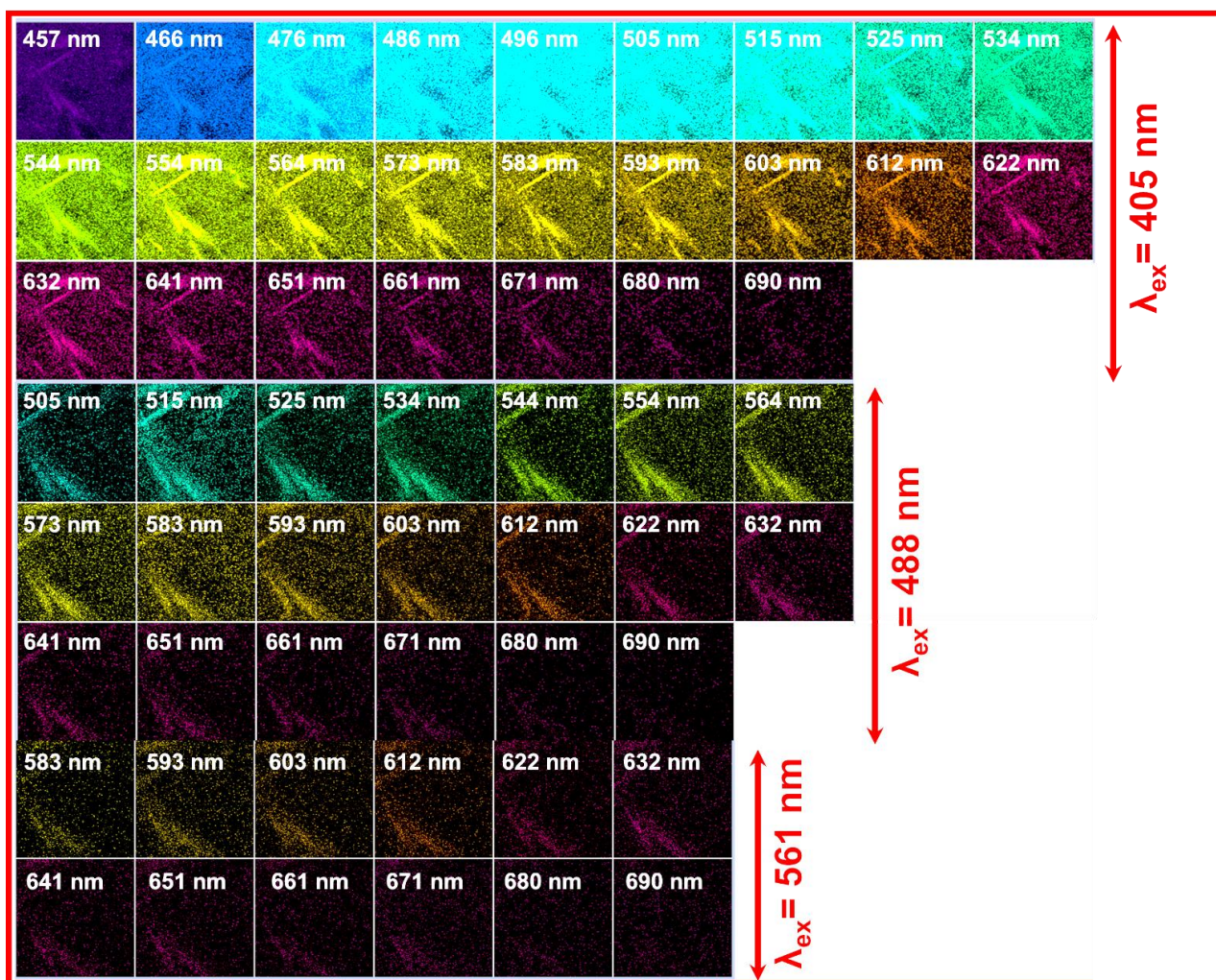


Figure S5.1. The confocal lambda scan of L-glutamine crystals excited at 405 nm, 488 nm, and 561 nm.

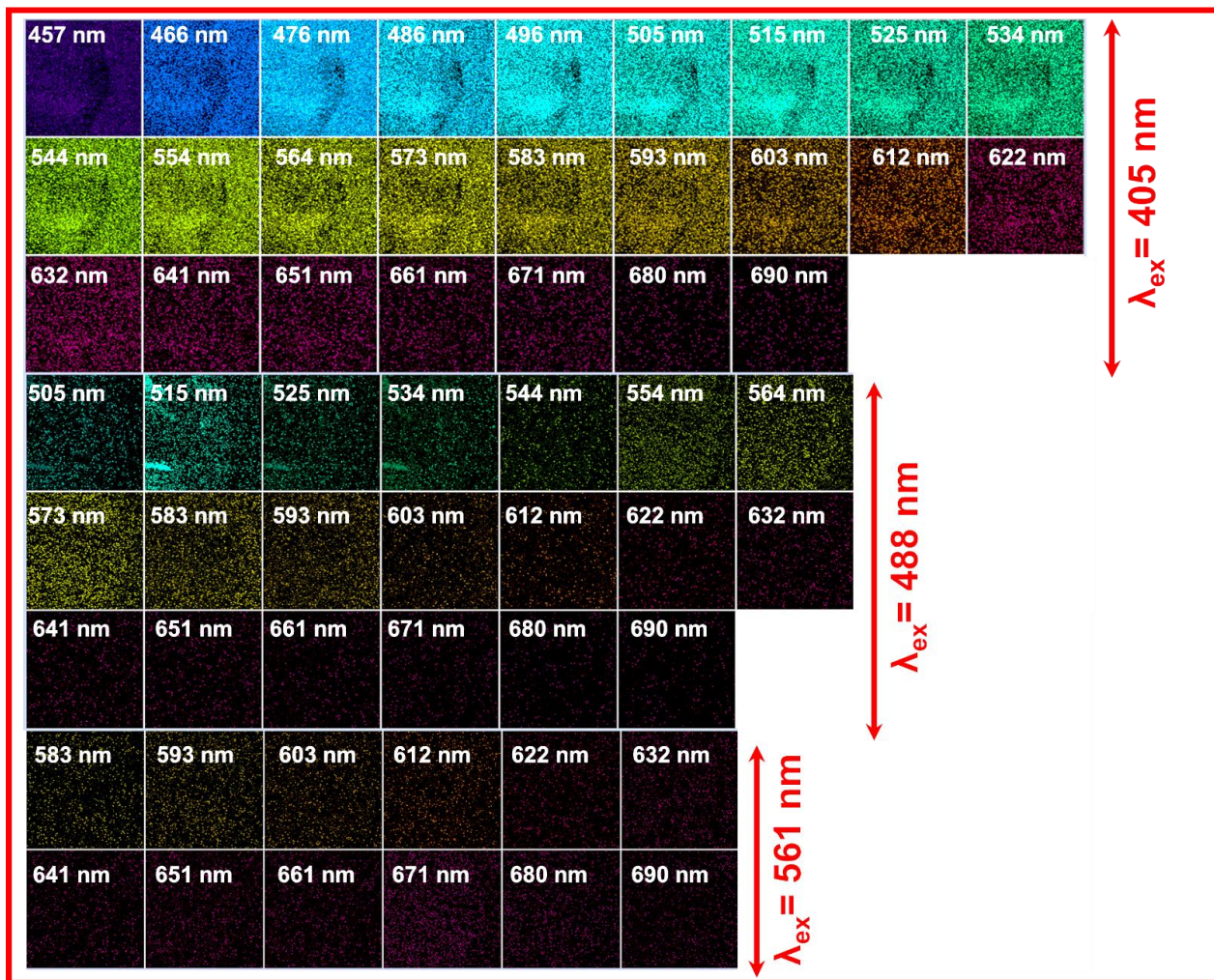


Figure S5.2. The confocal lambda scan of L-asparagine crystals excited at 405 nm, 488 nm, and 561 nm.

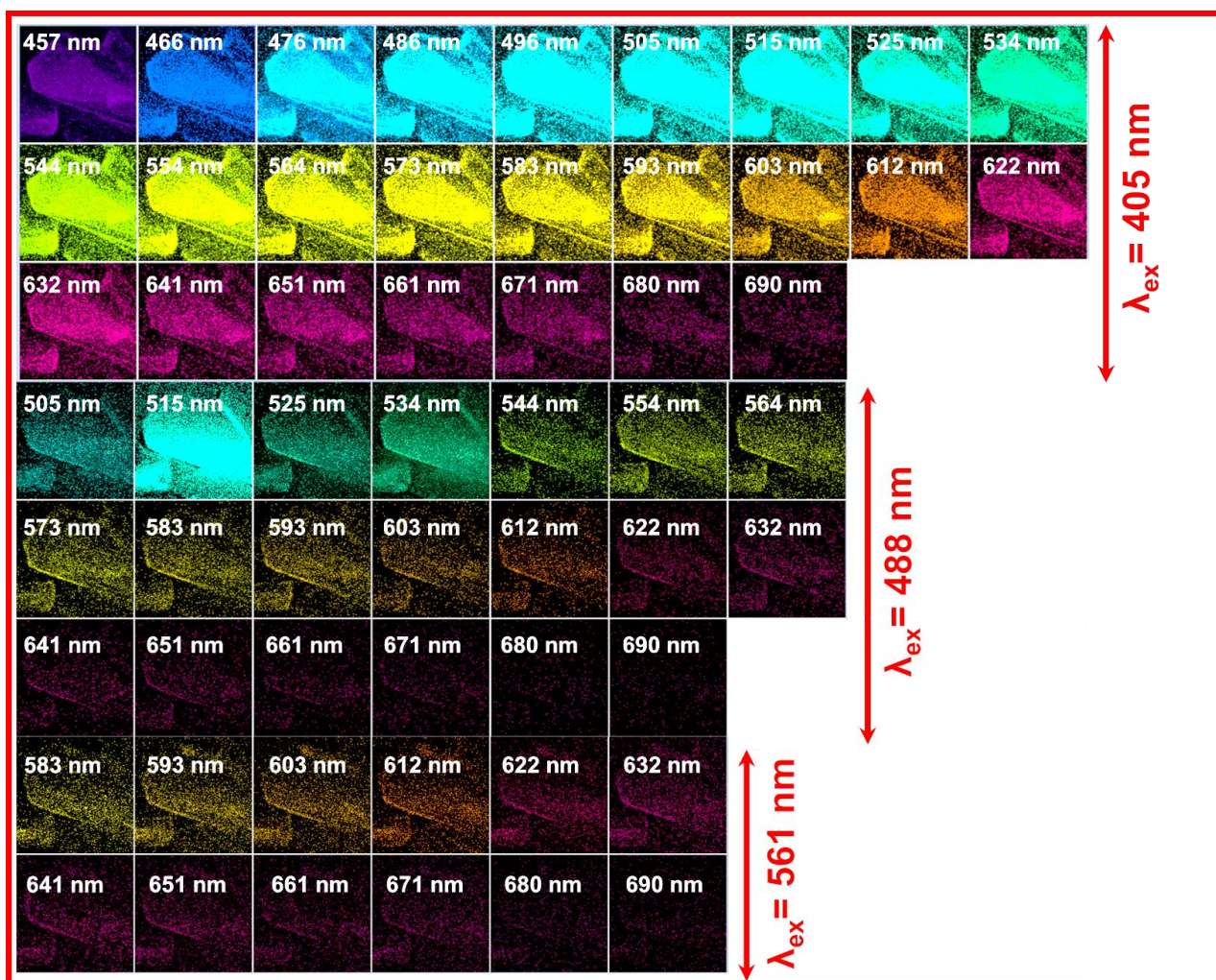


Figure S5.3. The confocal lambda scan of L-valine crystals excited at 405 nm, 488 nm, and 561 nm.

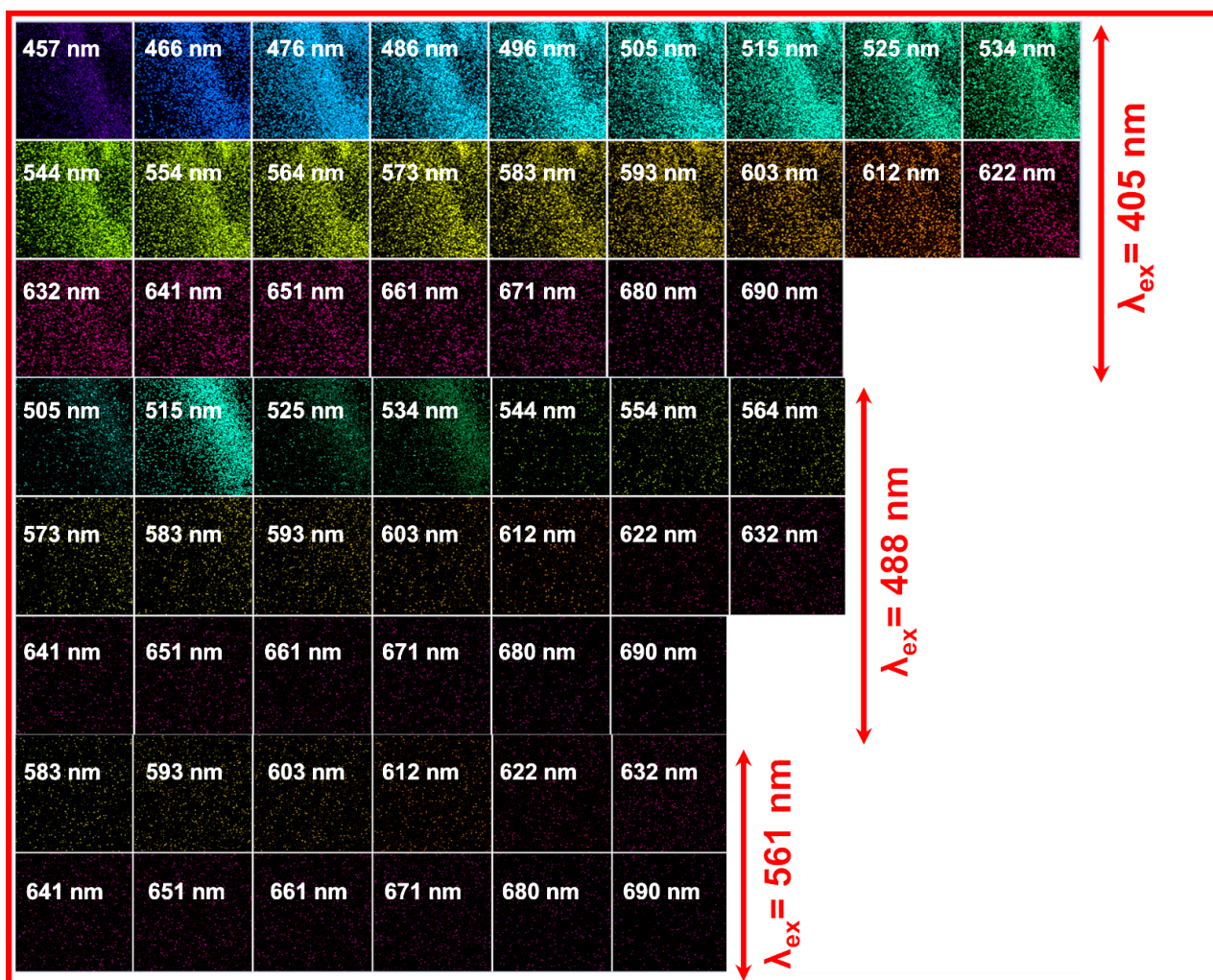


Figure S5.4. The confocal lambda scan of L-threonine crystals excited at 405 nm, 488 nm, and 561 nm.

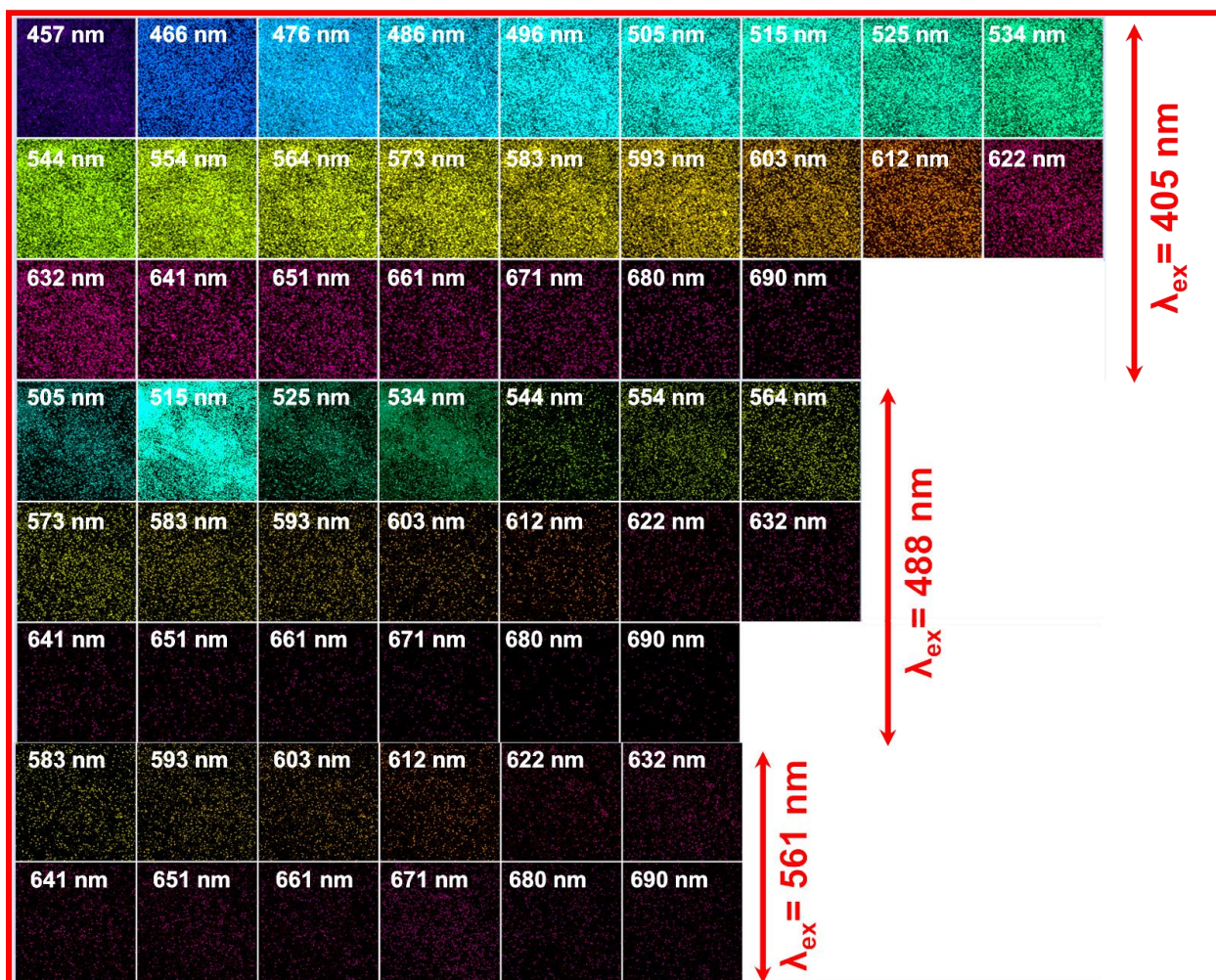


Figure S5.5. The confocal lambda scan of L-methionine crystals excited at 405 nm, 488 nm, and 561 nm.

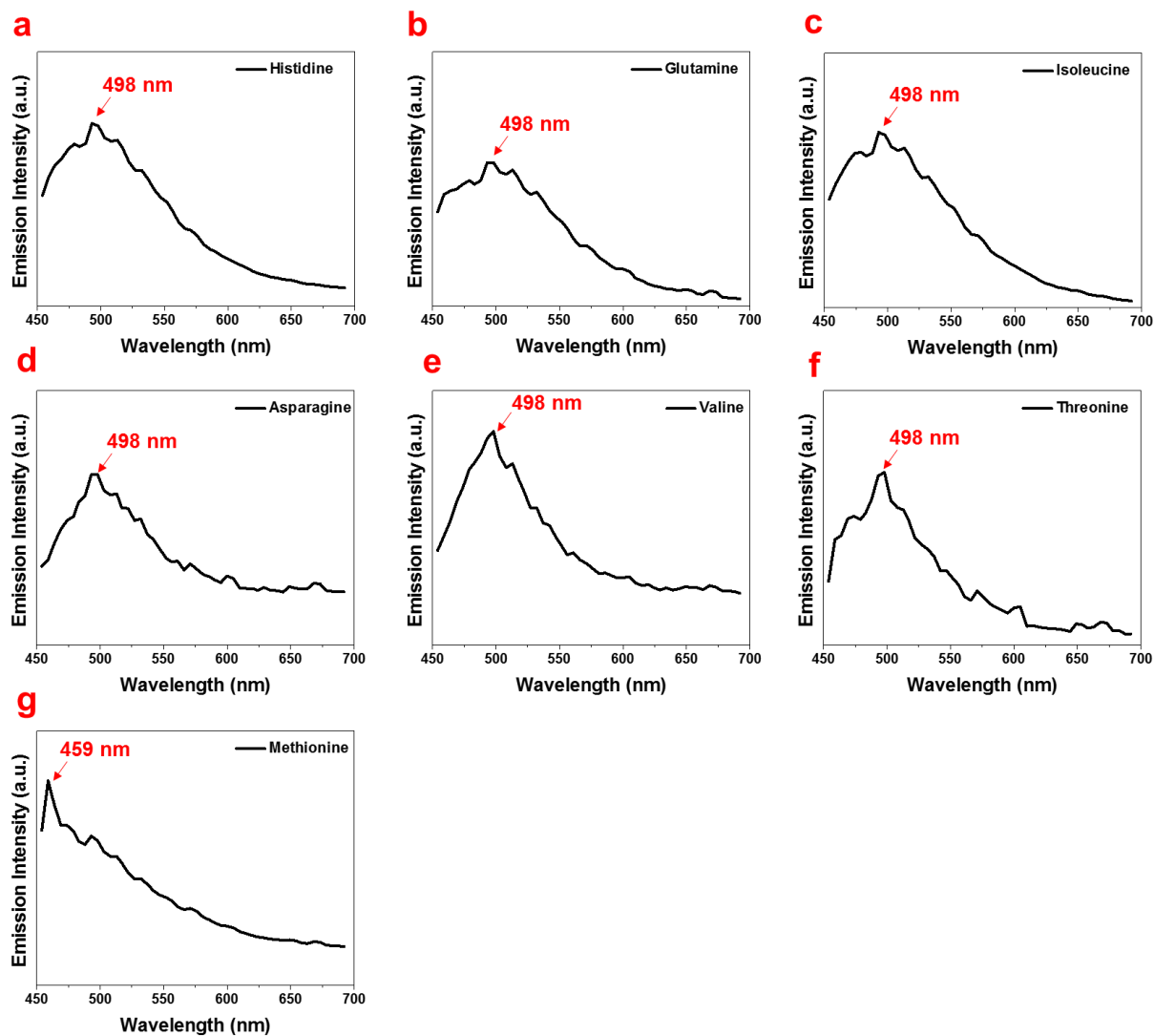


Figure S5.6. The emission spectra of amino acid crystals: a) L-histidine, b) L-glutamine, c) L-isoleucine, d) L-asparagine, e) L-valine, f) L-threonine, and g) L-methionine.

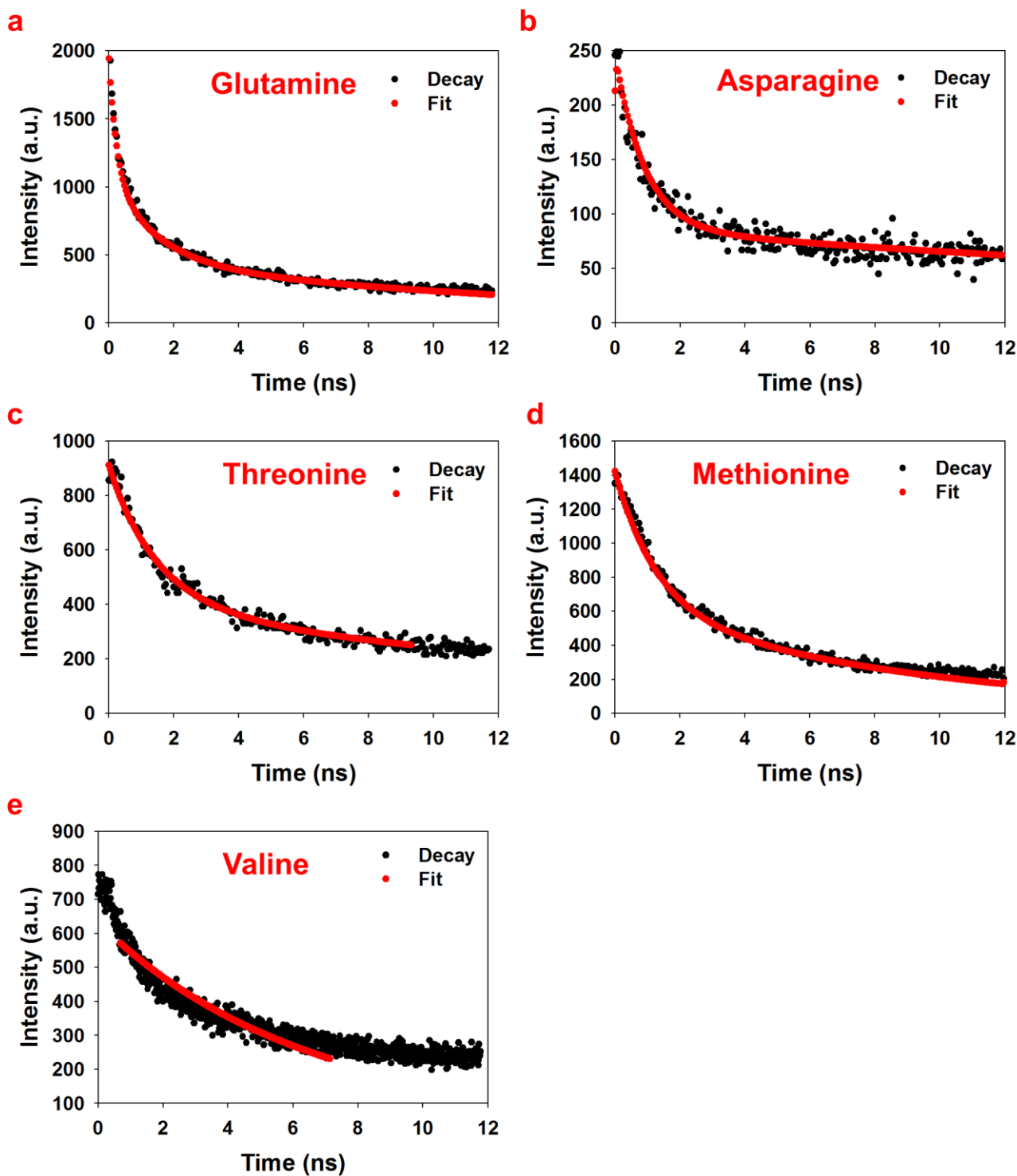


Figure S5.7. The fluorescent life-time of amino acid crystals at room temperature: a) L-glutamine, b) L-asparagine, c) L-threonine, d) L-methionine, and e) L-valine. The red lines represent the biexponential fits to the experimental data points (black lines).

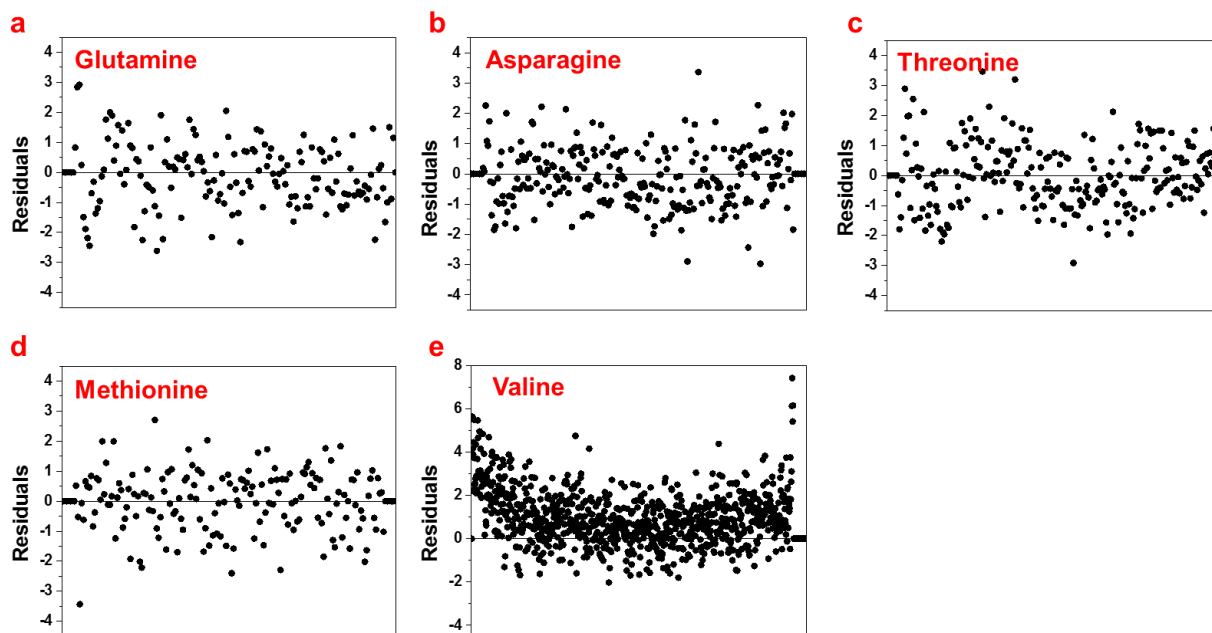


Figure S5.8. The residuals of fluorescent life-time of amino acid crystals fitted to a bi-exponential decay curve: a) L-glutamine, b) L-asparagine, c) L-threonine, d) L-methionine, and e) L-valine.

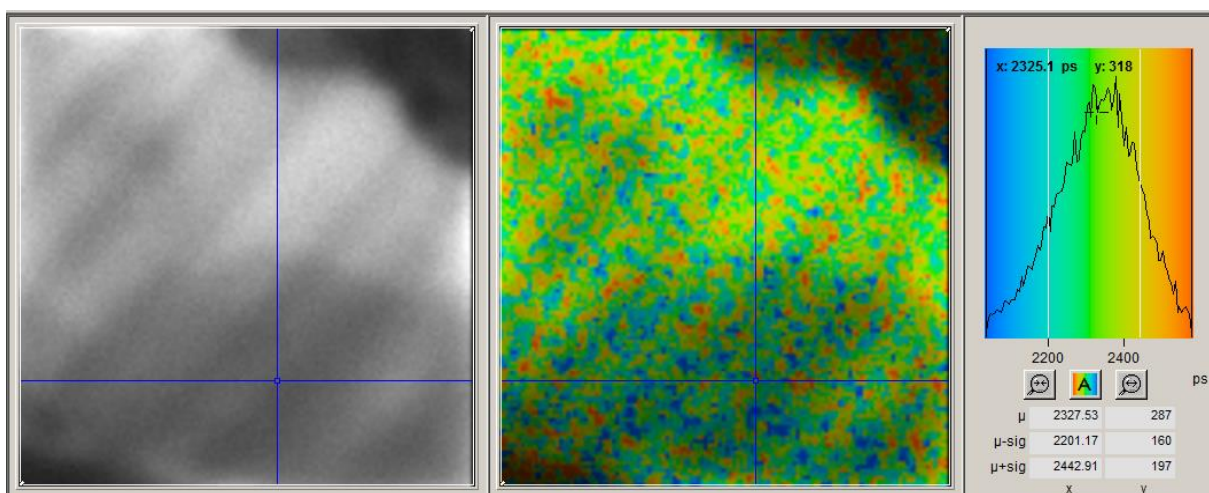


Figure S5.9. FLIM data of a histidine crystal. The image is color-coded by the weighed mean lifetime, showing that the value varies across the crystal surface. The histogram shows the distribution of lifetimes of all the pixels measured.

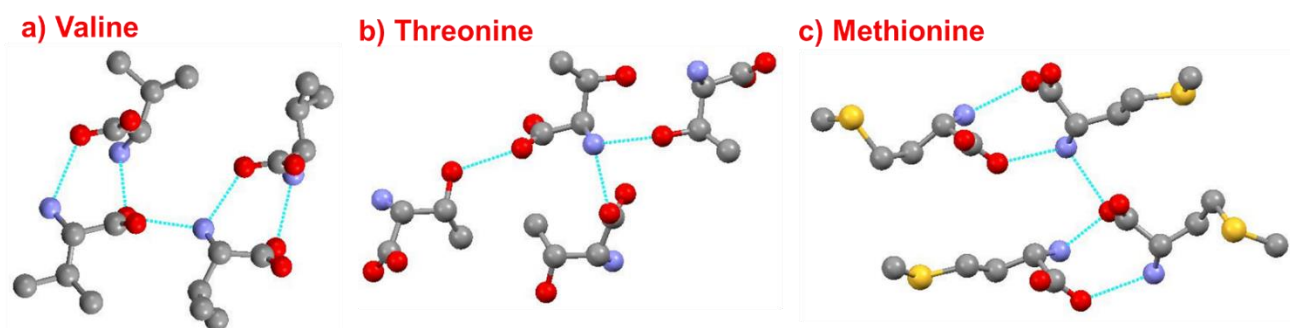


Figure S5.10. The crystalline structure of amino acids with their intermolecular hydrogen bonds: a) L-valine, b) L-threonine, and c) L-methionine.

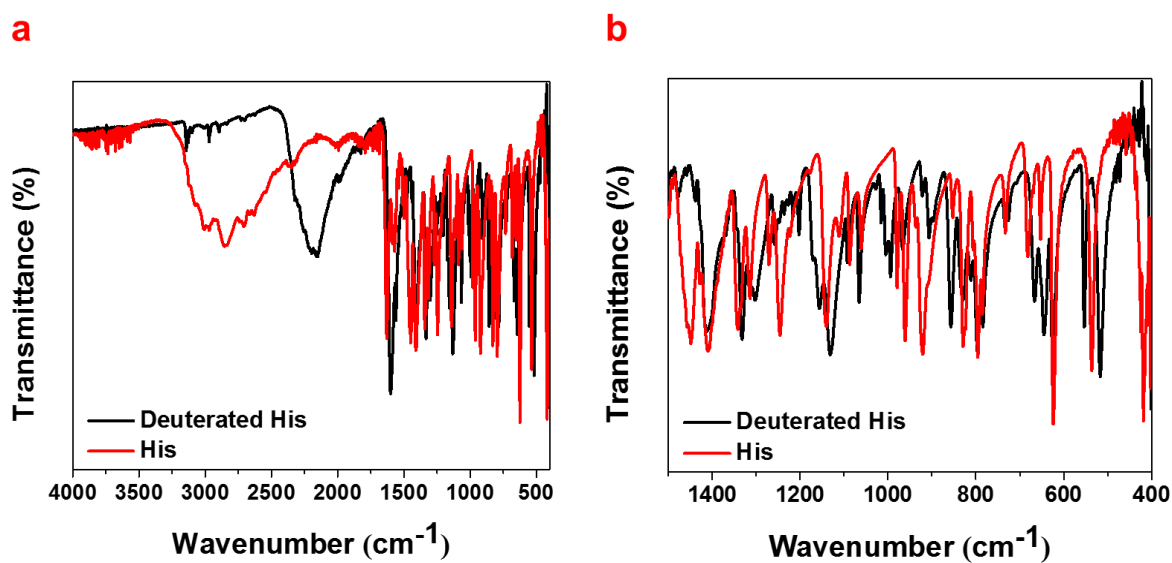


Figure S5.11. a) The FTIR spectra of the L-histidine and deuterated L-histidine crystals in the range of 400-4000 cm^{-1} . b) A close-up view of (a) in the range of 400-1400 cm^{-1} .

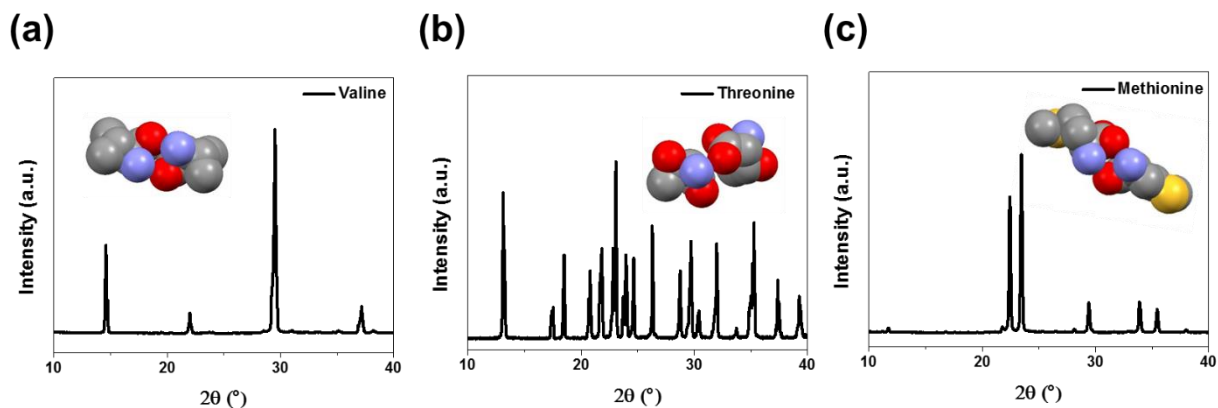


Figure S5.12. XRD spectra for the crystals of a) L-valine, b) L-threonine, and c) L-methionine.

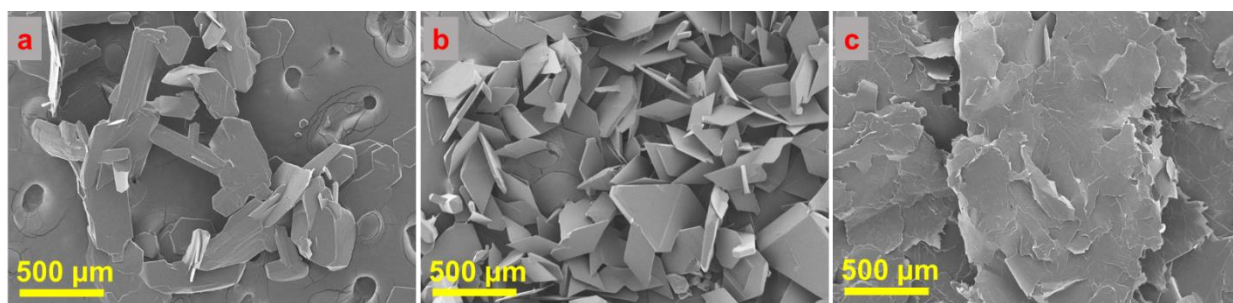


Figure S5.13. SEM images of amino acid crystals: a) L-valine, b) L-threonine, and c) L-methionine.

Table S5.1. The number and length of the hydrogen bonds in the unit cells of the amino acid crystals.

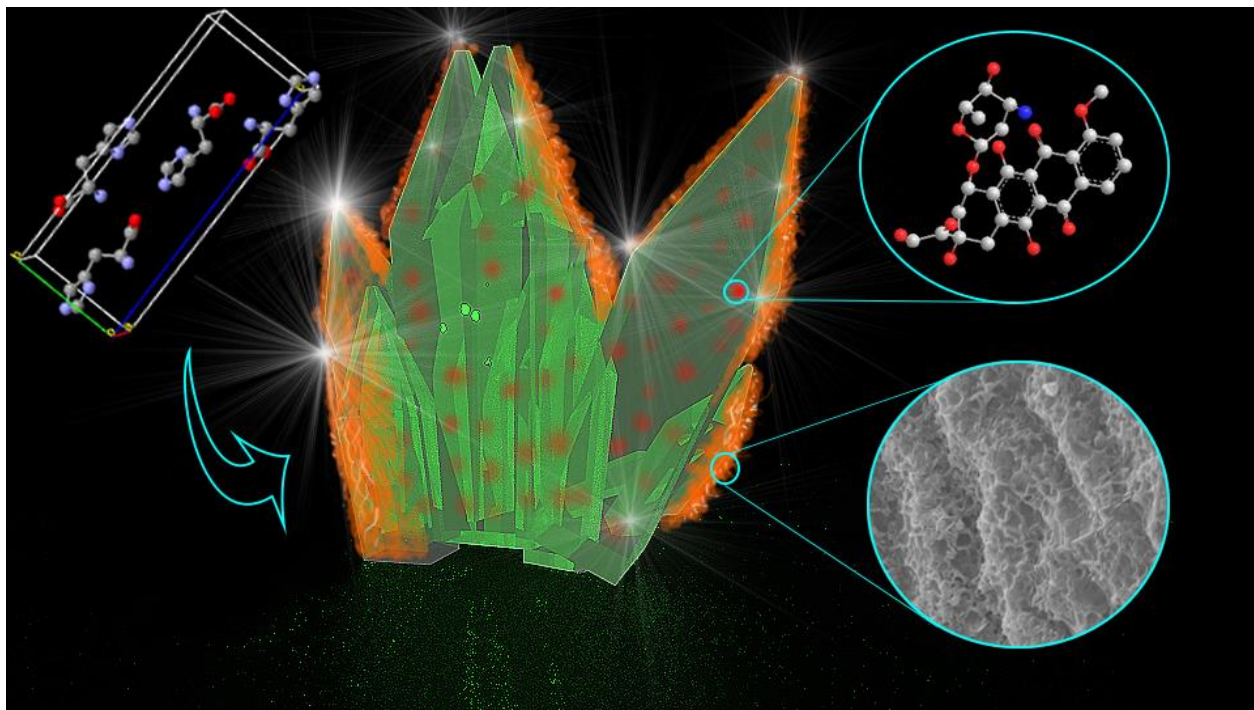
Amino acids	Number of H-bonds	Length of H-bonds (Å)
L-Histidine	7	2.8, 2.8, 2.8, 2.8, 2.8, 2.8, 3.0
L-Glutamine	3	2.8, 2.9, 2.9
L-Isoleucine	5	2.8, 2.8, 2.8, 2.8, 2.8
L-Asparagine	8	2.8, 2.8, 2.8, 2.8, 2.8, 2.8, 2.9, 2.9
L-Valine	5	2.8, 2.8, 2.8, 2.9, 2.9
L-Threonine	3	2.6, 2.8, 3.0
L-Methionine	5	2.8, 2.8, 2.8, 2.9, 2.9

Contributions

Raheleh Ravanfar wrote the manuscript and performed the experiments with support and advice from Dr. Alireza Abbaspourrad. Dr. Alireza Abbaspourrad supervised the project. Dr. Warren Zipfel helped with imaging and FLIM. Carol Bayles helped with Confocal microscopy. Dr. Justin J. Wilson and Joshua J. Woods provided invaluable comments.

CHAPTER 6

L-HISTIDINE CRYSTALS AS EFFICIENT VEHICLES TO DELIVER HYDROPHOBIC MOLECULES¹⁶



ABSTRACT

L-Histidine (L-His) molecules can form highly ordered fluorescent crystals with tunable size and geometry. The polymorph A crystal of L-His contains hydrophobic domains within the structure's interior. Here, we demonstrate that these hydrophobic domains can serve as vehicles for the highly efficient entrapment and transport of hydrophobic small molecules. This strategy shows the ability of L-His crystals to mask the hydrophobicity of various small molecules, helping to address issues related to their poor solubility and low bioavailability. Furthermore, we demonstrate that we can modify the surface of these crystals to define their function, suggesting the significance of L-His crystals in designing site-specific, and bioresponsive platforms.

As a demonstration, we use L-His crystals with loaded doxorubicin featuring hyaluronic acid covalently bonded on the crystal surface, controlling its release in response to the hyaluronidase (HAase). This strategy for entrapment of hydrophobic small-molecules suggests the potential of L-His crystals for targeted drug-delivery applications.

6.1. INTRODUCTION

The clinical use of various potent, hydrophobic molecules is often hampered by their poor water solubility.¹⁷³ Low water solubility results in poor absorption as well as low biodistribution and bioavailability of hydrophobic therapeutics upon oral administration.¹⁷⁴ Moreover, low water solubility causes drug aggregation upon intravenous administration, which is associated with local toxicity and lowered systemic bioavailability.¹⁷⁵⁻¹⁷⁶ For example, doxorubicin (DOX) is a widely used hydrophobic anticancer drug with excellent anti-neoplastic activity against a multitude of human cancers.¹⁷⁷ However, its clinical use is hindered by acute side effects, such as vomiting, bone marrow suppression, and drug-induced irreversible cardiotoxicity.¹⁷⁸⁻¹⁷⁹

These challenges have driven the development of drug-delivery systems to increase the efficacy of hydrophobic therapeutics through improved pharmacokinetics and biodistribution.¹⁸⁰ A wide variety of scaffolds, such as liposomes¹⁸¹ and stimuli-responsive polymeric particles,^{17, 182} have been explored, either covalently or noncovalently conjugating hydrophobic drugs with these systems.¹⁸⁰ Despite significant advances in the development of such drug carriers, there remain a few problems that have resulted in therapeutic failure, including the lack of site-specificity,¹⁸³ low

biocompatibility,¹⁸⁴ and inefficient drug entrapment within the carriers.¹⁸⁵ Moreover, covalent attachment in some cases requires chemical modification, which can reduce the efficiency of drug release or incomplete intracellular processing of a prodrug compound.¹⁸⁶ These strategies also involve additional complexities associated with mass production difficulties and cost. Thus, the fabrication of biocompatible platforms that can overcome these limitations remains an important yet unmet need.

Here, we demonstrate that L-histidine (L-His) crystals can function as efficient vehicles to entrap hydrophobic free drugs, such as DOX, as well as other hydrophobic small molecules, including Nile red, β -carotene, and pyrene (Figure 6.1a, b). The noncovalent inclusion of such hydrophobic molecules inside the hydrophobic domains within the interior of the polymorph A crystal structure of L-His suggests the capability for efficient drug transport and release, avoiding prodrug processing issues. As an essential amino acid, L-His crystals also have the advantage of being biocompatible and feature the ability to load a large quantity of hydrophobic molecules. Furthermore, we have recently discovered the natural fluorescent properties of L-His crystals (the results of which will be reported elsewhere), which suggests their potential as traceable compounds inside biological systems.

In this study, we further demonstrate that L-His crystals can be chemically modified at the surface to provide preferential biological targeting to the desired site of action (Figure 6.1c). By covalently cross-linking hyaluronic acid (HA) to the surface of L-His crystals (HA-His crystals), we show that hyaluronidase (HAase) is able to hydrolyze the HA on the HA-His crystals, allowing the L-His crystals to dissolve in an aqueous matrix and release encapsulated small molecules, such as DOX, to a desired

site. This scaffold provides highly efficient noncovalent inclusion of hydrophobic molecules or active drugs with excellent biocompatibility and efficient bioresponsive drug release. Moreover, the HA-His crystals are potentially site-specific, making them excellent candidates for targeting CD44-receptors overexpressed on tumors, and thus enhancing the permeability of anticancer drugs.

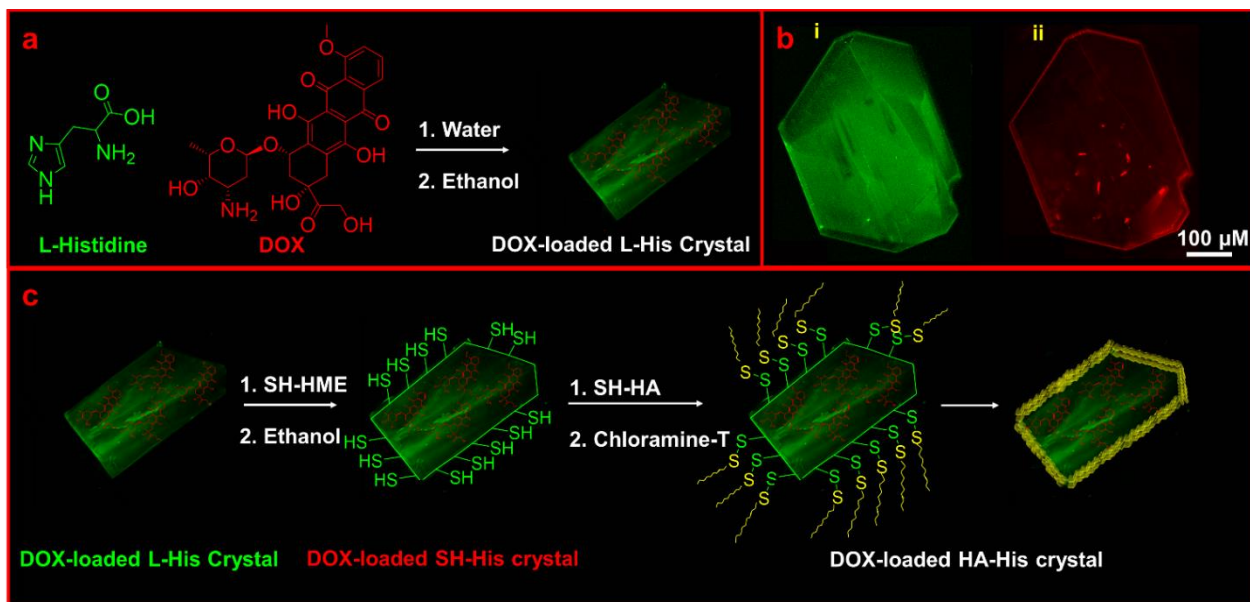


Figure 6.1. Schematic representation for the preparation of L-His crystals loaded with DOX molecules. b) CLSM images of i. L-His crystal emitted with green color, ii. DOX with red color in L-His crystal. c) Schematic representation for the preparation of L-His crystals surface-modified with tumor-specific HA for the targeted delivery of hydrophobic DOX molecules.

6.2. MATERIALS AND METHODS

6.2.1. Preparation and characterization of the L-His crystals with entrapped small molecules

A 30 mg/mL solution of L-His ($\geq 99\%$, Sigma-Aldrich) was prepared by dissolving L-His powder in milli-Q water using a vortex mixer at ambient temperature in a Corning® 15 mL centrifuge tube with a closed cap. Then 500 μ L of the aqueous solution of L-His and 500 μ L of 200 proof ethanol (KOPTEC, PA, US) were added to 200 μ L of the small molecule solution (2 mg/mL). The small molecules used in this study were Nile red ($> 98\%$, Sigma-Aldrich), pyrene ($> 98\%$, Sigma-Aldrich), β -carotene ($> 97\%$, Sigma-Aldrich), and doxorubicin HCl (DOX, $> 98\%$, Fluka, Mexico City, Mexico). The solution was vortexed for 15 s and kept static at ambient temperature. After 3 h, crystals were collected and washed with ethanol to remove the free small molecules from the surface of the crystals and the supernatant was collected to measure the concentration of non-entrapped small molecules using HPLC. An Agilent 1200 LC System with a Binary SL Pump & Diode Array Detector, Shodex RI-501 Refractive Index Detector (single channel), and an Agilent 1100 Column Compartment (G1316) was utilized to carry out the analysis. Each individual sample of small molecules was quantified based on an optimized method reported in the literature for β -carotene,¹⁸⁷ Nile red,¹⁸⁸ pyrene,¹⁸⁹ and DOX.¹⁹⁰ The entrapment efficiency of the crystals was calculated by subtracting the concentration of the non-entrapped small molecules in the supernatant from the primary amount of small molecules, as follows in equation 1:

$$\text{Entrapment efficiency (\%)} = \frac{M_0 - M_S}{M_0} * 100$$

(1)

in which M_0 is the primary concentration of small molecules used in the formulation, and M_S is the concentration of non-entrapped small molecules in the supernatant.

L-His crystal controls were prepared using the same procedure, but without the addition of small molecules. Unit cell data for the L-His crystals were collected on a Rigaku Synergy XtaLAB diffractometer. The morphologies of the crystals were observed using a Zeiss 710 Laser Scanning Confocal Microscope (Carl Zeiss Microscopy, Thornwood, NY), an inverted optical microscope (DMIL LED, Leica) connected to a fast camera (MicroLab 3a10, Vision Research), and an SEM (LEO Zeiss 1550 FESEM (Keck SEM) and Zeiss Gemini 500). All SEM images were obtained under high vacuum mode without sputter coating. XRD measurements were performed using a Bruker D8 Advance ECO powder diffractometer (MA) operated at 40 kV and 30 mA (Cu K α radiation). The crystals were scanned at room temperature from $2\theta = 10\text{--}60^\circ$ under continuous scanning in 0.02 steps of $2\theta \text{ min}^{-1}$.

6.2.2. *Synthesis of thiolated HA (SH-HA)*

Sodium hyaluronate (> 43% Glucuronic Acid, Bulk Supplements, Henderson, NV, USA) was used after being dialyzed against distilled water, followed by lyophilization. L-cysteine methyl ester was synthesized to protect the carboxyl groups of L-cysteine using a previously described method.¹⁹¹ The covalent attachment of L-cysteine methyl ester to sodium hyaluronate was achieved through the formation of amide bonds between the primary amino groups of the cysteine methyl ester and the carboxylic groups of hyaluronate. To synthesize SH-HA, we used a method previously reported in the literature.¹⁹² Briefly, sodium hyaluronate (2.5 mmol) was dissolved in 100 mL of distilled water, to which N-(3-Dimethylaminopropyl)-N'-ethylcarbodiimide hydrochloride (EDC) (0.5 mmol, > 98%, Sigma-Aldrich) and cysteine methyl ester (2.5

mmol) were added under slow stirring. The pH was adjusted to 5.3 by the addition of 1 M NaOH. After incubating the solution for 5 h, the solution was transferred to dialysis membrane discs (MWCO 3.5 kDa, Thermo Scientific) and dialyzed three-times against 1% NaCl for three days, and finally against distilled water for one day. The solutions were then freeze dried to obtain a white solid and investigated by FTIR in the region from 4000 to 400 cm^{-1} (120 scans, resolution of 2 cm^{-1}) using an IRAffinity-1S FTIR spectrophotometer (Shimadzu Scientific Instruments/Marlborough, MA).

6.2.3. Synthesis of thiolated histidine methyl ester (SH-HME)

Histidine methyl ester (HME) was synthesized using a previously described method.¹⁹¹ The SH-HME was synthesized by reacting HME (1 mmol) with 2-iminothiolane hydrochloride (0.4 mmol, > 98%, Sigma-Aldrich) in PBS (50 mL; pH 7.4) for 12 h at room temperature. After washing the SH-HME using deionized water, the solution was lyophilized to obtain a powder of SH-HME.

6.2.4. Synthesis of HAase-responsive, HA-modified histidine crystals with entrapped DOX (HA-His crystals)

After synthesizing the L-His crystals with entrapped DOX, as described in the first section of the Methods, SH-HME (0.01 g) was added to the crystal dispersion, followed by the addition of 200 μL ethanol to start growing the SH-HME crystals on the surface of the L-His crystals to form thiolated histidine crystals (SH-His crystals). The SH-His crystals were incubated at room temperature for 3 h. Next, SH-HA (0.03 g) was added to the SH-His crystal dispersion, and the pH was adjusted to 8 with 1 M NaOH. Then,

50 μ L of chloramine T solution (50 mM in PBS buffer, pH 7.4, > 98%, Sigma-Aldrich) was added, based on a previously reported method,¹⁹³ to induce thiol-mediated conjugation of the SH-HA onto the SH-His crystals. After 1 h incubation at room temperature, the resulting HA-modified histidine crystals (HA-His crystals) were collected from the falcon tubes by centrifugation at 1000 \times g for 5 minutes, washed with ethanol, freeze-dried, and stored at 4 $^{\circ}$ C.

6.2.5. In Vitro Enzyme-Triggered Drug Release of DOX-Loaded HA-His crystals

HAase-triggered drug release profiles of the DOX-loaded HA-His crystals were monitored using HPLC. The DOX-loaded HA-His crystals were incubated with different concentrations of HAase in an acetate buffer (pH = 4.3, 37 $^{\circ}$ C) for 72 h. To measure the drug release profiles of DOX, we used HPLC and attained the data at predetermined time points after incubating the DOX-loaded HA-His crystals with acetate buffer. Supernatants were used to measure the drug release profiles using a dialysis method. In brief, lyophilized HA-His crystals (5 mg) were dispersed in 1 mL of acetate buffer (pH = 4.3, 37 $^{\circ}$ C) containing different concentrations of HAase (0 U/mL, 1 U/mL, and 10 U/mL). The dispersed HA-His crystals were transferred to Spectra/Por[®] regenerated cellulose dialysis tubes (molecular weight cutoff = 10000, Float A lyzer) immersed in 15 mL of acetate buffer (pH = 4.3, 37 $^{\circ}$ C) containing 1.6% Triton X-100 and gently shaken at 37 $^{\circ}$ C in a water bath at 100 rpm. The medium was replaced with fresh medium at predetermined time points. The cumulative release of DOX was calculated as follows in equation 2:

$$\text{Cumulative release (\%)} = (M_t / M_{\infty}) * 100 \quad (2)$$

in which M_t is the amount of DOX released from the crystals at time t , and M_∞ is the amount of DOX in the crystals.

6.2.6. Statistical analysis

The results were subjected to analysis of variance (ANOVA) using SPSS software package version 15.0 for Windows. All measurements were performed in triplicate. Mean comparisons were performed using the post hoc multiple comparison Duncan test to determine if differences were significant at $P < 0.05$.

6.3. RESULTS AND DISCUSSION

In addition to its well-known roles as an electrophilic acid, L-His features two nitrogen atoms, designated as N δ 1 and N ϵ 2, in its heterocyclic imidazole system, which serve as hydrogen bond acceptor and hydrogen bond donor, respectively.¹⁹⁴⁻¹⁹⁶ To synthesize L-His crystals we performed antisolvent crystallization, adding ethanol as the antisolvent to an aqueous solution of L-His at a 1:1 volume ratio (Figure 6.2a). We note that the size of the crystals can be tuned from the sub-micron to micron scale, depending on the crystal growth time and antisolvent.¹⁹⁷ The L-His crystals display bright emission at 500 nm (405 nm excitation), which we attribute to suppressed nonradiative decay by intramolecular motion due to the close molecular packing of the crystal (the fluorescence properties of the L-His crystals will be reported elsewhere).

We also investigate the powder X-ray diffraction (XRD) pattern of L-His crystals. The diffraction peaks of the L-His crystal was in good agreement with the simulated diffraction peaks of the crystal from the Cambridge Crystallographic Data

Center (CCDC, CIF code 1206541) (Figure 6.2b). We measured the unit cell data of the resulting pure L-His crystals and found they were consistent with a previous study of L-His by Madden, et al.¹⁹⁸ (CIF code 1206541) (Figure 6.2c). X-ray crystallography of our L-His crystals showed a mixture of the stable polymorph A with the orthorhombic space group $P2_12_12_1$ and $Z=4$ molecules in the unit cell, and the metastable polymorph B with the majority being polymorph A. The relative fractions of these polymorphs can be tuned by changing the supersaturation ratio of L-His in aqueous solution, as has been shown in previous studies.^{197, 199} When the L-His molecules arrange in the stable polymorph A crystals, they orient imidazole rings in the vicinity of each other, creating a hydrophobic domain within the structure (Figure 6.2c).

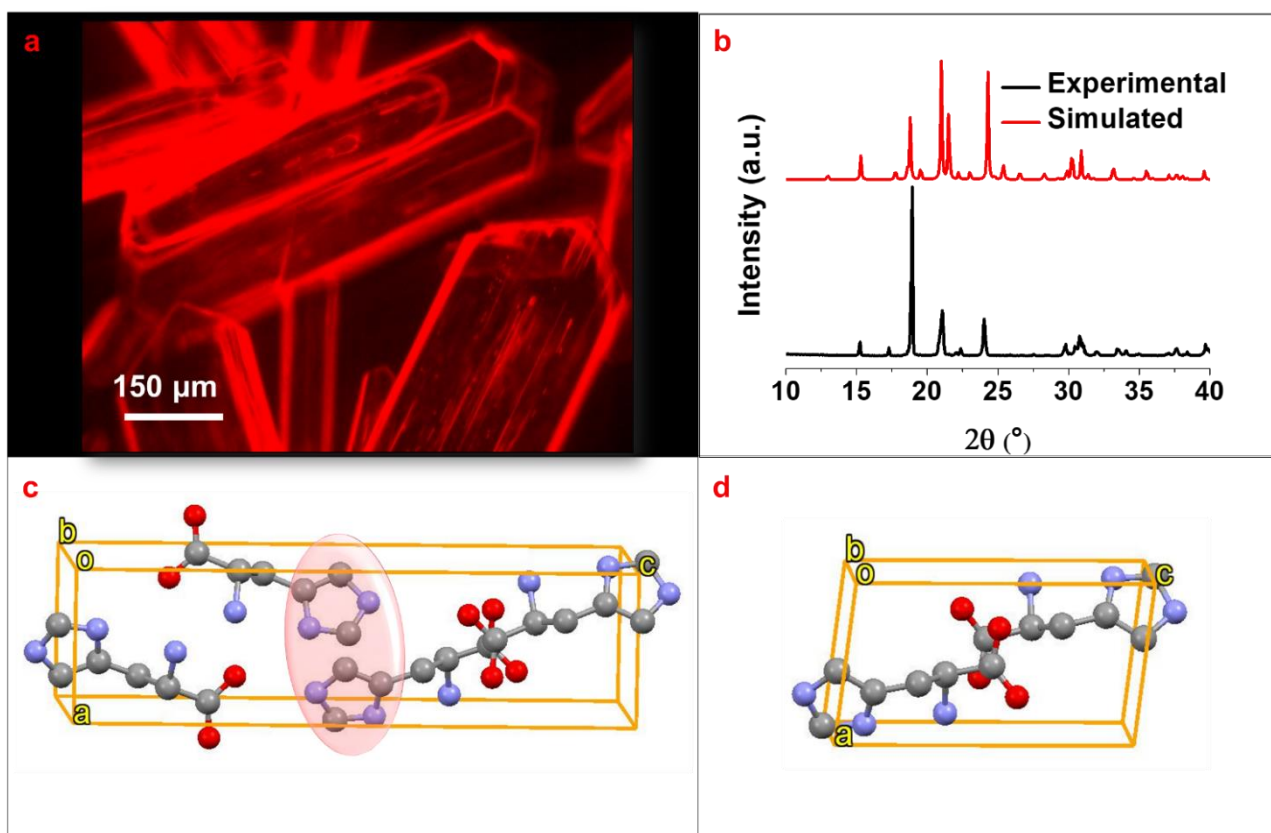


Figure 6.2. a) Fluorescence microscopy images of L-His crystals. b) The simulated and experimental XRD patterns of the pure L-His crystals. c) Ball and stick representation of four L-His molecules arranged in the polymorph A with the orthorhombic space group $P2_12_12_1$, showing the hydrophobic domain surrounded by imidazole rings of the L-His molecules. d) Ball and stick representation for the unit cell of crystals formed after loading the small molecules, showing two L-His molecules with monoclinic space group $P2_1$.

The structure of the L-His crystals therefore features several hydrophobic interior domains while displaying a hydrophilic exterior. To determine whether we could use these hydrophobic domains to entrap small molecules with a high entrapment efficiency, we chose three different hydrophobic guest compounds as fluorescent probes (Nile red, pyrene, and β -carotene) and two hydrophilic compounds (fluorescein isothiocyanate (FITC) and norbixin) for comparison. Adding the small molecules individually to aqueous solutions of L-His and subsequent mixing with ethanol, we then collected the resulting L-His crystals after 3 hours. X-ray crystallography of the L-His crystals loaded with small molecules showed the change of crystal's space group from orthorhombic space group $P2_12_12_1$ ($Z=4$) to the monoclinic space group $P2_1$ ($Z=2$) in the unit cell (Figure 6.2d). We also observed the materials using optical, scanning electron (SEM), and confocal laser scanning microscopy (CLSM; Figure 6.3a–d). The hydrophilic small molecules (FITC and norbixin) were not observed entrapped inside the L-His crystals, instead remaining in solution (data not shown). However, fluorescence by the hydrophobic β -carotene, Nile red, and pyrene compounds was

observed inside the crystals (Figure 6.3, a-d, iv). These observations demonstrate the entrapment of these molecules in the L-His crystals with entrapment efficiencies of ~ 96%, 62%, and 87%, respectively, as determined using high-performance liquid chromatography (HPLC; see Methods). These results indicate that the L-His crystals are specific for the entrapment of hydrophobic small molecules. We believe that the inclusion of such hydrophobic small molecules inside the L-His crystals is noncovalent in nature, driven by hydrophobic interactions, hydrogen bonding, and π - π stacking²⁰⁰⁻²⁰¹ between the imidazole rings of the L-His molecules and the aromatic regions and/or double bonds of the hydrophobic small molecules. The entrapment efficiency may depend on the molecular structure of the small molecules and their ability to fit inside the L-His crystal structure.

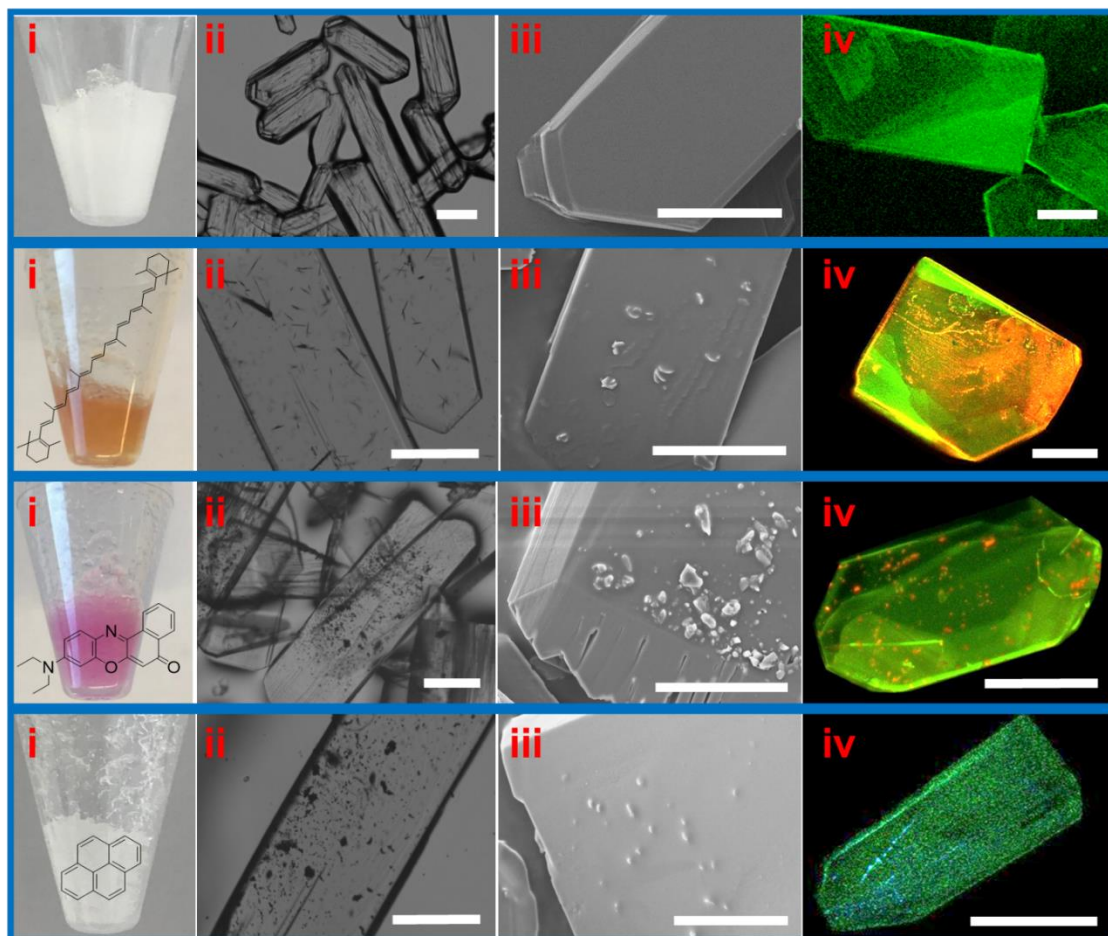


Figure 6.3. a) Pure L-His crystals; the green color in part iv represents the pure L-His crystals. b) β -carotene-entrapped L-His crystals; the green color represents the L-His crystals and the orange color represents β -carotene. c) Nile red-entrapped L-His crystals; the green color represents the L-His crystals and the red color represents Nile red. d) Pyrene-entrapped L-His crystals; the green color represents the L-His crystals and the blue color represents pyrene. First column (i): digital images; second column (ii): optical microscopy images; third column (iii): SEM images; fourth column (iv): CLSM images. Scale bars: 100 μm .

The CLSM imaging results of the loaded L-His crystals along the z optical axis (z-stack) indicates that the localization of the hydrophobic small molecules occurs at the central plane of focus (Figure 6.4). Figure 6.4 demonstrates the entrapment of hydrophobic Nile red (Figure 6.4a, b) and pyrene (Figure 6.4c) inside the L-His crystals from different dimensional perspectives. Figure 6.4 verifies that the fluorescent signal of the β -carotene (Figure 6.4d-f) and Nile red (Figure 6.4g-i) is indeed localized within the structure of the L-His crystals. The entrapment of small molecules inside the fluorescent L-His crystals not only offers the whole system a hydrophilic surface, which can address the challenges of poor solubility and distribution of hydrophobic small molecules in biological systems, but also provides protection and controlled release of the entrapped small molecules.

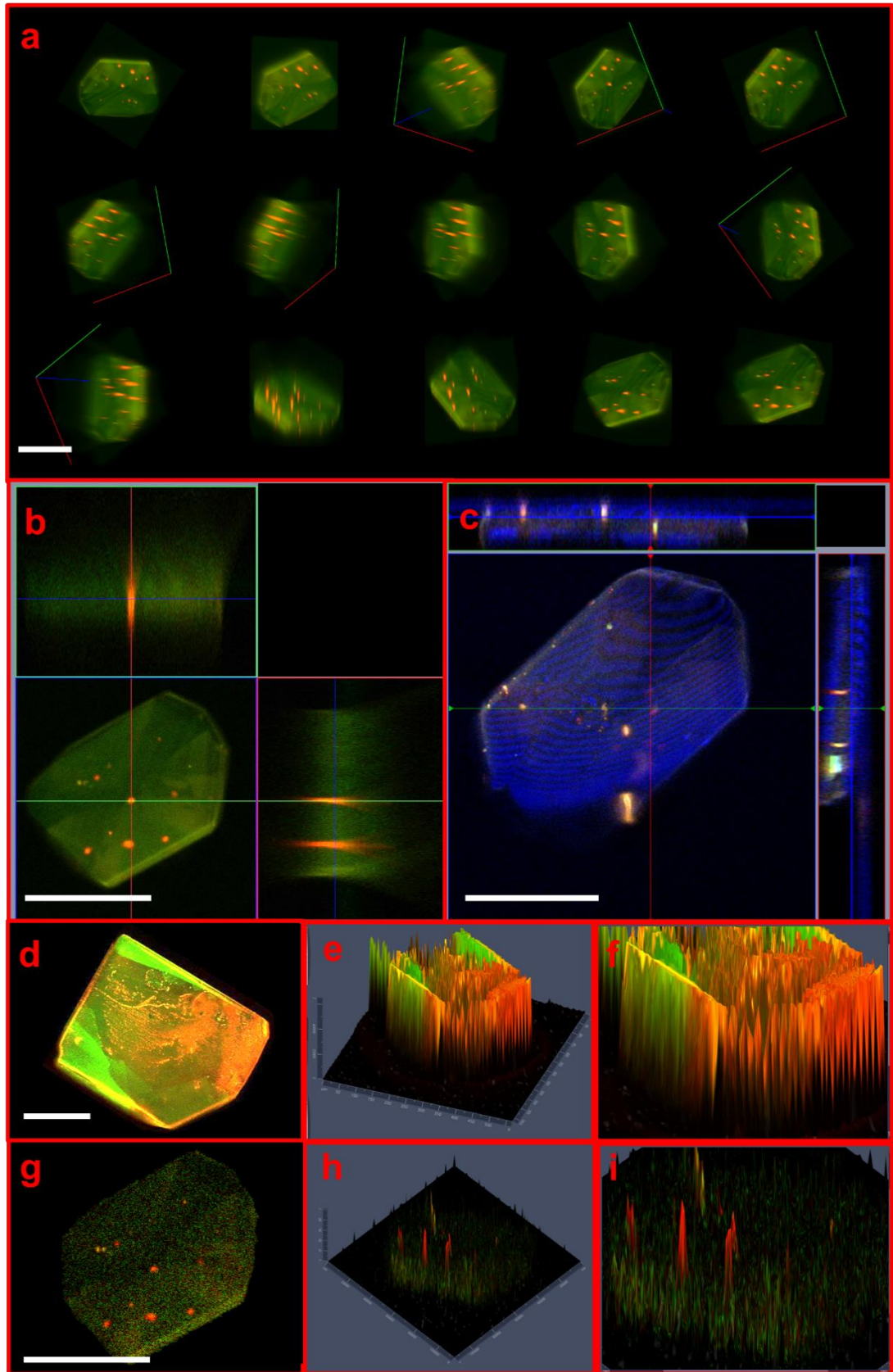


Figure 6.4. a) CLSM imaging data collected at different dimensions of the L-His crystals, confirming the localization of the hydrophobic Nile red inside the L-His crystals. b) Ortho demonstration of L-His crystals with entrapped Nile red. c) Ortho demonstration of L-His crystals with entrapped pyrene. d) The CLSM imaging data of L-His crystals with entrapped β -carotene in 2D. e, f) The CLSM imaging data of L-His crystals with entrapped β -carotene in 2.5D, with intensity on the Z-axis. g) L-His crystals with entrapped Nile red in 2D. h, i) L-His crystals with entrapped Nile red in 2.5D, confirming the localization of the hydrophobic small molecules inside the L-His crystals. The green and blue colors represent the L-His crystals, and the orange and red colors represent the β -carotene, pyrene, and Nile red, respectively. Scale bars: 100 μ m.

We also investigated XRD pattern of the L-His crystals loaded with the different small molecules. Figure 6.5a illustrates the XRD patterns of the pure small molecules (Figure 6.5a, black lines), pure L-His crystals (Figure 6.5a, red lines), a dry mixture made of the L-His crystals with the powders of the various small molecules (Figure 6.5a, blue lines), and the small molecule-loaded L-His crystals (Figure 6.5a, green lines), made as previously described. A characteristic powder diffraction peak of polymorph A appears at $2\theta \sim 19^\circ$ (Figure 6.5a, red lines). The XRD analysis of crystals obtained from small molecule-loaded L-His crystals (Figure 6.5a, green lines) yields a different XRD pattern in comparison with the pure L-His crystals (Figure 6.5a, red lines). The XRD patterns of the L-His crystals loaded with β -carotene and Nile red show an increase in the intensity of the peaks at $2\theta \sim 22^\circ$ and 24° , respectively, while the XRD pattern of the pyrene-loaded L-His crystals remains similar to the pure L-His crystals

(Figure 6.5a, i-iii, green lines). The changes in the peak intensities indicate the change of electron density inside the unit cell and where the atoms are located,²⁰² and can be influenced by the inclusion of hydrophobic small molecules. This result is in good agreement with the results of single crystal X-ray crystallography, showing the change of L-His crystals' unit cell upon the loading of small molecules (Figure 6.2c, d). The dominant peaks of the pure small molecules at $2\theta \sim 19^\circ$, 13° , and 12° for β -carotene, Nile red, and pyrene, respectively (black lines), disappear in the small molecule-loaded crystal samples (green lines), which confirms the loading of the small molecules inside the structure of the L-His crystals. In contrast, for the manual dry mixture of the L-His crystals and small molecules (blue lines), the XRD patterns are different and the dominant peaks of the small molecules at $2\theta \sim 19^\circ$, 13° , and 12° for β -carotene, Nile red, and pyrene remain (Figure 6.5a, i-iv).

Due to the exceptional ability of L-His crystals to fluoresce and entrap hydrophobic small molecules within their hydrophilic structure, we applied these crystals to entrap DOX, a highly hydrophobic chemotherapeutic, to address its poor solubility, which can cause cardiotoxicity and lowered systemic bioavailability.¹⁷⁹ Figure 6.1b shows the L-His crystals loaded with DOX, featuring an entrapment efficiency of 55%. The XRD patterns of the L-His crystals loaded with DOX show an increase in the intensity of the peak at $2\theta \sim 32^\circ$ (green line), indicating the change of electron density inside the unit cell is potentially influenced by the inclusion of DOX molecules (Figure 6.5a, iv).

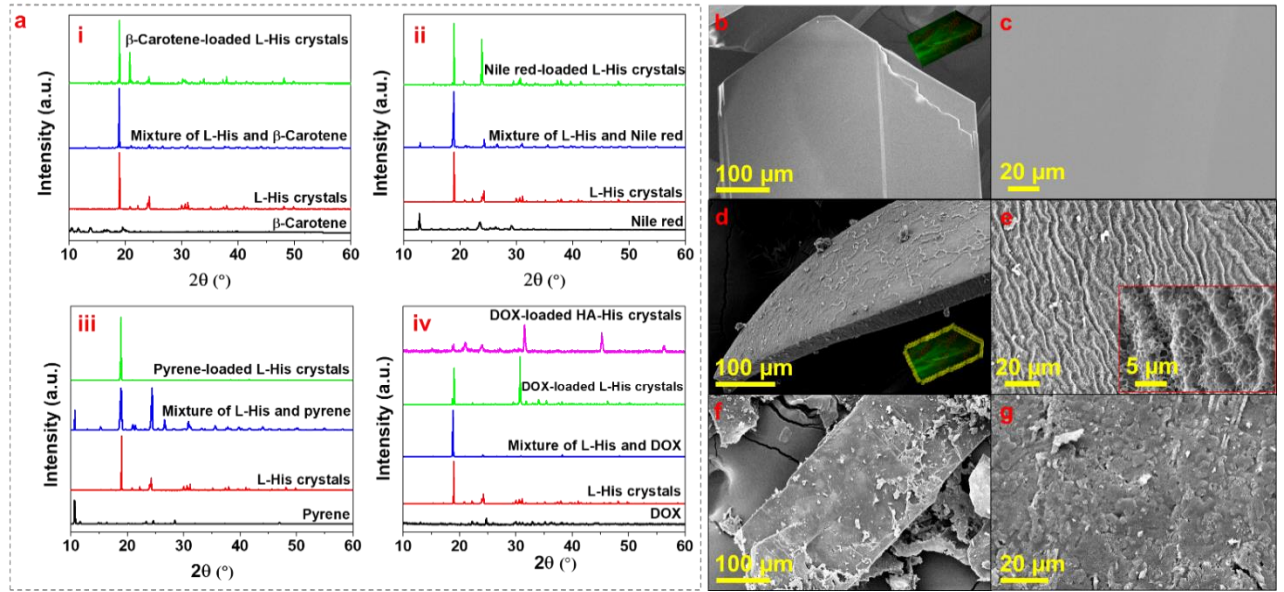


Figure 6.5. a) X-ray diffraction patterns of the L-His crystals with entrapped small molecules (green lines) in comparison with the L-His crystals (red lines), the small molecules (black lines), a mixture of L-His and the small molecules (blue lines), and surface-modified L-His crystals with entrapped small molecules (pink lines) for i) β -carotene, ii) Nile red, iii) pyrene, and iv) DOX. b) SEM images of the L-His crystals before surface modification; c) magnification of b. d) The L-His crystals after chemical surface modification through disulfide bonds with HA; e) magnification of d, with the inset showing a further-magnified image. f) The L-His crystals after surface modification through manual mixing of the crystals with HA solution; g) magnification of f.

We also demonstrate that the surface of these L-His crystals can be chemically modified to make them site-specific for targeted drug delivery to a specific site of action. Here, we modify the surface of the L-His crystals loaded with DOX using hyaluronic acid (HA) (Figure 6.1c). HA is a natural, non-toxic and biodegradable acidic

polysaccharide composed of N-acetylglucosamine and D-glucuronic acid disaccharide units.²⁰³ HA can serve as an active targeting ligand with high binding affinity to cell-membrane-bound CD44 receptors,¹⁸³ which are found on the surface of several malignant tumor cells.²⁰⁴⁻²⁰⁶ We propose to modify L-His crystals with HA to enhance the specificity of the L-His crystals to deliver DOX to tumor cells and decrease the chance of cytotoxicity and the drug's uptake by normal cells. More importantly, HAase, which plays a significant role in tumor growth, invasion, and metastasis, is widely distributed in the acidic tumor matrix and cleaves internal β -N-acetyl-D-glucosamine linkages in the HA.²⁰⁶ HAase is increased in various malignant tumors, including head and neck, colorectal, brain, prostate, bladder, and metastatic breast cancers.²⁰⁷ HA binds to the receptor (CD44) on the surface of the cancer cell and is then cleaved by HAase.²⁰⁷ We hypothesized that this enzyme could be used to hydrolyze HA on the surface of HA-His crystals, allowing the L-His crystals to dissolve in the aqueous matrix and efficiently release the entrapped DOX.

To modify the surface of L-His crystals with HA, we first modified the surface of the L-His crystals with thiolated histidine methyl ester (SH-HME), and then cross-linked the SH-HME with thiolated hyaluronic acid (SH-HA) through the formation of disulfide bonds (Figure 6.1c, see Methods for more details). Figure S6.1 (a) shows the schematic illustration for the synthesis of SH-HA, SH-HME. The comparison between Fourier transform infrared (FTIR) spectra of HA and SH-HA shows a significant decrease of the peak at 1610–1620 cm^{-1} associated with the HA carboxyl groups, confirming the formation of SH-HA (Figure S6.1, b). Figure S6.1 (c) shows the formation of disulfide bonds between SH-HA and SH-HME. The L-His crystals are

smooth before surface modification (SEM images, Figure 6.5b, c). The chemical modification of the L-His crystals through the formation of disulfide bonds between SH-HME and SH-HA forms a uniform layer of HA on the surface of the L-His crystals (Figure 6.5d, e). In contrast, applying HA solution directly to the surface of the L-His crystals does not result in a uniform layer on the crystal (Figure 6.5f, g). Surface modification of the L-His crystals with HA also changes the XRD pattern, showing two dominant peaks at $2\theta \sim 33^\circ$ and 46° (Figure 6.5a, iv, pink line).

We compared the release behaviors of DOX from the HA-His crystals after incubation with and without HAase (Figure 6.6, a-b). Figure 6.6a illustrates that the HA-His crystals start to disintegrate in the presence of HAase after 4 h. *In vitro* release experiments revealed that less than 35% of DOX is released from the HA-His crystals after 72 h in phosphate buffer, whereas 84% of DOX is released during that same time in the presence of 1 U/mL HAase (Figure 6.6b). In the presence of 10 U/mL HAase, the release rate is accelerated and 86% of DOX is released in 40 h (Figure 6.6b). This result indicates that the HA-His crystals incubated with HAase markedly increase the release of DOX. Thus, HA-His crystals can potentially bind to CD44 receptors on the surface of tumor cells, enhancing the cellular uptake, and then release entrapped DOX upon degradation by HAase to the intracellular compartments of tumors, increasing apoptosis of tumor cells (Figure 6.6c).

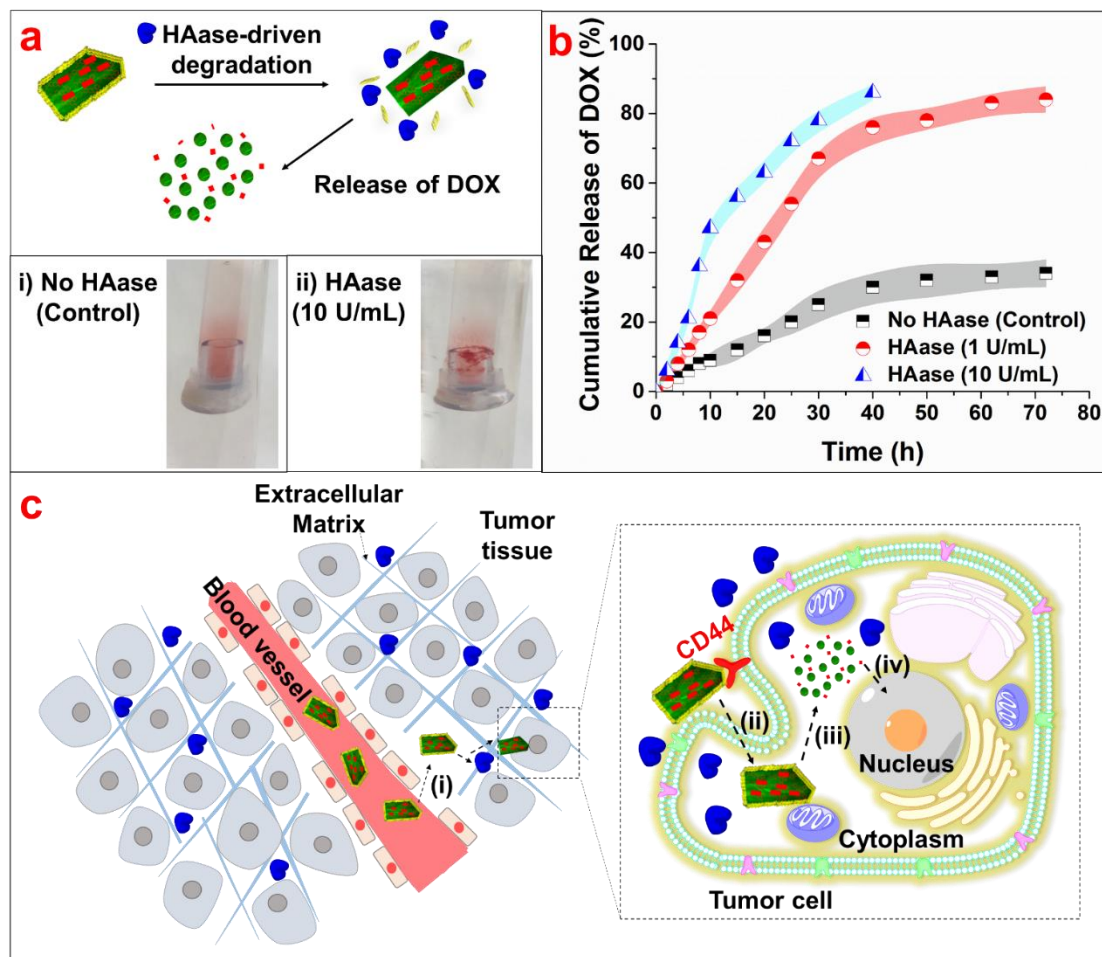


Figure 6.6. Enzymatic degradation of HA-His crystals in the presence of 1 or 10 U/mL HAase at 37 °C. a) Schematic of HA-His crystals that can be degraded by HAase, and digital images of the HA-His crystals after four hours without the presence of HAase (control, i) and in the presence of HAase (ii). b) Cumulative release of DOX from HA-His crystals. c) Schematic of the enhanced delivery of hydrophobic chemotherapeutics by the HA-His crystals for cancer therapy: (i) HA-His crystals accumulate in the tumor; (ii) HA-His crystals are internalized by the CD44 receptors on the tumor cells; iii) HAase leads to the degradation of HA on the crystal surface, dissolving the crystals; and iv) release of the hydrophobic chemotherapeutics over time to cause the tumor cell death.

6.4. CONCLUSION

In this work, we demonstrate the entrapment of hydrophobic small molecules inside the hydrophobic domains of L-His crystals, providing a potential biocompatible platform for protecting hydrophobic drugs. Since the entrapment of hydrophobic small molecules is at the molecular level, the entrapment efficiency is relatively high and possibly depends on the molecular structure of the small molecules. The modification of the L-His crystals at the surface using polymers and/or hydrogels could enable intracellular trafficking and site-specific delivery of hydrophobic therapeutics, providing a drug-delivery system with targeting features. For example, the L-His crystals with HA covalently bonded to their surface and loaded with DOX are able to target tumor cells and control the release of DOX in response to HAase overexpressed in these cells. The composition of the surface can be controlled and tuned for optimization with other enzymes and physiological media. Releasing the entrapped hydrophobic drugs as the HA-His crystals are degraded and dissolved in the aqueous media can also reduce the chance of local toxicity to normal cells due to drug aggregation. The successful entrapment and targeted release of hydrophobic small molecules in HA-His crystals suggests further study is warranted to probe the possible implementation of amino acid crystals in promoting the delivery of hydrophobic therapeutics with low solubility and/or delivery of a combination of hydrophobic drugs to treat multidrug resistance. This strategy helps to address issues related to the poor solubility and low bioavailability of such molecules. These L-His crystals can also be investigated in terms of improving the imaging and tracking of entrapped therapeutic agents due to the crystals' natural

fluorescence properties. However, further research and *in vivo* studies are essential before the potential of HA-His crystals in cancer therapy can become a reality.

6.5. SUPPORTING INFORMATION

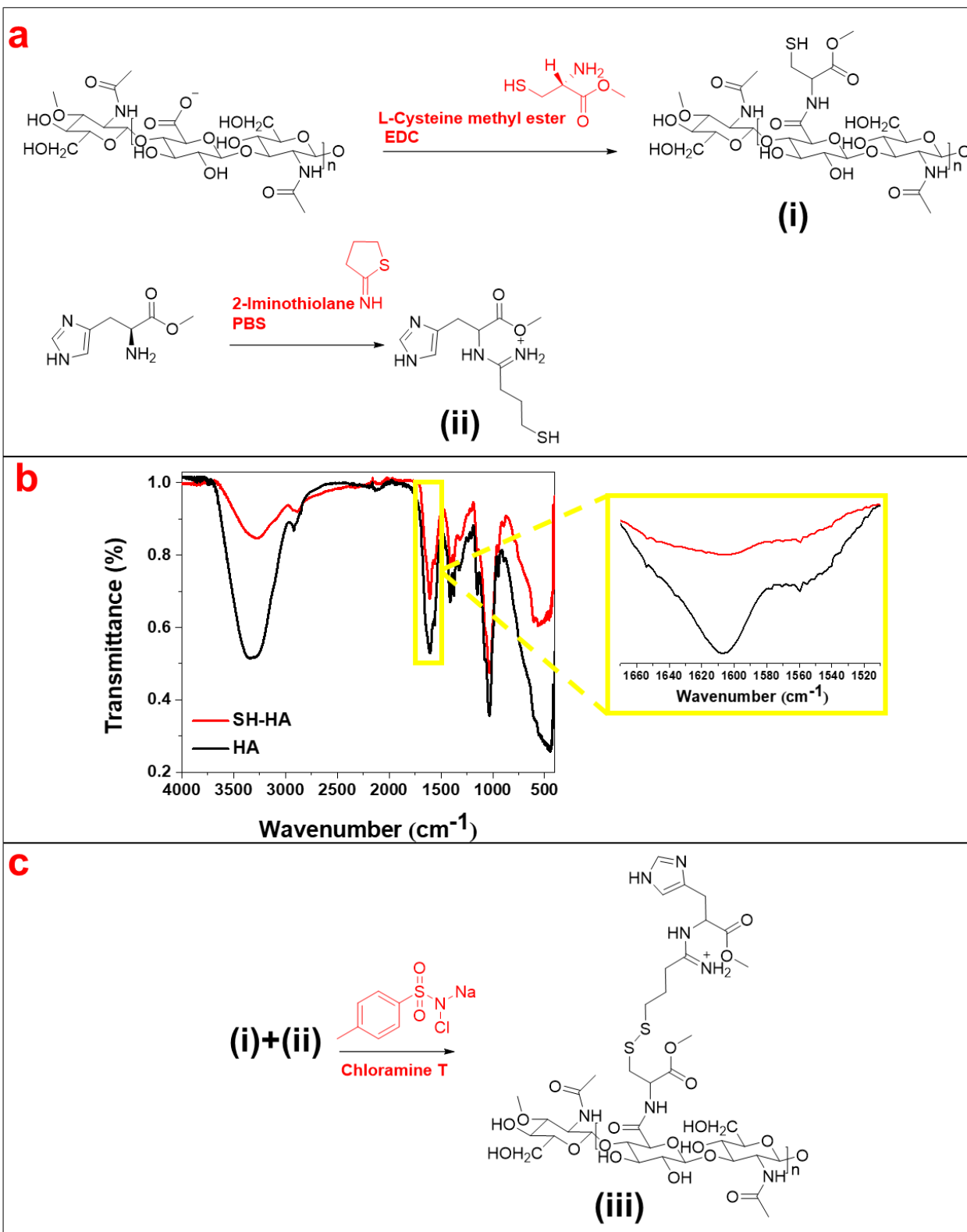


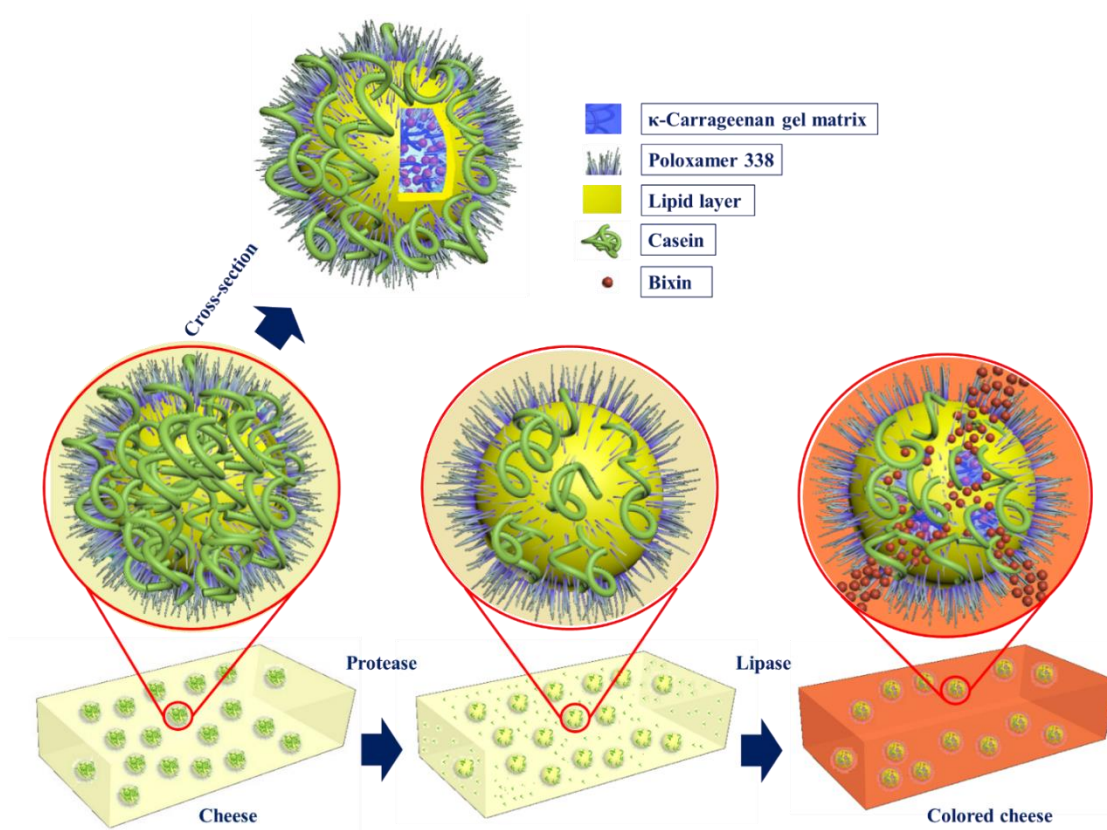
Figure S6.1. a) Schematic illustration for the synthesis of SH-HA (i), and SH-HME (ii). b) The Fourier transform infrared (FTIR) spectra of HA and SH-HA, showing a significant decrease of the peak at 1610–1620 cm^{-1} associated with the HA carboxyl groups, confirming the formation of SH-HA. c) The formation of disulfide bonds between i and ii, and formation of iii.

Contributions

Raheleh Ravanfar wrote the manuscript and performed the experiments with support and advice from Dr. Alireza Abbaspourrad. Dr. Alireza Abbaspourrad supervised the project.

CHAPTER 7

CONTROLLING THE RELEASE FROM ENZYME-RESPONSIVE MICROCAPSULES WITH A SMART NATURAL SHELL¹⁷



ABSTRACT

We design a natural and simple core-shell structured microcapsule, which releases its cargo only when exposed to lipase. The cargo is entrapped inside a gel matrix, which is surrounded by a double layer shell containing an inner solid lipid layer and an outer polymer layer. This outer polymer layer can be designed according to the intended biological system and is responsible for protecting the microcapsule architecture and transporting the cargo to the desired site of action. The lipid layer contains natural ester bonds, which

are digested by lipase, controlling the release of cargo from the microcapsule core. To demonstrate the feasibility of this approach, our model system includes the colorant bixin entrapped inside a κ -carrageenan gel matrix. This core is surrounded by an inner beeswax-palmitic acid layer and an outer casein-poloxamer 338 layer. These fabricated microcapsules are then applied into Cheddar cheese, where they selectively color the cheese matrix.

7.1. INTRODUCTION

Armed with a better understanding of various responsive mechanisms in biological systems, researchers have developed innovative delivery platforms with smart materials that are sensitive to specific stimuli.^{172, 182, 208-211} Application of these platforms demands a biocompatible structure with the ability to communicate with cells, improve the anti-inflammation capability, and prevent the formation of biofilms or fibrosis.²¹²⁻²¹³ Although significant progress has been made in biopolymeric or liposomal encapsulation systems,^{181, 214-219} there are critical limitations in synthesizing biocompatible capsules with highly controllable architectures and release mechanisms in complex biological systems.

Owing to the varied roles that enzymes have in different biological processes, enzyme-associated platform designs have recently become an emerging strategy for controlled delivery and release.²¹³ For example, the incorporation of ester bonds in the structure of the carriers can target esterases for site-specific release.²¹³ However, the incorporation of these enzyme-specific moieties in the platform requires organic synthesis steps, which are usually intricate, expensive, and time-consuming. Consequently, there is opportunity for designing simple, cost-effective platforms that respond to a specific enzyme and actuate a controlled release pattern.

In this study, we present a simple microcapsule design containing an enzymatically degradable shell, which provides the release of encapsulated compounds in response to lipase. This microcapsule can also transport its cargo to the desired region of the biological system without being affected by environmental conditions. We fabricate the microcapsules using a triple oil-in-water-in-oil-in-water (o/w/o/w) microemulsion. The microcapsule core contains oil-soluble cargo in a κ -carrageenan gel matrix. Meanwhile, the microcapsule shell contains an inner lipid layer and an outer polymer layer. Using natural lipids containing ester bonds in the lipid layer of the microcapsule shell, we fabricate microcapsules that specifically release their content in the presence of lipase. The polymer layer is engineered according to the biochemical environment of the biological system and guarantees the transportation and distribution of microcapsules to their desired site. This delivery platform could be used in different industrial and biological applications.

To demonstrate the performance of these microcapsules, we select Cheddar cheese as a model system. Lipases are mainly found in cheese curds during cheese ripening and are responsible for producing short-chain fatty acids which contribute to the flavor. Thus, we apply this platform to selectively deliver the color to the cheese curd by lipase-triggered release, leaving the whey colorless. To achieve this, oil-soluble bixin is incorporated into a κ -carrageenan gel matrix. The lipid layer of the microcapsule shell contains beeswax-palmitic acid. The ester bonds in this lipid layer are broken by lipase during cheese ripening and color is released from the microcapsules to the cheese matrix. The polymer layer consists of casein and poloxamer 338, which is vulnerable to protease and can be disintegrated by rennet during the coagulation step of the cheese-

making process. The presence of casein in the polymer layer also guarantees the transport of microcapsules to the cheese curd along with the other casein molecules of the milk. Thus, the encapsulated color is delivered primarily to the cheese curd and the recovered whey proteins remain white. Since the current industrial method to eliminate the yellow color of Cheddar cheese whey is using the oxidizing agents, such as hydrogen peroxide, obtaining the white whey through this enzyme-responsive microcapsules approach is of significant interest to the food industry. Exploiting this approach, we recover the white whey without using any oxidizing agents and enhance the nutritive value and flavors in the white whey.

7.2. MATERIALS AND METHODS

7.2.1. Materials

Oil-soluble bixin was provided by Chr. Hansen Laboratory A/S, Denmark. Beeswax was donated by Strahl & Pitsch Inc. (West Babylon, NY, US). Soy lecithin was donated by ADM (Decatur, IL, US). κ -Carrageenan was provided by Tic Gums, Inc. (Belcam, MD, US). Lipase (~150,000 FIP/g) was donated by Mak Wood Inc. (Grafton, WI, US). Triton X-100 was purchased from Fisher Scientific (Nepean, ON, Canada). Sodium caseinate and Poloxamer 338 (Pluronic® F108) were purchased from Sigma-Aldrich (St. Louis, MO, US).

7.2.2. Preparation of color-loaded microcapsules

Microcapsules were prepared using a microemulsion dilution method. Different formulations were examined to prepare the microcapsules (Table S7.1), and the best formulation was selected. The best formulation was prepared in the following manner: briefly, oil-soluble bixin (50%, w/w) was dispersed in an aqueous solution of κ -carrageenan (1%, w/w) and Triton X-100 (10%) under stirring to prepare an oil in water (o/w) single emulsion. This single emulsion was then added dropwise to the lipid oil phase at 64 °C containing a mixture of palmitic acid, beeswax, and soy lecithin (2:1:0.1) under vigorous stirring to prepare an o/w/o microemulsion. This o/w/o double emulsion was dispersed in a secondary aqueous solution (15:100, double emulsion : secondary aqueous solution), containing sodium caseinate (3.3%, w/w) and poloxamer 338 (1%, w/w) using a high-shear homogenizer (VWR 200 Homogenizer Unit, Randor, PA, USA) at 15000 rpm for 5 minutes in an ice bath (3 °C). This o/w/o/w triple microemulsion was spray-dried at an outlet temperature of 50 °C, inlet temperature of 160 °C, and flow rate of 3 L/h (Labplant Spray Dryer SD-Basic, Labplant, UK, Ltd. North Yorkshire, UK). The lipid phase was solidified at 3 °C and form a lipid layer. Following the spray-drying step, a polymer layer of casein-poloxamer was formed on top of the lipid layer (Figure S7.1).

7.2.3. Characterization of microcapsules

Optical microscopy

Optical images were obtained using an inverted optical microscope (DMIL LED, Leica) connected to a fast camera (MicroLab 3a10, Vision Research).

Scanning electron microscopy

Scanning electron microscopy (SEM) was conducted to characterize the surface morphology of the microcapsules. The samples were mounted on alumina stubs using double adhesive tape and coated with gold for 30 seconds. Then, the samples were observed using a JCM-6000 Benchtop Scanning Electron Microscope, software version 2.4 (JEOL Technics Ltd., Tokyo, Japan).

Cryo-scanning electron microscopy (Cryo-SEM)

Using cryo-SEM images, the structure of the microcapsules was assessed. Cryo-SEM experiments were performed using a Quorum P3010 system (Quorum Technologies, Newhaven, UK). The samples were plunge-frozen in liquid nitrogen, transferred under vacuum to the P3010, and coated with gold-palladium for 30 seconds. Samples were maintained at -165 °C in the preparation chamber. The samples were transferred to the focused ion beam (FIB) to take images at -165 °C.

Zeta-potential

The zeta-potential was determined with a NanoZS90 zeta-sizer (Malvern 142 Instrument Ltd., UK) with a He/Ne laser ($\lambda = 633$ nm) at a fixed scattering angle of 90° at 25 (± 0.1). The zeta potential values were automatically calculated from the

electrophoretic mobility based on the Smouluchowski model.²²⁰ All measurements were performed in triplicate and reported as averages thereof.

Size

Images of the samples were obtained using an inverted optical microscope (DMIL LED, Leica) and analyzed with ImageJ (Version 1.4.3.67) to measure the average particle size.

X-ray diffraction

X-ray diffraction (XRD) measurements were performed using a Bruker D8 Advance ECO powder diffractometer (MA, USA). The generator was operated at 40 kV and 30 mA (Cu K α radiation). Samples were scanned at room temperature from $2\theta = 2^\circ$ to 45° under continuous scanning in 0.02 steps of $2\theta \text{ min}^{-1}$.

Encapsulation efficiency and release kinetics

Microcapsules were centrifuged (10 minutes, 4 °C, 17000g) and the non-encapsulated free color was measured in the supernatant. The pellet was dissolved in 1 mL acetone, vortexed, centrifuged (10 minutes, 4 °C, 17000g) and the encapsulated color was measured using UV-VIS spectrophotometry (UV-Vis Spectrophotometer UV-2600, Shimadzu Scientific Instruments/ Marlborough, Massachusetts–USA) at a wavelength of 452 nm for bixin. The standard bixin curve was obtained through the color solutions

in a concentration gradient, and used to convert absorbance to concentration. The encapsulation efficiency (EE%) was calculated using the following equation:

$$\text{Encapsulation efficiency (\%)} = \frac{\text{The color in the pellet}}{\text{The color in the pellet} + \text{The color in the supernatant}} * 100$$

In addition, the release of color from the microcapsules was studied in citrate-phosphate buffer with a pH of 6.0, containing lipase (100 mg/ml), protease (50 mg/ml), a combination of lipase (100 mg/ml) and protease (50 mg/ml), and no enzyme (control) at a temperature of 26 °C. The released color from the microcapsules was measured in the supernatant using UV-VIS spectrophotometry at different time intervals (0, 3, 8, and 14 days).

7.2.4. Employing the microcapsules in the Cheddar cheese making process

Simulation of Cheddar cheese making process

The microcapsules (0.01 g) were added to whole milk (20 ml), and the pH was adjusted to 4.6 to precipitate casein. Then, the system was heated to 60 °C for 30 minutes and centrifuged at 15000g to separate the casein curd from whey proteins in the supernatant. The supernatant was freeze-dried to obtain the white whey, and the curd was transferred to the wells of a 24-well microplate to simulate the ripening step. To simulate the ripening process, the pH of the curd was adjusted to 6.0, then lipase (50 mg) was added to the curd. The curd was then incubated at 26 °C for 14 days.

Color measurements of the colored cheese

The color of the Cheddar cheese samples was measured using a Chroma Meter CR-400 (Konica Minolta Sensing Inc., Japan) and reported in terms of lightness (L^*), red–green (a^*), and blue–yellow (b^*).⁷⁷

Fourier Transform Infrared Spectroscopy of the colored cheese

The Fourier transform infrared spectroscopy (FTIR) spectra of the microcapsules in the Cheddar cheese were investigated in the region from 4000 to 400 cm^{-1} (120 scans, resolution of 2 cm^{-1}) using a IRAffinity-1S FTIR spectrophotometer (Shimadzu Scientific Instruments/ Marlborough, Massachusetts-USA).

7.2.5. Statistical analysis

Data were subjected to analysis of variance (ANOVA) using SPSS software package version 15.0 for Windows. All measurements were performed in triplicate. Mean comparisons were performed using the Post Hoc Multiple Comparison Duncan test to examine if differences were significant at $P < 0.05$. A two-sample t -test was used to compare the samples that contained microcapsules with the samples without microcapsules (control) at 95% confidence interval using Microsoft Excel.

7.3. RESULTS AND DISCUSSION

We design a novel enzymatically-triggered microcapsule with a core-shell structure (Fig. 7.1). The microcapsule shell contains both a lipid layer (composed of beeswax, palmitic acid, and lecithin) and a polymer layer (made of casein and poloxamer 338) (Figure 7.1). The lipid layer contains ester bonds, which is disintegrated in response to lipase. The lipid layer can be designed using lipids with different numbers of ester bonds and hydrocarbon chain lengths to control their availability to lipase in different biological systems. The polymer layer is engineered according to the environment of the biological system and guarantees the transportation and distribution of microcapsules to the desired site or step in a biological system. In this work, the microcapsule core contains a single emulsion of a lipophilic compound – bixin as our model system – in an aqueous solution of κ -carrageenan (Figure 7.1). κ -carrageenan contains ester sulfate groups and 3,6-anhydrogalactose²²¹ and forms a strong thermo-reversible gel through a coil-helix conformational transition, which may be accompanied by aggregative interactions between the ordered molecules, leading to the formation of an infinite biopolymeric network.²²² The incorporation of κ -carrageenan in the microcapsule core provides a gel matrix at ambient temperature, which prevents the movement of the entrapped bixin molecules due to the high gel viscosity.

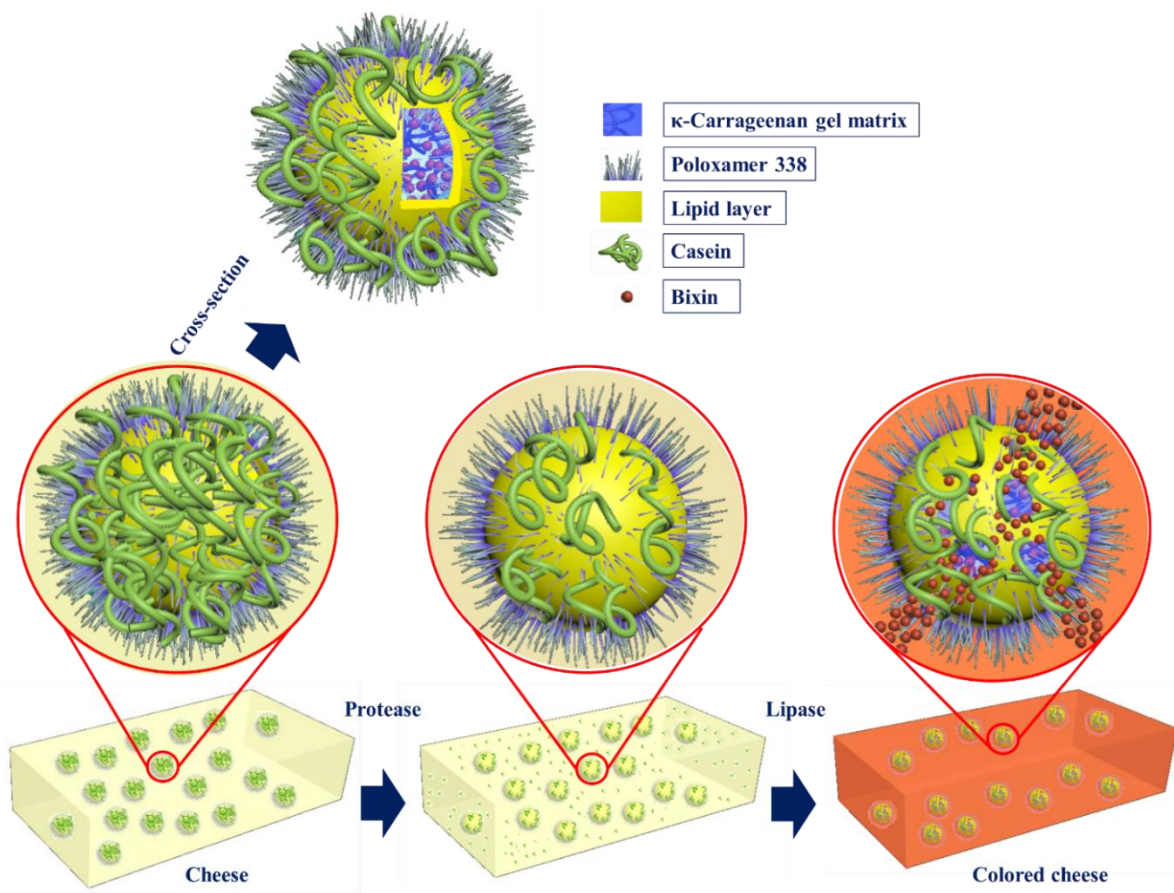


Figure 7.1. Schematic of the enzymatically-triggered microcapsules and their controlled-release by lipase.

Accordingly, we prepare a triple $o_1/w_1/o_2/w_2$ microemulsion to achieve this architecture, in which o_1 is the oil solution of bixin, w_1 is κ -carrageenan, o_2 is palmitic acid, beeswax and lecithin, and w_2 is casein and poloxamer 338. The lipid phase is solidified at ambient temperature and form the lipid layer of the microcapsule shell (Figure 7.1). The casein and poloxamer around this lipid layer form a polymer layer on top of the lipid layer (Figure 7.1) after the spray-drying step. During spray-drying, the outlet temperature is set to 50 °C (below the melting point of beeswax and palmitic acid) to avoid probable bixin leakage from the microcapsules. Therefore, the microcapsule

lipid layer remains solid and intact during the spray-drying process, while a layer of casein and poloxamer deposits on top of the lipid layer.

In this study, lipid layer positioning on the amorphous gel matrix results in a high encapsulation efficiency ($81.8 \pm 1.4\%$) of the microcapsules, as well as protection of the microcapsule architecture against undesired conditions, such as changes in pH, temperature, and ionic strength. Beeswax contains ester bonds in its molecular structure,²²³⁻²²⁴ and these ester bonds are broken down by lipase²²⁵ into very long chain fatty alcohols and fatty acids. These long chain fatty alcohols decrease plasma cholesterol in humans.²²⁵ The major component of beeswax is triacontanyl palmitate,²²⁶ which breaks down to palmitic acid and triacontanol by lipase (Figure S7.2).

Studies suggest that triacontanol decreases low-density lipoprotein (LDL) cholesterol levels and raises high-density lipoprotein cholesterol levels.²²⁷ Thus, using beeswax in the microcapsule shell does not interfere with the safety of the biological system. Besides improving the nutritional value of the biological system, the degradation of beeswax by lipase loosens the microcapsule shell structure and releases its cargo to the system. Recent studies report the use of short peptide sequences as linkers in the structure of liposome, which are cleaved by matrix metalloproteinases.²²⁸⁻²²⁹ Similarly, porous silica nanoparticles²³⁰ or liposomes²³¹ with a coating of protease-sensitive polymer are used for triggered release. In this study, casein and poloxamer 338 form a polymer layer of the microcapsule shell after the spray-drying step.

The rationale behind emulsifying bixin (oil) in water containing k-carrageenan to prepare the initial single emulsion was to use k-carrageenan as a gelling and protecting

agent, which prevents the coalescence and merging of bixin droplets (oil) with the third layer (palmitic acid and beeswax) upon emulsification. Therefore, upon injecting the heated (above the melting point of the wax and the gelling point of the carrageenan) double emulsion o/w/o (bixin/ k-carrageenan/ beeswax and palmitic acid) into the water continuous phase at 3 °C and applying 15000 rpm, the o/w/o double emulsion breaks up into smaller droplets in a short time, and concurrently the internal phases become solid. This means that within the first couple of seconds k-carrageenan forms a gel and beeswax becomes solid, which prevents merging of the internal bixin oil with the beeswax, and therefore this strategy provides a method to obtain a triple o/w/o/w emulsion with a high yield.

Almost 95% of the resulting microcapsules are in the size range of 3–9 μm with a zeta potential of -6.8 ± 0.7 mV, which are physicochemically stable in the biological system (Figure S7.3). We next investigate the XRD spectra of the microcapsules and microcapsule shell materials (Figure 7.2). Pure palmitic acid and beeswax exhibit crystalline structures and sharp peaks, while lecithin shows a broad peak at a lower 2θ value. However, the peaks for pure palmitic acid, beeswax, and lecithin do not superimpose completely with those for microcapsules containing a mixture of these materials in their shell. External factors, such as temperature, pressure, and impurity, can strongly influence crystal structure.²³² Therefore, the microcapsules may have a different polymorphism compared with the bulk materials. Moreover, surfactant can also influence the crystal behavior of lipids.²³³ The peaks at $2\theta = 22^\circ$ and 24° , corresponding to both palmitic acid and beeswax, the peak at $2\theta = 18^\circ$, corresponding to lecithin, and the peak by long spacing at $2\theta = 7^\circ$, corresponding to pure palmitic acid,

are superimposed with those of the microcapsules. Beeswax molecules can be incorporated into the crystal lattice of palmitic acid in the microcapsule shell containing ~67% palmitic acid. The microcapsules feature a lower crystallinity degree than pure palmitic acid, beeswax, and lecithin. The reduction in the proportion of crystalline to amorphous phases in the microcapsule shell implies a greater amorphous phase content in the microcapsules' shell, which can be positioned on top of the amorphous κ -carrageenan gel matrix in the microcapsule core without any difficulty (Figure 7.2).

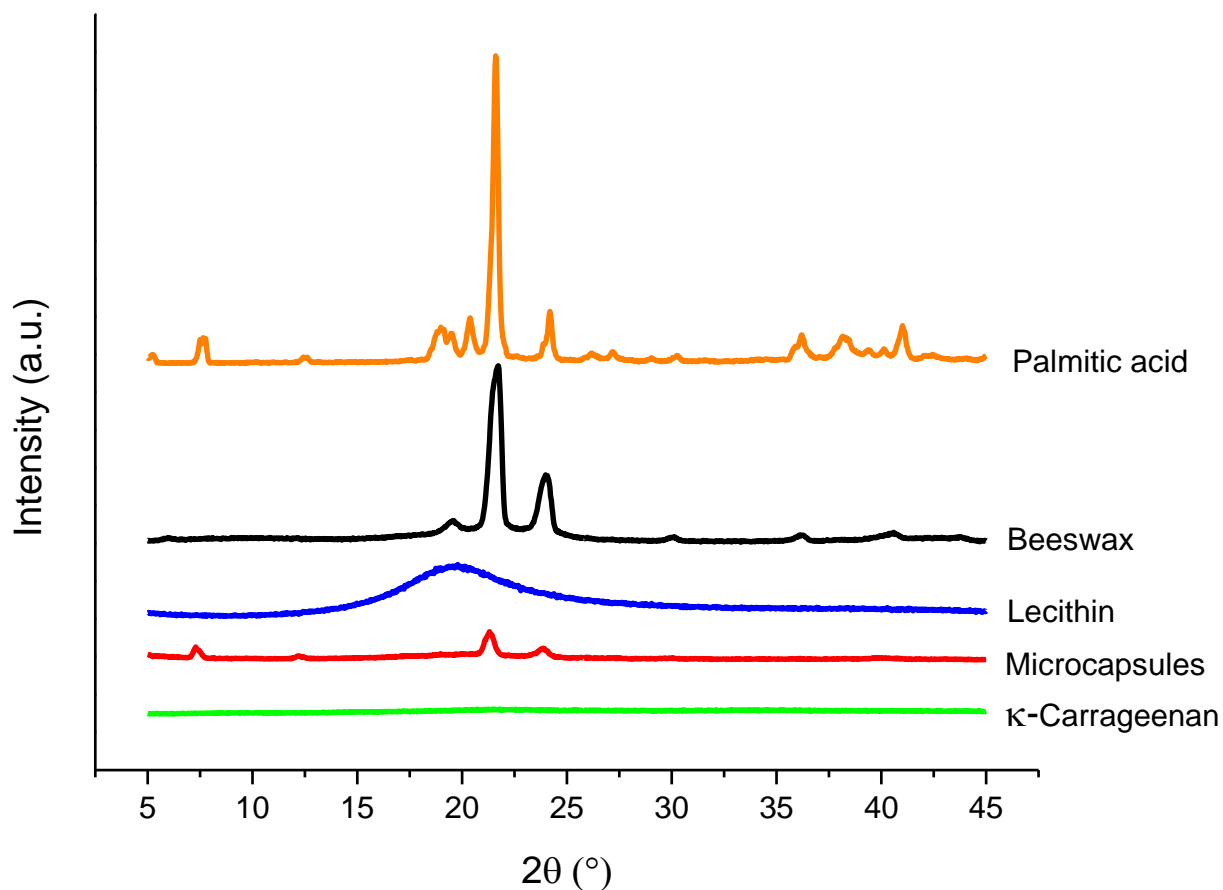


Figure 7.2. X-ray diffraction spectra of the microcapsules and shell materials.

The microcapsules observed using a light microscope exhibit a spherical shape with a lighter shade in the aqueous core and a darker shade in the shell (Figure 7.3a), confirming the core-shell structure of the microcapsules. The SEM images of the microcapsules reveal the non-smooth surface of the spherical microcapsules (Figures 7.3b and 7.3c). This non-smooth and non-uniform surface of the microcapsules is formed due to rapid cooling of the lipid shell, composed of palmitic acid and beeswax, during the homogenization step in the ice-bath. This rapid solidification of the lipids in the microcapsule shell can be ascribed to roughness observed on the surface of the microcapsules, as well as to the large size and high polydispersity of the microcapsules. Other studies have also shown that time and temperature are two main parameters that determine the shape and smoothness of the particles.²³⁴ Figures 7.3d, e, & f show the cryo-SEM images of the microcapsules cross-sectioned using a focused ion beam. This structure is attributed to the method that we use to prepare the microcapsules. The microcapsule shell with a thickness of $\sim 1 \mu\text{m}$ surrounds the core of the microcapsules. The swirling patterns observed in the cross-section of the microcapsule core demonstrates the presence of the aqueous gel matrix of κ -carrageenan, which is structurally looser than the solid lipid shell and becomes frozen quickly by liquid nitrogen during the sample preparation for cryo-SEM imaging. The presence of small, dark droplets in this core structure shows the bixin entrapped in the κ -carrageenan gel matrix. Additional images of the microcapsules can be found in the Supporting Information (Figure S7.4).

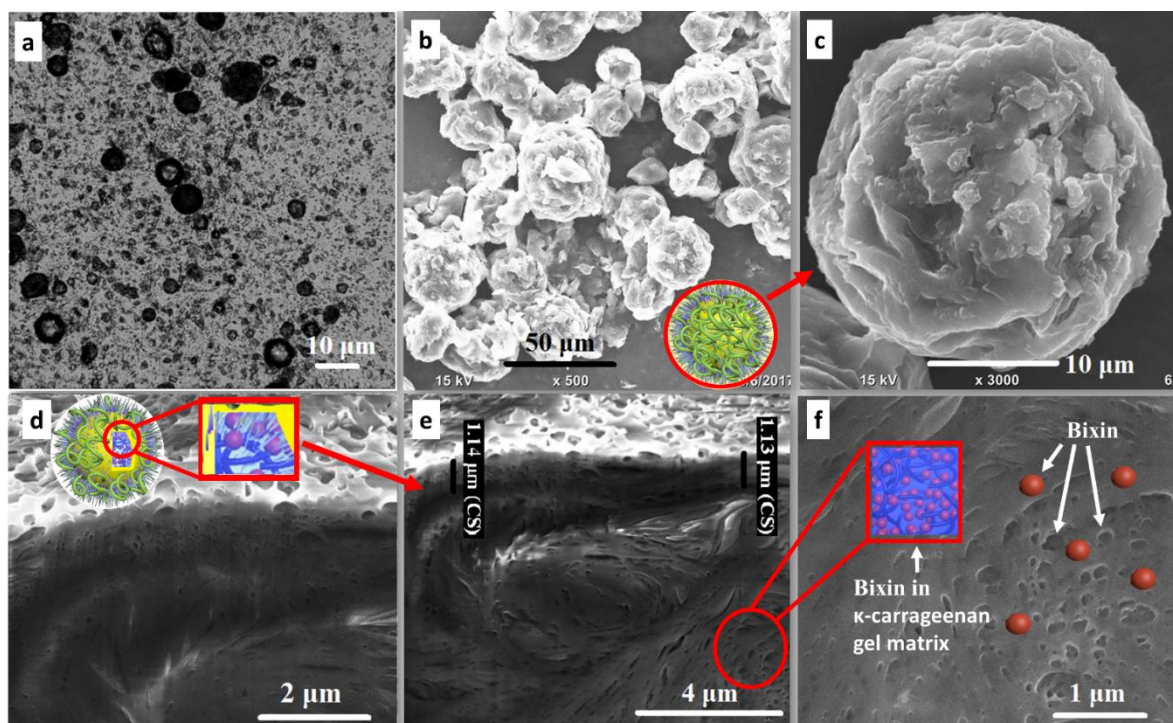


Figure 7.3. Microscopy images of the microcapsules taken using (a) light microscopy and (b, & c) SEM images of microcapsules;(d–f) Cryo-SEM of microcapsule cross-sectioned by focused ion beam.

Figure 7.4 shows the release of bixin from the microcapsules when exposed to lipase and protease enzymes. Following exposure, the results show a significant increase in bixin release from the microcapsules exposed to enzymes in comparison with the control (no enzymes; Figure 7.4a). The microcapsules exposed to lipase, and a combination of lipase and protease show significantly higher release in comparison with the microcapsules exposed to protease. However, there is no significant difference between the release of bixin from the microcapsules exposed to lipase and those exposed to the combination of lipase and protease. This result indicates the key role of lipase in the

disintegration of the microcapsule shell and the resulting bixin release. The release (%) of bixin from the control microcapsules increases over time, while the release (%) from the microcapsules exposed to enzymes shows a different pattern (Figure 7.4b). In the first three days of storage, the release (%) from the microcapsules exposed to the combination of lipase and protease is more than the release (%) from the microcapsules exposed to only lipase and only protease, respectively. Between the third to eighth days of storage, however, the release (%) from the microcapsules exposed to enzymes decreases. In the time between the eighth to fourteenth days of storage, the release (%) for the microcapsules exposed to enzymes increases again (Figure 7.4b). Thus, the enzymes change the profile of bixin release from the microcapsules and accelerate the release in the first three days of storage (Figure 7.4b). A study reports an increase in the released cargo from protease-responsive colloidal mesoporous silica shortly after the addition of trypsin.²³⁵ This system is used to close the pore system of colloidal mesoporous silica with the avidin–biotin system, and to release the loaded molecules subsequently by enzymatic hydrolysis of the caps.²³⁵

The release kinetic of the microcapsules can be controlled by internal phase composition, the solid lipid layer composition and the thickness of lipid or polymer layer. For example, we can increase the ratio of the beeswax in the lipid layer to delay the hydrolysis of the lipid layer by lipase. In addition, we can decrease the thickness of the polymer layer (casein) to hasten the degradation of this layer by protease.

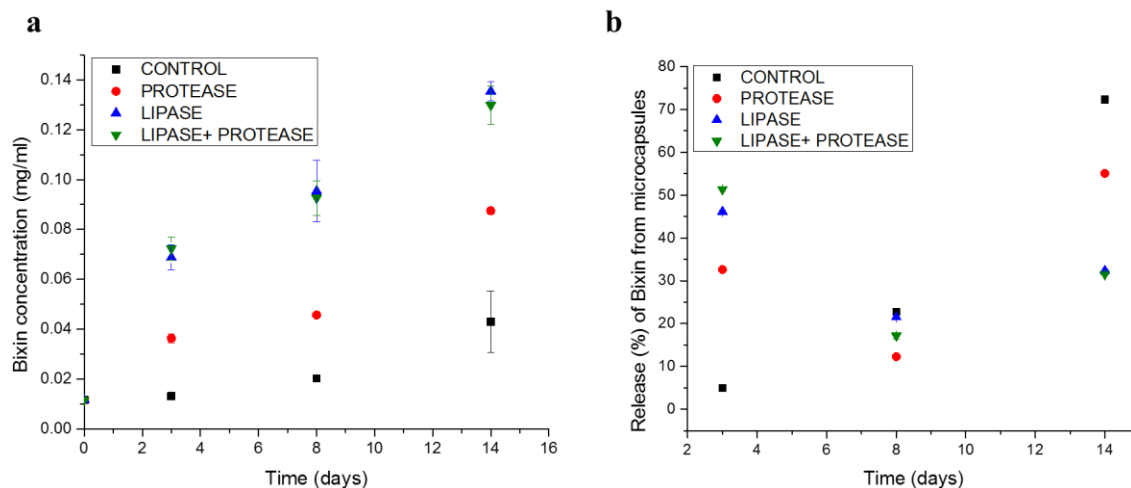


Figure 7.4. Bixin release patterns from the microcapsules when exposed to lipase and protease over 14 days. (a) Bixin concentration (mg/ml) in the medium. (b) Release (%) of bixin from the microcapsules.

This microcapsule design can be applied in the Cheddar cheese-making process to selectively color the cheese curd matrix. Using this platform, we obtain white whey from the Cheddar cheese making process without the addition of external bleaching agents (Figure 7.5). The microcapsules are not affected by the alteration of temperature, ionic strength, or pH of the cheese during the process, and deliver the colorant to the cheese ripening step (Figure 7.5). The presence of casein in the polymer layer of the microcapsule shell helps the microcapsules to be coagulated with the other casein molecules in the milk during the coagulation step of cheese making process (Figure 7.5).

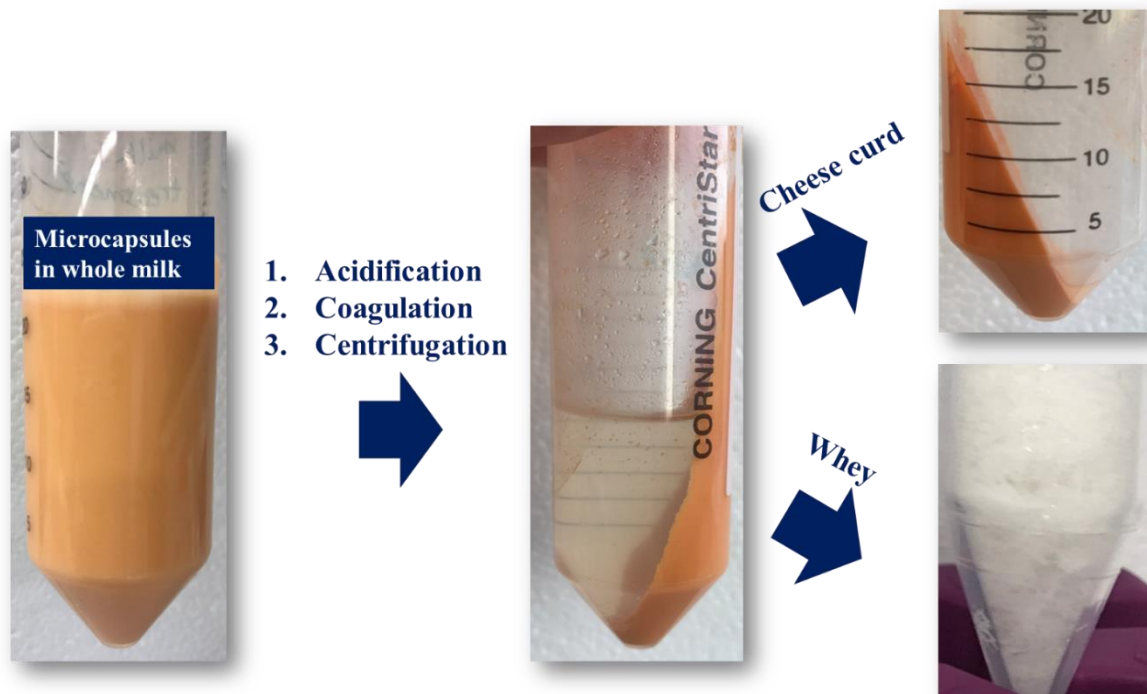


Figure 7.5. Simulation of the Cheddar cheese-making process for whole milk containing the enzymatically-triggered microcapsules.

The casein layer of the microcapsules is degraded through the cheese-making process by endogenous or exogenous proteases in the system, bringing the lipid layer of the microcapsule to the interface, as the microcapsules reach the cheese ripening step. The casein may also increase the yield of the Cheddar cheese, because it is coagulated in the curd along with the other casein molecules. Therefore, microcapsules do not enter the whey, and the whey stays colorless. The microcapsules localized in the cheese curd need a release mechanism to color the cheese curd selectively. We benefit from the ripening step as a turning point of the cheese-making process, in which the immature cheese turns to a matured and flavored cheese. One of the main flavor forming pathways in cheese during ripening involves lipolysis by lipases. These lipases can originate from milk, the

starter lactic acid bacteria, non-starter lactic acid bacteria, and exogenous enzymes.²³⁶ Studies show that the addition of phospholipase to milk prior to cheese manufacturing enhances lipolysis and improves the cheese flavor.²³⁷

The lipid layer of the microcapsule shell is specifically broken down by these endogenous and exogenous lipases during cheese ripening (Figure 7.1) and selectively colors the cheese matrix. To simulate the cheese making-process, we add the microcapsules to whole milk. Figure 7.5 shows the results of this simulated cheese making process for whole milk containing microcapsules. The components of the microcapsule shell and the density of the microcapsules are responsible for directing the microcapsules just to the curd. Supporting information (Table S7.1) shows the other formulations of the microcapsules that we tested, containing casein in the microcapsule shell. Although these other formulations contain casein, they are not able to partition into the curd. Instead, they float on the surface of the whey supernatant (Figure S7.5).

The best formulation for our color partitioning uses palmitic acid and beeswax (2:1) as the lipid layer of the microcapsule shell, as well as casein and poloxamer 338 in the protein-polymer layer. We also simulate the cheese-ripening step by adjusting the pH of the curd to 6.0, which is similar to the pH of Cheddar cheese just before ripening step. We add the lipase to the curd and incubate it at 26 °C for 14 days, and investigate the effect of lipase on the microcapsules and the release of color to the curd. Supporting information (Figure S7.6) shows the curd with lipase in comparison to the curd without lipase after 14 days incubation. The curd without lipase shows the microcapsules coagulated and creamed up on the surface of the curd, because the microcapsules are not broken by lipase. The curd with lipase, however, does not show any sign of the

microcapsules creaming, because the lipase breaks down the shell and releases the color uniformly to the curd.

Figure 7.6 shows the FTIR spectra for the curd with and without lipase after one day incubation at 26 °C. There are two peaks in the region between 1000 and 1300 cm^{-1} which are indicative of C-O bonds of esters. Both of these peaks show a lower intensity for the microcapsules triggered with lipase in comparison to the control (without lipase). This result proves the breakdown of ester bonds by lipase in the microcapsule shells. In addition, the peaks in the region between 1735 and 1750 cm^{-1} are diagnostic peaks for the carbonyl group of esters. The results show a lower intensity of the peaks at this region for the microcapsules triggered with lipase. The peaks in the region between 1705 and 1720 cm^{-1} , however, show a higher intensity in the microcapsules triggered by lipase in comparison to the control. The decrease in the carbonyl group of esters and increase in the carbonyl group of carboxylic acids confirm de-esterification of the beeswax in the microcapsule shells by lipase and the formation of carboxylic acid in the curd.

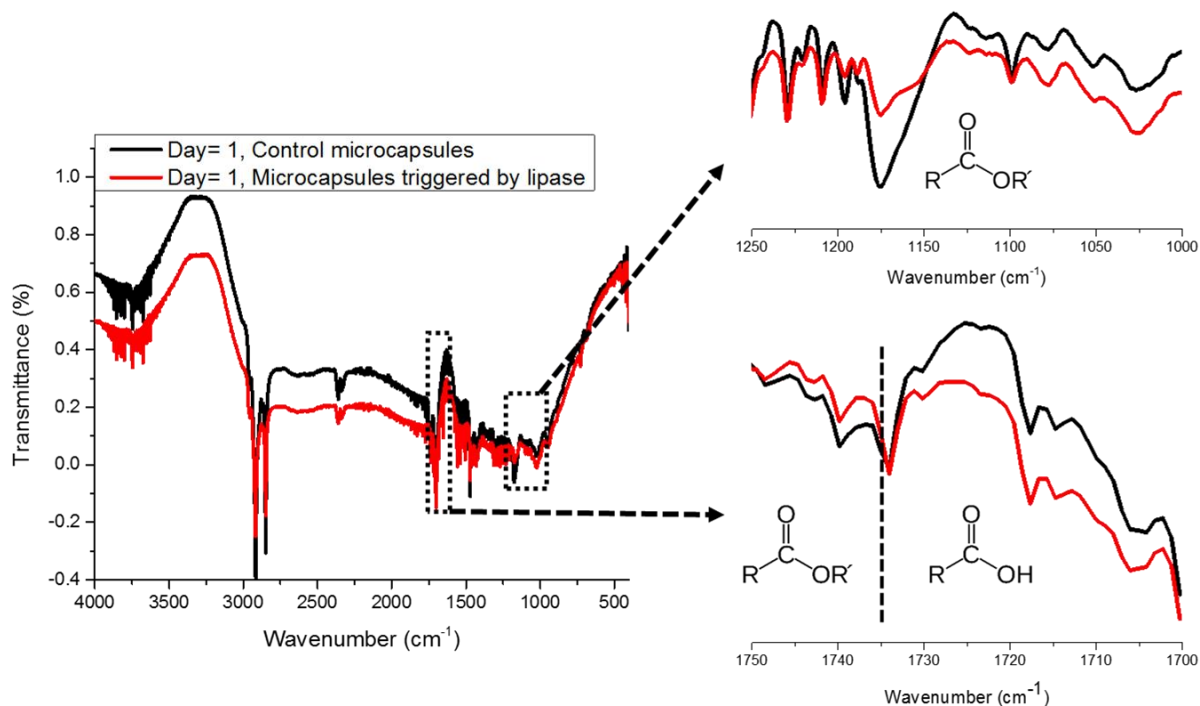


Figure 7.6. FTIR spectra of the cheese curd with and without lipase after one day incubation at 26 °C.

The major component of beeswax is triacontanyl palmitate, a wax ester, which during the de-esterification reaction by lipase breaks down to long hydrocarbon chain alcohol and acid (Figure S7.2). These are not volatile and do not interfere with the cheese flavor. Since breakdown of ester bonds in the microcapsules' shell structure loosens the shell, the entrapped bixin is released from the microcapsules and colors the curd selectively and uniformly. Therefore, we expect to see an increase in the redness of the curds after 14 days incubation. Table 7.1 shows the L^* , a^* , and b^* values of the cheese curd with lipase-triggered microcapsules. The lightness of the curd decreased significantly, while the redness of the curd increased significantly over the 14-day incubation period at 26

°C. This shows that the color intensity increases in the curd containing lipase-triggered microcapsules during ripening.

Table 7.1. L*, a*, and b* values for the cheese curd containing lipase-triggered microcapsules at 26 °C.

Day(s)	L*	a*	b*
1	54.92+ 6.27 ^a	23.20+ 0.79 ^a	40.72+ 8.40 ^a
3	47.03+ 2.31 ^b	23.51+ 0.41 ^b	43.39+ 4.65 ^a
7	46.99+ 1.01 ^c	25.79+ 1.94 ^c	43.90+ 4.17 ^a
14	41.37+ 7.41 ^d	26.82+ 1.93 ^d	43.76+ 3.37 ^a

Equal lower case in the same column does not differ statistically at a 5% level by the *t*-test.

7.4. CONCLUSIONS

An innovative microencapsulation design with an enzymatically controlled release is demonstrated, providing a controlled-release platform for the targeted delivery and release of color. We present this microcapsule design as an alternative method to isolate white whey from the Cheddar cheese-making process without the addition of external bleaching agents. The microcapsule shells are broken down during cheese ripening by lipases in the cheese curd and are shown to release the color evenly throughout the curd. The presence of casein, in combination with the other components in microcapsule

architecture, directs the microcapsules to partition into the cheese curd and prevents them from being distributed into the whey.

In this work, the microcapsule shell is designed using compounds that naturally contain ester bonds. In future applications, this design could incorporate other compounds that are artificially modified to contain ester bonds. Thus, the composition of the shell is controllable and tunable, and can be optimized²³⁸ to use with other enzymes in other food systems or physiological media.

Additionally, this platform can be modified for further applications, such as targeted delivery of hydrophobic drugs. This enzyme-responsive platform can reduce the interference of lipase function on the oral bioavailability of hydrophobic drugs. For instance, increasing the beeswax ratio in the lipid layer of the microcapsule shell can guarantee the specificity of the cargo release, mostly in the presence of lipase. The lipase-degradable lipid layer of the microcapsule shell can reduce the inherent limitations of slow and incomplete dissolution of poorly water soluble drugs and facilitate the formation of solubilized fragments from which absorption may occur. If such methodologies and platforms can be developed, it may then be possible to formulate bio-responsive platforms that offer substantial bioavailability advantages in a commercially relevant manner.

7.5. SUPPORTING INFORMATION

Table S7.1. Different formulations for microcapsules preparation

Formulation No.	Core oil phase	O/W Surfactant	Aqueous phase	Oil phase	Aqueous phase	Surfactant
1	Bixin	-	-	Beeswax	Casein/starch/chitosan	-
2	Bixin	Triton X-100	κ -Carrageenan	Beeswax	Casein/poloxamer 338	Soy lecithin
3	Bixin	Triton X-100	κ -Carrageenan	Carnauba wax	Casein/poloxamer 338	Soy lecithin
4	Bixin	Triton X-100	κ -Carrageenan	Beeswax/palmitic acid	Casein	Soy lecithin
5	Bixin	Triton X-100	κ -Carrageenan	Beeswax/palmitic acid	Casein/poloxamer 338	Soy lecithin

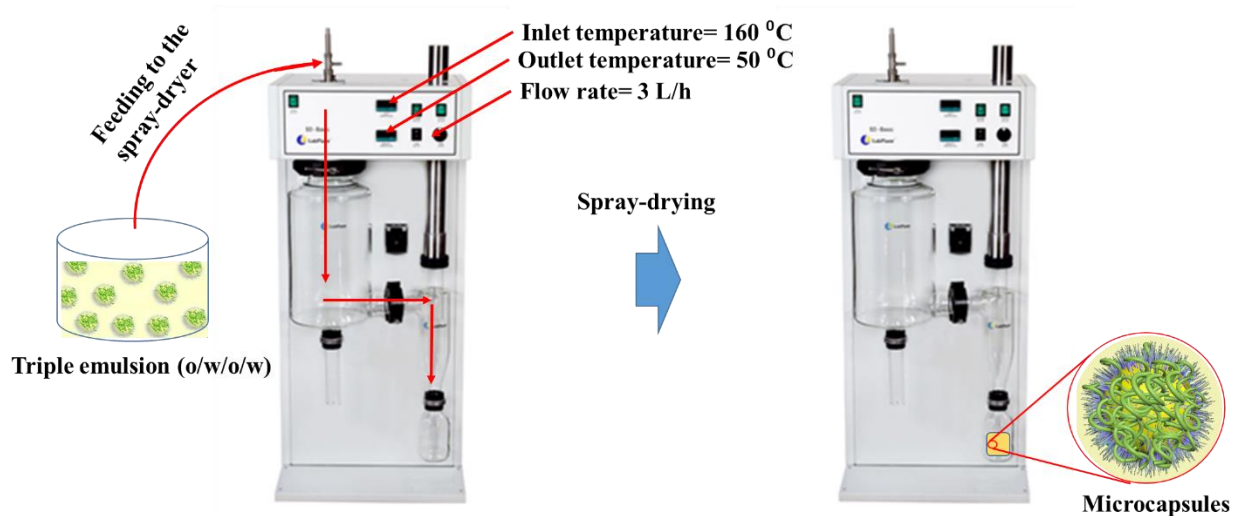


Figure S7.1. The schematic of spray-drying setup.

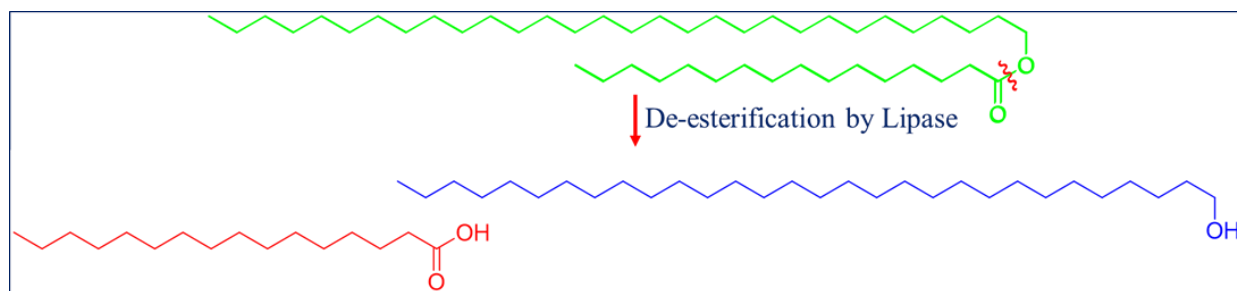


Figure S7.2. Proposed mechanism for de-esterification of triacontanyl palmitate by lipase

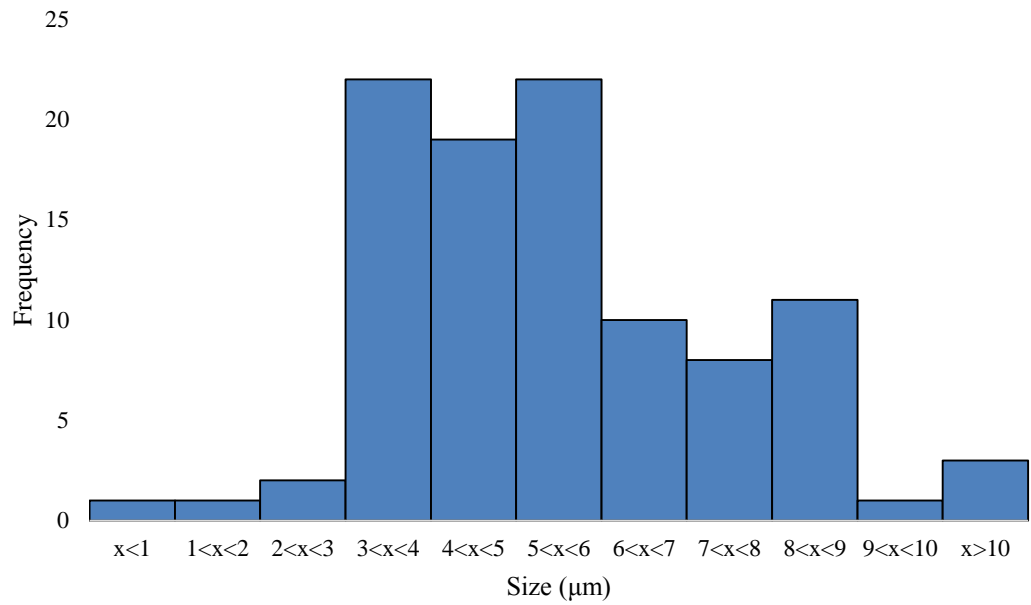


Figure S7.3. Size distribution of microcapsules.

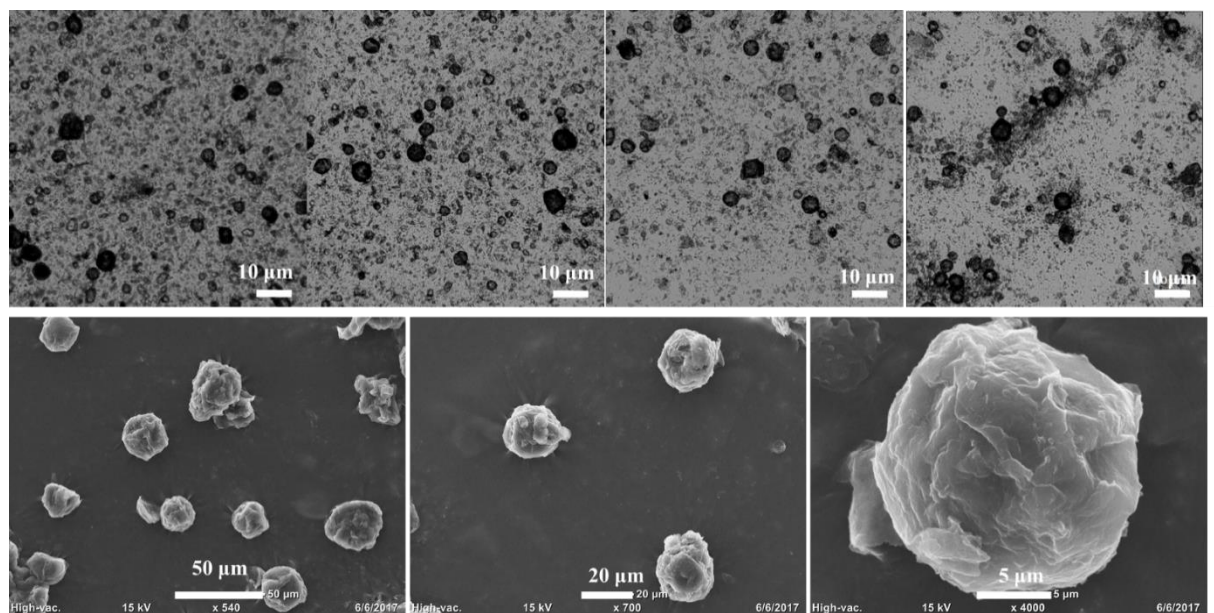


Figure S7.4. Additional Light microscopy (top) and electron microscopy (bottom) images of microcapsules.

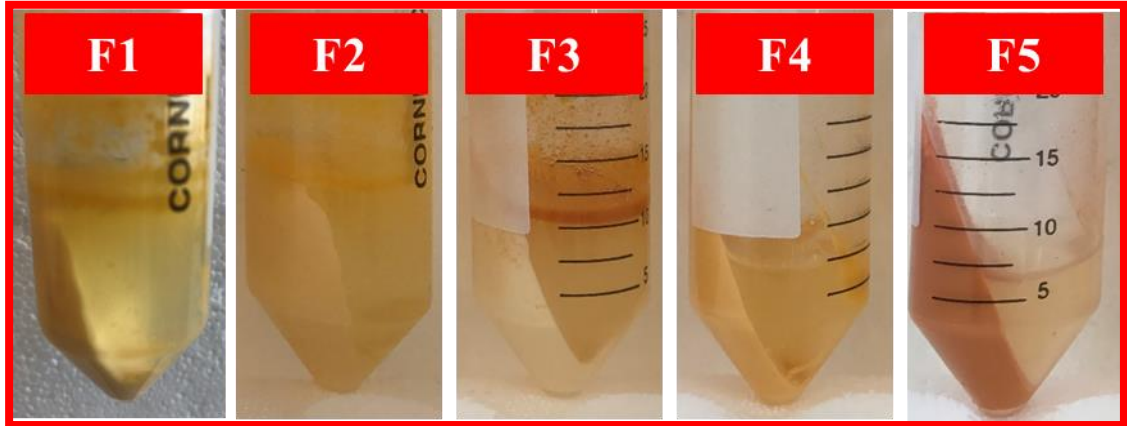


Figure S7.5. Simulation of Cheddar cheese making process for whole milk containing microcapsules obtained from different formulations

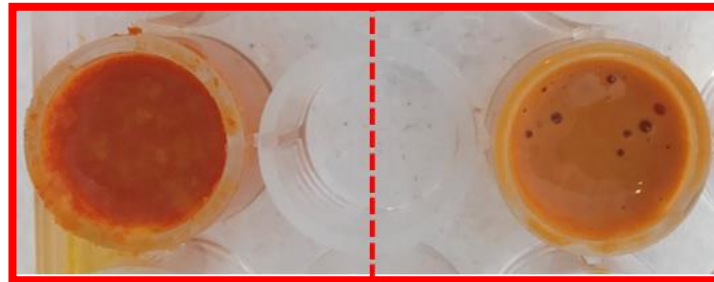


Figure S7.6. Cheese curd containing microcapsules after 14 days incubation at 26 °C; right: with lipase, left: without lipase (control)

Contributions

Raheleh Ravanfar wrote the manuscript and performed the experiments with support and advice from Dr. Alireza Abbaspourrad. Dr. Alireza Abbaspourrad supervised the project. Giovana Celli provided invaluable comments.

CHAPTER 8

CONCLUSION AND FUTURE DIRECTIONS

Our primary mission to find an alternative method to obtain the white whey was to extract annatto from the colored whey using a food-grade solvent, ethanol. However, upon the addition of ethanol we observed the whey to turn white in less than 5 s without the addition of any exogenous oxidizing agent. This observation sparks our attention to question if the addition of ethanol causes the oxidation of carotenoids in the presence of whey proteins. Thus, we thoroughly studied the catalyzed oxidation of carotenoids by lactoperoxidase in the presence of ethanol.¹⁵ Adding 30% (v/v) ethanol oxidizes annatto carotenoids in the presence of lactoperoxidase. This intriguing strategy catalyzes the oxidation of the carotenoids 360-times faster than hydrogen peroxide/lactoperoxidase oxidation and results in the conversion of more carotenoids to other colorless species and white whey proteins. Since ethanol is not an oxidizing agent, exploring the mechanism of the carotenoid catalyzed-oxidation reaction upon the addition of ethanol to the lactoperoxidase may have a prominent influence on the biochemistry of peroxidases. We chose horseradish peroxidase. The results showed that the heme in horseradish peroxidase is affected by ethanol. Thus, we proposed two hypothesis: first, ethanol can bind to the iron at the heme center of lactoperoxidase; second, ethanol can cause a conformational change in the enzyme in the way that the distal histidine at the top of heme center can bind to the iron at the heme center. We decided to use HRP to investigate these hypothesis because of its availability and the similarity of its heme structure to the heme structure of lactoperoxidase. We tested our first hypothesis, investigating the effect of ethanol on HRP. The results showed that ethanol contains

adventitious amount of H_2O_2 , which is not detectable by the current available methods such as hydrogen peroxide test strips. We showed that this adventitious amount of H_2O_2 was the reason for catalysis of oxidation reactions of carotenoids in the presence of heme-containing enzymes, such as lactoperoxidase and HRP. Our study resulted in presenting a new method to identify ultratrace amount of H_2O_2 in alcohols. We demonstrated that ferryl intermediates of HRP are potential candidates for the detection and quantification of H_2O_2 in alcohols at ppb levels through a simple UV/Vis spectrophotometric method. We measured the red shift in the Soret band in the optical spectra of the HRP from 402 nm up to 418 nm upon the addition of alcohols, and characterized the reversibility of this shift to 402 nm over time. Using this method, we can efficiently detect and quantify ppb levels of H_2O_2 in alcohols, where it is barely possible using other common methods such as hydrogen peroxide test strips. The EPR spectra and CV results confirm the formation and spontaneous decay of ferryl intermediates upon the reaction of ferric state of HRP and H_2O_2 . We also successfully detected an adventitious amount of H_2O_2 in alcohols, such as ethanol, glycerol, 2-chloroethanol, and isopropanol. This demonstration suggests a simple, cost-effective, and accurate method for the detection and quantification of ultratrace amount of H_2O_2 impurity in alcohols using UV/Vis spectrophotometry, which enables the use of this method in biological and chemical applications.

In parallel to test of the first hypothesis, we also examined the second hypothesis. We added exogenous histidine solution to the HRP to investigate the binding of histidine to the iron at the heme center. Despite our hypothesis, histidine could not react with the iron at the heme center. However, we demonstrate that histidine initiate a new

photocatalytic pathway of HRP without the addition of exogenous H_2O_2 . We demonstrate that HRP can catalyze the oxidation of organic molecules in the presence of His molecules 2-times faster than the traditional HRP/ H_2O_2 system. This HRP/His system is highly efficient under natural light and oxygen, however, these two key factors are critical to initiate the oxidation reactions. We probed the mechanism of how the HRP/His system oxidizes NBX, as a model organic substrate, and propose a new photocatalytic pathway for HRP to form ferryl intermediates. Our findings suggest that the His molecules are oxidized to cycloperoxide intermediates in the presence of light and oxygen, and this reaction can be facilitated by the heme group of HRP as a photosensitizer. The HRP captures the cycloperoxide to form ferryl intermediates of the heme, enabling the oxidation of organic substrates in the reaction mixture. We hypothesize that HRP/His system is faster because the cycloperoxide of His is more apt to polarize the O-O bond in comparison with H_2O_2 , expediting the formation of ferryl intermediates and the subsequent oxidation of organic substrates. This photocatalytic pathway of HRP can open potential applications, particularly in bioelectrocatalysis and catalysis of chemical reactions.

The study on HRP/histidine system also resulted in new discoveries: first, the crystallization-induced fluorescence of amino acids in the crystalline solid state. Due to the application of long lived luminescent solid organic materials in electroluminescent devices, sensors, and cell imaging there has been a resurgent interest in the past few years towards the development of new organic molecules with room temperature fluorescence in the solid state.^{153, 169} In this work, we demonstrate that pure crystals of L-histidine, L-glutamine, L-isoleucine, L-asparagine, L-valine, L-threonine, and L-

methionine amino acids are fluorescent at room temperature, while none of these molecules are fluorescent in solution. Crystal structure, an emergent property, is not simply related to molecular structure.¹⁷⁰ In this work, we confirm this statement and anticipate that the restriction of intramolecular motion and electronic interactions among electron-rich groups in amino acids favored by their close proximity in the crystalline state are the most important factors for observing fluorescent amino acid crystals. However, we note that a conformation may also be responsible for the differences observed in the fluorescence emission intensity of these aromatic and nonaromatic amino acids. With the understanding that active intramolecular motion can effectively dissipate exciton energy, while restricted intramolecular motions can activate radiative transitions, numerous opportunities can be explored. Indeed, the principle of crystallization-induced emission may trigger new developments in an array of fields, ranging from bioimaging, chemosensing, optoelectronics, and stimuli-responsive systems.^{17, 152, 171-172}

Second, the L-histidine crystals contain hydrophobic domains within the structure's interior, and can serve as vehicles for the highly efficient entrapment and transport of hydrophobic small molecules. We demonstrate the entrapment of hydrophobic small molecules inside the hydrophobic domains of L-His crystals, providing a potential biocompatible platform for protecting hydrophobic drugs. Since the entrapment of hydrophobic small molecules is at the molecular level, the entrapment efficiency is relatively high and possibly depends on the molecular structure of the small molecules. The modification of the L-His crystals at the surface using polymers and/or hydrogels could enable intracellular trafficking and site-specific delivery of hydrophobic

therapeutics, providing a drug-delivery system with targeting features. For example, the L-His crystals with HA covalently bonded to their surface and loaded with DOX are able to target tumor cells and control the release of DOX in response to HAase overexpressed in these cells. The composition of the surface can be controlled and tuned for optimization with other enzymes and physiological media. Releasing the entrapped hydrophobic drugs as the HA-His crystals are degraded and dissolved in the aqueous media can also reduce the chance of local toxicity to normal cells due to drug aggregation. The successful entrapment and targeted release of hydrophobic small molecules in HA-His crystals suggests further study is warranted to probe the possible implementation of amino acid crystals in promoting the delivery of hydrophobic therapeutics with low solubility and/or delivery of a combination of hydrophobic drugs to treat multidrug resistance. This strategy helps to address issues related to the poor solubility and low bioavailability of such molecules. These L-His crystals can also be investigated in terms of improving the imaging and tracking of entrapped therapeutic agents due to the crystals' natural fluorescence properties. However, further research and *in vivo* studies are essential before the potential of HA-His crystals in cancer therapy can become a reality.

None of these studies can address the issues associated with obtaining the white whey protein from the yellow whey recovered from the Cheddar cheese making process. However, the last study on the entrapment of hydrophobic small molecules in L-histidine crystals motivated us to propose a microencapsulation technique as an alternative to obtain the white whey. Thus, we present a natural and simple enzyme-responsive core-shell-structured microcapsule to encapsulate carotenoids in the core

and control their release only when exposed to lipase. Since lipases are mainly found in cheese curds during cheese ripening, we apply the platform to selectively deliver the color to the cheese curd by lipase-triggered release, leaving the whey proteins colorless.¹⁷ An innovative microencapsulation design with an enzymatically controlled release is demonstrated, providing a controlled-release platform for the targeted delivery and release of color. We present this microcapsule design as an alternative method to isolate white whey from the Cheddar cheese-making process without the addition of external bleaching agents. The microcapsule shells are broken down during cheese ripening by lipases in the cheese curd and are shown to release the color evenly throughout the curd. The presence of casein, in combination with the other components in microcapsule architecture, directs the microcapsules to partition into the cheese curd and prevents them from being distributed into the whey. In this work, the microcapsule shell is designed using compounds that naturally contain ester bonds. In future applications, this design could incorporate other compounds that are artificially modified to contain ester bonds. Thus, the composition of the shell is controllable and tunable, and can be optimized²³⁸ to use with other enzymes in other food systems or physiological media. Additionally, this platform can be modified for further applications, such as targeted delivery of hydrophobic drugs. This enzyme-responsive platform can reduce the interference of lipase function on the oral bioavailability of hydrophobic drugs. For instance, increasing the beeswax ratio in the lipid layer of the microcapsule shell can guarantee the specificity of the cargo release, mostly in the presence of lipase. The lipase-degradable lipid layer of the microcapsule shell can reduce the inherent limitations of slow and incomplete dissolution of poorly water

soluble drugs and facilitate the formation of solubilized fragments from which absorption may occur. If such methodologies and platforms can be developed, it may then be possible to formulate bio-responsive platforms that offer substantial bioavailability advantages in a commercially relevant manner.

Although we started from Cheddar cheese, we could propose the special capabilities of HRP in this work, which can expand its application in immunochemistry,¹⁸ diagnostic assays,¹⁹ chemical reactions,²⁰ bioremediation,²¹ and fuel cells.²²

REFERENCES

1. Ravanfar, R.; Lawrence, P.; Kriner, K.; Abbaspourrad, A., Catalyzed Oxidation of Carotenoids by Lactoperoxidase in the Presence of Ethanol. *Journal of agricultural and food chemistry* **2019**, *67* (6), 1742-1748.
2. Celli, G. B.; Ravanfar, R.; Kaliappan, S.; Kapoor, R.; Abbaspourrad, A., Annatto-entrapped casein-chitosan complexes improve whey color quality after acid coagulation of milk. *Food chemistry* **2018**, *255*, 268-274.
3. Giuliano, G.; Rosati, C.; Bramley, P. M., To dye or not to dye: biochemistry of annatto unveiled. *TRENDS in Biotechnology* **2003**, *21* (12), 513-516.
4. Seifu, E.; Buys, E. M.; Donkin, E., Significance of the lactoperoxidase system in the dairy industry and its potential applications: a review. *Trends in Food Science & Technology* **2005**, *16* (4), 137-154.
5. Tahboub, Y. R.; Galijasevic, S.; Diamond, M. P.; Abu-Soud, H. M., Thiocyanate modulates the catalytic activity of mammalian peroxidases. *Journal of Biological Chemistry* **2005**.
6. Bafort, F.; Parisi, O.; Perraudin, J.-P.; Jijakli, M., Mode of action of lactoperoxidase as related to its antimicrobial activity: a review. *Enzyme research* **2014**, *2014*.
7. Britton, G., Carotenoids. In *Natural food colorants*, Springer: 1996; pp 197-243.
8. Campbell, R.; Kang, E.; Bastian, E.; Drake, M., The use of lactoperoxidase for the bleaching of fluid whey. *Journal of dairy science* **2012**, *95* (6), 2882-2890.
9. Filatov, M. A.; Balushev, S.; Landfester, K., Protection of densely populated excited triplet state ensembles against deactivation by molecular oxygen. *Chemical Society Reviews* **2016**, *45* (17), 4668-4689.
10. Winterbourn, C. C., Reconciling the chemistry and biology of reactive oxygen species. *Nature chemical biology* **2008**, *4* (5), 278.

11. Croissant, A.; Kang, E.; Campbell, R.; Bastian, E.; Drake, M., The effect of bleaching agent on the flavor of liquid whey and whey protein concentrate. *Journal of dairy science* **2009**, *92* (12), 5917-5927.
12. van Scheppingen, W. B.; Boogers, I. A.; Duchateau, A. L., Study on decomposition products of norbixin during bleaching with hydrogen peroxide and a peroxidase by means of UPLC-UV and mass spectrometry. *Food chemistry* **2012**, *132* (3), 1354-1359.
13. Qiu, Y.; Smith, T.; Foegeding, E.; Drake, M., The effect of microfiltration on color, flavor, and functionality of 80% whey protein concentrate. *Journal of dairy science* **2015**, *98* (9), 5862-5873.
14. Kang, E.; Campbell, R.; Bastian, E.; Drake, M., Invited review: Annatto usage and bleaching in dairy foods. *Journal of dairy science* **2010**, *93* (9), 3891-3901.
15. Ravanfar, R.; Lawrence, P.; Kriner, K.; Abbaspourrad, A., Catalyzed Oxidation of Carotenoids by Lactoperoxidase in the Presence of Ethanol. *Journal of agricultural and food chemistry* **2019**.
16. Ravanfar, R.; Abbaspourrad, A. J. A. A. M.; Interfaces, L-Histidine Crystals as Efficient Vehicles to Deliver Hydrophobic Molecules. **2019**.
17. Ravanfar, R.; Celli, G. B.; Abbaspourrad, A., Controlling the Release from Enzyme-responsive Microcapsules with a Smart Natural Shell. *ACS Applied Materials & Interfaces* **2018**, *10* (6), 6046-6053.
18. Xianyu, Y.; Chen, Y.; Jiang, X., Horseradish peroxidase-mediated, iodide-catalyzed cascade reaction for plasmonic immunoassays. *Analytical chemistry* **2015**, *87* (21), 10688-10692.
19. Martinez, A. W.; Phillips, S. T.; Butte, M. J.; Whitesides, G. M., Patterned paper as a platform for inexpensive, low-volume, portable bioassays. *Angewandte Chemie International Edition* **2007**, *46* (8), 1318-1320.
20. Lin, Y.; Zhou, Q.; Lin, Y.; Tang, D.; Niessner, R.; Knopp, D., Enzymatic hydrolysate-induced displacement reaction with multifunctional silica beads doped with horseradish peroxidase–thionine conjugate for ultrasensitive electrochemical immunoassay. *Analytical chemistry* **2015**, *87* (16), 8531-8540.
21. Bilal, M.; Iqbal, H. M.; Hu, H.; Wang, W.; Zhang, X., Development of horseradish peroxidase-based cross-linked enzyme aggregates and their environmental exploitation for bioremediation purposes. *Journal of environmental management* **2017**, *188*, 137-143.
22. Ramanavicius, A.; Kausaite-Minkstimiene, A.; Morkvenaite-Vilkonciene, I.; Genys, P.; Mikhailova, R.; Semashko, T.; Voronovic, J.; Ramanaviciene, A., Biofuel cell based on glucose oxidase from *Penicillium funiculosum* 46.1 and horseradish peroxidase. *Chemical Engineering Journal* **2015**, *264*, 165-173.
23. Zhang, Y.; Tsitkov, S.; Hess, H., Proximity does not contribute to activity enhancement in the glucose oxidase–horseradish peroxidase cascade. *Nature communications* **2016**, *7*, 13982.
24. Gosling, J. P., A decade of development in immunoassay methodology. *Clinical chemistry* **1990**, *36* (8), 1408-1427.
25. Krainer, F. W.; Glieder, A., An updated view on horseradish peroxidases: recombinant production and biotechnological applications. *Applied microbiology and biotechnology* **2015**, *99* (4), 1611-1625.

26. Fukuoka, T.; Tonami, H.; Maruichi, N.; Uyama, H.; Kobayashi, S.; Higashimura, H., Peroxidase-Catalyzed Oxidative Polymerization of 4, 4'-Dihydroxydiphenyl Ether. Formation of α , ω -Hydroxyoligo (1, 4-phenylene oxide) through an Unusual Reaction Pathway. *Macromolecules* **2000**, *33* (24), 9152-9155.
27. PAPPAS, H. S.; CASS, A. E., A step towards understanding the folding mechanism of horseradish peroxidase: tryptophan fluorescence and circular dichroism equilibrium studies. *European journal of biochemistry* **1993**, *212* (1), 227-235.
28. Dequaire, M.; Limoges, B.; Moiroux, J.; Savéant, J.-M., Mediated electrochemistry of horseradish peroxidase. Catalysis and inhibition. *Journal of the American Chemical Society* **2002**, *124* (2), 240-253.
29. Campomanes, P.; Rothlisberger, U.; Alfonso-Prieto, M.; Rovira, C., The molecular mechanism of the catalase-like activity in horseradish peroxidase. *Journal of the American Chemical Society* **2015**, *137* (34), 11170-11178.
30. Erman, J. E.; Vitello, L. B.; Miller, M. A.; Kraut, J., Active-site mutations in cytochrome c peroxidase: a critical role for histidine-52 in the rate of formation of compound I. *Journal of the American Chemical Society* **1992**, *114* (16), 6592-6593.
31. Poulos, T. L.; Kraut, J., The stereochemistry of peroxidase catalysis. *Journal of Biological Chemistry* **1980**, *255* (17), 8199-8205.
32. Henriksen, A.; Smith, A. T.; Gajhede, M., The structures of the horseradish peroxidase C-ferulic acid complex and the ternary complex with cyanide suggest how peroxidases oxidize small phenolic substrates. *Journal of Biological Chemistry* **1999**, *274* (49), 35005-35011.
33. Casadei, C. M.; Gumiero, A.; Metcalfe, C. L.; Murphy, E. J.; Basran, J.; Teixeira, S. C.; Schrader, T. E.; Fielding, A. J.; Ostermann, A.; Blakeley, M. P., Neutron cryo-crystallography captures the protonation state of ferryl heme in a peroxidase. *Science* **2014**, *345* (6193), 193-197.
34. Karlin, K. D., Bioinorganic chemistry: model offers intermediate insight. *Nature* **2010**, *463* (7278), 168.
35. Sligar, S. G., Glimpsing the critical intermediate in cytochrome P450 oxidations. *Science* **2010**, *330* (6006), 924-925.
36. Groves, J. T., Enzymatic C-H bond activation: Using push to get pull. *Nature chemistry* **2014**, *6* (2), 89.
37. Patterson, W. R.; Poulos, T. L.; Goodin, D. B., Identification of a Porphyrin. π . Cation Radical in Ascorbate Peroxidase Compound I. *Biochemistry* **1995**, *34* (13), 4342-4345.
38. Chreifi, G.; Baxter, E. L.; Doukov, T.; Cohen, A. E.; McPhillips, S. E.; Song, J.; Meharena, Y. T.; Soltis, S. M.; Poulos, T. L., Crystal structure of the pristine peroxidase ferryl center and its relevance to proton-coupled electron transfer. *Proceedings of the National Academy of Sciences* **2016**, *113* (5), 1226-1231.
39. Rodríguez-López, J. N.; Lowe, D. J.; Hernández-Ruiz, J.; Hiner, A. N.; García-Cánovas, F.; Thorneley, R. N., Mechanism of reaction of hydrogen peroxide with horseradish peroxidase: identification of intermediates in the catalytic cycle. *Journal of the American Chemical Society* **2001**, *123* (48), 11838-11847.
40. Dawson, J. H., Probing structure-function relations in heme-containing oxygenases and peroxidases. *science* **1988**, *240* (4851), 433-439.

41. Gajhede, M.; Schuller, D. J.; Henriksen, A.; Smith, A. T.; Poulos, T. L., Crystal structure of horseradish peroxidase C at 2.15 Å resolution. *Nature Structural and Molecular Biology* **1997**, *4* (12), 1032.
42. Vidossich, P.; Fiorin, G.; Alfonso-Prieto, M.; Derat, E.; Shaik, S.; Rovira, C., On the role of water in peroxidase catalysis: a theoretical investigation of HRP compound I formation. *The Journal of Physical Chemistry B* **2010**, *114* (15), 5161-5169.
43. Berglund, G. I.; Carlsson, G. H.; Smith, A. T.; Szöke, H.; Henriksen, A.; Hajdu, J., The catalytic pathway of horseradish peroxidase at high resolution. *Nature* **2002**, *417* (6887), 463.
44. Meharena, Y. T.; Doukov, T.; Li, H.; Soltis, S. M.; Poulos, T. L., Crystallographic and single-crystal spectral analysis of the peroxidase ferryl intermediate. *Biochemistry* **2010**, *49* (14), 2984-2986.
45. Rodriguez-Lopez, J. N.; Smith, A. T.; Thorneley, R. N., Role of arginine 38 in horseradish peroxidase a critical residue for substrate binding and catalysis. *Journal of Biological Chemistry* **1996**, *271* (8), 4023-4030.
46. Blumberg, W.; Peisach, J.; Wittenberg, B. A.; Wittenberg, J. B., The Electronic Structure of Protoheme Proteins I. An Electron Paramagnetic Resonance and Optical Study of Horseradish Peroxidase and its Derivatives. *Journal of Biological Chemistry* **1968**, *243* (8), 1854-1862.
47. Kwon, H.; Basran, J.; Casadei, C. M.; Fielding, A. J.; Schrader, T. E.; Ostermann, A.; Devos, J. M.; Aller, P.; Blakeley, M. P.; Moody, P. C., Direct visualization of a Fe (IV)-OH intermediate in a heme enzyme. *Nature communications* **2016**, *7*, 13445.
48. Wittenberg, B. A.; Kampa, L.; Wittenberg, J. B.; Blumberg, W.; Peisach, J., The Electronic Structure of Protoheme Proteins II. AN ELECTRON PARAMAGNETIC RESONANCE AND OPTICAL STUDY OF CYTOCHROME c PEROXIDASE AND ITS DERIVATIVES. *Journal of Biological Chemistry* **1968**, *243* (8), 1863-1870.
49. Dunford, H. B.; Hewson, W. D., Effect of mixed solvents on the formation of horseradish peroxidase compound I. The importance of diffusion-controlled reactions. *Biochemistry* **1977**, *16* (13), 2949-2957.
50. Tonomura, Y., Mechanism of action of peroxidase. *J. Jap. Biochem. Soc* **1953**, *25*, 175-183.
51. Baek, H. K.; Van Wart, H. E., Elementary steps in the reaction of horseradish peroxidase with several peroxides: kinetics and thermodynamics of formation of compound 0 and compound I. *Journal of the American Chemical Society* **1992**, *114* (2), 718-725.
52. Brill, A. S.; Castleman, B. W.; McKnight, M. E., Association of methanol and ethanol with heme proteins. *Biochemistry* **1976**, *15* (11), 2309-2316.
53. Herskovits, T. T.; Gadegbeku, B.; Jaillet, H., On the structural stability and solvent denaturation of proteins I. Denaturation by the alcohols and glycols. *Journal of Biological Chemistry* **1970**, *245* (10), 2588-2598.
54. Asakura, T.; Adachi, K.; Schwartz, E., Stabilizing effect of various organic solvents on protein. *Journal of Biological Chemistry* **1978**, *253* (18), 6423-6425.
55. Ryu, K.; Dordick, J. S., How do organic solvents affect peroxidase structure and function? *Biochemistry* **1992**, *31* (9), 2588-2598.

56. Sato, K.; Hasumi, H.; Tsukidate, A.; Sakurada, J.; Nakamura, S.; Hosoya, T., Effects of mixed solvents on three elementary steps in the reactions of horseradish peroxidase and lactoperoxidase. *Biochimica et Biophysica Acta (BBA)-Protein Structure and Molecular Enzymology* **1995**, *1253* (1), 94-102.
57. Marklund, S.; Ohlsson, P.-I.; Opara, A.; Paul, K.-G., The substrate profiles of the acidic and slightly basic horseradish peroxidases. *Biochimica et Biophysica Acta (BBA)-Enzymology* **1974**, *350* (2), 304-313.
58. Sivakolundu, S. G.; Mabrouk, P. A., Cytochrome c structure and redox function in mixed solvents are determined by the dielectric constant. *Journal of the American Chemical Society* **2000**, *122* (7), 1513-1521.
59. Yang, Y. R.; Liu, Y.; Yan, H., DNA nanostructures as programmable biomolecular scaffolds. *Bioconjugate chemistry* **2015**, *26* (8), 1381-1395.
60. Wilner, O. I.; Shimron, S.; Weizmann, Y.; Wang, Z.-G.; Willner, I., Self-assembly of enzymes on DNA scaffolds: en route to biocatalytic cascades and the synthesis of metallic nanowires. *Nano letters* **2009**, *9* (5), 2040-2043.
61. Wilner, O. I.; Weizmann, Y.; Gill, R.; Lioubashevski, O.; Freeman, R.; Willner, I., Enzyme cascades activated on topologically programmed DNA scaffolds. *Nature nanotechnology* **2009**, *4* (4), 249.
62. Fu, J.; Liu, M.; Liu, Y.; Woodbury, N. W.; Yan, H., Interenzyme substrate diffusion for an enzyme cascade organized on spatially addressable DNA nanostructures. *Journal of the American Chemical Society* **2012**, *134* (12), 5516-5519.
63. Fu, J.; Yang, Y. R.; Johnson-Buck, A.; Liu, M.; Liu, Y.; Walter, N. G.; Woodbury, N. W.; Yan, H., Multi-enzyme complexes on DNA scaffolds capable of substrate channelling with an artificial swinging arm. *Nature nanotechnology* **2014**, *9* (7), 531.
64. Hewson, W.; Dunford, H., Horseradish Peroxidase. XVIII. The Arrhenius Activation Energy for the Formation of Compound I. *Canadian Journal of Chemistry* **1975**, *53* (13), 1928-1932.
65. Rao, A. V.; Rao, L. G., Carotenoids and human health. *Pharmacological research* **2007**, *55* (3), 207-216.
66. Woodall, A. A.; Lee, S. W.-M.; Weesie, R. J.; Jackson, M. J.; Britton, G., Oxidation of carotenoids by free radicals: relationship between structure and reactivity. *Biochimica et Biophysica Acta (BBA)-General Subjects* **1997**, *1336* (1), 33-42.
67. Perera, C. O.; Yen, G. M., Functional properties of carotenoids in human health. *International Journal of Food Properties* **2007**, *10* (2), 201-230.
68. Foote, C. S.; Chang, Y. C.; Denny, R. W., Chemistry of singlet oxygen. X. Carotenoid quenching parallels biological protection. *Journal of the American Chemical Society* **1970**, *92* (17), 5216-5218.
69. Ramel, F.; Birtic, S.; Ginies, C.; Soubigou-Taconnat, L.; Triantaphylidès, C.; Havaux, M., Carotenoid oxidation products are stress signals that mediate gene responses to singlet oxygen in plants. *Proceedings of the National Academy of Sciences* **2012**, *109* (14), 5535-5540.
70. Krinsky, N. I.; Yeum, K.-J., Carotenoid-radical interactions. *Biochemical and biophysical research communications* **2003**, *305* (3), 754-760.

71. Kanner, J.; Kinsella, J. E., Lipid deterioration initiated by phagocytic cells in muscle foods: beta-carotene destruction of a myeloperoxidase-hydrogen peroxide-halide system. *Journal of Agricultural and Food Chemistry* **1983**, *31* (2), 370-376.
72. Young, R. H.; Wehrly, K.; Martin, R. L., Solvent effects in dye-sensitized photooxidation reactions. *Journal of the American Chemical Society* **1971**, *93* (22), 5774-5779.
73. Feldmeier, C.; Bartling, H.; Magerl, K.; Gschwind, R. M., LED-Illuminated NMR Studies of Flavin-Catalyzed Photooxidations Reveal Solvent Control of the Electron-Transfer Mechanism. *Angewandte Chemie International Edition* **2015**, *54* (4), 1347-1351.
74. Chen, Q.; Sheng, L.; Du, J.; Xi, G.; Zhang, S. X.-A., Photooxidation of oxazolidine molecular switches: uncovering an intramolecular ionization facilitated cyclization process. *Chemical Communications* **2018**, *54* (40), 5094-5097.
75. Preston, H.; Rickard, M., Extraction and chemistry of annatto. *Food Chemistry* **1980**, *5* (1), 47-56.
76. Pruitt, K.; Kamau, D., The lactoperoxidase system of bovine and human milk. Elsevier Applied Science, London: 1991; pp 133-74.
77. Ravanfar, R.; Niakousari, M.; Maftoonazad, N., Postharvest sour cherry quality and safety maintenance by exposure to Hot-water or treatment with fresh Aloe vera gel. *Journal of food science and technology* **2014**, *51* (10), 2872-2876.
78. Chiu, C. K.; Etzel, M. R., Fractionation of lactoperoxidase and lactoferrin from bovine whey using a cation exchange membrane. *Journal of Food Science* **1997**, *62* (5), 996-1000.
79. Listiyani, M.; Campbell, R.; Miracle, R.; Barbano, D.; Gerard, P.; Drake, M., Effect of temperature and bleaching agent on bleaching of liquid Cheddar whey. *Journal of dairy science* **2012**, *95* (1), 36-49.
80. Virion, A.; Pommier, J.; Deme, D.; Nunez, J., Kinetics of thyroglobulin iodination and thyroid hormone synthesis catalyzed by peroxidases: the role of H₂O₂. *European journal of biochemistry* **1981**, *117* (1), 103-109.
81. Board, R., Natural antimicrobials from animals. In *New methods of food preservation*, Springer: 1995; pp 40-57.
82. Paul, K.; Ohlsson, P., The chemical structure of lactoperoxidase. Marcel Dekker: New York: 1985; pp 15-30.
83. Kussendrager, K. D.; Van Hooijdonk, A., Lactoperoxidase: physico-chemical properties, occurrence, mechanism of action and applications. *British Journal of Nutrition* **2000**, *84* (S1), 19-25.
84. Mansson-Rahemtulla, B.; Baldone, D.; Pruitt, K.; Rahemtulla, F., Specific assays for peroxidases in human saliva. *Archives of oral biology* **1986**, *31* (10), 661-668.
85. Shing, K.-P.; Cao, B.; Liu, Y.; Lee, H. K.; Li, M.-D.; Phillips, D. L.; Chang, X.-Y.; Che, C.-M., Arylruthenium (III) Porphyrin-Catalyzed C-H Oxidation and Epoxidation at Room Temperature and [RuV (Por)(O)(Ph)] Intermediate by Spectroscopic Analysis and Density Functional Theory Calculations. *Journal of the American Chemical Society* **2018**.
86. Berthomieu, C.; Boussac, A.; Maentele, W.; Breton, J.; Nabdryk, E., Molecular changes following oxidoreduction of cytochrome b559 characterized by Fourier

transform infrared difference spectroscopy and electron paramagnetic resonance: photooxidation in photosystem II and electrochemistry of isolated cytochrome b559 and iron protoporphyrin IX-bisimidazole model compounds. *Biochemistry* **1992**, *31* (46), 11460-11471.

87. Nakamura, S.; Nakamura, M.; Yamazaki, I.; Morrison, M., Reactions of ferryl lactoperoxidase (compound II) with sulfide and sulfhydryl compounds. *Journal of Biological Chemistry* **1984**, *259* (11), 7080-7085.

88. Gazaryan, I. G.; Lagrimini, L. M., Purification and unusual kinetic properties of a tobacco anionic peroxidase. *Phytochemistry* **1996**, *41* (4), 1029-1034.

89. Dawson, J. H.; Sono, M., Cytochrome P-450 and chloroperoxidase: thiolate-ligated heme enzymes. Spectroscopic determination of their active-site structures and mechanistic implications of thiolate ligation. *Chemical Reviews* **1987**, *87* (5), 1255-1276.

90. Rhee, S. G.; Kang, S. W.; Jeong, W.; Chang, T.-S.; Yang, K.-S.; Woo, H. A., Intracellular messenger function of hydrogen peroxide and its regulation by peroxiredoxins. *Current opinion in cell biology* **2005**, *17* (2), 183-189.

91. Halliwell, B.; Gutteridge, J., Free radicals, other reactive species and disease. *Free radicals in biology and medicine* **1999**, *3*, 617-783.

92. Ohshima, H.; Tatemichi, M.; Sawa, T., Chemical basis of inflammation-induced carcinogenesis. *Archives of biochemistry and biophysics* **2003**, *417* (1), 3-11.

93. Shah, A.; Channon, K., Free radicals and redox signalling in cardiovascular disease. *Heart* **2004**, *90* (5), 486-487.

94. Barnham, K. J.; Masters, C. L.; Bush, A. I., Neurodegenerative diseases and oxidative stress. *Nature reviews Drug discovery* **2004**, *3* (3), 205.

95. Usui, Y.; Sato, K.; Tanaka, M., Catalytic Dihydroxylation of Olefins with Hydrogen Peroxide: An Organic-Solvent-and Metal-Free System. *Angewandte Chemie International Edition* **2003**, *42* (45), 5623-5625.

96. Khorami, H. A.; Botero-Cadavid, J. F.; Wild, P.; Djilali, N., Spectroscopic detection of Hydrogen peroxide with an optical fiber probe using chemically deposited Prussian blue. *Electrochimica Acta* **2014**, *115*, 416-424.

97. Pozio, A.; Silva, R.; De Francesco, M.; Giorgi, L., Nafion degradation in PEFCs from end plate iron contamination. *Electrochimica acta* **2003**, *48* (11), 1543-1549.

98. Kinumoto, T.; Inaba, M.; Nakayama, Y.; Ogata, K.; Umabayashi, R.; Tasaka, A.; Iriyama, Y.; Abe, T.; Ogumi, Z., Durability of perfluorinated ionomer membrane against hydrogen peroxide. *Journal of power Sources* **2006**, *158* (2), 1222-1228.

99. Salimi, A.; Hallaj, R.; Soltanian, S.; Mamkhezri, H., Nanomolar detection of hydrogen peroxide on glassy carbon electrode modified with electrodeposited cobalt oxide nanoparticles. *Analytica Chimica Acta* **2007**, *594* (1), 24-31.

100. Cohen, G.; Hochstein, P., Generation of hydrogen peroxide in erythrocytes by hemolytic agents. *Biochemistry* **1964**, *3* (7), 895-900.

101. Albers, A. E.; Okreglak, V. S.; Chang, C. J., A FRET-based approach to ratiometric fluorescence detection of hydrogen peroxide. *Journal of the American Chemical Society* **2006**, *128* (30), 9640-9641.

102. Wang, J., Glucose biosensors: 40 years of advances and challenges. *Electroanalysis: An International Journal Devoted to Fundamental and Practical Aspects of Electroanalysis* **2001**, *13* (12), 983-988.

103. Quintino, M. S.; Winnischofer, H.; Araki, K.; Toma, H. E.; Angnes, L., Cobalt oxide/tetraruthenated cobalt-porphyrin composite for hydrogen peroxide amperometric sensors. *Analyst* **2005**, *130* (2), 221-226.
104. Cai, H.; Liu, X.; Zou, J.; Xiao, J.; Yuan, B.; Li, F.; Cheng, Q., Multi-wavelength spectrophotometric determination of hydrogen peroxide in water with peroxidase-catalyzed oxidation of ABTS. *Chemosphere* **2018**, *193*, 833-839.
105. Yuan, L.; Lin, W.; Xie, Y.; Chen, B.; Zhu, S., Single fluorescent probe responds to H₂O₂, NO, and H₂O₂/NO with three different sets of fluorescence signals. *Journal of the American Chemical Society* **2011**, *134* (2), 1305-1315.
106. King, D. W.; Cooper, W. J.; Rusak, S. A.; Peake, B. M.; Kiddle, J. J.; O'Sullivan, D. W.; Melamed, M. L.; Morgan, C. R.; Theberge, S. M., Flow injection analysis of H₂O₂ in natural waters using acridinium ester chemiluminescence: method development and optimization using a kinetic model. *Analytical Chemistry* **2007**, *79* (11), 4169-4176.
107. Ju, J.; Chen, W., In situ growth of surfactant-free gold nanoparticles on nitrogen-doped graphene quantum dots for electrochemical detection of hydrogen peroxide in biological environments. *Analytical chemistry* **2015**, *87* (3), 1903-1910.
108. Roberts, J. G.; Voinov, M. A.; Schmidt, A. C.; Smirnova, T. I.; Sombers, L. A., The hydroxyl radical is a critical intermediate in the voltammetric detection of hydrogen peroxide. *Journal of the American Chemical Society* **2016**, *138* (8), 2516-2519.
109. Yang, X.; Ma, K., Determination of hydrogen peroxide generated by reduced nicotinamide adenine dinucleotide oxidase. *Analytical biochemistry* **2005**, *344* (1), 130-134.
110. Wen, F.; Dong, Y.; Feng, L.; Wang, S.; Zhang, S.; Zhang, X., Horseradish peroxidase functionalized fluorescent gold nanoclusters for hydrogen peroxide sensing. *Analytical chemistry* **2011**, *83* (4), 1193-1196.
111. Diaz, A. N.; Peinado, M. R.; Minguez, M. T., Sol-gel horseradish peroxidase biosensor for hydrogen peroxide detection by chemiluminescence. *Analytica Chimica Acta* **1998**, *363* (2-3), 221-227.
112. Campos-Martin, J. M.; Blanco-Brieva, G.; Fierro, J. L., Hydrogen peroxide synthesis: an outlook beyond the anthraquinone process. *Angewandte Chemie International Edition* **2006**, *45* (42), 6962-6984.
113. Erman, J. E.; Yonetani, T., A kinetic study of the endogenous reduction of the oxidized sites in the primary cytochrome c peroxidase-hydrogen peroxide compound. *Biochimica et Biophysica Acta (BBA)-Protein Structure* **1975**, *393* (2), 350-357.
114. Zamocky, M.; Furtmüller, P. G.; Obinger, C., Evolution of catalases from bacteria to humans. *Antioxidants & redox signaling* **2008**, *10* (9), 1527-1548.
115. Mukai, M.; Nagano, S.; Tanaka, M.; Ishimori, K.; Morishima, I.; Ogura, T.; Watanabe, Y.; Kitagawa, T., Effects of concerted hydrogen bonding of distal histidine on active site structures of horseradish peroxidase. Resonance Raman studies with Asn70 mutants. *Journal of the American Chemical Society* **1997**, *119* (7), 1758-1766.
116. Zhou, S.; Fushinobu, S.; Kim, S.-W.; Nakanishi, Y.; Wakagi, T.; Shoun, H., *Aspergillus oryzae* flavohemoglobins promote oxidative damage by hydrogen peroxide. *Biochemical biophysical research communications* **2010**, *394* (3), 558-561.

117. Sampson, J. B.; Beckman, J. S., Hydrogen peroxide damages the zinc-binding site of zinc-deficient Cu, Zn superoxide dismutase. *Archives of biochemistry biophysics* **2001**, *392* (1), 8-13.
118. Newmyer, S. L.; de Montellano, P. R. O., Horseradish Peroxidase His-42→Ala, His-42→Val, and Phe-41→Ala Mutants HISTIDINE CATALYSIS AND CONTROL OF SUBSTRATE ACCESS TO THE HEME IRON. *Journal of Biological Chemistry* **1995**, *270* (33), 19430-19438.
119. Mukai, M.; Nagano, S.; Tanaka, M.; Ishimori, K.; Morishima, I.; Ogura, T.; Watanabe, Y.; Kitagawa, T., Effects of concerted hydrogen bonding of distal histidine on active site structures of horseradish peroxidase. Resonance Raman studies with Asn70 mutants. *Journal of the American Chemical Society* **1997**, *119* (7), 1758-1766.
120. Tomita, M.; Irie, M.; Ukita, T., Sensitized photooxidation of histidine and its derivatives. Products and mechanism of the reaction. *Biochemistry* **1969**, *8* (12), 5149-5160.
121. Agon, V. V.; Bubb, W. A.; Wright, A.; Hawkins, C. L.; Davies, M. J., Sensitizer-mediated photooxidation of histidine residues: evidence for the formation of reactive side-chain peroxides. *Free Radical Biology and Medicine* **2006**, *40* (4), 698-710.
122. Buettner, G. R., Spin Trapping: ESR parameters of spin adducts 1474 1528V. *Free radical biology and medicine* **1987**, *3* (4), 259-303.
123. Hawkins, C. L.; Davies, M. J., Detection and characterisation of radicals in biological materials using EPR methodology. *Biochimica et Biophysica Acta -General Subjects* **2014**, *1840* (2), 708-721.
124. Saito, I.; Matsuura, T.; Inoue, K., Formation of superoxide ion from singlet oxygen. Use of a water-soluble singlet oxygen source. *Journal of the American Chemical Society* **1981**, *103* (1), 188-190.
125. Camara, S.; Gilbert, B. C.; Meier, R. J.; van Duin, M.; Whitwood, A. C., EPR studies of peroxide decomposition, radical formation and reactions relevant to cross-linking and grafting in polyolefins. *Polymer* **2006**, *47* (13), 4683-4693.
126. Mauk, M. R.; Girotti, A. W., Protoporphyrin-apoperoxidase complex. Photooxidation studies. *Biochemistry* **1974**, *13* (8), 1757-1763.
127. Schneider, H. J., Binding mechanisms in supramolecular complexes. *Angewandte Chemie International Edition* **2009**, *48* (22), 3924-3977.
128. Gallivan, J. P.; Dougherty, D. A., Cation- π interactions in structural biology. *Proceedings of the National Academy of Sciences* **1999**, *96* (17), 9459-9464.
129. Rybtchinski, B., Adaptive supramolecular nanomaterials based on strong noncovalent interactions. *ACS nano* **2011**, *5* (9), 6791-6818.
130. Zeng, C.; Chen, Y.; Kirschbaum, K.; Lambright, K. J.; Jin, R., Emergence of hierarchical structural complexities in nanoparticles and their assembly. *Science* **2016**, *354* (6319), 1580-1584.
131. Liu, K.; Kang, Y.; Wang, Z.; Zhang, X., 25th anniversary article: Reversible and adaptive functional supramolecular materials: "Noncovalent interaction" matters. *Advanced Materials* **2013**, *25* (39), 5530-5548.
132. Liang, G.; Weng, L.-T.; Lam, J. W.; Qin, W.; Tang, B. Z., Crystallization-induced hybrid nano-sheets of fluorescent polymers with aggregation-induced emission characteristics for sensitive explosive detection. *ACS Macro Letters* **2013**, *3* (1), 21-25.

133. Morikawa, T. J.; Fujita, H.; Kitamura, A.; Horio, T.; Yamamoto, J.; Kinjo, M.; Sasaki, A.; Machiyama, H.; Yoshizawa, K.; Ichimura, T., Dependence of fluorescent protein brightness on protein concentration in solution and enhancement of it. *Scientific reports* **2016**, *6*, 22342.
134. Yang, Z.; Mao, Z.; Xie, Z.; Zhang, Y.; Liu, S.; Zhao, J.; Xu, J.; Chi, Z.; Aldred, M. P., Recent advances in organic thermally activated delayed fluorescence materials. *Chemical Society Reviews* **2017**, *46* (3), 915-1016.
135. Sinkeldam, R. W.; Greco, N. J.; Tor, Y., Fluorescent analogs of biomolecular building blocks: design, properties, and applications. *Chemical reviews* **2010**, *110* (5), 2579-2619.
136. Li, Q.; Tang, Y.; Hu, W.; Li, Z., Fluorescence of nonaromatic organic systems and room temperature phosphorescence of organic luminogens: The intrinsic principle and recent progress. *Small* **2018**, *14* (38), 1801560.
137. Ye, R.; Liu, Y.; Zhang, H.; Su, H.; Zhang, Y.; Xu, L.; Hu, R.; Kwok, R. T.; Wong, K. S.; Lam, J. W., Non-conventional fluorescent biogenic and synthetic polymers without aromatic rings. *Polymer Chemistry* **2017**, *8* (10), 1722-1727.
138. Zhou, Q.; Cao, B.; Zhu, C.; Xu, S.; Gong, Y.; Yuan, W. Z.; Zhang, Y., Clustering-Triggered Emission of Nonconjugated Polyacrylonitrile. *Small* **2016**, *12* (47), 6586-6592.
139. Del Mercato, L. L.; Pompa, P. P.; Maruccio, G.; Della Torre, A.; Sabella, S.; Tamburro, A. M.; Cingolani, R.; Rinaldi, R., Charge transport and intrinsic fluorescence in amyloid-like fibrils. *Proceedings of the National Academy of Sciences* **2007**, *104* (46), 18019-18024.
140. Wu, W.; Tang, R.; Li, Q.; Li, Z., Functional hyperbranched polymers with advanced optical, electrical and magnetic properties. *Chemical Society Reviews* **2015**, *44* (12), 3997-4022.
141. Pinotsi, D.; Grisanti, L.; Mahou, P.; Gebauer, R.; Kaminski, C. F.; Hassanali, A.; Kaminski Schierle, G. S., Proton transfer and structure-specific fluorescence in hydrogen bond-rich protein structures. *Journal of the American Chemical Society* **2016**, *138* (9), 3046-3057.
142. Shukla, A.; Mukherjee, S.; Sharma, S.; Agrawal, V.; Kishan, K. R.; Guptasarma, P.; biophysics, A novel UV laser-induced visible blue radiation from protein crystals and aggregates: scattering artifacts or fluorescence transitions of peptide electrons delocalized through hydrogen bonding? *Archives of biochemistry and biophysics* **2004**, *428* (2), 144-153.
143. Lukk, T.; Gillilan, R. E.; Szebenyi, D. M.; Zipfel, W. R., A visible-light-excited fluorescence method for imaging protein crystals without added dyes. *Journal of applied crystallography* **2016**, *49* (1), 234-240.
144. Yang, J.; Li, L.; Yu, Y.; Ren, Z.; Peng, Q.; Ye, S.; Li, Q.; Li, Z., Blue pyrene-based AIEgens: Inhibited intermolecular π - π stacking through the introduction of substituents with controllable intramolecular conjugation, and high external quantum efficiencies up to 3.46% in non-doped OLEDs. *Materials Chemistry Frontiers* **2017**, *1* (1), 91-99.
145. Wang, C.; Li, L.; Zhan, X.; Ruan, Z.; Xie, Y.; Hu, Q.; Ye, S.; Li, Q.; Li, Z., Blue AIEgens bearing triphenylethylene peripheral: adjustable intramolecular conjugation and good device performance. *Science bulletin* **2016**, *61* (22), 1746-1755.

146. Zhu, S.; Song, Y.; Shao, J.; Zhao, X.; Yang, B., Non-Conjugated Polymer Dots with Crosslink-Enhanced Emission in the Absence of Fluorophore Units. *Angewandte Chemie International Edition* **2015**, *54* (49), 14626-14637.
147. Wang, R.-b.; Yuan, W.-z.; Zhu, X.-y., Aggregation-induced emission of non-conjugated poly (amido amine) s: discovering, luminescent mechanism understanding and bioapplication. *Chinese Journal of Polymer Science* **2015**, *33* (5), 680-687.
148. Niu, S.; Yan, H.; Chen, Z.; Li, S.; Xu, P.; Zhi, X., Unanticipated bright blue fluorescence produced from novel hyperbranched polysiloxanes carrying unconjugated carbon-carbon double bonds and hydroxyl groups. *Polymer Chemistry* **2016**, *7* (22), 3747-3755.
149. Feng, T.; Zhu, S.; Zeng, Q.; Lu, S.; Tao, S.; Liu, J.; Yang, B.; interfaces, Supramolecular cross-link-regulated emission and related applications in polymer carbon dots. *ACS Applied Materials & Interfaces* **2017**, *10* (15), 12262-12277.
150. Teale, F.; Weber, G., Ultraviolet fluorescence of the aromatic amino acids. *Biochemical Journal* **1957**, *65* (3), 476.
151. Karreman, G.; Steele, R. H.; Szent-Györgyi, A., On resonance transfer of excitation energy between aromatic aminoacids in proteins. *Proceedings of the National Academy of Sciences* **1958**, *44* (2), 140.
152. Mei, J.; Leung, N. L.; Kwok, R. T.; Lam, J. W.; Tang, B. Z., Aggregation-induced emission: together we shine, united we soar! *Chem. Rev* **2015**, *115* (21), 11718-11940.
153. Mei, J.; Hong, Y.; Lam, J. W.; Qin, A.; Tang, Y.; Tang, B. Z., Aggregation-induced emission: the whole is more brilliant than the parts. *Advanced materials* **2014**, *26* (31), 5429-5479.
154. Gopikrishna, P.; Iyer, P. K., Monosubstituted Dibenzofulvene-Based Luminogens: Aggregation-Induced Emission Enhancement and Dual-State Emission. *The Journal of Physical Chemistry C* **2016**, *120* (46), 26556-26568.
155. Nishiuchi, T.; Tanaka, K.; Kuwatani, Y.; Sung, J.; Nishinaga, T.; Kim, D.; Iyoda, M., Solvent-Induced Crystalline-State Emission and Multichromism of a Bent π -Surface System Composed of Dibenzocyclooctatetraene Units. *Chemistry—A European Journal* **2013**, *19* (13), 4110-4116.
156. Madden, J. J.; McGandy, E. L.; Seeman, N. C., The crystal structure of the orthorhombic form of L-(+)-histidine. *Acta Crystallographica Section B* **1972**, *28* (8), 2377-2382.
157. Wagner, A.; Luger, P., Charge density and topological analysis of l-glutamine. *Journal of Molecular Structure* **2001**, *595* (1-3), 39-46.
158. Weisinger-Lewin, Y.; Frolow, F.; McMullan, R.; Koetzle, T.; Lahav, M.; Leiserowitz, L., Reduction in crystal symmetry of a solid solution: a neutron diffraction study at 15 K of the host/guest system asparagine/aspartic acid. *Journal of the American Chemical Society* **1989**, *111* (3), 1035-1040.
159. Taratin, N.; Lorenz, H.; Binev, D.; Seidel-Morgenstern, A.; Kotelnikova, E., Solubility Equilibria and Crystallographic Characterization of the L-Threonine/L-allo-Threonine System, Part 2: Crystallographic Characterization of Solid Solutions in the Threonine Diastereomeric System. *Crystal Growth Design* **2014**, *15* (1), 137-144.

160. Görbitz, C.; Dalhus, B., l-Isoleucine, Redetermination at 120K. *Acta Crystallographica Section C: Crystal Structure Communications* **1996**, *52* (6), 1464-1466.
161. Torii, K.; Iitaka, Y., The crystal structure of L-valine. *Acta Crystallographica Section B: Structural Crystallography* **1970**, *26* (9), 1317-1326.
162. Dalhus, B.; Görbitz, C. H., Crystal structures of hydrophobic amino acids I. Redeterminations of L-Methionine and L-Valine at 120 K. *Acta Chemica Scandinavica* **1996**, *50* (6), 544-548.
163. Zhang, F.; Wang, H.-W.; Tominaga, K.; Hayashi, M., Intramolecular vibrations in low-frequency normal modes of amino acids: L-alanine in the neat solid state. *Acta Chemica Scandinavica* **2015**, *119* (12), 3008-3022.
164. Bernstein, J.; Davis, R. E.; Shimoni, L.; Chang, N. L., Patterns in hydrogen bonding: functionality and graph set analysis in crystals. *Angewandte Chemie International Edition in English* **1995**, *34* (15), 1555-1573.
165. Dong, Y.; Lam, J. W.; Qin, A.; Li, Z.; Sun, J.; Sung, H. H.-Y.; Williams, I. D.; Tang, B. Z., Switching the light emission of (4-biphenyl) phenyldibenzofulvene by morphological modulation: crystallization-induced emission enhancement. *Chemical Communications* **2007**, (1), 40-42.
166. Dong, Y.; Xu, B.; Zhang, J.; Tan, X.; Wang, L.; Chen, J.; Lv, H.; Wen, S.; Li, B.; Ye, L., Piezochromic Luminescence Based on the Molecular Aggregation of 9, 10-Bis ((E)-2-(pyrid-2-yl) vinyl) anthracene. *Angewandte Chemie International Edition* **2012**, *51* (43), 10782-10785.
167. Han, T.; Feng, X.; Chen, D.; Dong, Y., A diethylaminophenol functionalized Schiff base: crystallization-induced emission-enhancement, switchable fluorescence and application for security printing and data storage. *Journal of Materials Chemistry C* **2015**, *3* (28), 7446-7454.
168. Potticary, J.; Jensen, T. T.; Hall, S. R., Nanostructural origin of blue fluorescence in the mineral karpaitite. *Scientific reports* **2017**, *7* (1), 9867.
169. Baroncini, M.; Bergamini, G.; Ceroni, P., Rigidification or interaction-induced phosphorescence of organic molecules. *Chemical Communications* **2017**, *53* (13), 2081-2093.
170. Desiraju, G. R., Crystal engineering: from molecule to crystal. *Journal of the American Chemical Society* **2013**, *135* (27), 9952-9967.
171. Ravanfar, R.; Comunian, T. A.; Abbaspourrad, A., Thermoresponsive, Water-dispersible Microcapsules with a Lipid-polysaccharide Shell to Protect Heat-sensitive Colorants. *Food Hydrocolloids* **2018**.
172. Ravanfar, R.; Tamaddon, A. M.; Niakousari, M.; Moein, M. R., Preservation of Anthocyanins in Solid Lipid Nanoparticles: Optimization of a Microemulsion Dilution Method Using the Plackett-Burman and Box-Behnken Designs. *Food Chemistry* **2016**, *199*, 573-580.
173. Liu, Z.; Robinson, J. T.; Sun, X.; Dai, H., PEGylated Nanographene Oxide for Delivery of Water-insoluble Cancer Drugs. *Journal of the American Chemical Society* **2008**, *130* (33), 10876-10877.
174. Lipinski, C. A.; Lombardo, F.; Dominy, B. W.; Feeney, P., Experimental and Computational Approaches to Estimate Solubility and Permeability in Drug Discovery and Development Settings. *Advanced Drug Delivery Reviews* **2012**, *64*, 4-17.

175. Fernandez, A.-M.; Van derpoorten, K.; Dasnois, L.; Lebtahi, K.; Dubois, V.; Lobl, T. J.; Gangwar, S.; Oliyai, C.; Lewis, E. R.; Shochat, D., N-Succinyl-(β -Alanyl-L-Leucyl-L-Alanyl-L-Leucyl) Doxorubicin: An Extracellularly Tumor-activated Prodrug Devoid of Intravenous Acute Toxicity. *Journal of Medicinal Chemistry* **2001**, *44* (22), 3750-3753.
176. Allen, T. M.; Cullis, P. R., Drug Delivery Systems: Entering the Mainstream. *Science* **2004**, *303* (5665), 1818-1822.
177. Fritze, A.; Hens, F.; Kimpfler, A.; Schubert, R.; Peschka-Süss, R., Remote Loading of Doxorubicin into Liposomes Driven by a Transmembrane Phosphate Gradient. *Biochimica et Biophysica Acta (BBA)-Biomembranes* **2006**, *1758* (10), 1633-1640.
178. Wang, S.; Konorev, E. A.; Kotamraju, S.; Joseph, J.; Kalivendi, S.; Kalyanaraman, B., Doxorubicin Induces Apoptosis in Normal and Tumor Cells via Distinctly Different Mechanisms Intermediacy of H₂O₂-and p53-Dependent Pathways. *Journal of Biological Chemistry* **2004**, *279* (24), 25535-25543.
179. Torchilin, V., Targeted polymeric micelles for delivery of poorly soluble drugs. *Cellular and Molecular Life Sciences CMLS* **2004**, *61* (19-20), 2549-2559.
180. Kim, C. K.; Ghosh, P.; Pagliuca, C.; Zhu, Z.-J.; Menichetti, S.; Rotello, V. M., Entrapment of Hydrophobic Drugs in Nanoparticle Monolayers with Efficient Release into Cancer Cells. *Journal of the American Chemical Society* **2009**, *131* (4), 1360-1361.
181. Allen, T. M.; Cullis, P. R., Liposomal Drug Delivery Systems: from Concept to Clinical Applications. *Advanced Drug Delivery Reviews* **2013**, *65* (1), 36-48.
182. Hoffman, A. S., Stimuli-responsive Polymers: Biomedical Applications and Challenges for Clinical Translation. *Advanced Drug Delivery Reviews* **2013**, *65* (1), 10-16.
183. Zhu, Q.; Chen, X.; Xu, X.; Zhang, Y.; Zhang, C.; Mo, R., Tumor-Specific Self-Degradable Nanogels as Potential Carriers for Systemic Delivery of Anticancer Proteins. *Advanced Functional Materials* **2018**, *28* (17), 1707371.
184. Maiti, C.; Parida, S.; Kayal, S.; Maiti, S.; Mandal, M.; Dhara, D., Redox-Responsive Core Cross-Linked Block Copolymer Micelles for Overcoming Multidrug Resistance in Cancer Cells. *ACS Applied Materials & Interfaces* **2018**.
185. Miatmoko, A.; Kawano, K.; Yonemochi, E.; Hattori, Y., Evaluation of Cisplatin-Loaded Polymeric Micelles and Hybrid Nanoparticles Containing Poly (Ethylene Oxide)-Block-Poly (Methacrylic Acid) on Tumor Delivery. *Pharmacology & Pharmacy* **2016**, *7* (01), 1.
186. Morgan, M. T.; Nakanishi, Y.; Kroll, D. J.; Griset, A. P.; Carnahan, M. A.; Wathier, M.; Oberlies, N. H.; Manikumar, G.; Wani, M. C.; Grinstaff, M. W., Dendrimer-encapsulated Camptothecins: Increased Solubility, Cellular Uptake, and Cellular Retention Affords Enhanced Anticancer Activity In Vitro. *Cancer Research* **2006**, *66* (24), 11913-11921.
187. Etbach, L.; Pfeiffer, A.; Weber, F.; Schieber, A., Characterization of Carotenoid Profiles in Goldenberry (*Physalis peruviana* L.) Fruits at Various Ripening Stages and in Different Plant Tissues by HPLC-DAD-APCI-MSn. *Food Chemistry* **2018**, *245*, 508-517.

188. Wu, X.; Biatry, B.; Cazeneuve, C.; Guy, R. H., Drug Delivery to the Skin from Sub-micron Polymeric Particle Formulations: Influence of Particle Size and Polymer Hydrophobicity. *Pharmaceutical Research* **2009**, *26* (8), 1995-2001.
189. Jia, H.; Hou, D.; Dai, M.; Lu, H.; Yan, C., Effects of Root Exudates on the Mobility of Pyrene in Mangrove Sediment-water System. *Catena* **2018**, *162*, 396-401.
190. Chi, Y.; Yin, X.; Sun, K.; Feng, S.; Liu, J.; Chen, D.; Guo, C.; Wu, Z., Redox-sensitive and Hyaluronic Acid Functionalized Liposomes for Cytoplasmic Drug Delivery to Osteosarcoma in Animal Models. *Journal of Controlled Release* **2017**, *261*, 113-125.
191. Hosangadi, B. D.; Dave, R. H., An Efficient General Method for Esterification of Aromatic Carboxylic Acids. *Tetrahedron Letters* **1996**, *37* (35), 6375-6378.
192. Ouasti, S.; Donno, R.; Cellesi, F.; Sherratt, M. J.; Terenghi, G.; Tirelli, N., Network Connectivity, Mechanical Properties and Cell Adhesion for Hyaluronic Acid/PEG Hydrogels. *Biomaterials* **2011**, *32* (27), 6456-6470.
193. Fan, Y.; Sahdev, P.; Ochyl, L. J.; Akerberg, J. J.; Moon, J. J., Cationic Liposome-hyaluronic Acid Hybrid Nanoparticles for Intranasal Vaccination with Subunit Antigens. *Journal of Controlled Release* **2015**, *208*, 121-129.
194. Warzajtis, B.; Glišić, B. Đ.; Savić, N. D.; Pavic, A.; Vojnovic, S.; Veselinović, A.; Nikodinovic-Runic, J.; Rychlewska, U.; Djuran, M. I., Mononuclear Gold (III) Complexes with L-Histidine-containing Dipeptides: Tuning the Structural and Biological Properties by Variation of the N-terminal Amino Acid and Counter Anion. *Dalton Transactions* **2017**, *46* (8), 2594-2608.
195. Preimesberger, M. R.; Majumdar, A.; Rice, S. L.; Que, L.; Lecomte, J. T., Helix-Capping Histidines: Diversity of N-H...N Hydrogen Bond Strength Revealed by 2h J NN Scalar Couplings. *Biochemistry* **2015**, *54* (46), 6896-6908.
196. Li, S.; Hong, M., Protonation, Tautomerization, and Rotameric Structure of Histidine: A Comprehensive Study by Magic-angle-spinning Solid-state NMR. *Journal of the American Chemical Society* **2011**, *133* (5), 1534-1544.
197. Roelands, C. M.; Jiang, S.; Kitamura, M.; ter Horst, J. H.; Kramer, H. J.; Jansens, P., Antisolvent Crystallization of the Polymorphs of L-Histidine as a Function of Supersaturation Ratio and of Solvent Composition. *Crystal Growth and design* **2006**, *6* (4), 955-963.
198. Madden, J. J.; McGandy, E. L.; Seeman, N. C., The Crystal Structure of the Orthorhombic Form of L-(+)-Histidine. *Acta Crystallographica Section B: Structural Crystallography* **1972**, *28* (8), 2377-2382.
199. Wantha, L.; Punmalee, N.; Sawaddiphol, V.; Flood, A. E., Effect of Ethanol on Crystallization of the Polymorphs of L-Histidine. *Journal of Crystal Growth* **2018**, *490*, 65-70.
200. Chen, R. J.; Zhang, Y.; Wang, D.; Dai, H., Noncovalent Sidewall Functionalization of Single-walled Carbon Nanotubes for Protein Immobilization. *Journal of the American Chemical Society* **2001**, *123* (16), 3838-3839.
201. Liu, Z.; Sun, X.; Nakayama-Ratchford, N.; Dai, H., Supramolecular Chemistry on Water-soluble Carbon Nanotubes for Drug Loading and Delivery. *ACS Nano* **2007**, *1* (1), 50-56.
202. Guo, W.; Liu, J.; Weidler, P. G.; Liu, J.; Neumann, T.; Danilov, D.; Wenzel, W.; Feldmann, C.; Wöll, C., Loading of Ionic Compounds into Metal-organic Frameworks:

A Joint Theoretical and Experimental Study for the Case of La 3+. *Physical Chemistry Chemical Physics* **2014**, *16* (33), 17918-17923.

203. Lee, M.-Y.; Park, S.-J.; Park, K.; Kim, K. S.; Lee, H.; Hahn, S. K., Target-specific Gene Silencing of Layer-by-layer Assembled Gold–cysteamine/siRNA/PEI/HA Nanocomplex. *ACS Nano* **2011**, *5* (8), 6138-6147.

204. Wang, L.; Su, W.; Liu, Z.; Zhou, M.; Chen, S.; Chen, Y.; Lu, D.; Liu, Y.; Fan, Y.; Zheng, Y., CD44 Antibody-targeted Liposomal Nanoparticles for Molecular Imaging and Therapy of Hepatocellular Carcinoma. *Biomaterials* **2012**, *33* (20), 5107-5114.

205. Li, J.; Huo, M.; Wang, J.; Zhou, J.; Mohammad, J. M.; Zhang, Y.; Zhu, Q.; Waddad, A. Y.; Zhang, Q., Redox-sensitive Micelles Self-assembled from Amphiphilic Hyaluronic Acid-deoxycholic Acid Conjugates for Targeted Intracellular Delivery of Paclitaxel. *Biomaterials* **2012**, *33* (7), 2310-2320.

206. Jiang, T.; Zhang, Z.; Zhang, Y.; Lv, H.; Zhou, J.; Li, C.; Hou, L.; Zhang, Q., Dual-functional Liposomes Based on pH-responsive Cell-penetrating Peptide and Hyaluronic Acid for Tumor-targeted Anticancer Drug Delivery. *Biomaterials* **2012**, *33* (36), 9246-9258.

207. Choi, K. Y.; Yoon, H. Y.; Kim, J.-H.; Bae, S. M.; Park, R.-W.; Kang, Y. M.; Kim, I.-S.; Kwon, I. C.; Choi, K.; Jeong, S. Y., Smart Nanocarrier Based on PEGylated Hyaluronic Acid for Cancer Therapy. *ACS Nano* **2011**, *5* (11), 8591-8599.

208. Rosenbauer, E.-M.; Wagner, M.; Musyanovych, A.; Landfester, K., Controlled release from polyurethane nanocapsules via pH-, UV-light-or temperature-induced stimuli. *Macromolecules* **2010**, *43* (11), 5083-5093.

209. Abbaspourrad, A.; Carroll, N. J.; Kim, S.-H.; Weitz, D. A., Polymer microcapsules with programmable active release. *Journal of the American Chemical Society* **2013**, *135* (20), 7744-7750.

210. Abbaspourrad, A.; Datta, S. S.; Weitz, D. A., Controlling release from pH-responsive microcapsules. *Langmuir* **2013**, *29* (41), 12697-12702.

211. Comunian, T. A.; Ravanfar, R.; de Castro, I. A.; Dando, R.; Favaro-Trindade, C. S.; Abbaspourrad, A., Improving Oxidative Stability of Echium Oil Emulsions Fabricated by Microfluidics: Effect of Ionic Gelation and Phenolic Compounds. *Food Chemistry* **2017**, *233*, 125-134.

212. Wang, S.; Huang, P.; Chen, X., Hierarchical targeting strategy for enhanced tumor tissue accumulation/retention and cellular internalization. *Advanced Materials* **2016**, *28* (34), 7340-7364.

213. Lu, J.; Jiang, F.; Lu, A.; Zhang, G., Linkers having a crucial role in antibody–drug conjugates. *International journal of molecular sciences* **2016**, *17* (4), 561.

214. Yingchoncharoen, P.; Kalinowski, D. S.; Richardson, D. R., Lipid-based drug delivery systems in cancer therapy: what is available and what is yet to come. *Pharmacological reviews* **2016**, *68* (3), 701-787.

215. Imran, M.; Revol-Junelles, A.-M.; Paris, C.; Guedon, E.; Linder, M.; Desobry, S., Liposomal nanodelivery systems using soy and marine lecithin to encapsulate food biopreservative nisin. *LWT-Food Science and Technology* **2015**, *62* (1), 341-349.

216. Joye, I. J.; McClements, D. J., Biopolymer-based nanoparticles and microparticles: fabrication, characterization, and application. *Current Opinion in Colloid & Interface Science* **2014**, *19* (5), 417-427.

217. Mehrad, B.; Ravanfar, R.; Licker, J.; Regenstein, J. M.; Abbaspourrad, A., Enhancing the physicochemical stability of β -carotene solid lipid nanoparticle (SLNP) using whey protein isolate. *Food Research International* **2017**.
218. Comunian, T. A.; Ravanfar, R.; Selig, M. J.; Abbaspourrad, A., Influence of the Protein Type on the Stability of Fish Oil in Water Emulsion Obtained by Glass Microfluidic Device. *Food Hydrocolloids* **2017**.
219. Ravanfar, R.; Comunian, T. A.; Dando, R.; Abbaspourrad, A., Optimization of Microcapsules Shell Structure to Preserve Labile Compounds: A Comparison between Microfluidics and Conventional Homogenization Method. *Food Chemistry* **2018**, *241*, 460-467.
220. Fukui, Y.; Fujimoto, K., The preparation of sugar polymer-coated nanocapsules by the layer-by-layer deposition on the liposome. *Langmuir* **2009**, *25* (17), 10020-10025.
221. Tecante, A.; Santiago, M. d. C. N., Solution properties of κ -carrageenan and its interaction with other polysaccharides in aqueous media. In *Rheology*, InTech: 2012.
222. Mangione, M.; Giacomazza, D.; Bulone, D.; Martorana, V.; San Biagio, P., Thermoreversible gelation of κ -Carrageenan: relation between conformational transition and aggregation. *Biophysical Chemistry* **2003**, *104* (1), 95-105.
223. Wlodawer, P.; Lagwińska, E.; Barańska, J., Esterification of fatty acids in the wax moth haemolymph and its possible role in lipid transport. *Journal of insect physiology* **1966**, *12* (5), 547-560.
224. Wang, L.; Ando, S.; Ishida, Y.; Ohtani, H.; Tsuge, S.; Nakayama, T., Quantitative and discriminative analysis of carnauba waxes by reactive pyrolysis-GC in the presence of organic alkali using a vertical microfurnace pyrolyzer. *Journal of Analytical and Applied Pyrolysis* **2001**, *58*, 525-537.
225. Hargrove, J. L.; Greenspan, P.; Hartle, D. K., Nutritional significance and metabolism of very long chain fatty alcohols and acids from dietary waxes. *Experimental Biology and Medicine* **2004**, *229* (3), 215-226.
226. Abdikheibari, S.; Parvizi, R.; Moayed, M. H.; Zebarjad, S. M.; Sajjadi, S. A., Beeswax-colophony blend: a novel green organic coating for protection of steel drinking water storage tanks. *Metals* **2015**, *5* (3), 1645-1664.
227. Torres, O.; Agramonte, A.; Illnait, J.; Ferreiro, R. M.; Fernández, L.; Fernández, J. C., Treatment of hypercholesterolemia in NIDDM with policosanol. *Diabetes Care* **1995**, *18* (3), 393-397.
228. Zhu, L.; Kate, P.; Torchilin, V. P., Matrix metalloprotease 2-responsive multifunctional liposomal nanocarrier for enhanced tumor targeting. *ACS nano* **2012**, *6* (4), 3491-3498.
229. Harris, T. J.; von Maltzahn, G.; Lord, M. E.; Park, J. H.; Agrawal, A.; Min, D. H.; Sailor, M. J.; Bhatia, S. N., Protease-Triggered Unveiling of Bioactive Nanoparticles. *small* **2008**, *4* (9), 1307-1312.
230. Singh, N.; Karambelkar, A.; Gu, L.; Lin, K.; Miller, J. S.; Chen, C. S.; Sailor, M. J.; Bhatia, S. N., Bioresponsive mesoporous silica nanoparticles for triggered drug release. *Journal of the American Chemical Society* **2011**, *133* (49), 19582-19585.
231. Banerjee, J.; Hanson, A. J.; Gadam, B.; Elegbede, A. I.; Tobwala, S.; Ganguly, B.; Wagh, A. V.; Muhonen, W. W.; Law, B.; Shabb, J. B., Release of liposomal contents

- by cell-secreted matrix metalloproteinase-9. *Bioconjugate chemistry* **2009**, *20* (7), 1332-1339.
232. Chernov, A., Challenges in crystal growth science and the microgravity tool. *Advances in Crystal Growth Research*, ed. K. Sato, Y. Furokawa, K. Nakajima, Elsevier, Amsterdam **2001**.
233. Bunjes, H.; Koch, M. H.; Westesen, K., Influence of emulsifiers on the crystallization of solid lipid nanoparticles. *Journal of pharmaceutical sciences* **2003**, *92* (7), 1509-1520.
234. Wang, T. Y.; Huang, J., Synthesis and characterization of microencapsulated sodium phosphate dodecahydrate. *Journal of Applied Polymer Science* **2013**, *130* (3), 1516-1523.
235. Schlossbauer, A.; Kecht, J.; Bein, T., Biotin–Avidin as a Protease-Responsive Cap System for Controlled Guest Release from Colloidal Mesoporous Silica. *Angewandte Chemie* **2009**, *121* (17), 3138-3141.
236. Wilkinson, M.; Kilcawley, K., Mechanisms of incorporation and release of enzymes into cheese during ripening. *International Dairy Journal* **2005**, *15* (6), 817-830.
237. Nielsen, P. M., Process for producing cheese. Google Patents: 2003.
238. Ravanfar, R.; Tamadon, A. M.; Niakousari, M., Optimization of ultrasound assisted extraction of anthocyanins from red cabbage using Taguchi design method. *Journal of food science and technology* **2015**, *52* (12), 8140-8147.